# Mapping the Impact of Aerosol-Cloud Interactions on Cloud Formation and Warm-season Rainfall in Mountainous Regions Using Observations and Models

by

Yajuan Duan

Department of Civil and Environmental Engineering
Duke University

Date:_____

Approved:

_____
Ana P. Barros, Supervisor

_____
Michael H. Bergin

_____
Wenhong Li

_____
Markus D. Petters

_____
Jordi Vila-Guerau de Arellano

Dissertation submitted in partial fulfillment of
the requirements for the degree of Doctor
of Philosophy in the Department of
Civil and Environmental Engineering in the Graduate School
of Duke University

2017

ABSTRACT

Mapping the Impact of Aerosol-Cloud Interactions on Cloud Formation and Warm-season Rainfall in Mountainous Regions Using Observations and Models

by

Yajuan Duan

Department of Civil and Environmental Engineering
Duke University

Date:_____

Approved:

_____
Ana P. Barros, Supervisor

_____
Michael H. Bergin

_____
Wenhong Li

_____
Markus D. Petters

_____
Jordi Vila-Guerau de Arellano

An abstract of a dissertation submitted in partial
fulfillment of the requirements for the degree
of Doctor of Philosophy in the Department of
Civil and Environmental Engineering in the Graduate School of
Duke University

2017

## Abstract

Light rainfall (< 3 mm/hr) amounts to 30–70% of the annual water budget in the Southern Appalachian Mountains (SAM), a mid-latitude mid-mountain system in the SE CONUS. Topographic complexity favors the diurnal development of regional-scale convergence patterns that provide the moisture source for low-level clouds and fog (LLCF). Low-level moisture and cloud condensation nuclei (CCN) are distributed by ridge-valley circulations favoring LLCF formation that modulate the diurnal cycle of rainfall especially the mid-day peak. The overarching objective of this dissertation is to advance the quantitative understanding of the indirect effect of aerosols on the diurnal cycle of LLCF and warm-season precipitation in mountainous regions generally, and in the SAM in particular, for the purpose of improving the representation of orographic precipitation processes in remote sensing retrievals and physically-based models.

The research approach consists of integrating analysis of *in situ* observations from long-term observation networks and an intensive field campaign, multi-sensor satellite data, and modeling studies. In the first part of this dissertation, long-term satellite observations are analyzed to characterize the spatial and temporal variability of LLCF and to elucidate the physical basis of the space-time error structure in precipitation retrievals. Significantly underestimated precipitation errors are attributed to variations in low-level rainfall microstructure undetected by satellites. Column model simulations including observed LLCF microphysics demonstrate that seeder-feeder interactions (SFI) among

upper-level precipitation and LLCF contribute to an three-fold increase in observed rainfall accumulation and can enhance surface rainfall by up to ten-fold. The second part of this dissertation examines the indirect effect of aerosols on cloud formation and warm-season daytime precipitation in the SAM. A new entraining spectral cloud parcel model was developed and applied to provide the first assessment of aerosol-cloud interactions in the early development of mid-day cumulus congestus over the inner SAM. Leveraging comprehensive measurements from the Integrated Precipitation and Hydrology Experiment (IPHEx) in 2014, model results indicate that simulated spectra with a low value of condensation coefficient (0.01) are in good agreement with IPHEx aircraft observations. Further, to explore sensitivity of warm-season precipitation processes to CCN characteristics, detailed intercomparisons of Weather Research and Forecasting (WRF) model simulations using IPHEx and standard continental CCN spectra were conducted. The simulated CDNC using the local spectrum show better agreement with IPHEx airborne observations and better replicate the widespread low-level cloudiness around mid-day over the inner region. The local spectrum simulation also indicate suppressed early precipitation, enhanced ice processes tied to more vigorous vertical development of individual storm cells. The studied processes here are representative of dominant moist atmospheric processes in complex terrain and cloud forests in the humid tropics and extra-tropics, thus findings from this research in the SAM are transferable to mountainous areas elsewhere.

# Dedication

To my loving parents, Renhui Duan and Xiaoqin Sun, and my beloved husband Travis K. Knoll for their unconditional love and enduring support that always lighted up the road ahead.

# Contents

# List of Tables

# List of Figures

# Acknowledgements

There have been many people who have helped, encouraged, and supported me along the way in my dissertation work. To them I am extremely grateful because without them this dissertation would have not been possible.

First and foremost, I am greatly indebted to my advisor Ana P. Barros for her great mentorship and funding support throughout my graduate study and research work at Duke, which are essential to the completion of this dissertation. I particularly appreciate the amazing learning opportunity she has given me to work on several interesting and meaningful projects.

I am deeply grateful to my committee members Michael H. Bergin, Wenhong Li, Markus D. Petters, and Jordi Vila-Guerau de Arellano for their kind support and research guidance. I would like to extend special thanks to Markus D. Petters for providing aerosol and CCN measurements and valuable comments in Chapter 4.

Anna M. Wilson and Malarvizhi Arulraj deserve special thanks for the fog microphysics measurements used in Chapter 3. The work in Chapter 4 benefited greatly from the dedicated collaboration of many researchers during the IPHEx campaign: University of North Dakota flight scientists in particular Michael Poellot, Andrew Heymsfield, and David J. Delene for the flight data and advice with airborne data analysis, ACHIEVE team (Si-Chee Tsay and Adrian Loftus) for providing the W-band radar data, Anna M. Wilson for the deployment and maintenance of Duke's H2F mobility facility.

I would also like to gratefully acknowledge generous support from the NASA PMM program and from the Civil and Environmental Engineering Department at Duke University for my first year graduate fellowship. I am also thankful to my current and past members of the Barros group for their constant encouragement and all the wonderful moments we had over the years, and department staff for their assistance with administrative procedures.

Lastly, I would like to express my gratitude to my family, especially my parents Renhui and Xiaoqin, and my husband Travis for their unwavering support and confidence in me. Their love has been a constant source of hope and strength.

# 1. Introduction

In cloud- or fog-dominated montane regions, fog water has been demonstrated to be closely linked to ecosystem hydrology, nutrient budgets, and pollutant dynamics, as well as species distribution and abundance (Bruijnzeel, 2004;Goldsmith et al., 2013;Gotsch et al., 2014;Oliveira et al., 2014;Weathers, 1999). The ridges of the Black Mountains (BM, see map in Figure 1-1b) on the eastern slopes of the Southern Appalachian Mountains (SAM), near the highest point (Mt. Mitchell: 2,037 m) in the eastern United States, are home to spruce-fir refugia forests, which only exist above 1,500 m elevation. Remnants of the most southern boreal forest in the SAM, these relic forests dominated the lower altitudes of the southeastern (SE) United States during the late Pleistocene (Berry and Smith, 2013). The existence of these boreal, spruce-fir forest communities at such low latitudes is primarily attributed to frequent cloud cover and immersion that maintain low air and ground temperatures as well as high ambient humidity. The cloud forests of the SAM at high altitude often experience cloud immersion over 60 - 75% of the summer days, mostly present during morning hours (Berry and Smith, 2012). Persistent cloud immersion creates favorable conditions for direct foliar water uptake (the direct absorption of water through leaves), enhances root uptake by improving soil moisture, and alleviates water stress in harsh environmental conditions. Fog water in the SAM cloud forests has been found to contribute significantly to the overall plant water budget, as much as 31% throughout the entire summer growing period (Berry et al., 2014). Moreover,

it also modulates available photosynthetically active radiation (PAR), enhancing photosynthesis and leaf conductance, thus improving the carbon gain and water conservation of plants (Berry and Smith, 2013;Johnson and Smith, 2006).

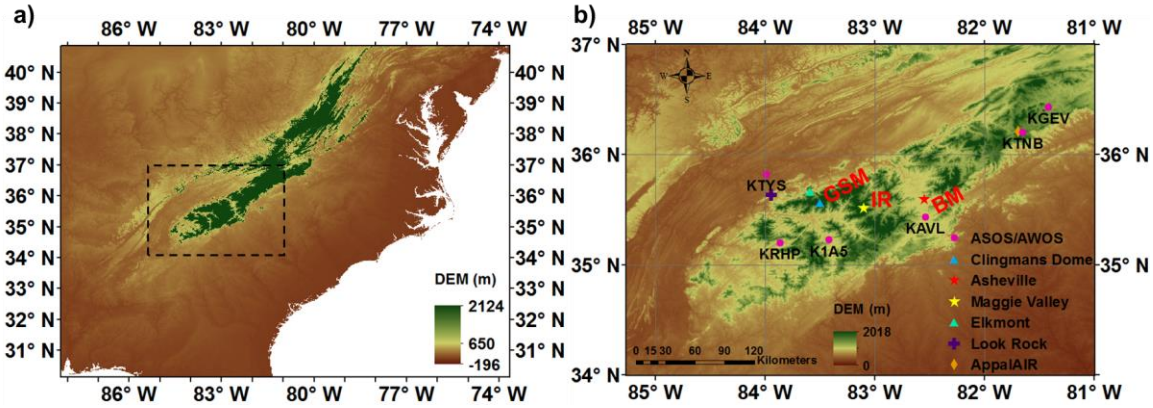


**Figure 1-1: a) Region of study (in the black box) in context of SE United States map; b) Topographic map of the SAM including groud observation sites referred to in this study. GSM denotes Great Smoky Mountains, IR denotes inner region, and BM denotes Black Mountains. Ground ceilometer stations are marked by pink dots.**

Cloud base height (CBH) indicates the altitude at which condenstion can occur, which has been demonstrated to have significant effects on cloud radiative forcing and climate (Ramanathan et al., 1989). Ground ceilometer data from 223 National Weather Service (NWS) stations from the National Oceanic and Atmospheric Administration (NOAA) and 117 military stations during 1951-2003 report a general increase of CBH over the United States accompanied with surface warming and atmosphere drying after the early 1970s (Sun et al., 2007). Lifted cloud base has also been observed in fog-dominated temperate regions. For example, in coastal Southern California, ceilometers measurements from airports also record increased CBH and reduced fog occurrences due

to continuned warming effects from urbanization (Williams et al., 2015). Over the Appalachian Mountains, Richardson et al. (2003) found that surface observations (e.g., ceilometer CBH, visibility) from NOAA airport weather stations have shown a significant rising trend (increasing rate of 4.14 m/year on average) in cloud ceiling during 1973-1999.

In this study, similar analysis in the SAM was performed using recent (2006-2016) ceilometer observations from the Automated Surface Observing System (ASOS) and Automated Weather Observing System (AWOS), as shown in Figure 1-2. The measurements from each ceilometer site (see location in Figure 1-1b) illustrate strong interannual and seasonal variabilites of the mean CBHs (Figure 1-2). As expected, the mean CBHs over moutain ridges (see KTNB and KGEV, their elevations in the parentheses after site names) in the SAM appear to be lower than the ones over valley locations (see KRHP, K1A5, and KAVL). Moreover, ceilometer measurements in the SAM (KRHP, K1A5, KAVL, KTNB, and KGEV, represented by solid lines) indicate generally decreasing mean CBHs from 2006 to 2013 and increasing values from 2014 to 2016 for while CBH observations from an adjacent lowland site (Knoxville Airport TN; KTYS, denoted by red dotted lines) indicate a sudden increase in 2013 and remain significatnly higher than measurements from the mountain locations afterwards. Since 2014, the lifted cloud ceiling levels revealed from groud observations in the SAM is expected to have a substantial influence on these spruce-fir ecosystems, likely resulting in an upslope shift in elevational occurrences and affecting the photosynthesis and carbon gain of the spruce-

fir forests (Reinhardt and Smith, 2008). The lifting of orographic cloud banks has also been observed worldwide in various mountain forests such as Costa Rica, Puerto Rico, Hawaii, Mexico, and the Andes, likely ascribed to global warming (Bradley et al., 2006;Diaz et al., 2011;Foster, 2001;Hu and Riveros-Iregui, 2016;Pounds et al., 1999). Montane cloud forests typically harbour a large population of endemic species; therefore, these changes have key implications on ecosystem conservation efforts and biodiversity overall (Oliveira et al., 2014;Still et al., 1999). Reliable monitoring and understanding of potential changes in fog and cloud regimes are crucial to the survival of endangered cloud forests of the SAM and worldwid, and could provide important guidance to sustain the biodiversity of mountain ecosystems.

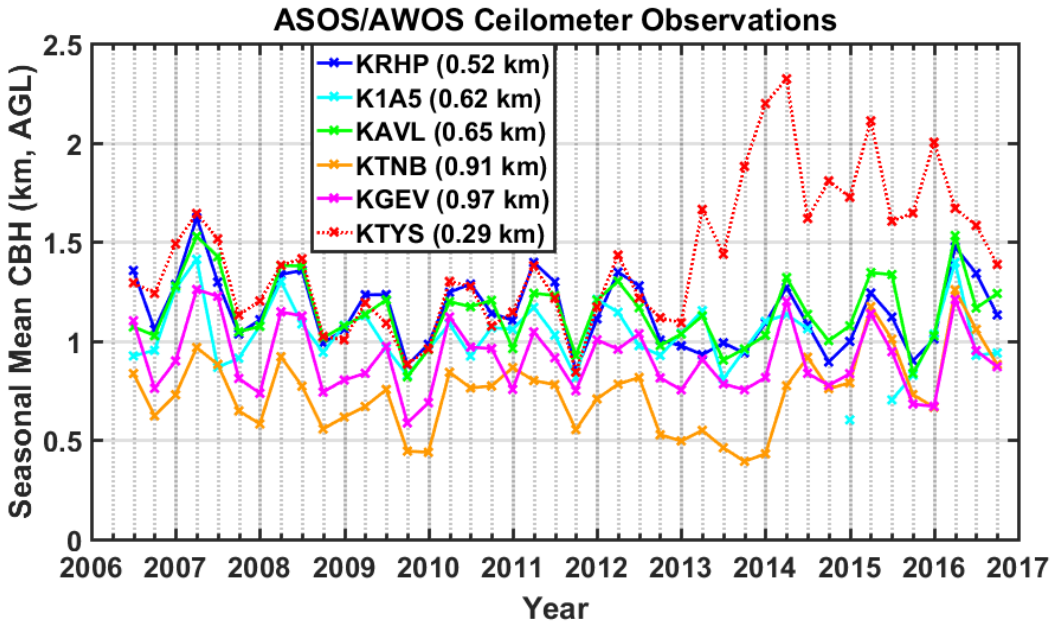


**Figure 1-2: Interannual variability of seasonal mean CBH from ASOS/AWOS ceilometer sites. Note that the seasonal mean starts with the winter season (J-F-M),**

**followed by spring (A-M-J), summer (J-A-S), and fall (O-N-D) season. The elevation of each site is indicated in the paretheses after its name.**

Low-level clouds and fog (LLCF) also have a significant impact on the hydrological regime and freshwater resources in the mountainous regions. Analysis of 6-yrs (2007-2013) precipitation observations from a high-density raingauge network in the Great Smoky Mountains National Park (GSMNP) shows that light rainfall (< 3 mm/hr, averaged over a time scale of 5 mins) accounts for 30-50% (even higher during the severe drought of 2008) of annual freshwater input to the headwater catchments (Wilson and Barros, 2014). On the other hand, lateral precipitation that results from fog advection and low-level cloud (LLC) immersion, hereafter referred to simply as fog, also accounts for a significant fraction of the annual freshwater input, which is especially critical in the warm seasons and in drought years. This can be illustrated by the fog observations collected during the warm season of 2014 (a very dry year) at one ridge-top location (Clingmans Dome, marked as the blue triangle in Figure 1-1b) on the western slopes of the SAM, in the Great Smoky Mountains (GSM, see map in Figure 1-1b). As noted in Figure 1-3a, this western ridge site appears to experience high frequency of fog occurrences with peaks at early morning and late night. The comparison with a co-located raingauge (RG) during June 2014 indicates that water accumulation recorded by the fog collector is as much as two times larger than the precipitation reported by the RG at Clingmans Dome, as shown in Figure 1-3b (Wilson and Barros, 2015). Therefore, it is of significant hydrological and

ecological relevance to quantify the contribution of lateral precipitation for maintaining mountain forest systems, especially in dry seasons (Bruijnzeel, 2004).

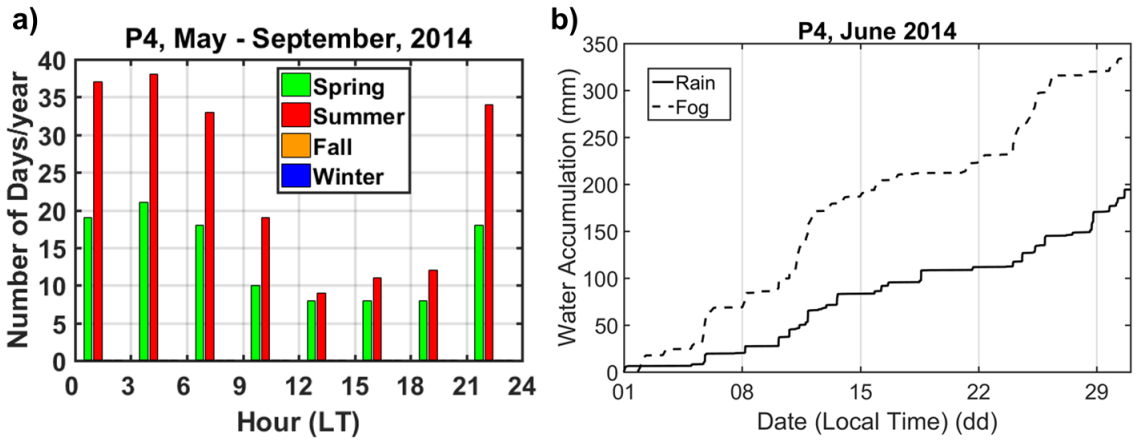


**Figure 1-3: a) Diurnal cycles of fog occurrences in the late spring (M-J) and summer season (J-A-S) of 2014, sampled by the fog collector at a high elevation station (Clingmans Dome, 1956 m MSL) in the GSM (see Section 3.4.1). b) Rain accumulations from co-located fog and rain gauges at the same location during June 2014 (Wilson and Barros, 2015);**

In the inner mountain region (IR, see map in Figure 1-1b), the raingauge observations in the GSMNP also reveal a spatial variability in average daily rainfall with higher accumulations recorded in the valleys and at ridge tops as compared to intermediate elevations (Duan et al., 2015). As documented by Barros (2013b) and Wilson and Barros (2014, 2015), the heavy surface rainfall in the valleys and along ridgelines during the warm season in the SAM can be explained by the seeder-feeder interactions (SFI), also referred as Bergeron processes (Bergeron, 1960). Results from Barros (2013) and Wilson and Barros (2014, 2015) suggest that SFI between upper-level precipitation systems and relatively deep fog layers and shallow orographic clouds are often observed in the

inner region valleys of the SAM that host mixed forests and are among the most biodiverse in the world. As illustrated in Figure 1-4, small droplets in low-level "feeder" clouds and fog interact with raindrops produced by the high-level "seeder" clouds, significantly increasing coalescence efficiency thus enhancing surface precipitation especially at low elevations (Barros and Kuligowski, 1998;Barros and Lettenmaier, 1993). Indeed, this low-level process (i.e., SFI) is a common feature of precipitation formation in mountainous regions around the world (Bergeron, 1965).

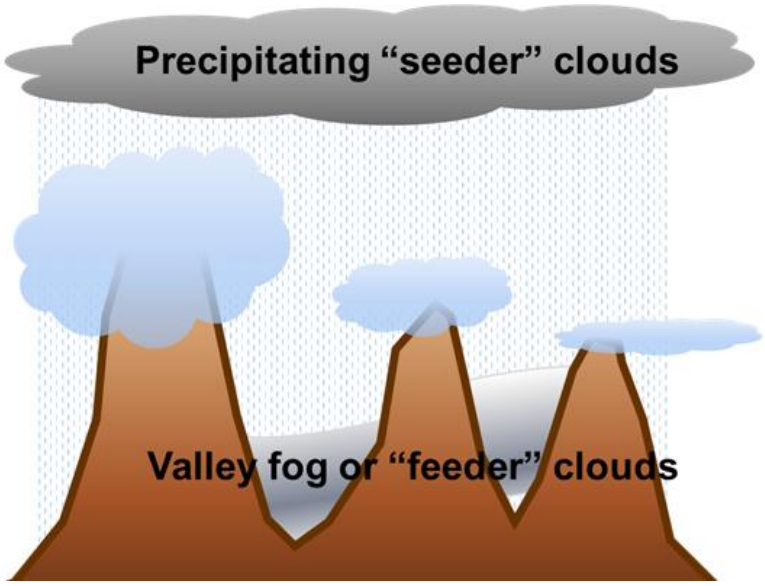


**Figure 1-4: Conceptual representation of the SFI between precipitating "seeder" clouds and valley fog/ "feeder" clouds over complex terrain.**

Figure 1-5 demonstrates one example of this low-level process at a valley station in the inner mountain region during a frontal passage on 11 July 2012, which recorded significantly larger cumulative rainfall in the valley site (P8, denoted by the dashed line) compared to the surrounding ridge locations (P1 and P3, denoted by solid lines). High

values of reflectivity are observed throughout the atmospheric column at the ridge location (P1) in contrast to strong reflectivity gradients toward the surface shown at the valley site (P8), which is the typical signature of low-level enhancement induced by SFI. Thus, LLCF act as a significant modifier to the classical notion of orographic enhancement of rainfall with increasing elevation and can explain higher rainfall intensity at low elevations observed in the inner mountain valleys of the SAM when interacting with upper precipitation systems (i.e., SFI). Indeed, similar phenomena can be identified in middle mountains of Central America, the Himalayas, and the Andes. Therefore, understanding and quantifying SFI is a fundamental question that has immediate hydrological influences in mountainous areas.

Beyond their impacts on plant water budgets and freshwater resources, mountain LLCF also play a significant role in modulating the terrestrial energy budget by altering net radiation, surface heat flux, and vegetation distribution (Gultepe et al., 2007;Hartmann et al., 1992;Ramanathan et al., 1989). Furthermore, vegetation characteristics also have an impact on albedo and surface roughness, and hence governing the energy exchange between the land surface and the atmosphere (Pacifico et al., 2009). This regulation function manifests in biodiversity hotspots with high vegetation cover in regions of complex terrain around the world, including the SAM (Guenther et al., 2006;Unger et al., 2013).

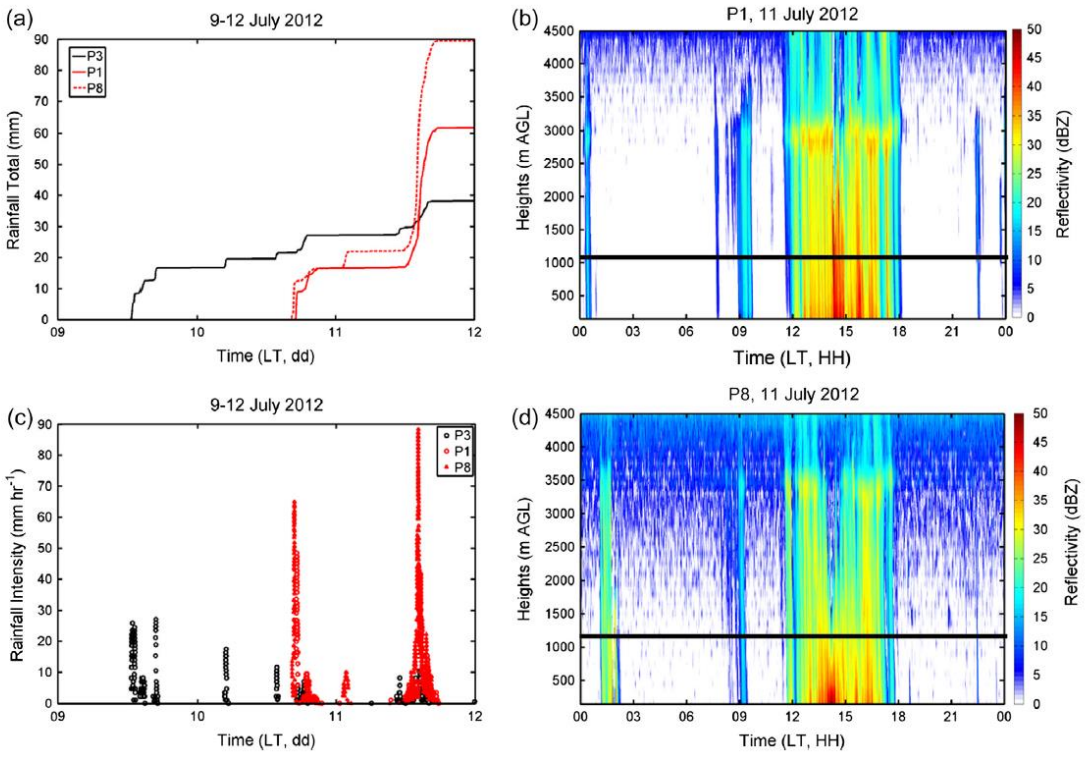


**Figure 1-5: Left panel: Cumulative rainfall and rain intensity of a summer event (July 09-12, 2012) in the inner SAM region during Intensive Observing Periods (IOPs). Note that P1 and P3 are two ridges locations and P8 is the valley site; Right panel: Observations from the co-located Micro Rain Radar (MRR) at P1 and P8 on July 11, 2012 (Wilson and Barros, 2015).**

The GSMNP has been designated as an International Biosphere Reserve and World Heritage Site by the United Nations Economic Scientific and Conservation Organization (UNESCO) because of the high biological diversity of its old-growth, temperate forest ecosystems (Hermann and Bratton, 1977). In densely forested regions lacking substantial anthropogenic aerosol sources, biogenic emissions of hydrocarbon compounds (e.g., isoprenes, terpenes, monoterpenes) via gas-to-particle formation make substantial contribution to the total aerosol mass and number concentrations during the

warm season (Tunved et al., 2006). The SAM referred to as the "Smoky Mountains", is a place where fog, mist, and haze are commonly observed in summer due to high biogenic aerosol loading (Fink 1934;Link et al., 2015;Kelly, 2011;Spira 2011). Figure 1-6 presents the interannual variability of isoprene concentrations at Asheville (denoted by the red star in Figure 1-1b). As expected, the year-to-year variations in isoprene concentrations follow the same pattern of annual rainfall in the SAM, with large values in the warm-season of wet hydrometeorological years compared to dry years (2008 is a severe drought year). This can be attributed to stronger physiological activity during the wet season, thus yielding higher emissions of isoprene from vegetation (Holzinger et al., 2002).

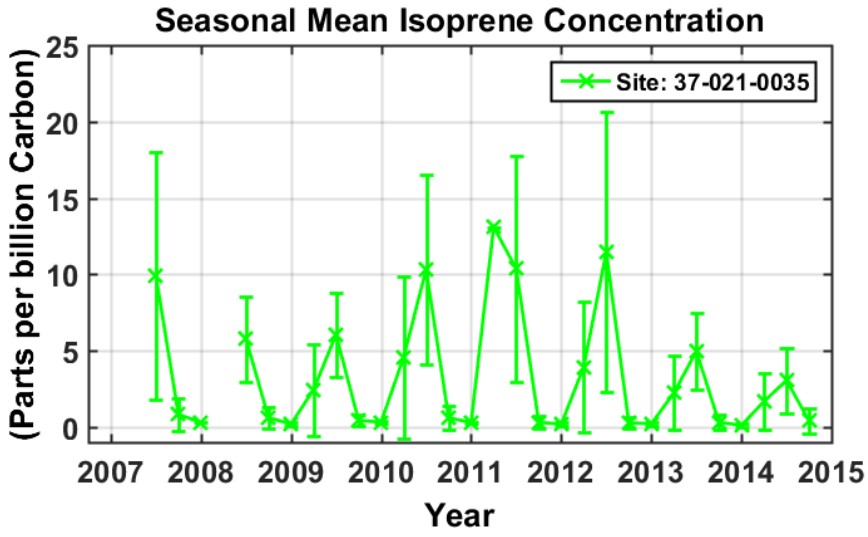


**Figure 1-6: Interannual variability of isoprene concentration at Asheville station from Environmental Protection Agency's Air Quality System (EPA-AQS). Note that the seasonal mean starts with the winter season (J-F-M).**

There is also strong evidence in the literature suggesting that organic aerosols, and especially giant aerosols of biogenic origin, are closely linked to the time-scales of cloud

development, and presumably fog in forested ecosystems (Pauliquevis et al., 2012;Pöschl et al., 2010, among others). This is referred as the indirect effect of aerosols, associated with aerosols serving as cloud condensation nuclei (CCN) or ice nuclei (IN) by altering microphysical properties of clouds (Lohmann and Feichter, 2005).

**The <u>overarching objective</u> of this dissertation is to advance the quantitative understanding of the indirect effect of aerosols on the diurnal cycle of LLCF and warm-season precipitation in mountainous regions generally, and in the SAM in particular, for the purpose of improving the representation of orographic precipitation processes in remote sensing retrievals and physically-based models.**

## *1.1 Previous work*

### 1.1.1 Aerosol characterization in the SAM

Multiple aerosol characterization studies have been conducted in the SAM over the past decade. The characterization of fine organic aerosols, collected in the Southeastern Aerosol and Visibility Study (SEAVS) at the GSMNP during July-August 1995 points out the dominant role of water-soluble organic species (WSOS), contributing to 76-98% of the total organic mass in most daytime samples while higher concentrations of solvent-soluble organic species (SSOS) over WSOS are identified from nighttime samples (Yu et al., 2005). At a ridge-top site on the north-western edge of the GSMNP (Look Rock TN, elevation 820 m MSL; marked by the purple plus in Figure 1-1b), characterization of the chemical composition of fine particles ($PM_{2.5}$) was conducted at an

Interagency Monitoring of PROtected Visual Environments (IMPROVE) monitoring site from 1988 to 2003 (Kim and Hopke, 2006). They found that three subtypes of secondary sulfate (summer-high secondary sulfate, carbon-rich secondary sulfate, and summer-low secondary sulfate) amount to 73% of the $PM_{2.5}$ composition, and in particular carbon-rich secondary sulfate particles are likely formed as a combination of biogenic and anthropogenic secondary particles due to local and regional influences. A similar study was conducted at the same IMPROVE site (Look Rock TN) during the summer of 2006 (Lowenthal et al., 2009). Their results show that $PM_{2.5}$ aerosol concentrations are dominated by sulfates and organic carbon (OC), and in particular water-soluble organic carbon accounts for 22% of total OC on average. During the summer of 2013, a chemical characterization of organic aerosol (OA) composition was conducted at Appalachian Atmospheric Interdisciplinary Research facility (AppalAIR, elevation 1100 MSL; marked by the orange diamond in Figure 1-1b) in the SAM (Link et al., 2015). Their results indicate that the low-volatility oxygenated OA, semi-volatile oxygenated OA and isoprene derived OA (isoprene SOA) contribute to $35\pm15$, $24\pm12$, and $42\pm17$%, respectively of the total measured OA. They describe the regional background of atmospheric chemistry in a typical rural setting, which is influenced episodically by regional urban pollution transported by synoptic flow. Using long-term (1999-2013) air quality measurements at Look Rock TN, Tanner et al. (2015) investigated the temporal trends in concentrations of atmospheric gaseous and particulate species in the GSMNP. During the study period, they

reported that organic carbonaceous material (OM) comprised 30-40% of fine particulate mass at this ridge-top site. They also found consistently reductions in primary pollutant species (e.g., $SO_2$ and $NO_x$) since 1999 and, specifically, a significant drop of emission levels in 2009. This is consistent with our observations that concentrations of $PM_{2.5}$ and $PM_{10}$ in the SAM dramatically decreased since 2009 as indicated by *in situ* measurements from the EPA-AQS (not shown here). This is likely the outcome of stricter federal and state regulatory pollution policies (e.g., the Clean Air Act on industrial emissions since the early 2000's) well implemented in this region. Before and after the advent of industrial and urban anthropogenic pollution, the long-standing historical presence of haze and fog is evident in the SAM. With substantially reduced anthropogenic emissions in this region since 2009, persistent biogenic aerosols likely serve as an explanation of consistent LLCF observed across the SAM.

The analysis from SEAVS also found that secondary formation processes have a large influence on the concentration, composition, and size distribution of fine aerosols in the GSM (Blando et al., 1998). In terms of secondary organic aerosol (SOA), highly oxygenated compounds as volatile organic compounds (VOCs) undergo atmospheric oxidation to form new particles or condense on pre-existing particles (Hallquist et al., 2009;Kanakidou et al., 2005). Isoprene and terpene are typical biogenic precursors of SOA (Tsigaridis and Kanakidou, 2007). The formation of isoprene-derived SOA was investigated in the 2013 Southern Oxidant and Aerosol Study (SOAS) at Look Rock TN

and key findings in Budisulistiorini et al. (2015) include that the sum of isoprene-derived SOA tracers makes a considerable contribution to the total OA mass (~9% on average, up to 28%) using offline chemical analysis of $PM_{2.5}$ samples and accounts for a larger component (32%) of total OA using the real-time mass spectrometric data. The near-real-time measurements of non-refractory submicron aerosol (NR-$PM_1$) collected at Look Rock TN during the entire year of 2013 (Budisulistiorini et al., 2016) reveal that OA is the dominant contributor (50-65%) to the NR-$PM_1$ and the seasonal characterization of average OA loadings suggests an increasing tendency from spring to summer and a decreasing tendency in fall and winter, likely attributed to the variations in biogenic volatile organic compound (BVOC) emission that depend on changes in leaf surface area, solar radiation, and ambient temperature in different seasons (Guenther et al., 2006). Moreover, BVOC emissions from the forests are found to have a larger impact on the spatial and temporal distribution of aerosol optical thickness (AOT) in the SE United States (Goldstein et al., 2009). They pointed out that secondary aerosols formed from anthropogenic and biogenic aerosols contribute mostly to high summer AOT values, thus corresponding to a remarkable radiative impact (cooling) in summer over the SE United States.

### 1.1.2 Effects of Aerosol-cloud Interactions on precipitation

Aerosols exert a strong influence on the earth-atmosphere system, primarily through two mechanisms: a radiative (direct) effect and a microphysical (indirect) effect

(Rosenfeld et al., 2008). Aerosol direct effects on the Earth's energy budget occur via scattering and absorbing of shortwave and longwave radiation in the atmosphere, hence modulating net radiation and the climate (Haywood and Boucher, 2000;Ramanathan et al., 2001). Shortwave radiation absorbed by tropospheric aerosols (e.g., black carbon and mineral dust) also significantly changes the diabatic heating in the atmosphere and hence enhances cloud evaporation or inhibit cloud formation, which affects the lifetimes of clouds (Koren et al., 2004). The indirect effect refers to aerosols acting as CCN or IN through altering cloud microphysical properties and consequently leading to suppression or enhancement of precipitation (Lohmann and Feichter, 2005). These changes in aerosol properties modify the size distribution of cloud droplets and ice particles, cloud radiative properties and precipitation efficiency (Jiang et al., 2008). For a fixed liquid water path (LWP), an increase in aerosol concentration results in an increase in the number of cloud droplets, which in turn reduces the size of cloud droplets (Twomey, 1977), and leads to suppression of precipitation initiation and thus longer cloud lifetimes (Albrecht, 1989). This is because small cloud droplets diminish the rate of drop collisions, thus reducing coalescence efficiency and consequently hindering the growth of raindrops (Khain et al., 2005). Previous studies have demonstrated that fine aerosol particles produced from increased air pollution can result in suppressed precipitation (Andreae et al., 2004;Givati and Rosenfeld, 2004;Rosenfeld and Givati, 2006).

Depending on the cloud types and synoptic conditions, variations in aerosol number concentration and chemical properties can have distinct influences on the microphysical pathways of aerosol-cloud-precipitation interactions (ACPI), resulting in either enhancement or suppression of precipitation (Rosenfeld et al., 2008). Typically, large hydrophilic aerosols such as sea salt tend to promote droplets' growth and rainfall and therefore serve as more efficient CCN (Rudich et al., 2002). Petzold et al. (2005) demonstrated the water-soluble sulphuric acid coating of combustion particles, primarily composed of insoluble black carbon, enhances potential CCN activation. Large amounts of small particles produced by the smoke from biomass burning can serve as small CCN and inhibit or suppress the onset of precipitation due to reduced efficiencies of collision and coalescence of small droplets (Diehl et al., 2007;Andreae et al., 2004). In mixed-phase clouds, the glaciation effect of aerosols tends to produce more IN and enhance precipitation efficiency, while the de-activation effect is also found to make IN less effective due to anthropogenic sulfate coating (Lohmann and Hoose, 2009). Even though increased aerosol concentrations cause delayed onset of precipitation, more cloud water can be uplifted above the freezing level and release additional latent heating, which invigorate deep convection thereby leading to violent storms and heavy rainfall (Bell et al., 2008;Khain et al., 2005).

Moreover, shallow orographic clouds are particularly sensitive to the indirect effects of anthropogenic aerosols (Givati and Rosenfeld, 2004, 2005;Rosenfeld and Givati,

2006). Over complex terrain in California and Israel, Givati and Rosenfeld (2004) attributed the reduction (15–25%) in annual precipitation to air-pollution aerosols transported from upwind urban areas. Using visibility as a proxy to CCN concentration, Rosenfeld at al. (2007) found a decreasing trend of precipitation at Mr. Hua China, which is located near highly polluted urban and industrial areas, associated with increased anthropogenic aerosols. Muhlbauer and Lohmann (2008) demonstrated that aerosol-induced suppression of upslope orographic precipitation can lead to enhancement of downslope precipitation and this shift can redistribute the water budget, which strongly influence the hydrological cycle on the local scales.

## *1.2 Challenges and Motivation*

Growing awareness of the aerosols' indirect effect (AIE) on cloud and precipitation has triggered extensive research, however this impact is still far from understood (Menon, 2004). ACPI have been found to vary significantly with location, season, and spatiotemporal scale of the analysis (Koren et al., 2012). Moreover, factors such as the nature of local cloud and precipitation regimes and aerosol characteristics (Li et al., 2011;Lee et al., 2010;Storer et al., 2010) as well as regional topography make attribution and quantification of ACPI nontrivial.

Remote sensing techniques and ground-based measurements are widely utilized to study the indirect effect of aerosols on cloud and precipitation (Kaufman et al., 2002;Stevens and Feingold, 2009). Observations from satellite remote sensing developed

over the past two decades provide a global view of aerosol, cloud, and precipitation distributions and enable long-term monitoring of the Earth's systems, in particular with the advent of active sensors (Stephens et al., 2002). However, inconsistencies among satellite estimates such as Aerosol Optical Depth (AOD), Cloud Optical Depth (COD), and Aerosol Index (AI) and ground observations remain major obstacles to the validation of AIE (Chin, 2009). Due to coarse spatial resolution of remote sensing, it is difficult to distinguish between clouds and aerosols from space, which poses a grand challenge to establish satellite-derived correlations between cloud amount and aerosol optical properties (Stevens and Feingold, 2009). Retrievals from different satellite products also show large discrepancies and biases over similar study regions (Rosenfeld and Feingold, 2003) due to inherent retrieval uncertainties and limitations of each sensor (Menon, 2004). Furthermore, surface contamination of sensor signals due to ground clutter effects remains problematic for the application of spaceborne observations in complex topography. In particular, precipitation regime in mountainous regions is found to be governed by significant low-level processes (e.g., SFI), thus resulting in considerable variations in the vertical structure of rainfall near the ground and large surface heterogeneities at subgrid scales. However, due to the coarse spatial resolution and ground clutter effects of satellite sensors, the pronounced variability of orographic precipitation at low-levels are difficult to detect from space.

In summary, there are three major motivations for this study:

1) Freshwater resources from mountainous regions support more than half of the world's population and the agricultural production in adjacent lowlands (Garrido and Dinar 2008; Nellemann et al. 2009). In particular, headwater catchments in mountainous regions supply most of sediment, nutrients, and organic matter required to sustain the ecology and hydrology of downstream regions (Alexander et al., 2007;Hill et al., 2014;MacDonald and Coe, 2007). This highlights the importance of orographic precipitation on regional hydrologic, economic and social aspects of downstream river basins. Over remote mountainous areas, ground-based measurements are severely lacking and *in situ* datasets collected in field campaigns are limited by their relatively short duration and small spatial coverage, and hence consistent and reliable remote-sensing observations of precipitation systems are necessary in mountainous regions. Nevertheless, the performance of satellite-based measurements in complex terrain suffers severe limitations especially at low-levels. Therefore, it is essential to identify error sources of satellite-based precipitation estimates especially for light rainfall and at low-levels, thereby providing insight on improving satellite retrievals over mountainous regions.
2) Due to frequent occurrences of LLCF, mountain ecosystems heavily rely on the moisture input from fog, cap clouds and light rainfall (Barros, 2013). Because of steep altitudinal gradients, there is a strong synergy among surface

radiation, water cycle, and ecosystems at local scales that is manifested by spatially and temporally persistent patterns of cloudiness and precipitation. Lateral precipitation from LLCF serves as a substantial moisture source to plants and is capable to compensate for reductions in other water supply during dry seasons. Therefore, a better understanding of the spatial and temporal variability of LLCF as well as their characteristics in mountainous regions is required to aid in future conservation and management of mountain ecosystems, especially for the survival of relic mountaintop forests in the SAM.

3) Previous studies (Ames et al., 2000;Hand et al., 2000;Lowenthal et al., 2009) have shown that the GSM area often experiences degraded visibility in summer due to high particulate mass concentration of biogenic aerosols emitted from the forest as well as anthropogenic aerosols produced from major combustion sources. Persistent high ambient relative humidity in this region favors aerosol growth from water uptake, leading to substantial light extinction. Local and synoptic meteorological changes also strongly influence the temporal variability of local aerosol properties. Nevertheless, the indirect effect of aerosols on cloud formation and precipitation evolution in this region is not well understood. Therefore, elucidating the role of local aerosol characteristics on the spatiotemporal development of cloud and consequently precipitation initiation, duration and intensity can advance our understanding

of the regional water cycle and facilitate equitable and sustainable water resource management in the SAM, which can also be applicable in mountainous areas elsewhere.

## *1.3 Research Objectives and Hypothesis*

The specific research objectives of this dissertation work are: 1) to identify sources of ambiguity in the satellite precipitation retrievals over complex terrain especially for the lower troposphere and derive satellite-based climatology of LLCF in the SAM. 2) to elucidate the role of aerosol-cloud interactions (ACI) in determining the vertical structure of cumulus development prior to precipitation onset; 3) to investigate the effect of aerosol characteristics on cloud formation and precipitation evolution in the warm season, focusing on the impact on the spatial variability and diurnal cycle of LLC and consequent implications on the microphysical and dynamical processes of precipitation fields at local (ridge-valley) and regional scales.

The following science questions (SQs) will be addressed specifically:

1) What is the error structure of satellite precipitation estimates in the SAM? What is the satellite-based climatology of LLCF in the Southern Appalachians (SA) using multi-satellite measurements from the A-Train? What is the contribution of LLCF to the observed surface precipitation enhancement induced by SFI?

2) How do variations in aerosol properties and key physical processes (e.g., condensation, coalescence, and entrainment) influence the microphysical evolution and thermodynamic state of cumulus clouds developed in the inner SAM?

3) How do changes in aerosol characteristics affect the spatial distribution of LLC and subsequently the dynamical and microphysical processes of warm-season precipitation? What is the role of local aerosols in controlling the diurnal cycle of LLC and rainfall?

The underlying hypothesis is that the availability of aerosols plays an important role in the microphysics and space-time distribution of LLCF, which are persistently observed in the mountainous regions. In turn, LLCF modulate the spatial variability and temporal evolution of orographic precipitation. In particular, substantial low-level enhancement of observed precipitation can be explained by the interactions between persistent LLCF in the SAM and incoming precipitation systems (i.e., SFI). This dissertation research will focus on the SAM to leverage the existing wealth of data and modeling experience. Findings and products from this work can be transferable to other regions of complex topography with high biogenic aerosol loading and persistent LLCF, such as cloud forests in the humid tropics and extra-tropics.

## *1.4 Approach and Outline*

This dissertation addresses fundamental aerosol, cloud, and precipitation processes and their interactions in the context of complex topography, including aerosol-cloud interactions and their impacts on warm LLC microphysics as well as the consequent effects on the microphysical and dynamical processes of warm-season precipitation. To investigate the processes that explain the observed cloud and rainfall regimes in mountainous regions, the research approach consists of integrating *in situ* observations from long-term observation networks (e.g., GSMNP raingauge, ASOS/AWOS) and the Integrated Precipitation and Hydrology Experiment (IPHEx) field campaign (including aerosol instruments, large-scale ground-based radars, and aircraft), multi-satellite data from the Tropical Rainfall Measuring Mission (TRMM), Cloud Aerosol Lidar Infrared Pathfinder Satellite Observations (CALIPSO), CloudSat, and Moderate Resolution Imaging Spectroradiometer (MODIS), and modeling studies (parcel, column and numerical weather prediction models).

To address the first part of SQ1, TRMM precipitation radar (PR) 2A25 products were compared with long-term observations (2008-2013) from a high-spatial resolution raingauge network operating in the GSMNP to perform a diagnostic analysis of the space-time structure of errors in Quantitative Precipitation Estimates (QPE) from TRMM over the SAM. As a predecessor of the Global Precipitation Measurement (GPM) mission, the design and development of GPM sensors and retrieval algorithms greatly depends on

valuable knowledge learnt from the former TRMM mission. The findings about precipitation retrievals and their associated uncertainties from TRMM are important lessons to guide future development of GPM algorithms, especially to improve precipitation retrievals at low-levels over complex terrain.

To address the second part of SQ1, this study will make contributions to improve the detectability of orographic LLCF and develop satellite-based climatology of LLCF properties in the SAM. To improve LLCF detections in mountainous regions, CALIPSO and CloudSat products were merged and evaluated against ground ceilometer measurements from the ASOS/AWOS network. 10-year MODIS observations were also used to study the spatial distribution and seasonal cycle of LLCF as well as their optical and microphysical properties in this region. However, both active (CALIPSO and Cloudsat) and passive (MODIS) sensors from space have major limitations in capturing significant low-level processes (e.g., SFI) observed in the SAM. To overcome this deficiency, the Duke Rain Microphysics Column Model (Prat and Barros, 2007b;Prat et al., 2008) was employed to elucidate the role of LLCF in low-level rainfall enhancement induced by SFI. This highlights the need to address this observation challenge for satellites by using physical-based retrievals in mountainous regions.

To address SQ2, a new spectral cloud parcel model was first developed to solve activation, condensation, collision-coalescence, and lateral entrainment processes in a rising air parcel. To assess the application of this parcel model, we took advantage of the

comprehensive dataset from IPHEx, the first GPM ground validation field campaign. In particular, surface aerosol measurements were used to initiate the model simulations and airborne observations of cloud microphysics were used to evaluate the modeling results. Moreover, we explored the space of ACI physical parameters that govern cumulus congestus growth in the inner SAM, which are not available in the campaign or before. Sensitivity tests were conducted to examine how variations in aerosol properties and major physical processes control the early development of orographic cumulus congestus observed during IPHEx.

To address SQ3, high-resolution numerical simulations of summer precipitation events during IPHEx were performed using the Weather Research and Forecasting (WRF) model with specific CCN activation parameterization (Cohard et al., 1998). To better describe local aerosol characteristics in the SAM, the CCN spectra estimated from *in situ* measurements in the inner SAM during the IPHEx campaign was incorporated to the model microphysics scheme. Thus, sensitivity tests were conducted using the default continental CCN spectrum from the model and the local CCN spectrum to investigate the changes of cloud formation and warm-season precipitation in the SAM to variations in aerosol properties, in particular linking the aerosol effects to the spatial pattern and diurnal cycle of LLC and precipitation evolution at local (ridge-valley) and regional scales.

The structure of this dissertation is as follows: Chapter 2 addresses the first part of SQ1 and this study is published in the *Hydrology and Earth System Sciences* (Duan et al.,

2015). The study presented in Chapter 3 address the second part of SQ1 and the corresponding manuscript is under review for Remote Sensing. Chapter 4 describes the study addressing SQ2 and this work is published as a discussion paper (Duan et al., 2017) in Atmospheric Chemistry and Physics Discussion (ACPD), under review for Atmospheric Chemistry and Physics (ACP). To address SQ3, an exploratory study was conducted and the preliminary results are discussed in Chapter 5, which will be submitted to Atmospheric Research. Chapter 6 will summarize the major findings of this dissertation and provide a brief outlook for future research.

# 2. Error diagnostics of TRMM PR estimates in complex terrain as a basis for IPHEx2014

Note this chapter appeared as reference (Duan et al., 2015).

## *2.1 Introduction*

Reliable quantitative measurement of rainfall distribution over mountainous regions is essential for climate studies, hydrological and hazard forecasting, and the management of water and ecosystem resources (Viviroli, 2011). Recent advances toward high spatial and temporal resolution satellite-based quantitative precipitation estimation (QPE) make these estimates potentially attractive for flood forecasting and other operational hydrology studies (e.g. Tao and Barros, 2013 and 2014 and references therein). Numerous studies have been conducted to compare satellite products against ground measurements to quantify errors and to improve retrieval algorithms (Amitai et al., 2009;Amitai et al., 2012;Barros et al., 2000;Kirstetter et al., 2013;Tao and Barros, 2010;Wolff and Fisher, 2008). For long-term monitoring, raingauges remain the most autonomous and affordable instruments, but large errors can be introduced in extrapolating point observations to represent areal means (Prasetia et al., 2012). Considering the large uncertainties due to satellite temporal sampling and volume sampling discrepancies, and the challenges in accounting for atmospheric heterogeneity and landform complexity, direct comparison of satellite-based precipitation estimates with ground-based point measurements (e.g., raingauges) poses many challenges, especially at short time scales

over small areas (< 1000 km; Amitai et al., 2012; Barros and Tao, 2008; Fisher, 2004; among many others).

In mountainous regions, terrain complexity is a key complicating factor not only because it introduces spatial variability, but also because land in this region is difficult to access. This tends to constrain the type, density and locations of ground-based observations, leading to sparse, poorly maintained, and irregularly distributed observing networks. Furthermore, observations from operational ground-based radar systems cannot be relied upon to monitor the lower troposphere due to blockage and ground-clutter effects, and thus satellite-based observations provide an opportunity for long-term monitoring at high spatial resolution with consistent measurement quality. Studies evaluating satellite QPE consistently report widespread underestimation of rainfall in mountainous regions independently of the temporal scale (Barros et al., 2000;Barros and Tao, 2008;Lang and Barros, 2002;Prat and Barros, 2010b). In the Southern Appalachians and the adjacent Piedmont, light rainfall (≤ 3mm/hr) accounts for 30-50% and higher of annual freshwater input to headwater catchments (Wilson and Barros, 2014) and therefore light rainfall detection and estimation, which has been a long-standing challenge in remote sensing of rainfall, is critical to water cycle studies. On the other hand, vertical complexity and high spatial variability of heavy rainfall and mixed precipitation events associated with severe weather pose major challenges to operational weather and hydrological forecasting of extreme events.

A diagnostic analysis of the space-time structure of error in QPE from the Precipitation Radar (PR) on the Tropical Rainfall Measurement Mission (TRMM) satellite in preparation for the Integrated Precipitation and Hydrology Experiment (IPHEx) in 2014 is reported here. In particular, we examine the physical basis of false alarm (FA), missed detection (MD), underestimation (UND) and overestimation (OVR) errors with the purpose of designing and implementing a Ground-Validation Observing System that captures the range of key conditions and hydrometeorological regimes linked to various types of retrieval errors, and thus can inform improvements in retrieval algorithms and precipitation product development in regions of complex orography.

IPHEx is the first ground-validation field campaign after the launch of the Global Precipitation Measurement (GPM) satellite (Barros et al., 2014). The configuration of the terrain and TRMM overpasses and the complex regional meteorology necessitate a comprehensive assessment of the spatial and temporal structure of uncertainty conditional on observing geometry and hydrometeorological regime. In anticipation of IPHEx, a science-grade high-density raingauge network was deployed at mid to high elevations in the Southern Appalachian Mountains, USA since 2007. This network allows for direct comparison of ground-based measurements from raingauges and satellite-based QPE from the TRMM precipitation radar (specifically, PR 2A25 V7), and the GPM Dual-Frequency Precipitation Radar (DPR) when these become available. Specifically, raingauge measurements were compared against 5 years of TRMM orbital precipitation

estimates PR 2A25 collected between 2008 and 2013. The satellite-based estimates were evaluated via gauge-to-pixel analysis for spatiotemporally matched gauges and areal average analysis at the PR pixel scale. Case studies were conducted to characterize the vertical profiles of reflectivity and rain rate associated with large uncertainty, as well as the spatial distribution for typical cases of quantitative errors [underestimation (UND) and overestimation (OVR)] and detection errors [false alarm (FA) and missed detection (MD)] for stratiform and convective precipitation.

Kirstetter et al. (2013) performed a comprehensive study and reported improvements of TRMM PR 2A25 V7 over version 6 (V6) across the southern conterminous US (CONUS) using the National Weather Service (NWS) operational radars and raingauges as reference. Several changes were implemented in the TRMM PR algorithm of V7 including the vertical profile of hydrometeor characteristics, which affects the reflectivity-to-rainfall rate (Z-R) relationship and attenuation correction, and the reintroduction of a correction for non-uniform beam-filling (NUBF) effects (described in Kozu and Iguchi, 1999) that had been removed from V6. Because there are large gaps in the NWS operational observing system in mountainous regions, we build on earlier work by Prat and Barros (2010b) and overlapping V6 and V7 products (TRMM PR 2A25) are also compared here for the 3 years of concurrent availability in the study region (2008-2011).

Section 2.2 briefly describes the TRMM PR products and the climatology of rainfall observed from the raingauge network, and includes a comparison of TRMM 2A25 V7 and V6 estimates with respect to reference ground measurements focusing on rainfall detectability and quantitative accuracy. Section 2.3 is devoted to an examination of the vertical reflectivity structures of underestimation (UND), overestimation (OVR), false alarm (FA) and missed detection (MD) errors for stratiform and convective rainfall as defined by TRMM-based criteria with the purpose of characterizing the uncertainty in each class and exploring the physical basis of associated errors. Section 2.4 focuses on diagnosing the potential sources of errors for illustrative case studies. Summary and conclusions follow in Section 2.5.

## *2.2 Data*

### 2.2.1 The GSMNP Raingauge Network

A high-spatial resolution raingauge network has been installed in the Great Smoky Mountains National Park (GSMNP) in the Southern Appalachians since 2007 (Prat and Barros, 2010a). In this study, 32 stations equipped with tipping bucket (TB) gauges operating for the longest continuous period, distributed at mid to high elevations (from 1150 m to 1920 m) on mountain ridges, will be used as reference "ground-truth" (Table 2-1, Figure 1-1). The current network configuration includes additional raingauges, disdrometers, MicroRain Radars (MRRs) and weighing raingauges (Barros et al., 2014), but in this study we use only the TB raingauge data that have several years of record

length during the 2008-2013 period, thus assuring robust statistics. The raingauges provide point observations of surface rainfall at different measurement resolution: seven raingauges use the TB3 model (RG0XX: catchment size of 200 mm; 0.2 mm/tip), 13 are TB3/0.1 (RG1XX: catchment size of 282.2 mm; 0.1 mm/tip) and 12 are HS305 (RG3XX: catchment size of 305 mm; 1 mm/tip). Note the RG3XX data are available only from 2009 onward. Although higher resolution TB gauges were co-located with several RG3XX gauges since their initial deployment, their record is short and thus those observations are not used here. To reiterate, a note of caution is warranted with regard to the many potential errors due to spatial density and geolocation distribution of the gauges, wind effects, surface wetting of the gauge funnel, animal and human interference, evaporation, and splashing that may introduce error in the raingauge observations independently of the measurement accuracy proper. For example, for high wind speeds, the reported rain rate is typically 2-18% lower than the actual value (Chen et al., 2013; Wang and Wolff, 2010). Nevertheless, the raingauge measurements provide a reliable and independent reference to evaluate uncertainties and identify possible biases associated with remote-sensing estimates.

Over the Southern Appalachians, most precipitation is associated with stratiform systems, although isolated thunderstorms and mesoscale convective systems are dominant in the warm season. Figure 1-1 shows a map of the study region, where the GSMNP network is a relatively dense raingauge network deployed in the Pigeon River

basin in the Southern Appalachians spanning an area of about 1,400 km$^2$. As can be seen in Figure 1-1, the RG0XX (easternmost) and RG3XX (westernmost) gauges are clustered over the outer ridges, whereas the RG1XX gauges are distributed in the inner mountain region.

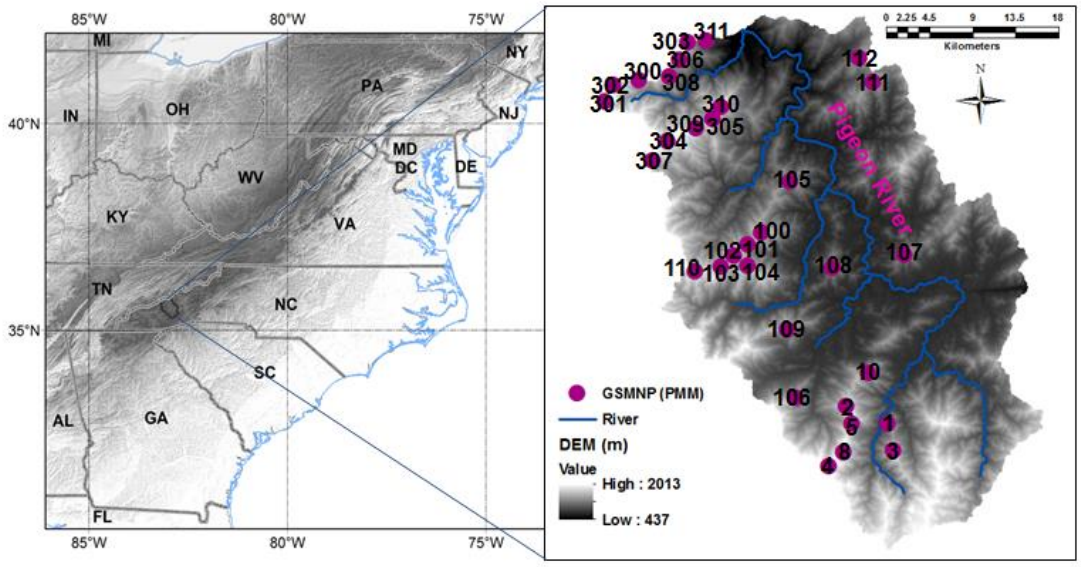


**Figure 2-1: Region of study including the Great Smoky Mountains National Park (GSMNP) in the Southern Appalachians. The right panel shows the Pigeon River basin where the raingauges are installed. Note RG0XX, RG1XX, and RG3XX were installed in summer 2007, 2008, and 2009 respectively. Additional raingauges and other instrumentation placed in the region are not shown here (see http://iphex.pratt.duke.edu).**

**Table 2-1: Inventory of long-term raingauges in the Pigeon River basin including the Great Smoky Mountains National Park (GSMNP) in the Southern Appalachians used in this study.**

| *Raingauge* | *Latitude* | *Longitude* | *Elevation (m)* | *Series* |
|---|---|---|---|---|
| *RG001* | 35.4 | -82.91 | 1156 | RG0XX Eastern Ridge |
| *RG002* | 35.43 | -82.97 | 1731 | |
| *RG003* | 35.38 | -82.92 | 1609 | |
| *RG004* | 35.37 | -82.99 | 1922 | |
| *RG005* | 35.41 | -82.96 | 1520 | |
| *RG008* | 35.38 | -82.97 | 1737 | |
| *RG010* | 35.46 | -82.95 | 1478 | |
| *RG100* | 35.59 | -83.07 | 1495 | RG1XX Inner Ridge |
| *RG101* | 35.58 | -83.09 | 1520 | |
| *RG102* | 35.56 | -83.1 | 1635 | |
| *RG103* | 35.55 | -83.12 | 1688 | |
| *RG104* | 35.55 | -83.09 | 1587 | |
| *RG105* | 35.63 | -83.04 | 1345 | |
| *RG106* | 35.43 | -83.03 | 1210 | |
| *RG107* | 35.57 | -82.91 | 1359 | |
| *RG108* | 35.55 | -82.99 | 1277 | |
| *RG109* | 35.5 | -83.04 | 1500 | |
| *RG110* | 35.55 | -83.15 | 1563 | |
| *RG111* | 35.73 | -82.95 | 1394 | |
| *RG112* | 35.75 | -82.96 | 1184 | |
| *RG300* | 35.73 | -83.22 | 1558 | RG3XX Western Ridge |
| *RG301* | 35.71 | -83.26 | 2003 | |
| *RG302* | 35.72 | -83.25 | 1860 | |
| *RG303* | 35.76 | -83.16 | 1490 | |
| *RG304* | 35.67 | -83.18 | 1820 | |
| *RG305* | 35.69 | -83.13 | 1630 | |
| *RG306* | 35.75 | -83.17 | 1536 | |
| *RG307* | 35.65 | -83.2 | 1624 | |
| *RG308* | 35.73 | -83.18 | 1471 | |
| *RG309* | 35.68 | -83.15 | 1604 | |
| *RG310* | 35.7 | -83.12 | 1756 | |
| *RG311* | 35.77 | -83.14 | 1036 | |

Figure 2-2 shows the spatial variability of average daily precipitation raingauge accumulations over the period of study. Note the lack of classic orographic rainfall enhancement with elevation (Figure 2-2b), as well as the stronger variability for the RG1XX gauges in the inner mountain region (blue colors) with higher rainfall totals at lower elevations in the valleys and at ridge tops and a decrease at intermediate elevations on hill slopes. The high values in the valleys reflect the contribution of seeder-feeder processes resulting from the interaction of stratiform rainfall with low level clouds and thick fog banks (Wilson and Barros, 2014). Complex orographic precipitation effects in the Southern Appalachian Mountains and high intra-annual variability in large-scale weather conditions explain the high spatial variability in the diurnal cycle of rainfall frequency from one season to another as depicted in Figure 2-3. During the summer, rainfall frequency peaks in the late afternoon (15:00 EDT to 18:00 EDT) with daytime convection accounting for nearly 20% of the seasonal total and is somewhat uniform in the remainder of the day with each period contributing about 10-15%; during the winter, rainfall frequency reveals a strong diurnal cycle characterized by a high-amplitude maximum in the early afternoon (12:00 to 15:00 EDT) and a relative minimum occurring between 21:00 and 06:00 EDT. Spring and fall seasons, on the other hand, exhibit a much weaker diurnal cycle, with a relative maximum occurring in the afternoon, and otherwise more or less constant throughout the rest of the day.

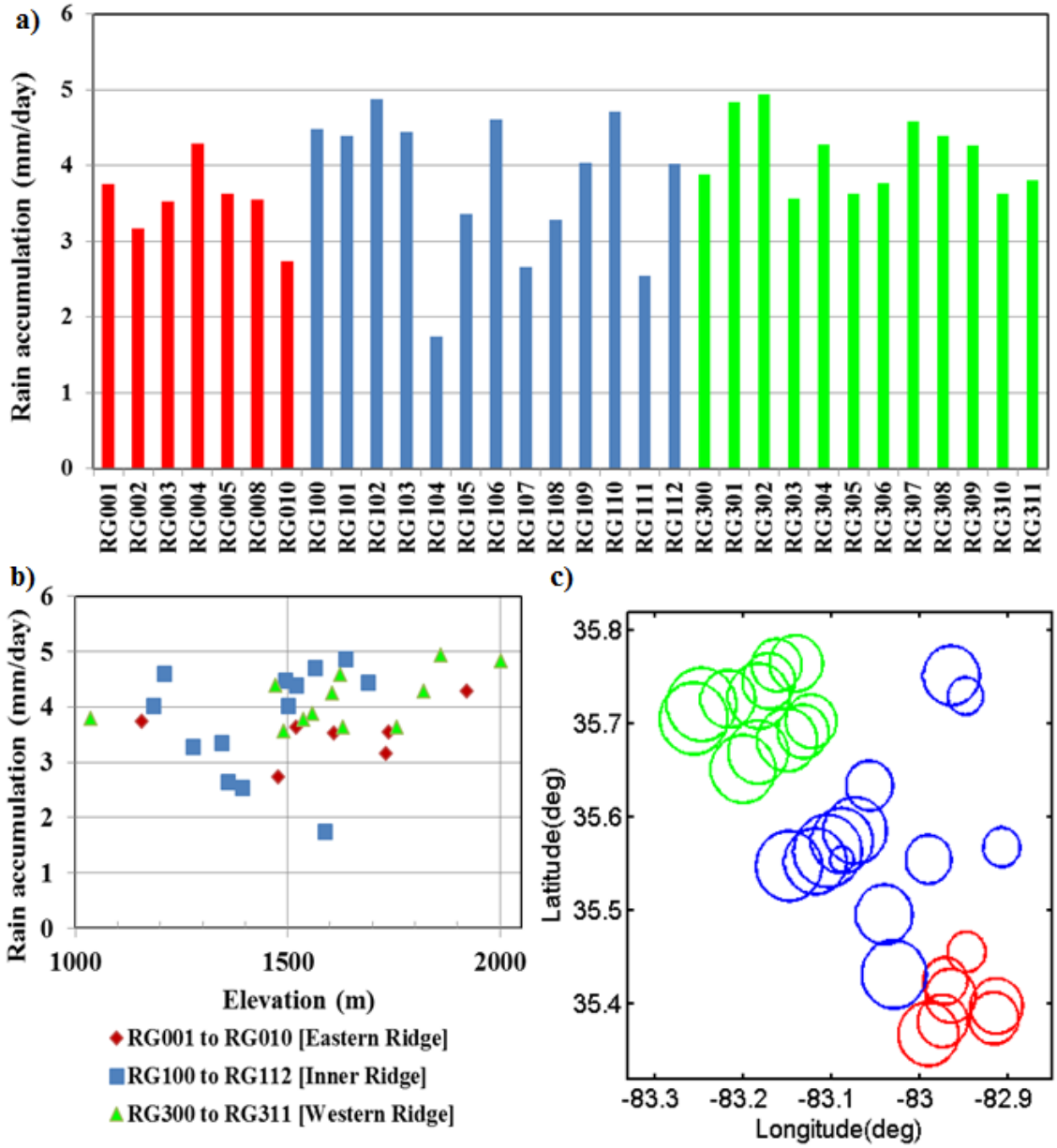


**Figure 2-2: a) Average rain accumulation (mm/day) for the raingauges deployed in the GSMRGN. Average rain accumulation as a function of: b) Elevation. c) Geolocation of each raingauge with circle size indicating relative magnitude of the daily rain accumulation.**

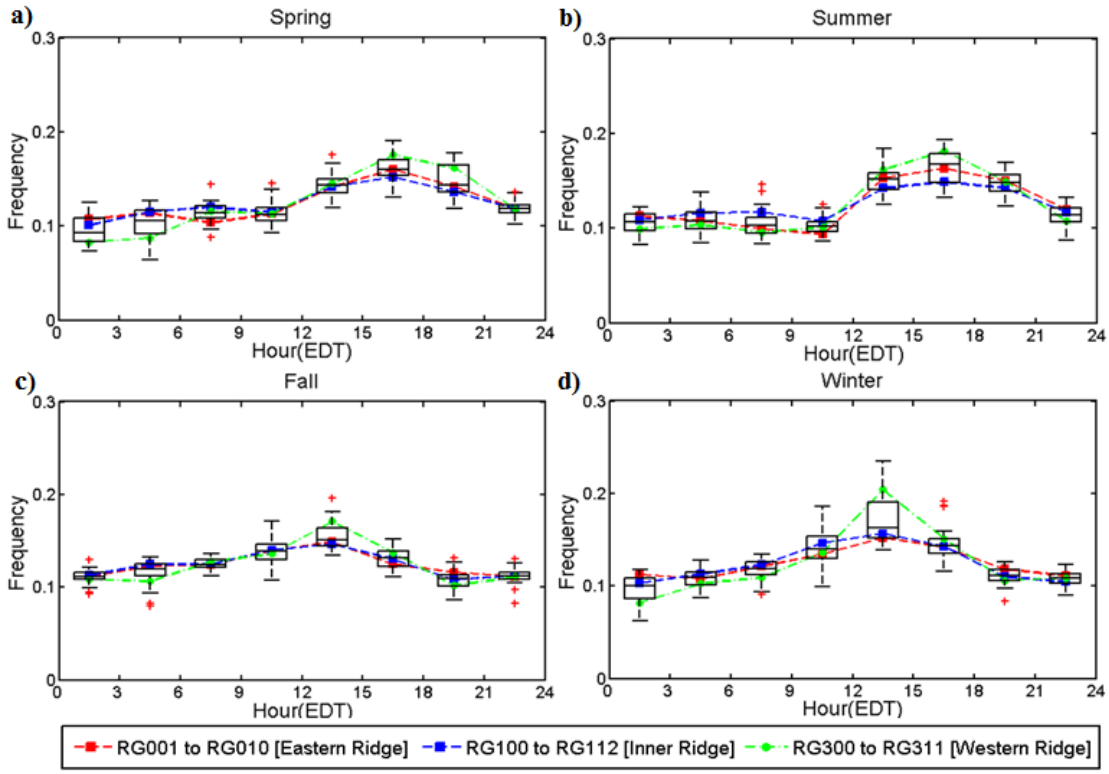


**Figure 2-3: Three-hourly diurnal cycle as a function of the season of the year and the raingauge network location (Eastern, Inner, and Western Ridge) for: a) spring (April-May-June), b) summer (July-August-September), c) fall (October-November-December), d) winter.**

### 2.2.2 TRMM PR 2A25 Products

The TRMM satellite was launched in November 1997 and operated on a non-sun-synchronous orbit designed to capture precipitation structure in the tropics. On July 8, 2014 NASA ceased station keeping maneuvers and TRMM is currently drifting downward from its operating altitude of 402 km to 335 km, expected to be reached around February 2016, at which point data collection will be terminated. The Precipitation Radar (PR) was the first active microwave instrument for measuring three-dimensional rainfall

structure over the tropics and subtropics from space(Kozu et al., 2001), and produces more reliable near surface estimates of precipitation at higher spatial resolution than radiometers including in mountainous regions (Barros et al., 2000;Barros and Tao, 2008;Nesbitt, 2000). The PR operates at 13.8 GHz frequency with 250 m vertical resolution, and is thus capable of penetrating dense cloud layers to detect underlying precipitation (Prasetia et al., 2012) . Retrieval errors such as the uncertainty of the assumed drop size distribution (DSD), incorrect physical assumptions (freezing-level height, hydrometeor temperatures), possible contamination by surface backscatter, the reliability and physical basis of the stratiform-convective classification, attenuation and extinction of the signal and NUBF effects, light rain sensitivity (minimum detectable signal), and surface clutter rejection all contribute to uncertainty in PR rainfall estimates, and the respective effects are corrected to varying degrees (Iguchi et al., 2009;Wolff and Fisher, 2008).

Specifically, a hybrid of the surface reference technique and the Hitschfeld and Bordan method is applied to correct for atmospheric attenuation (Iguchi et al., 2000). The PR attenuation correction is adequate in stratiform rain but is underestimated in convective rain, particularly for heavy rain accumulations (Liao and Meneghini, 2009). Generally, application of the attenuation correction can change the estimated rain rate by an order of magnitude in cases of heavy precipitation (Bindlish and Barros, 2000;Iguchi et al., 2000;Meneghini et al., 2000). Generally, the NUBF effects refer to underestimation errors in the presence of reflectivity gradients, that is, subgrid-scale volume heterogeneity

at the relatively coarse resolution of the PR footprint (Durden et al., 1998;Nakamura, 1991). Previous studies evaluating the impact of NUBF have been conducted for ocean conditions and for moderate to heavy rainfall conditions, and results suggested very small errors due to NUBF for the TRMM PR, but no studies focused on subgrid-scale effects in mountainous regions where there is a strong co-organization of landform and precipitation along with strong space-time variability. Other sources of errors include the orbital geometry of the satellite at relatively high latitude (Fisher, 2004), and local hydrometeorological regimes which may present cloud and rainfall vertical structure very different from that implied in the retrieval algorithm's microphysical assumptions. Intercomparison of precipitation estimates from different algorithms allows examination of the specific impacts of algorithm differences on QPE reliability and accuracy. For instance, the underestimation of rain rate in V6 (Prat and Barros, 2010b) was addressed in the V7 algorithm revisions by recalibration of the Z-R relationship over land, and implementation of the NUBF correction to produce larger estimates both over land and over ocean (Seto et al., 2011). Finally, sampling errors are subject to sampling frequency and the spatiotemporal structure of precipitation associated with diurnal, seasonal, and inter-annual variability of rainfall within a region. Even though sampling errors are more randomly distributed, they can be a significant contribution to the total error (Fisher, 2004). The main TRMM product used in this work is the PR 2A25 V7 product, described at (http://disc.sci.gsfc.nasa.gov/precipitation/documentation/TRMM_README). V6

products are used for assessing V7 algorithm improvements, specifically with regard to instantaneous precipitation estimates. For this purpose, all rainfall measurements observed coincidentally by TRMM overpasses and the GSMNP network from June 2008 to May 2011 are used.

An important challenge in the validation of satellite-derived estimations against ground measurements is the resolution discrepancy of different datasets. Here, all the raingauge measurements within a 2.5-km radius from the center of the PR pixel position for each PR overpass within a selected time-scale are integrated into one. Nevertheless, matching the observations from raingauges and TRMM PR at the nominal pixel scale (~5 km) in space and time introduces uncertainties due to differences in the measurement control-volume, generally referred to as representativeness error (i.e. Porcù et al., 2014), which is further aggravated due to sparse spatial sampling and topographic variations: raingauges report near-surface point rainfall rate while satellite estimates correspond to a cloud volume-averaged rainfall rate, which is also highly dependent on the precipitation system, cloud physics and morphology, and associated rainfall (e.g. Habib and Krajewski, 2002;Prat and Barros, 2010b). However, this discrepancy can be alleviated by using an optimal integration time interval for gauge observations (Prat and Barros, 2009;Wang and Wolff, 2010) as it is done in this manuscript (see Section 2.2). Despite these challenges, comparisons with ground reference gauges constitute a critical component in evaluating the accuracy of the PR estimates of surface precipitation, reflectivity and rain rate.

## 2.2.3 Comparison of TRMM PR 2A25 V7 versus V6

### 2.2.3.1 Rainfall Detection

As stated earlier, the objective of the revisions implemented in the TRMM PR V7 algorithm was to correct some key deficiencies identified in the V6 algorithm, namely the large underestimation of rain over land relative to ground-based measurements, and the relatively large dependence of rain estimates on the viewing angle (Iguchi et al., 2009). A detailed summary of the major changes in the TRMM PR retrieval algorithm are summarized in Iguchi et al. (2009) and Okamoto et al. (2008). Here, V6 and V7 rain rates from June 2008 to May 2011 corresponding to three years of satellite overpasses over the Southern Appalachians are compared. Note that V6 data are only available up to summer 2011. To evaluate the satellite estimates, rain rate estimates for a given pixel are compared to the observed values at raingauges located within the pixel's fingerprint (~5 km diameter). The number of raingauges varies from pixel to pixel, but on average, about 2 gauges can be found in each PR field of view. To determine whether there is an optimal time-scale that reconciles the nearly instantaneous (point in time) satellite-based areal rainfall estimates (pixel scale) with raingauge observations (point in space) with different measurement resolution (TB size), the gauge rain rates are integrated over a range of time-scales (10–60 min) centered at the time of overpass and spatially averaged at the PR pixel scale. To evaluate precipitation detectability (contingency tables and statistical skill scores), point-to-pixel comparisons were applied to increase the sample size and avoid ambiguity associated with the spatial representativeness of the gauges within the pixel.

When multiple gauges exist in the same pixel, the PR measurements are paired separately with different raingauges. It is assumed that the PR resolution remains constant for both near-nadir and off-nadir inclination angles. To avoid contamination due to the resolution deformation, the PR-RG pairs were segregated into "near-nadir" (scanning inclination angles ranging from 0˚ to 9˚) and "off-nadir" (scanning inclination angles beyond 9˚) comparisons. Off-nadir pairs are discarded in some quantitative comparisons to exclude the angle deformation in exploring other sources of error. In this section, the TRMM PR 2A25 near surface rain rate was analyzed with respect to the independent ground reference rainfall data to examine the detectability performance of satellite rainfall retrievals using contingency tables and statistical skill scores. The rain detection and surface clutter discrimination are primarily handled by the Level 1 algorithms (e.g., 1B21 and 1C21 products), which have been improved over time (e.g., change of clutter routine module in PR 1B21 from V6 to V7). Level 1 products are used subsequently as input to the Level 2 algorithm. For example, the near-surface rain rate from 2A25 is retrieved based on the identification of clutter free ranges from 1C21. Therefore, the higher level product 2A25 reflects the integration of Level 1 results, and can serve as a fair indicator of effective rainfall detectability of TRMM.

The contingency matrices of PR estimates with regard to the gauge observations at 10-min time-scale for all angles (a) and for near-nadir cases only (b) are presented in Table 2-2. Table 2-3 provides a summary of detection metrics (i.e. skill scores) based on

the counts of hits (YY), misses (NY), false alarms (YN) and correct rejections (NN) inferred from contingency matrices at time-scales ranging from 10 to 60 min: accuracy, frequency bias (FB), probability of detection (POD), false alarm ratio (FAR), probability of false detection (POFD), and threat score (TS). The equations to calculate the skill scores are included as footnotes to Table 2-3.

**Table 2-2: Contingency matrices for TRMM 2A25 V7 surface rain rate and 10-min raingauge rain rates for: a) all angles; and b) near-nadir cases. Counts are expressed as a percentage of the total number of observations. Values in parentheses are for V6. The 10-min time scale is centered over the time of the satellite overpass during 06/2008 – 05/2011.**

| **a)** | All angles (RG0XX and RG1XX) | | | |
|---|---|---|---|---|
| TRMM PR 2A25 | | Yes | No | Tot. |
| | Yes | 1.18(1.12) | 2.73(3) | 3.91(4.12) |
| | No | 0.74(0.71) | 95.35(95.17) | 96.09(95.88) |
| | Tot. | 1.93(1.83) | 98.07(98.17) | 100(100) |
| **b)** | Near-nadir cases (RG0XX and RG1XX) | | | |
| TRMM PR 2A25 | | Yes | No | Tot. |
| | Yes | 2.23(2.01) | 2.83(3.12) | 5.06(5.13) |
| | No | 1.24(1.28) | 93.7(93.59) | 94.94(94.87) |
| | Tot. | 3.47(3.29) | 96.53(96.71) | 100(100) |

The results for all raingauges (see Table 2-2a) for V7 show the percentage of correct detections (rain events detected simultaneously by the TRMM PR and raingauges: ~1%) is lower than the number of false alarms (events registered by the TRMM and not recorded by raingauge: ~3%), but higher than the number of missed detections (events observed by raingauges but missed by TRMM: ~0.7%). The agreement in the number of rejections (when both TRMM and raingauges do not detect rain) is expected. Although the specific

quantitative values are different, the skill for near-nadir viewing angles (Table 2b) is nearly the same as that for all cases (Table 2-2a). Overall, V7 exhibits slightly better detection skill than V6 as indicated by the higher probability of correct detection and correct rejection, and lower probability of false alarms and missed detection.

**Table 2-3: Rainfall detection metrics for TRMM 2A25 V7 (V6) compared to RG observations as a function of time scale (10-, 20-, 30-, 60-min) during 06/2008 – 05/2011. Note the definitions of the skill scores are provided below. Y indicates positive detection; N indicates no detection.**

| | Time window (min) | | | | | | | | | | | | Perfect Score |
|---|---|---|---|---|---|---|---|---|---|---|---|---|---|
| | 10min | | | 20min | | | 30min | | | 60min | | | |
| | All | 0XX | 1XX | All | 0XX | 1XX | All | 0XX | 1XX | All | 0XX | 1XX | |
| Accuracy[a] | 0.97 (0.96) | 0.96 (0.96) | 0.97 (0.97) | 0.96 (0.96) | 0.96 (0.96) | 0.97 (0.96) | 0.96 (0.96) | 0.96 (0.96) | 0.96 (0.96) | 0.95 (0.94) | 0.94 (0.94) | 0.95 (0.95) | 1 |
| FB[b] | 1.5 (1.65) | 1.7 (1.84) | 1.39 (1.55) | 1.02 (1.12) | 1.05 (1.12) | 1.01 (1.12) | 0.83 (0.89) | 0.83 (0.87) | 0.82 (0.91) | 0.59 (0.63) | 0.56 (0.59) | 0.6 (0.66) | 1 |
| POD[c] | 0.61 (0.61) | 0.6 (0.58) | 0.61 (0.62) | 0.55 (0.55) | 0.55 (0.54) | 0.55 (0.56) | 0.49 (0.49) | 0.51 (0.5) | 0.48 (0.49) | 0.4 (0.4) | 0.42 (0.4) | 0.39 (0.4) | 1 |
| FAR[d] | 0.59 (0.63) | 0.65 (0.68) | 0.56 (0.6) | 0.46 (0.51) | 0.47 (0.52) | 0.45 (0.5) | 0.41 (0.45) | 0.39 (0.43) | 0.42 (0.46) | 0.32 (0.36) | 0.26 (0.31) | 0.36 (0.39) | 0 |
| POFD[e] | 0.02 (0.03) | 0.03 (0.03) | 0.02 (0.03) | 0.02 (0.02) | 0.02 (0.02) | 0.02 (0.02) | 0.02 (0.02) | 0.02 (0.02) | 0.02 (0.02) | 0.01 (0.02) | 0.01 (0.01) | 0.01 (0.02) | 0 |
| TS[f] | 0.32 (0.3) | 0.28 (0.26) | 0.35 (0.32) | 0.37 (0.35) | 0.37 (0.34) | 0.38 (0.36) | 0.37 (0.35) | 0.38 (0.36) | 0.36 (0.34) | 0.34 (0.33) | 0.36 (0.34) | 0.32 (0.32) | 1 |

[a] *Accuracy = [YY + NN] / Total*

[b] *Frequency Bias = FB = [YY + YN] / [YY + NY]*

[c] *Probability of detection = POD = YY / [YY + NY]*

[d] *False alarm ratio = FAR = YN / [YY + YN]*

[e] *Probability of False Detection = POFD = YN / [NN + YN]*

[f] *Threat Score = TS = YY /[YY + NY + YN]*

Results from the sensitivity study of the skill scores to time-scale of integration of raingauge observations centered at the time of TRMM overpasses are summarized in Table 2-3. TB RG3XX data are excluded from this comparison considering its coarse measurement accuracy (1 mm/tip), and due to the fact that the record length of concurrent

V6 and V7 is too short. V6 and V7 exhibit similar skill in accuracy and POFD at different time scales. The FB scores, which indicate whether TRMM has a tendency to underestimate (<1) or overestimate (>1) rainfall, show strong sensitivity to the time-scale of integration, followed by the gauge measurement sensitivity. Unbiased results are obtained at the 20 min time scale with skill scores close to perfect (1). The POD scores decrease with the time-scale as expected due to the space-time intermittency of rainfall, and no significant improvements were found in V7 as compared to V6. FAR scores, which count how often the satellite products detect rainfall in the absence of rainfall at the gauges, are slightly lower for V7. Lower scores are observed in RG1XX series in the inner mountain region than in the RG0XX series on the eastern ridges, possibly because of raingauge measurement threshold (RG0XX: 0.2 mm/tip, RG1XX: 0.1 mm/tip) and location (RG0XX: outer ridge, RG1XX: inner ridge). The TS values, which are sensitive to correct detection and penalize for both missed detections and false alarms, are consistently higher in V7 as compared to V6, but only slightly so. Overall, this analysis indicates that V7 improvements in rainfall detection in the Southern Appalachians are minimal relative to V6. This result is consistent with Kirstetter et al. (2013), who reported improvement in QPE but not in detection metrics for 2A25 V7 products relative to V6.

#### 2.2.3.2 Quantitative Precipitation Estimation (QPE)

To assess the accuracy of TRMM PR rainfall estimates, histograms of concurrent satellite near surface rain rate (NSR) estimates and gauge observations for the near-nadir

cases are displayed in Figure 2-4a, using the average raingauge rates at the PR pixel scale. Only non-zero data pairs are used, and thereby large amounts of non-rainy days are excluded from this comparison. The overestimation of the relative frequency of light rainfall (< 5mm/hr) results from QPE underestimation of heavier rainfall. Figure 2-4b suggests that V7 NSR estimates of moderate rainfall rates are higher than estimated surface rain rate (ESR) estimates. In addition, scatterplots and regression analysis were examined (not shown here) for ESR and NSR against raingauge observations with similar results to those reported by Prat and Barros (2010b). Compared to V6, a smaller slope is obtained in V7 for these two TRMM products, which is consistent with Seto et al. (2011) who showed that V7 rain rate estimates are larger than in V6 over land and over ocean. The tendency to underestimate rain rate (slope >1) has been mitigated in V7 with slopes closer to unity, thus indicating better agreement with the reference ground observations. The severe underestimation of heavy rainfall rates in both versions can be attributed at least in part to the lack of areal representativeness of the raingauges which are point estimates in contrast with the area-averaged (5×5 $km^2$) TRMM rainfall estimates, although the point estimates of rain rate are reduced by using a time-scale of at least 10 minutes centered at the satellite overpass time.

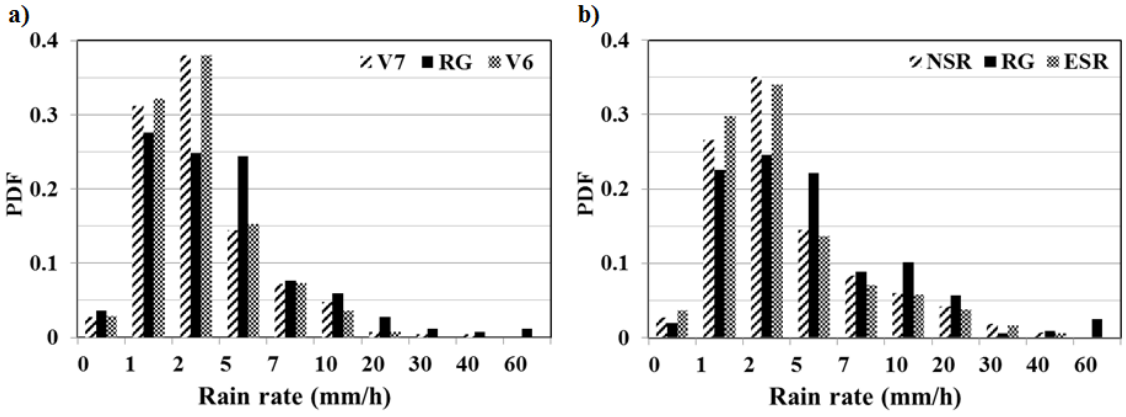


**Figure 2-4: a) Probability distributions of rain rates for V7 and V6 comparison of non-null TRMM 2A25 Near Surface Rain Rate (NSR) estimates and average raingauge rain rates for near-nadir pixels (scanning inclination angles ranging from 0° to 9°) during the period 06/01/2008-05/31/2011; b) Probability distribution of non-null TRMM 2A25 V7 surface rain rate products [Estimated Surface Rain Rate (ESR) and NSR] and average gauge rain rates during the period 06/01/2008-05/31/2013. Raingauge rain rates are calculated using time-scales of 10-min (RG0XX and RG1XX) and 30-min (RG3XX) corresponding to the interval centered at the time of satellite overpasses.**

## *2.3 Statistics and Physical Basis of PR 2A25 V7 Error Structure*

The physical basis of error structure in V7 is assessed focusing on the space-time variability of error and how it relates to storm structure for underestimation (UND), overestimation (OVR), false alarm (FA) and missed detection (MD) cases. This section is organized by first evaluating the overall quantitative performance of TRMM precipitation estimates compared to gauge data, next examining the rain type, rain rate, and the temporal distribution over a spectrum of time scales (e.g., diurnal and seasonal), and finally exploring the relationship between rainfall error and vertical reflectivity structure.

### 2.3.1 Surface Rain Rate Classes

Error analysis of TRMM estimates for 1820 PR overpasses in the Southern Appalachians during 2008-2013 is presented here. The reference rainfall is computed in a similar manner to that described earlier by selecting raingauges that lie within a 2.5 km radius around the center of the PR pixel. A sensitivity analysis of bias was conducted on four TRMM PR 2A25 precipitation products: estimated surface rain rate (ESR), near surface rain rate (NSR), 2-4 km averaged rain rate, and integrated column rain rate at various time scales ranging from 10- to 60-min (not shown here). Results for TRMM NSR indicate that bias is minimized at 10min time scales for RG0XX & RG1XX, and 30min for RG3XX estimates (RG0XX: ~0.5, RG1XX:~0.2, RG3XX:~0). Consequently, 10- and 30- min (centered at the time of overpass) rain rates from RG0XX & RG1XX and RG3XX respectively will be used as reference hereafter. As seen in Figure 2-5a, bias is lowest overall in the inner mountain region (RG1XX). Overestimation of light rainfall leads to large positive bias everywhere, but is much larger on the western ridges (RG3XX) than on the eastern ridges (RG0XX) or in the inner region (RG1XX) consistent with the gauges' measurement resolution (Figure 2-5a); for moderate and heavier rain rates (> 5 mm/hr), the bias is negative, relatively small, and uniformly distributed.

Regression analysis (not shown here) of PR 2A25 V7 rainfall estimates (NSR and ESR) versus averaged gauge data indicates that for non-null PR-gauge pairs, both estimates derived from PR are in good agreement (regression slope close to one) with the

ranges of rainfall intensity associated with the regional hydrometeorological regimes, but the $R^2$ value is very low for both estimates (NSR: 0.09, ESR: 0.08), which likely results from significant discrepancies for heavy rainfall events.

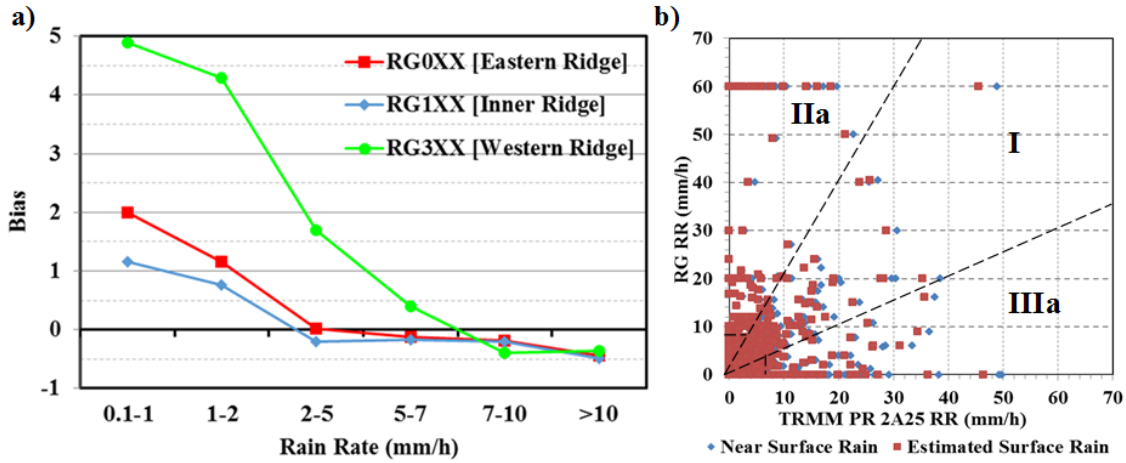


**Figure 2-5: a) Bias between TRMM 2A25 V7 NSR and average raingauge rain rates for different series: RG0XX, RG1XX, and RG3XX (see Table 2-1); b) Scatterplot for TRMM 2A25 V7 surface rain rates (NSR and ESR) and average raingauge rain rates during the period 06/01/2008-05/31/2013. Raingauges rain rates are using a 10-min (RG0XX and RG1XX) and 30-min (RG3XX) scale centered at the time of the satellite overpasses. Note raingauge measurements and TRMM profiles classification as described in Table 2-4 (5 primary categories, I-II-III-IV-V, and two subcategories, IIa-IIIa).**

In order to better understand the quantitative discrepancy between TRMM and RG, the matched PR pixels and raingauge cluster pairs are classified into five distinct categories corresponding to the relative difference (ε) of the 2A25 estimates with respect to raingauge observations (see Figure 2-5b and Table 2-4). The same classes are used later in the manuscript to examine TRMM reflectivity profiles. In Table 2-4, regardless of the value of the discrepancy in the rainfall rate estimates, conditions when rain was

simultaneously observed by the satellite and raingauges (cases I, II, III), correspond to approximately 31% of all cases, while about 50% report rain for TRMM only (case IV, FA), and about 19% report rain for raingauges only (case V, MD). As will be shown later in more detail (see Figure 2-7a), a large fraction of FAs and MDs occurs at larger viewing angles (> 8°) in which case NUBF uncertainty is expected to be higher. However, the predominance of FAs raises concerns about the reliability of the algorithm in mountainous regions. In order to address this question, an evaluation was conducted by comparing concurrent TB and weighing raingauge observations (not shown here). The analysis indicates that the TB raingauges miss detection of light rainfall events of short duration (< 30 min) with accumulations below their measurement sensitivity, corresponding to circumstances when wind and turbulence under-catch effects can be dominant, but these circumstances are not statistically meaningful. Significant discrepancies between TB and weighing raingauges occur for snowfall conditions when near-surface air temperature is below 0°C, but this is still a small number of events (~ 15% of FAs) in the region of study. Thus, the problem of excessive spurious detection cannot be explained by TB raingauge measurement limitations alone.

**Table 2-4: Classification of TRMM 2A25 reflectivity profiles as a function of the difference (ε) [RR_TRMM2A25 – RR_RG]/RR_RG that represents the relative error of the 2A25 estimates with respect to the raingauge observations. The time-scale of integration is 10-min for RG0XX and RG1XX and 30-min for RG3XX, which**

**corresponds to the minimum error bias for the period of record. Bold values correspond to ε = 0.5.**

| Class | Diff (ε) = [RR_TRMM – RR_RG]/RR_RG | | |
|---|---|---|---|
| | ε = 0.25 | **ε = 0.50** | ε = 0.75 |
| I : Abs(Diff) < ε | 126 | **237** | 368 |
| II : Diff < -ε | 259 | **174** | 70 |
| IIa : Diff < -ε and RR_RG > 7mm/h | 99 | **76** | 45 |
| III : Diff > ε | 165 | **139** | 112 |
| IIIa : Diff > ε and RR_TRMM > 7mm/h | 50 | **43** | 35 |
| IV : RR_RG = 0 and RR_TRMM ≠ 0 | 863 | **863** | 863 |
| V : RR_RG ≠ 0 and RR_TRMM = 0 | 330 | **330** | 330 |
| Total | 1743 | **1743** | 1743 |

An overview of the organization of error categories as a function of rain type and rain rate is provided in Figure 2-6. The rain type (derived in TRMM 2A23 as a parameter to separate convective and stratiform rain) and rain rate categories follow the error classification framework described in Table 2-4. A large fraction of UND errors (class II) is associated with "probably stratiform" (rain type: 120) rainfall by the TRMM PR algorithm in the winter, but over 60% correspond to heavy rainfall events (see Table 2-4, IIa) and most convective rainfall (200 & 210) occurs during the summer. There is a relatively small number of samples overall (the UND 5-year total is only 174, see Table 2-4). The errors tend to cluster at specific times-of-day that are consistent with the regional hydrometeorology, thus enhancing our confidence on the diurnal cycle and providing a physical basis for attribution. Indeed, a survey of the results shows that the diurnal cycle of UND error peaks during the period 15-18 EDT (not shown here), a time of day typically associated with daytime solar forcing of convective activity. The histograms of TRMM

and raingauge rain rate estimates for UND events (Figure 2-6a, right panel) have different skew with TRMM PR NSR estimates mostly below 5 mm/hr, whereas most raingauge observations exceed 10 mm/hr. This indicates that UND errors cannot be corrected using linear bulk adjustments such as bias correction; rather, physical insight is needed to improve retrievals.

Overestimation (OVR, class III) errors are mostly associated with wintertime precipitation classified as "probably stratiform". Inspection (not shown here) of the apparent annual and diurnal cycles of OVR errors (note again the limited sample size on an hourly basis: 5-year total OVR is 139, Table 2-4, III) indicates that these errors exhibit a diurnal cycle peaking in January and March during daytime (9-15 EDT) consistent with the diurnal cycle of rainfall in winter (Figure 2-3d). A good overall agreement between the histograms of raingauge and TRMM rain rates (Figure 2-6b, right panel) for these events suggests that bias correction of OVR errors should lead to immediate improvements in TRMM PR products. Figure 2-6c shows that FA (IV) errors are also associated with "stratiform" and "probable stratiform" rainfall throughout the year and light rainfall rates (< 5 mm/hr).

Overall, the results show that the error budget of TRMM PR NSR estimates is largely controlled by ambiguity in the detection of the bright band (stratiform conditions) for significantly off-nadir observations (significant NUBF effects) for light rainfall conditions in all seasons, and in the wintertime generally.

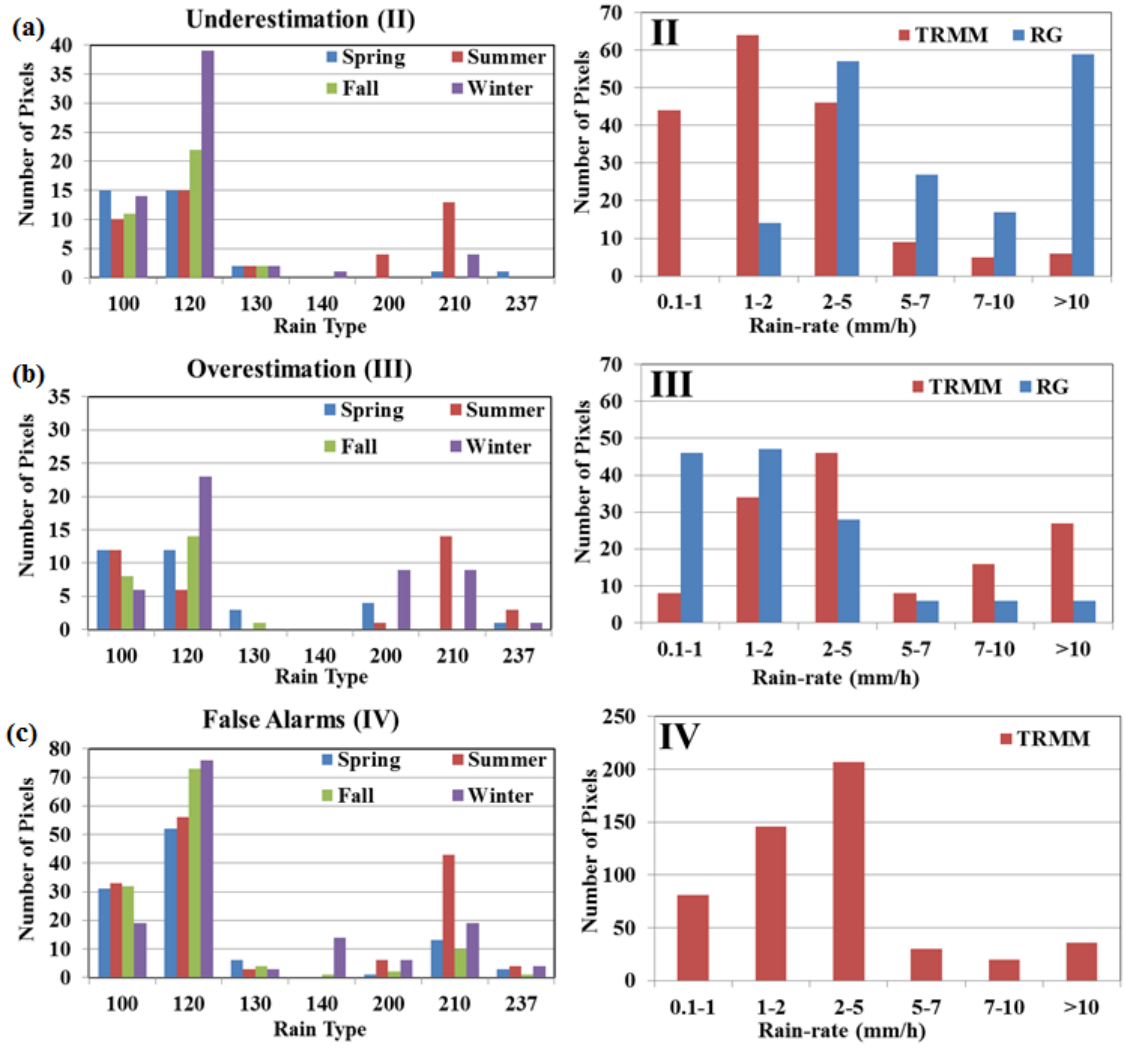


**Figure 2-6: Histogram of rain type (left panels) and observed RG rain rate and NSR from TRMM (right panels) distributions for the different errors: a) II (UND); b) III (OVR); and c) IV (FA). The error classification is provided in Table 2-4. The rain type categories correspond to the TRMM 2A23 Rain Type Flag: 100- Stratiform certain, 120- Probably stratiform, 130- Maybe stratiform, 140- Maybe stratiform or maybe transition or something else, 200 & 210- Convective certain, 237- Probably convective. (For further details please see the 2A23 documentation at http://disc.sci.gsfc.nasa.gov/precipitation/documentation/TRMM_README).**

### 2.3.2 Space-Time Error Structure

A survey of precipitation detectability skill in the TRMM PR 2A25 V7 from the point of view of FA and MD errors is presented in Figure 2-7. The impact of observing geometry is explored in Figure 2-7a, focusing specifically on the interplay between complex orography, satellite orbit, and the viewing angle for each pixel in the satellite's swath. Detection skill depends on the orbit and the specific trajectory of the satellite over the region. For the eastern ridges (RG0XX series), a large portion of FA occurs at small angles, in particular ~5°, reflecting the geometry of the overpasses and the terrain underneath as the satellite approaches the Appalachians; in the inner ridges (RG1XX series), more cases are observed around 8° and 11°; for the western ridges (RG3XX series), almost all cases are registered at off-nadir angles (≥9°), especially around 11°. Note that at larger viewing angles (RG1XX and RG3XX) the radar signal also travels through a longer trajectory, and thus an extended liquid water path. Figures 2-7b and c display the diurnal and seasonal distributions of FAs and MDs corresponding to rainfall classes IV and V (Table 2-3). Note the strong diurnal cycle of FAs peaking at mid-day and early afternoon, especially in the case of the inner region (blue color). The seasonal cycle shows that FAs in the eastern ridges and western ridges are relatively uniformly distributed throughout the year, whereas they peak in the summer in the inner ridges. Furthermore, the number of FAs and MDs in the inner region is very high and dominates overall statistics. Close examination of the diurnal cycle reveals that most FAs in the summer occur in the

afternoon (12-18 EDT) corresponding to diurnal convective activity, while winter cases follow the diurnal cycle of precipitation pattern peaking in the early afternoon (not shown here).

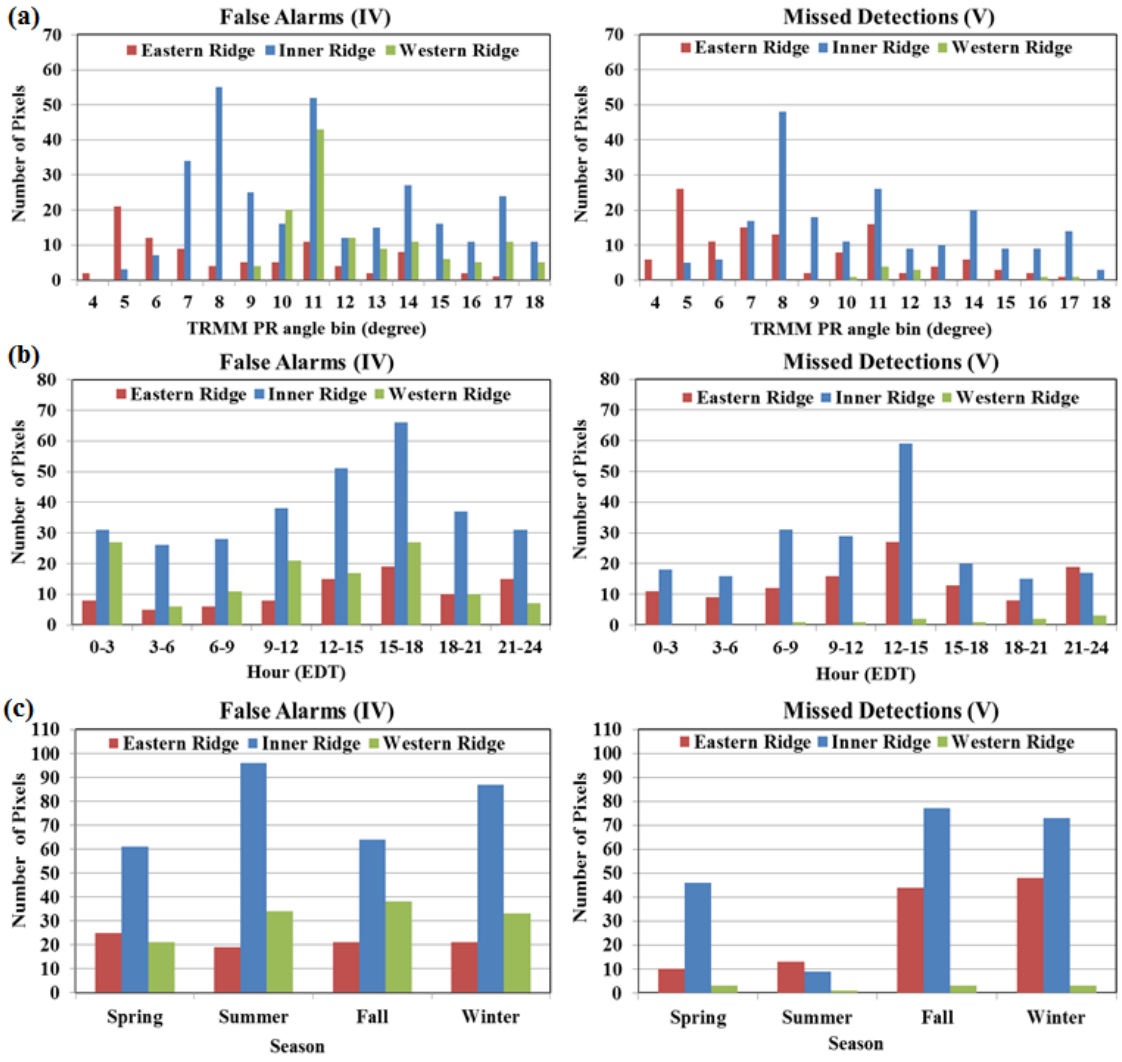


**Figure 2-7: Histograms of FA (left panel) and MD (right panel) occurrences as a function of the viewing angle (a), time of the day (b) and season of the year (c). As previously, the colors correspond to raingauges aligned with the eastern (red, RG0XX), western (green, RG3XX) and inner ridges (blue, RG1XX) in the region of study (Figure 2-1, Table 2-1).**

Among all MD cases, most are classified as "no rain" and some are categorized as "other", whereas only 3 are classified as stratiform, and none are considered convective (not shown here). Figures 2-7b and c for MDs (class V) show a strong diurnal cycle with most occurring around 12-15 EDT and a seasonal trend with a large proportion occurring during the cold season, which is attributed to the frequent presence of fog and low level clouds in the fall and winter seasons, especially in the inner region (RG1XX). The very small count of MDs in the western ridges (RG3XX) is explained in part by the coarse gauge sensitivity (1mm/tip, 30-min time-scale), and because fog seldom develops over this region due to strong winds. Dense and deep fog formation during the fall and winter seasons in the inner mountain region establishes conditions for enhanced stratiform rainfall via seeder-feeder mechanisms at low levels (<1 km) that is measured by the gauges in the inner mountain region (e.g. Wilson and Barros, 2014), but cannot be detected by the TRMM PR due to the topography and automatic ground clutter correction. In addition, the minimum detectable signal of TRMM PR is approximately 18 dBZ (0.4 mm/h) (Heymsfield et al., 2000;Yang and Nesbitt, 2014), and thus weak radar reflectivity for light rainfall can also partly explain MD statistics.

### 2.3.3 TRMM PR Reflectivity Profile and Rainfall Detectability

Here, we examine the relationship between rainfall detectability and the vertical reflectivity structure of TRMM PR. To facilitate the comparison of various types of precipitation including the distinction between convective and stratiform precipitation by

TRMM-derived criteria, three categories of reflectivity profiles have been identified (see Figure 2-8): 1) stratiform with bright band (BB); 2) stratiform without bright band (BB); and 3) convective. Note that the reflectivity profile is used in the rain classification algorithm, in addition to the precipitation rate estimation proper.

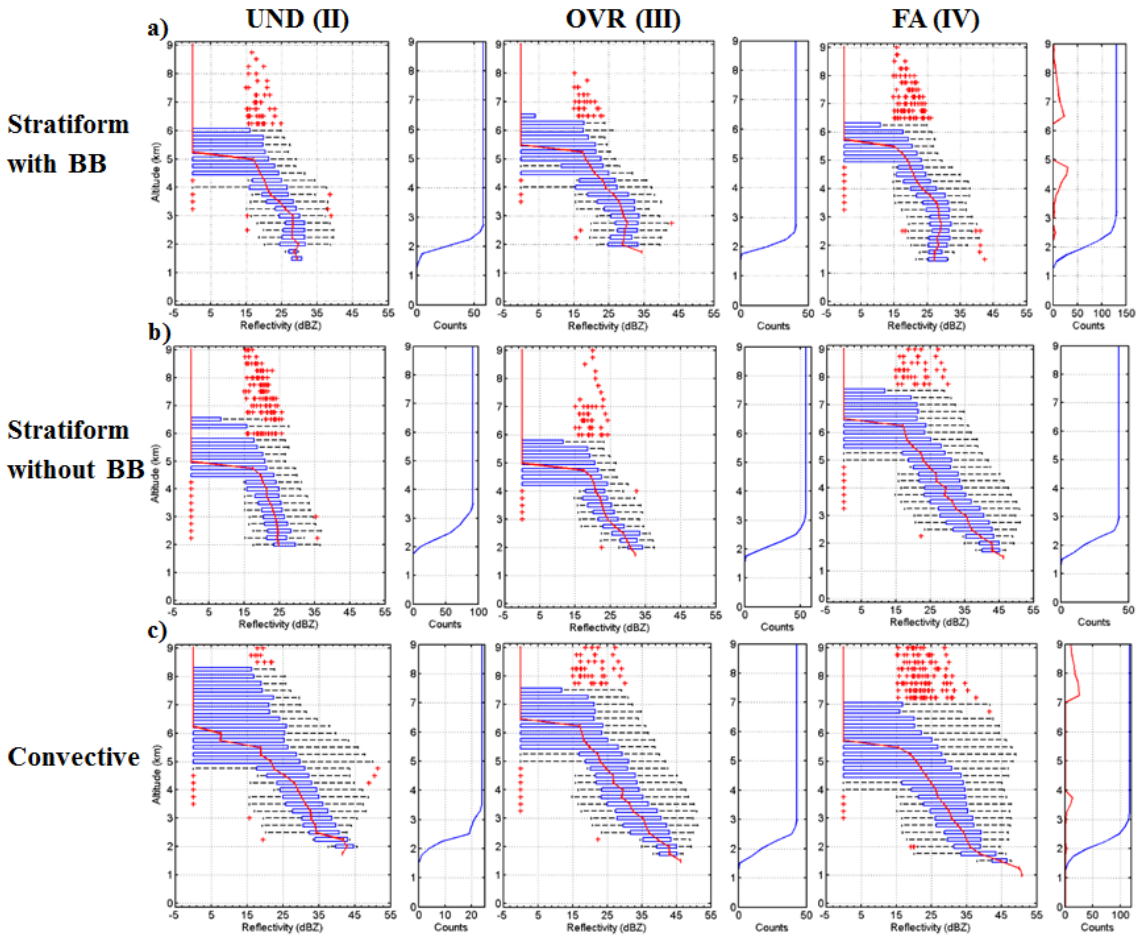


**Figure 2-8: TRMM 2A25 reflectivity profiles for error classes II (UND), III (OVR), and IV (FA): a) Stratiform conditions with BB detected (Rain Type: 100 and 130, Figure 2-6); b) Stratiform conditions without BB detected (Rain Type: 120 and 140, Figure 2-6); and c) Convective conditions (Rain Type: 200, 210, and 237, Figure 2-6). The blue box denotes the interquartile range (IQR) from the lower quartile (25$^{th}$) to the upper quartile (75$^{th}$); the median is indicated by the red mark inside the box. The red line connects the median reflectivity at all levels to yield the median reflectivity profile.**

**The two horizontal lines ("whiskers") extending from the central box represent the ± 1.5 IQR interval. Outliers (points falling out of ± 1.5 IQR) are marked as red crosses. For each error class, the right panel shows the number of observations with height; the red line for error class IV (FA) shows the distribution of outliers with height.**

For stratiform UND cases (see Figures 2-8a and 2-8b, class II), the reflectivity gradually decreases with altitude and the median values between 2 km and 4 km are in the range of 20 – 30 dBZ approximately. Some UND cases (see the red outliers in Figure 2-8b, II) display high cloud tops (up to 9 km), consistent with the heavy rainfall events in Figure 2-6a that are indicative of warm rain with embedded convection. Reflectivity data below 2 km are often removed due to ground clutter contamination. In Figure 2-8a (III), the mean reflectivity profile shows a decreasing tendency with height (from 2.75 km toward the ground surface), suggesting that summertime OVR errors are likely linked to light rainfall evaporating before it reaches the ground (see rain type: 100 in Figure 2-6b). Compared to the UND (II) cases (left panels in Figure 2-8), the reflectivity profiles for OVR cases show steeper positive gradients at lower levels, in particular below 3 km, and more measurements are available below 2 km altitude in the convective cases(see Figures 2-8b and 2-8c, III). The downward decreasing trend of reflectivity toward the surface is also evident in the reflectivity profiles of FAs for stratiform conditions with and without bright band (see Figure 2-8a, IV), which can also be explained by raindrop evaporation during the summer (see rain type: 100 in Figure 2-6c). Compared to the UND and OVR cases in Figure 2-8a and b, the FA stratiform reflectivity profiles decrease more gradually with altitude at lower levels. Note the rapid reflectivity increase (35-50 dBZ) below 2 km in the

convective cases (IV, Figure 2-8c). This feature will be further discussed next in the context of error diagnosis and interpretation. Overall, steeper positive gradients in reflectivity are displayed in OVR cases at lower levels, while the decreasing trend with height shown in UND and FA possibly indicates light rainfall evaporation before reaching the ground. The high cloud tops in UND are characteristics of warm stratiform rainfall with embedded convection, resulting in heavy rainfall events.

## *2.4 Physical Context of Retrieval Error*

In this section, we focus primarily on diagnosing the potential sources of errors in the retrieval algorithm by studying selected representative TRMM overpasses with substantial discrepancies between 2A25 V7 NSR estimates and raingauge observations, including isolated thunderstorms, mesoscale convective systems, cold fronts, hail events, and snow showers. Figure 2-9 shows the TRMM overpass in the region of study for each of the selected cases overlaid on the base reflectivity fields from the KMRX and KGSP NWS (National Weather Service) radars respectively in Knoxville, TN and Greer, SC.

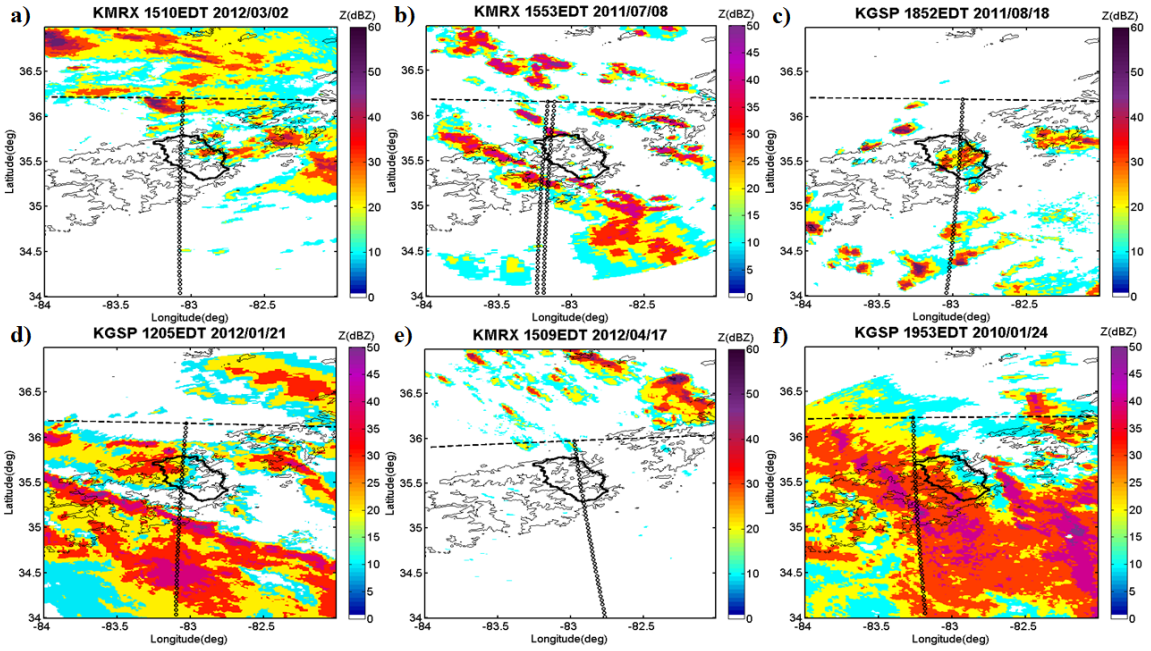


**Figure 2-9: Base reflectivity composites from KMRX (Knoxville, TN) and KGSP (Greer, SC) National Weather Service radars corresponding to the overpass times shown in Figures 2-10, 2-11, 2-12 below. The lines of black circles show the overpass tracks corresponding to the cross-sections in Figures 2-10, 2-11, 2-12. The dashed line delimits the northern boundary of TRMM PR swath over the Southern Appalachians, and the 1,000 m terrain elevation contour line and the outline of the study region (the Pigeon River basin) are marked in solid black for reference.**

### 2.4.1 Local Underestimation (II)

Figure 2-10a depicts a vertical cross-section from the TRMM overpass at 15:08 EDT during a tornado outbreak event on 2 March 2012 as the primary squall line was moving over the region (Figure 2-9a). After applying the ground clutter correction, the near surface rain rate of 4.5 mm/hr at the location marked by the black arrow (viewing angle 7.6°) is estimated at 2.25 km altitude. The collocated raingauge (RG104, Figure 2-1) is placed at a much lower elevation (~1.6 km) and records very heavy rainfall intensity (60 mm/h). In the presence of low level fog and orographic clouds, this difference in elevation

(~ 650 m) is sufficient to explain the one order of magnitude difference in rainfall intensities by seeder-feeder enhanced coalescence (Wilson and Barros, 2014). The PR reflectivity profile extends up to 8 km in altitude, and there is no indication of bright band or large ice-scattering aloft; nevertheless, this pixel is classified as "probably stratiform" (rain type: 120) based on the H method because of the weak echo. In addition to the ground-clutter filter that eliminates a significant fraction of the measured reflectivity profile at lower levels, the incorrect classification of shallow convection as probably stratiform is also due in part to the effect of spatial averaging over the PR's relatively coarse horizontal resolution, a smoothing effect that is amplified at off-nadir viewing angles. Similar results were reported by Heymsfield et al. (2000) who found that convective precipitation often falls from cells smaller than the PR footprint and its average reflectivity tends to be underestimated due to the NUBF effects, consequently leading to the rain-type classification being artificially biased toward the stratiform type. Nevertheless, an examination of the TRMM reflectivity cross-section in Figure 2-10a as well as PR 4 km reflectivity fields (not shown here) clearly reveals the substantial advantage of the satellite based radar in mountainous regions, where the terrain blocks the monitoring effectiveness of the ground radars (see Figure 2-9a).

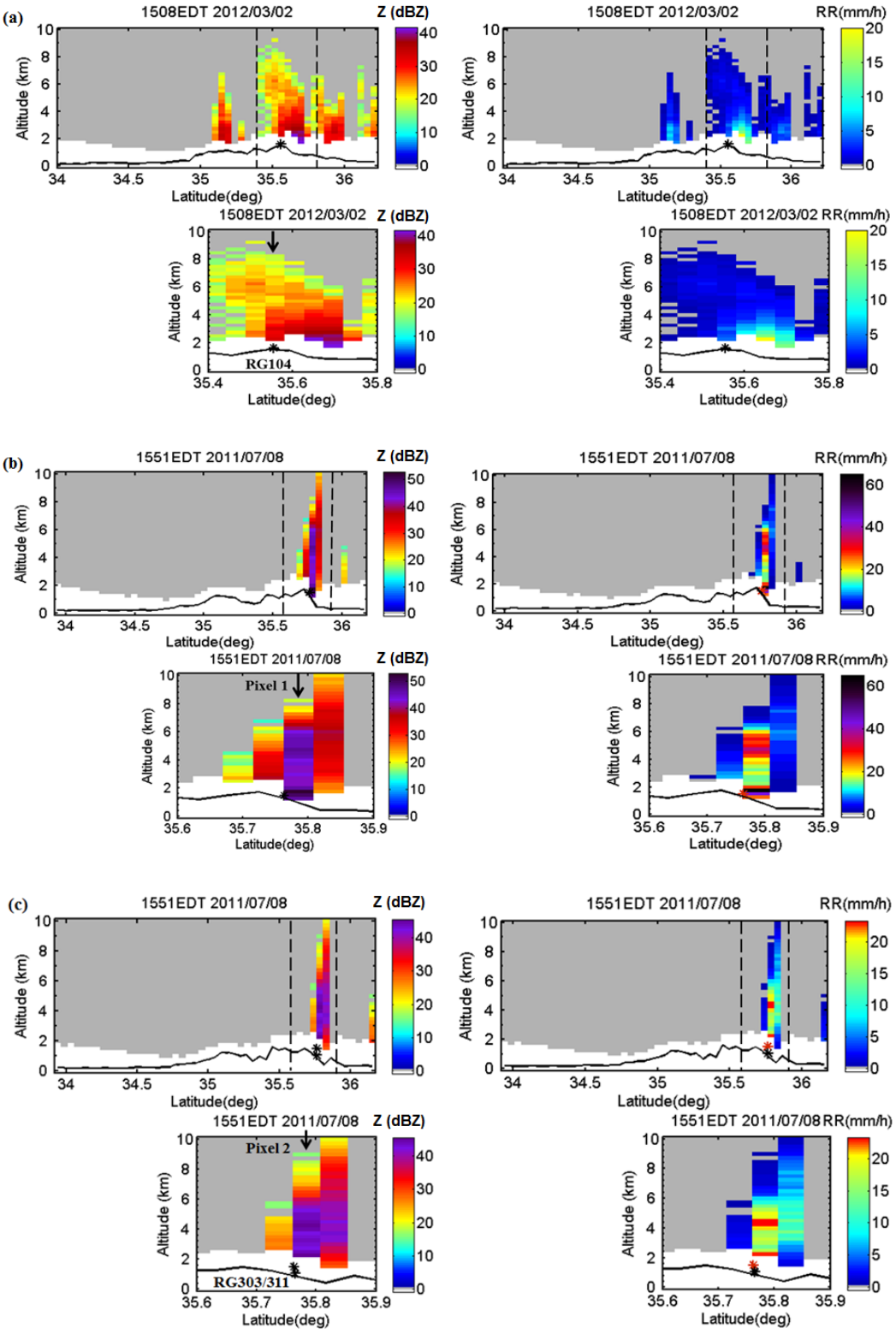
(a)
1508EDT 2012/03/02
Z (dBZ)
RR(mm/h)
Altitude (km)
Latitude(deg)
RG104
(b)
1551EDT 2011/07/08
Pixel 1
(c)
Pixel 2
RG303/311

**Figure 2-10: Cross section of reflectivity (Z) and rain rate estimates (RR) from TRMM 2A25 for three underestimation cases: a) 15:08 EDT on 2 March 2012; and for two different cross-sections at 15:51 EDT on 8 July 2011 (b, c). The top row shows the overpass cross-section. The bottom row shows the cross-section between the two dashed vertical lines in the top rows. Asterisks denote the position of the raingauges as marked, and the color in the right panel is consistent with the measured rain-rate. The black arrow identifies the PR profile used to make the error determination. Ground clutter flags are shown in white. The black continuous line represents the topography.**

Figures 2-10b and c display the vertical cross-section of reflectivity and rain rate of two adjacent scans on 8 July 2011 15:51 EDT associated with the presence of small bands and clusters of severe summer thunderstorms in the region of interest at the time of overpass (Figure 2-9b). Two selected pixels (denoted as pixel 1 on one scan and pixel 2 on the other) observed at ~12.1° angle among those corresponding to the high altitude outliers (red + signs) in Figure 2-8c (II) are highlighted here. Note the steep increase in profile reflectivity at altitudes above 4 km followed by a decrease with height that indicates the existence of a bright band; along with high low-level reflectivity, the vertical structure of reflectivity suggests that over the western slopes of the Appalachians high precipitation rates were produced by a stratiform system with embedded convection. Although gauges RG303 (40 mm/hr) and RG311 (60 mm/hr) are very close together (Figure 2-1), RG303 is located at a higher elevation (~1. 5 km) on the wall of a valley running nearly perpendicular to the western ridge of the Southern Appalachians, whereas RG311 is at lower elevation (~1.25 km) in the valley proper. The TRMM near surface estimate for both scans is between 22-25 mm/hr. The effect of the ground clutter correction is evident in Figure 2-10b and 10c. In addition, note the relative location of the gauges at

the boundary between two columns, one with low to moderate reflectivity and one with very high reflectivity in Figure 2-10b and 10c. Because the clusters of shallow embedded convection are very small, averaging significantly reduces the TRMM estimated rainfall and reduces spatial variability. Therefore, TRMM appears to underestimate rainfall from the isolated small-scale summer convective cells, consistent with previous studies demonstrating the underestimation of convection over land by the TRMM PR algorithm (Iguchi et al., 2009;Rasmussen et al., 2013).

Among the two raingauge observations in pixel 2, more intense rainfall is observed in the nearby valley (RG311) than on the ridge (RG303), and the PR reflectivity in the valley is much higher than surrounding ridges. Despite horizontal separation in addition to the elevation difference, the low level enhancement of rainfall at RG311 compared to RG303 is consistent with the increased depth of the precipitation column thus enhanced raindrop growth by coalescence (Prat and Barros, 2010a;Wilson and Barros, 2014). In such circumstances, orographic rainfall does not increase with elevation as in the canonical model. This event highlights detectability challenges over mountainous regions at coarse horizontal scales (e.g., high spatial variability due to the inability to resolve the complexity of the physics of orographic enhancement). The effective resolution deformation at far-range viewing angles may further contribute to the large underestimation.

### 2.4.2 Local Overestimation (III)

At the time of the TRMM overpass on 18 August 2011 18:53 EDT, there were small convective clusters and isolated thunderstorms scattered across the region (Figure 2-9c). The KMRX radar located in Knoxville, TN shows no activity over the Appalachians, but the KGSP radar located in Greer, SC does show activity over the eastern ridges, which is consistent with the shallow isolated cells detected by the TRMM PR shown in Figure 2-11a. Classified as "certainly convective" (the reflectivity profiles show no signal of ice scatter aloft), the retrieved near surface rain rate overestimates the observed precipitation at RG005 (~1.52 km; 12 mm/hr) and RG008 (~1.74 km; 18 mm/hr) by nearly 60% on average (viewing angle is 5.2°). Interestingly, despite very different vertical structure including the bright band effects for the UND (II) case on 8 July 2011 discussed in Section 2.4.1, the near surface precipitation estimates derived from TRMM for both cases are about the same (~ 24 mm/hr). However, the OVR(III) problem could be related to the relative position of the two gauges at the edge of the isolated convective cluster (Figure 2-9c) as the satellite moves over the orography, in which case NUBF artifacts should lead to overestimation of reflectivity over the gauges outside of the convective cluster. Indeed, the TRMM PR reflectivity between 2 and 4 km is in the 40-50 dBZ range, whereas the base-reflectivity from KGSP at gauge locations is in the 20-30 dBZ range.

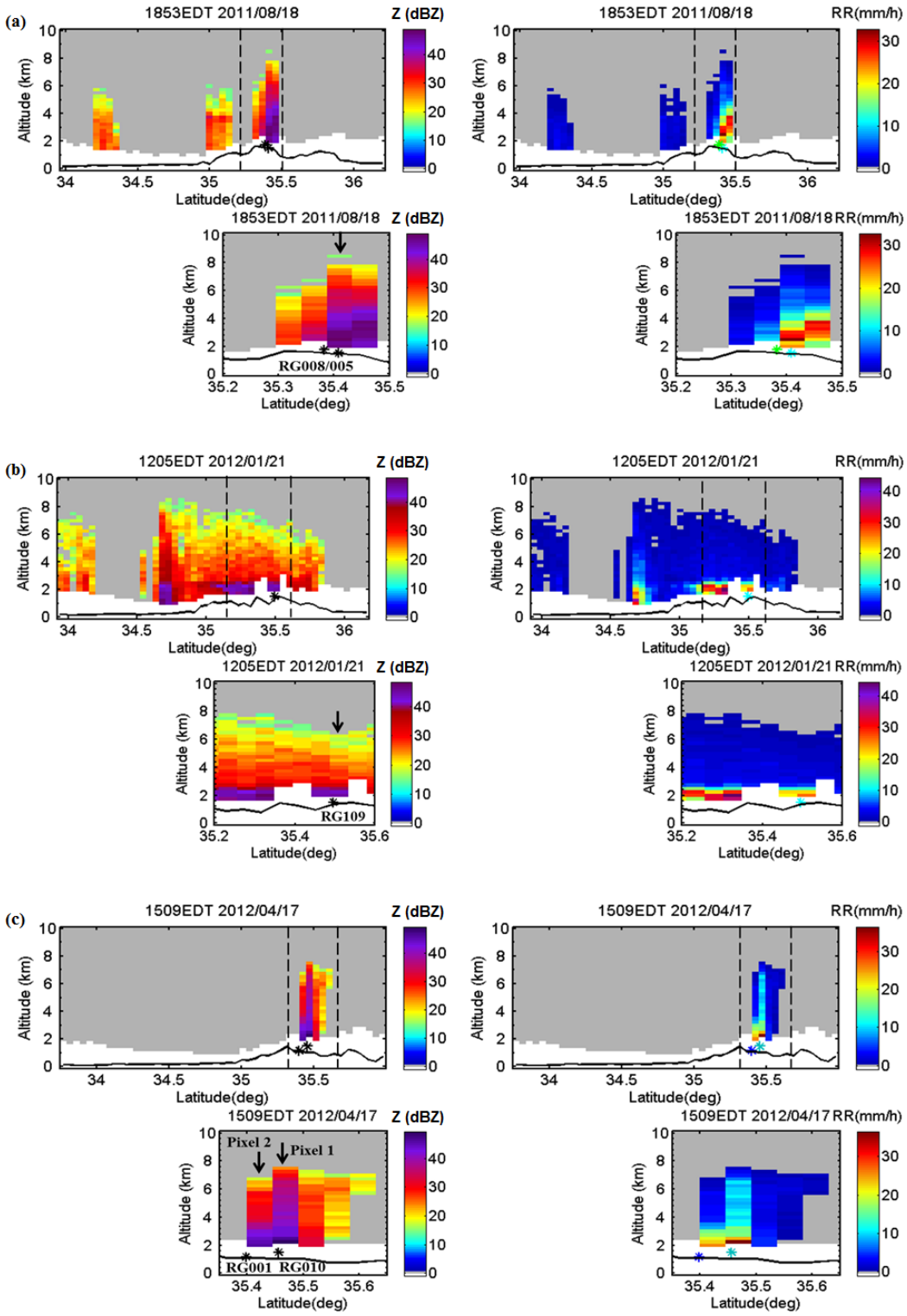
(a)
1853EDT 2011/08/18
Z (dBZ)
RR(mm/h)
Altitude (km)
Latitude(deg)
RG008/005
(b)
1205EDT 2012/01/21
RG109
(c)
1509EDT 2012/04/17
Pixel 2
Pixel 1
RG001
RG010

**Figure 2-11: Cross section of reflectivity (Z) and rain rate estimates (RR) from TRMM 2A25 for three overestimation cases, respectively: a) 18:53 EDT on 18 August 2011; b) 12:05 EDT on 21 January 2012; and c) 15:09 EDT on 17 April 2012. The top row shows the overpass cross-section. The bottom row shows the cross-section between the two dashed vertical lines in the top row plots. Asterisks denote the position of the raingauges as marked, and the color in the right panel is consistent with the measured rain-rate. The black arrow identifies the PR profile corresponding to the 2A25 used to make the error determination. Ground clutter flags are shown in white. The black continuous line represents the topography.**

Two other relevant OVR (III) cases coincided with the passage of a cold front with a leading pre-frontal convection line in the Piedmont on 21 January 2012 that was captured by the TRMM overpass at 12:05 EDT (Figure 2-9d), and a pattern of disorganized thunderstorm activity ahead of the propagation of a westerly convective system on 17 April 2012 with overpass at 15:09 EDT (Figure 2-9e). The winter system produced major winter snow and ice precipitation from western North Carolina to New York State. In the reflectivity cross-section (Figure 2-11b), the vertical profiles exhibit a sharp decrease of about 16 dBZ in reflectivity between 2 km and 3 km. The TRMM PR rain rate at ~2 km and the value observed at RG109 in the inner mountain region (~1.5 km, Figure 2-1) are 26.3 mm/h and 10.8 mm/h respectively, resulting in an overestimation of 140%. However, raingauge measurements are expected to exhibit significant errors (~ up to 60%) for frozen precipitation, and even higher for snow in the presence of strong winds. Since this event produced significant snow accumulations and frozen rain, error attribution is an ambiguous proposition.

Both ground-based radars (KMRX, KGSP) miss the deep isolated convective activity in the mountains that is detected by the TRMM PR (Figure 2-11c). The vertical profiles for pixel 1 and 2 over the locations of RG001 and RG010 on the eastern slopes of the Appalachians show large reflectivity (>30 dBZ) up to around 6-7 km, suggesting the presence of ice/hail aloft. Records held by the State Climate Office of North Carolina (http://www.nc-climate.ncsu.edu/lsrdb/index.php) reveal multiple reports of intense hail over large areas in the Southern Appalachian Mountains at the time. However, raingauge records indicate only 1.2- and 9-mm/hr compared to 25.8- and 36.5-mm/h from TRMM estimates for pixel 2 (RG001) and pixel 1 (RG010) respectively. Again, this reflects the deficiency of tipping-bucket gauges to capture frozen precipitation, and hail in particular. Conditions in the two pixels are classified as "certainly convective" because of the high horizontal reflectivity gradients. The TRMM PR demonstrates good capability to detect this hail-producing storm.

### 2.4.3 Local False Alarms (IV)

FA (IV) errors can result from NUBF effects for certain viewing angles, terrain and weather configurations due to coarse resolution leading to spatial deformation in reflectivity similar to the problems leading to overestimation in the August 2011 case (Figure 2-11a) discussed above. Such errors could result from non-precipitating ice clouds, or from light snowfall under windy conditions that is missed by the raingauges. Indeed, blizzard conditions were present for the TRMM overpass 24 January 2010 19:54 EDT

(Figure 2-9f). Note the extremely large reflectivity values in the lowest levels in the cross-section on the western ridges of the Appalachians displayed in Figure 2-12. The vertical profiles exhibit large increments of reflectivity (22 dBZ) and rain rate (47 mm/h) below 4 km. The pixel identified by the black arrow is classified as "certainly convective" and the retrieved near surface rain rate is ~50 mm/h at 1.75 km elevation, whereas the nearest raingauge (RG302, at 1.86 km) does not register precipitation. According to winter storm reports from the State Climate Office of North Carolina (http://www.nc-climate.ncsu.edu/climate/winter_wx/database.php), snow showers developed across the mountains on 12 January 2010, resulting in ice and snow accumulation in the lower valleys. The substantial increase in reflectivity at lower levels in the TRMM PR profiles likely results from frozen precipitation particles in cold clouds and/or the accumulated ice and snow in the valleys detected by TRMM.

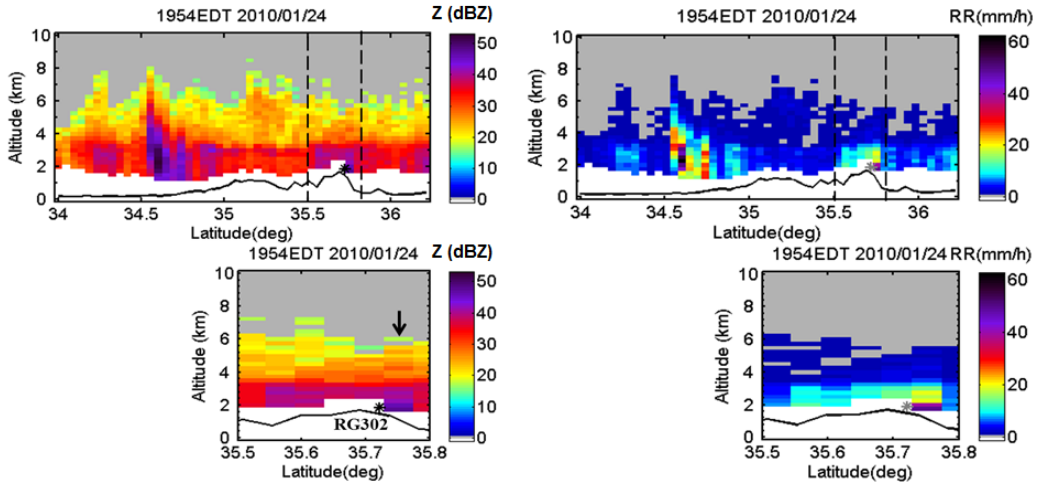


**Figure 2-12: Cross section of reflectivity (Z) and rain rate estimates (RR) from TRMM 2A25 for a selected case of incorrect False Alarm determination at 19:54 EDT on 24 January 2010. The top row shows an overpass cross-section. The bottom row shows**

**the cross-section between the two dashed vertical lines in the top row plots. Asterisks denote the position of RG302, and the color in the right panel is consistent with the measured rain-rate. The black arrow identifies the PR profile used to make the error determination. Ground clutter flags are shown in white. The black continuous line represents the topography.**

## *2.5 Summary and Conclusions*

TRMM PR 2A25 QPE products were spatiotemporally matched and compared with ground gauges in the Southern Appalachian Mountains over a five-year period 2008-2013, which provides a statistically large sample of comparisons performed at PR-pixel resolution. The quantitative comparisons yield favorable agreement of the PR with raingauge observations, with clear advantage over remote ground-based operating radars, but errors can be significant depending on the underlying rainfall regimes.

First, V7 and V6 QPEs were inter-compared in order to assess the impact of retrieval algorithm changes such as reintroducing the NUBF correction, recalibration of the Z-R relationship over land, and attenuation correction of the PR radar signal. Although a small improvement from V6 to V7 was identified at high to moderate rainfall rates, the results do not show significant differences in warm-season precipitation detection skill.

Based on the TRMM rain-type classification, characteristic features in the vertical structure of reflectivity and retrieved rainfall profiles that can be associated with distinct error characteristics under various precipitation regimes were identified. Regardless of error type, a significant fraction of estimation errors occurs when rainfall is classified as

"probably stratiform", which is hypothesized to result from the compounded effect of radar sensitivity and NUBF that renders the PR detectability of bright band unreliable for small-scale systems, especially at far-viewing angles. The statistics of FAs are highly sensitive to the measurement threshold of the raingauges (TB tip size) and the phase of precipitation. Nevertheless, the errors exhibit a relatively constant rate of occurrence throughout the year, a strong diurnal cycle with early and mid-afternoon peaks, a large skew of the rain rates toward low values (< 5 mm/hr), and the highest incidence is in the inner mountain region. This suggests that averaging at the coarse resolution of the PR pixel eliminates the signature of the small-scale complex structure of isolated orographic convection and localized multi-layered clouds and fog that are dominant in the region, and thus explains the high number of FA counts using the point-to-pixel strategy used here.

MDs show a strong annual cycle occurring predominantly during the cold season and into the spring with very low values in the summer. The diurnal cycle indicates that MDs appear linked to fog and multi-tiered low-level clouds especially in the inner mountain region, which the TRMM PR products fail to detect due to the ground clutter correction. The high reflectivity sensitivity threshold of the PR can also result in failure to detect weak echoes, thus missing detection of light rainfall. Ground-clutter contamination is not a problem inherent to the TRMM PR alone, but it is rather a general challenge for all space-based radars such as the DPR (Dual-frequency Precipitation Radar) on the GPM

satellite. This work took advantage of multiple sources of concurrent and co-located observations to investigate in detail the conditions associated with different types of error, which should be helpful to identify opportunities for improving retrieval algorithms in regions of complex terrain, despite the challenges, particularly at the current spatial resolution. Specifically in the case of surface contamination, special precaution should be taken when strong echoes are observed near the surface, an indication of surface clutter artifacts that should be excluded from rain analysis. Because of the importance of persistent low-level clouds and light rainfall in mountainous regions generally, there is a critical need to develop retrieval strategies that can capture the vertical structure of low-level reflectivity and the associated rainfall in complex terrain. This can be accomplished for instance by integrating operational satellite retrieval algorithms with simple physical models targeting local processes (e.g. Prat and Barros, 2009; Wilson and Barros, 2014).

Albeit of low frequency, heavy precipitating events have significant hydrologic impact leading to extreme floods and landslides in the region. Six representative case studies with substantial discrepancies between TRMM and gauge references provide insight into the characteristics of PR rainfall retrieval errors that need to be taken into consideration for applications in complex terrain. The results show that TRMM tends to underestimate small-scale winter storms and embedded convection in the summer, which can be attributed to the averaging effects of NUBF at TRMM PR coarse horizontal resolution as well as misclassification of convective systems as stratiform, especially at

large incidence angle. Precipitation from warm season convective systems smaller than the PR footprint is either underestimated or overestimated depending on the size of the system footprint and the depth of active convection. In particular, TRMM tends to underestimate rainfall from embedded convection, and overestimates rainfall from isolated small-scale shallow convection when and where it is detected. Cold-season mixed-phase precipitation (i.e., hail, ice falling through melting layers, etc.) is associated with strong scattering signal from ice crystals and can be misclassified as "certain convective". Mixed-phase precipitation cannot be estimated by the convective Z-R (reflectivity –rainfall) relationship in the algorithm, leading to the severe overestimation or false alarm errors in the winter and spring seasons.

Diagnostic analysis focusing on the characterization of the physical basis of QPE error provides a framework for error source attribution and subsequent correction or mitigation of satellite retrievals generally and can be applied elsewhere. Based on the results presented here, the observing strategy devised for IPHEx placed strong emphasis on documenting the spatial and temporal heterogeneity of rainfall microphysics conditional on time-of-day, prevalent hydrometeorological regime, and topographic and physiographic context (Barros et al., 2014). Special emphasis was placed on the vertical structure of precipitation in the lower troposphere. Analysis of IPHEx results is ongoing.

# 3. Understanding how low-level clouds and fog modify the diurnal cycle of orographic precipitation using *in situ* and satellite observations

## *3.1 Introduction*

In mountainous areas, low-level clouds and fog (LLCF) have significant implications on the regional hydrological cycle by affecting the diurnal cycle and spatial organization of precipitation and surface fluxes (Barros, 2013a;Gultepe et al., 2007). In cloud- or fog-dominated montane regions, cloud immersion and fog water are closely linked to ecosystem hydrology, nutrient budgets, and pollutant dynamics, as well as species distribution and abundance (Bruijnzeel, 2004;Goldsmith et al., 2013;Gotsch et al., 2014;Oliveira et al., 2014;Weathers, 1999). Based on National Climatic Data Center (NCDC) records between 1961 and 1990 (National Climatic Data Center, 2000), the Southern Appalachian Mountains (SAM) stands out in the continental US with dense fog frequently reported (> 40 days/year at regional scale). The cloud forests of the SAM at relatively high altitude (above ~1,500 m elevation) experience cloud immersion about 60–75% of the summer days, mostly occurring during morning hours (Berry and Smith, 2012). In the SAM, and generally in tropical and mid-latitude montane cloud forests, frequent cloud immersion creates favorable conditions for direct foliar water uptake (the direct absorption of water through leaves), enhances root uptake by improving top soil moisture, and reduces incoming shortwave radiation and the amplitude of the diurnal cycle of canopy temperature. Water from cloud immersion and fog has been found to

contribute significantly to the overall plant water budget in the SAM, up to 31% throughout the entire summer growing period, especially for high-elevation plants (Berry et al., 2014). Moreover, LLCF also modulates available photosynthetically active radiation, enhancing photosynthesis and leaf conductance, thereby leading to improved carbon uptake and water conservation of plants (Berry and Smith, 2013;Johnson and Smith, 2006). Mapping LLCF and understanding their role in the water cycle of mountain regions is therefore a critical research need.

Observations from raingauge and disdrometer networks in the SAM (Figure 3-1) show a complex relationship with elevation and landform that does not fit the classical orographic enhancement conceptual model with terrain elevation (Barros and Lettenmaier, 1993;Duan et al., 2015). Instead, *in situ* data show strong west-east variability with small differences between rainfall accumulations at low and high elevations at annual time-scales, but large differences under strong synoptic forcing from event to event depending on whether LLCF are present either at high or low elevations, that is the reverse orographic enhancement effect (Wilson and Barros, 2015). One distinctive feature of the SAM rainfall is the existence of a mid-day rainfall peak in all seasons, which is similar to that observed at mid-elevations in the forested slopes of the central Andes and in tropical cloud forests (Barros, 2013a;Duan et al., 2015;Prat and Barros, 2010a). Prat and Barros (Prat and Barros, 2010a;Prat and Barros, 2010b) reported number concentrations of small drops in the inner SAM up to two orders of magnitude higher than the values used

in common parameterizations of rain drop size distributions (R-DSDs, e.g. Marshall-Palmer distribution among others). They also documented robust ridge-valley differences in the seasonal climatology of R-DSDs with larger drop sizes at lower elevations. Wilson and Barros (2014) found that the microphysics of the mid-day rainfall peak at paired ridge-valley sites in the inner mountain region are characterized by very large number concentrations of small drops and light rainfall intensity in the presence of thick fog at both locations (concurrently or not) with large increases in the number of large drops under moderate and heavy rainfall conditions. Concurrent bottom-heavy radar reflectivity profiles further indicated that these microphysical changes took place within the lower 500 m suggesting seeder-feeder interactions (SFI) between rainfall aloft and low-level fog. This hypothesis was tested by Wilson and Barros (2014) using a raindrop dynamics column model (Prat and Barros, 2007b;Prat and Barros, 2007a;Prat et al., 2012) modified to include fog. Due to the lack of in situ observations, they synthesized fog spectra from the literature for their model experiments and showed that increased coalescence efficiency between precipitating clouds aloft and thick fog in the inner SAM could explain the observed increase in rainfall rate and DSD modification.

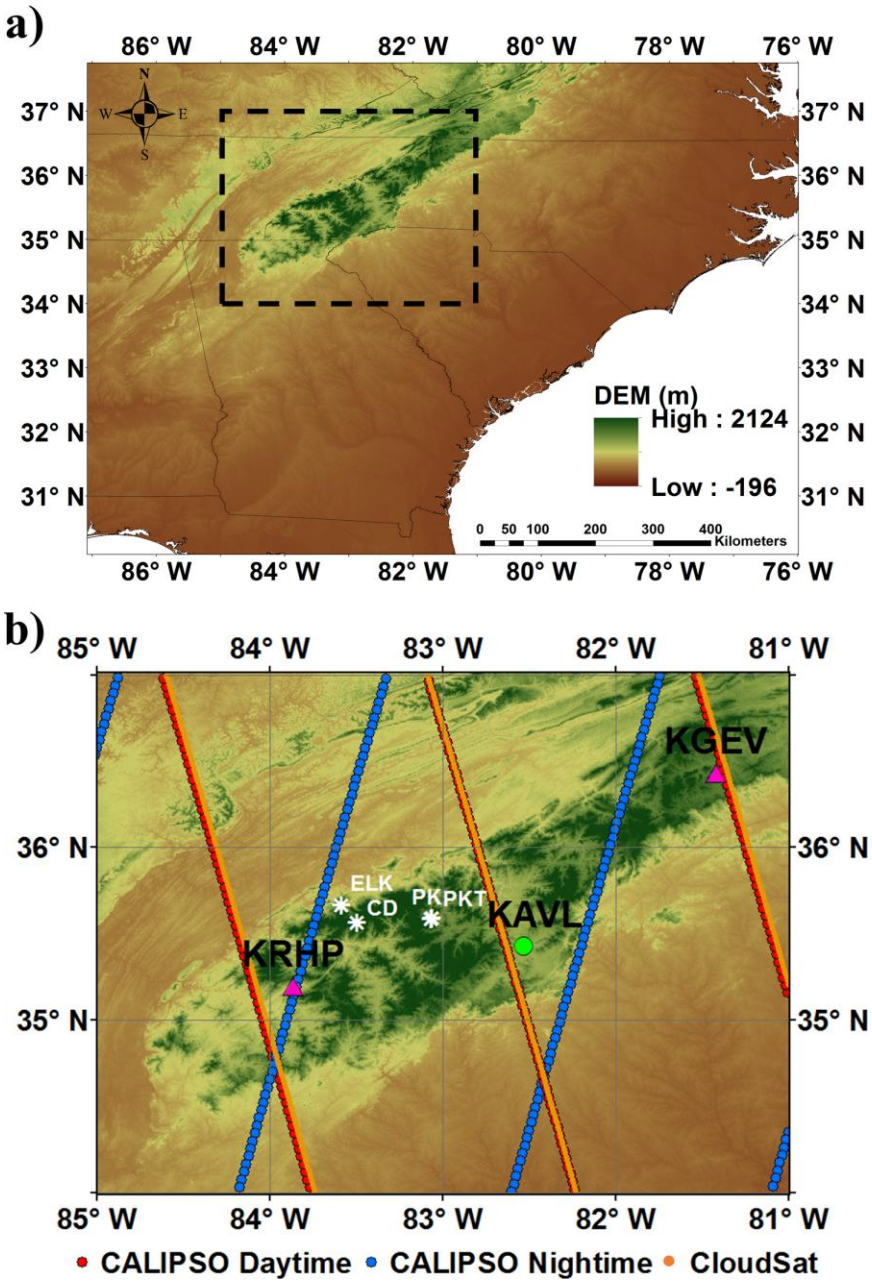


**Figure 3-1: a) Region of study (in the black box) in context of southeastern United States map; b) Overview of CALIPSO and CloudSat overpasses over the study region. Note the CALIPSO daytime tracks are represented by red dotted lines and the nighttime ones by the blue dotted lines. The CloudSat daytime tracks are indicated by orange lines. From left to right, the three ground ceilometer stations are located at Andrews Murphey Airport (KRHP, marked by the pink triangle), Asheville Airport (KAVL, marked by the green circle), and Jefferson Ashe County Airport (KGEV,**

**marked by the pink triangle). White asterisks denote the locations of four ground fog collectors at Elkmont (ELK), Clingmans Dome (CD), Purchase Knob (PK), and Purchase Knob Tower (PKT).**

The present study aims to generalize the quantitative understanding of how LLCF modify the diurnal cycle of orographic precipitation from local scales to regional-scale in the SAM using *in situ* and satellite observations. This encompasses characterizing SFI processes on the upwind slopes of the SAM with distinct hydrometeorology from the inner region, and the process chain by which the observed regional-scale organization of the diurnal-cycle emerges. The specific research objectives are two-fold: 1) to elucidate the physical mechanisms of rainfall amplification by LLCF at local scales, and 2) to elucidate the role of LLCF at regional-scale by demonstrating the spatial co-organization of the diurnal cycle of LLCF and orographic precipitation. First, microphysical observations of LLCF immersion are used to constrain a spectral model of rain microphysical dynamics to investigate how fast SFI can modify the R-DSDs on upwind slopes. Second, systematic analysis of satellite observations that enable mapping LLCF features during the observed all-season mid-day rainfall peak is conducted. Specifically, satellite observations from CALIOP (Cloud-Aerosol Lidar with Orthogonal Polarization) on the CALIPSO (Cloud-Aerosol Lidar and Infrared Pathfinder Satellite Observations) satellite (www.nasa.gov/mission_pages/calipso), from CPR (Cloud Profiling Radar) on the CloudSat satellite (www.nasa.gov/mission_pages/cloudsat), and from MODIS (Moderate Resolution Imaging Spectroradiometer) on the Aqua satellite

(https://modis.gsfc.nasa.gov/) are used toward developing a satellite-based climatology and physical characterization of orographic LLCF regimes focusing on the Southern Appalachians (SA) using a general methodology that can be applied to mountainous regions elsewhere. A simple method to merge CALIPSO and CloudSat products was developed to improve cloud base height (CBH) estimates and evaluated against ground ceilometer observations in the SAM. MODIS cloud top, optical, and microphysical properties are explored to map the spatial distribution of LLCF and further describe various aspects of LLCF characteristics over this region. The paper is organized as follows. A description of satellite products, *in situ* fog observations, and an overview of 10-year ceilometer ground-based observations over the study region are provided in Section 3.2. Section 3.3 describes the modeling study to addresses Objective 1. The combined CBH algorithm using CALIOP and CPR along with an evaluation of merged CBH estimates against in situ ceilometer observations is presented in Section 3.4. The MODIS climatology of cloud top, optical, and microphysical properties of LLCF in the SAM is discussed in Section 3.5. In Section 3.6, we summarize the findings and provide an overall assessment on the application of multi-satellite observations and model simulations to map LLCF distribution and SFI modulation of orographic precipitation.

## *3.2 Data*

### 3.2.1 Satellite Products

Due to the sparse distribution of in situ measurement networks in remote mountainous areas, satellite-based observations provide an opportunity for long-term monitoring of regional cloud systems with wide spatial coverage. NASA's EOS (Earth Observing System) passive satellites have enabled global coverage of cloud observations, but their retrieval algorithms are unable to resolve cloud vertical structure, especially under multilayer scenarios (Chen et al., 2007;Hagihara et al., 2010). The availability of satellite-based active sensors allows to investigate cloud structure directly including detailed vertical profiles, as well as their optical and microphysical properties at unprecedented resolutions (Stephens et al., 2002;Winker et al., 2007). Launched in 2006, CloudSat and CALIPSO aim to monitor the vertical distribution of clouds at high spatial resolution and to bring new insights on their evolution throughout the atmosphere (Mace et al., 2009;Stephens et al., 2002). CPR and CALIOP, the active sensors on CloudSat and CALIPSO, respectively provide a nadir view of vertical cloud profiles, complemented by the wide-view images from the MODIS instrument on the Aqua satellite. As part of the A-Train constellation, these three satellites maintain a close formation with each other, and are in nearly the same orbit with approximately fixed distance from each other. This flying array enables similar sampling volume of the atmosphere and facilitates the integration of their respective data sets. In April 2011, CloudSat experienced a severe

battery anomaly and only daytime data are available after October 2011. Prior to the anomaly, CloudSat and CALIPSO maintained a spatial separation of the ground tracks within 1 km and a temporal difference of 15 seconds on average, trailing the Aqua satellite by approximately 60 and 75 seconds, respectively. The data analysis presented in this study was performed from June 2006 to October 2016, using 10 years of spaceborne measurements from CALIPSO, CloudSat, and MODIS.

*CALIOP* - The CALIOP is a two-wavelength (532 and 1064 nm) polarization-sensitive Lidar, that provides high-resolution vertical profiles of aerosols and clouds (Winker et al., 2007). CALIOP profiles have a circular footprint of ~ 70 m in diameter with vertical resolution of 30 m, and are collected every ~333 m along the track. This highest resolution is only available for those portions of the profiles lower than 8.2 km, and the data are recorded at 1 km horizontal and 60 m vertical resolution above 8.2 km. The CALIPSO Level 2 (version 3) cloud layer products are also derived on horizontal grids of 1 km and 5 km. The layer products include number of vertical cloud layers, cloud top height (CTH) and CBH for each of these layers (up to five layers per profile). Level 2 processing consists of three major steps: selective iterative boundary locator (SIBYL), scene classification algorithm (SCA), and hybrid extinction retrieval algorithm (HERA) (Young and Vaughan, 2009). Additional information can be found in the CALIPSO algorithm theoretical basis documents (ATBDs) and Winker et al. (2009). All data products and ATBDs are available from the Atmospheric Science Data Center at NASA (National

Aeronautics and Space Administration) Langley Research Center (https://eosweb.larc.nasa.gov/). The main documented limitations of CALIOP are: (1) the laser pulse suffers complete attenuation beyond optical depth of ~5 from the top layer, thus likely leading to overestimated cloud base retrievals (Winker et al., 2003); and (2) the solar background signal dominates the total background signal in daylight profiles, decreasing CALIOP sensitivity to optically thin clouds (Vaughan et al., 2009).

*CloudSat* - The CPR is a nadir-looking 94 GHz millimeter-wavelength radar and enables matching of CALIOP observations to collect similar sampling volumes with slight time and space offsets between CloudSat and CALIPSO as part of the A-Train constellation (Stephens et al., 2002). CPR backscattered pulses are resampled to generate range bins of 240 m vertical resolution and the profiles are produced every 1.1 km along the orbit track with a horizontal footprint of 1.8 km along track and 1.4 km across track (Stephens et al., 2008). Herein we use the CloudSat 2B-GEOPROF (geometrical profiling product), including information on the cloud mask and radar reflectivity (Marchand et al., 2008). To differentiate clouds and other hydrometeors from instrument noises, a cloud mask is created to identify the presence of hydrometeors and to estimate the confidence levels of hydrometeor detection. Its value ranges from 0 to 40, with higher values indicating lower probability of false detections. In this study, CPR bins with the cloud mask level exceeding 20 are considered as cloudy, corresponding to a false-positive probability of less than 5% (Mace et al., 2009). Details about the hydrometeor mask

algorithm are described in Marchand et al. (2008). The 2B-GEOPROF data set can be acquired from the CloudSat data processing center (http://www.cloudsat.cira.colostate.edu/). The main documented limitations of CPR are (1) low sensitivity of the radar pulse in the lowest 1 km above the surface, likely producing spurious echoes due to the ground clutter effects; (2) the detection threshold of CPR is -30 dBZ, thus making it unable to capture some fraction of high thin cirrus and non-precipitating shallow boundary layer clouds; and (3) the relatively coarse horizontal and vertical resolution likely result in missing small-scale clouds (Mace and Zhang, 2014). Thus, bins in the bottom 1 km (lowest four bins) above the surface were excluded from the analysis to avoid ambiguity from reduced CPR sensitivities.

*MODIS* - Maintaining a close formation with CALIPSO and CloudSat, the Aqua satellite carries a passive sensor MODIS, which operates in the visible and infrared regions of the spectrum with measurements at 36 wavelengths from 0.4 to 14.5 μm (Ackerman et al., 1998). Since February 2000, MODIS has provided global distributions of clouds (aerosols) and their physical and optical properties with a wide-swath scanner (2330-km cross-track and 10-km along-track at nadir) and a scan angle of ±55°. In this study, daytime MODIS cloud optical and microphysical properties in Collection 6 (C6) are obtained from the Level 2 MYD06 product at 1 km horizontal resolution (Platnick et al., 2017). MODIS cloud mask product (MYD35) is also used in this study and it reports four confidence levels of cloudiness conditions (confident cloudy, probably cloudy, probably clear, and

confident clear) (Frey et al., 2008). The MODIS C6 data can be retrieved from the NASA Level 1 and Atmosphere Archive and Distribution System (https://ladsweb.nascom.nasa.gov/). Leveraging collocated CALIOP observations, significant refinements and extensive testing have been put into the C6 algorithm development. In C6, a modified $CO_2$-slicing method is applied to retrieve the cloud top pressure (CTP) for mid- and high-level clouds based on cloud emissivity ratios from multiple bands (bands: 29–32). Compared to collocated CALIOP CTH of single-layer clouds, substantial improvements have been shown in the overall global detection skill in semi-transparent cirrus and low-level liquid phase clouds in C6 versus C5 (Baum et al., 2012). Additional changes in C6 include introducing separate tests (i.e., tri-spectral IR tests, cloud top temperature tests, 1.38 μm channel test, and spectral cloud effective radii tests) with assigned weights for the cloud phase classification, but challenges still remain for mixed-phase clouds (Marchant et al., 2015). Cloud thermodynamic phase classification is a critical component, which is subsequently used for retrieving cloud optical and microphysical properties. Cloud particle effective radius (CER) and cloud optical thickness (COT) are derived simultaneously based on reflected solar radiation at two or more wavelength bands (Nakajima and King, 1990). The retrievals of CER and COT are combined subsequently to estimate cloud water path (CWP), which is proportional to the product of CER and COT (King et al., 1992). Earlier studies indicate that the minimum optical depth for cloud detection in MODIS is 0.4 (Ackerman et al., 2008), whereas the

sensitivity of CALIOP signals is sufficient to detect thin cirrus with optical depths of 0.01 or less (McGill et al., 2007).

Both CALIOP and CPR measurements can be used to infer cloud phases and other microphysical properties from the information on the polarization of the backscattered signals at different frequencies (Weisz et al., 2007). Because of different wavelengths, CALIOP (visible and near-infrared) and CPR (microwave) have distinct sensitivities to cloud particle sizes, thus resulting in different characteristics of bias and estimation errors. The CPR is capable of penetrating optically thick hydrometeor layers, and has higher sensitivity to large particles existing in cloud top regions (Hagihara et al., 2014), but suffers significant attenuation of radar signals in moderate to heavy rainfall (Haynes and Stephens, 2007). The Lidar is superior in detecting tenuous and optically thin clouds, which are below radar reflectivity thresholds due to its limited sensitivity to small cloud droplets and ice particles. However, Lidar observations suffer strong signal attenuation beyond an optical depth of about 3, especially at lower levels due to opaque thick tropospheric clouds and multilayer clouds above (Kim et al., 2011). Integration of CPR and CALIOP observations should help minimize the respective cloud detection deficiencies of each sensor by leveraging their strengths. Nevertheless, difficulties still remain in detecting shallow liquid clouds (weakly reflective to the radar and/or below 1 km) beneath higher-level opaque clouds that completely extinguish Lidar signals (Mace et al., 2009).

### 3.2.2 Surface Observations

#### 3.2.2.1 Fog Observations

Over the western ridge of the SAM and the inner mountain region, fog collectors were deployed at four ground stations (marked by white asterisks in Figure 3-1b) for different sampling periods during June 2013 − December 2015. Descriptions about these sites and the corresponding observation periods are summarized in Table 3-1. The fog collectors used in this study are designed and manufactured by Professor James Juvik at University of Hawaii. Details about the fog collectors are described in Juvik and Nullet (1995) and Wilson and Barros (2015). Figure 3-2 shows the diurnal and seasonal cycles of fog occurrences sampled by the fog collectors at Purchase Knob (PK), Purchase Knob Tower (PKT), and Clingmans Dome (CD). The observations at Elkmont (ELK) are not shown here due to its shorter sampling period. Over the inner mountain region, longer records (~ two years) were reported at PK and PKT, which are approximately 0.7 km apart. As noted in Figures 3-2a and b, distinct diurnal features are manifest at these two nearby sites. PK, which is at one ridge location with widely open area, reveals a mid-day peak of fog occurrences in winter associated with advection fog whereas weak diurnal variations are indicated for other seasons. PKT, an open area location surrounded by dense forests, shows less frequent fog occurrences around the mid-day maximum in the winter season while a pronounced morning peak of radiation fog is manifest in the warm season (spring and summer). On the western ridges, observations at CD in late spring and summer of 2014 indicate a strong diurnal variability with fog (radiation fog) peaking at early morning

and late night as a result of nocturnal cooling near the ground surface. The remarkably high frequency of fog occurrences at CD supports previous reports that this site CD is constantly immersed in the cloud deck (Wilson and Barros, 2015).

**Table 3-1: Descriptions of the fog collectors and their deployment periods in the Southern Appalachian Mountains (SAM).**

| Site Name | Latitude | Longitude | Elevation (m) | Fog Obs. Period |
|---|---|---|---|---|
| **Purchase Knob (PK)** | 35.586 | -83.073 | 1495 | 01/06/2013–19/05/2015 |
| **Purchase Knob Tower (PKT)** | 35.588 | -83.065 | 1485 | 04/07/2013–05/10/2015 |
| **Clingmans Dome (CD)** | 35.562 | -83.497 | 1956 | 01/06/2014–10/09/2014 |
| **Elkmont (ELK)** | 35.665 | -83.590 | 634 | 25/09/2015–10/12/2015 |

To characterize fog microphysical properties in the SAM, a meteorological particle spectrometer (MPS, manufactured by Droplet Measurement Technologies, Inc., Boulder, CO, USA) was deployed along the fog collector at ELK site during September – December 2015. The MPS measures droplet concentrations, sizes, shapes, and fall velocities over the diameter size range from 12.5 μm to 1.56 mm in 62 evenly spacing bins (25 μm resolution) (Baumgardner et al., 2002). The MPS uses a collimated laser beam of light (a linear array of 64 photodiodes) between two vertical arms to measure the shadow images of falling particles that form on the array (Knollenberg, 1970). Significant improvements have been made in the MPS to mitigate measuring issues under windy conditions and provide high resolution of fall velocities better than 0.01 mm $s^{-1}$ (Baumgardner et al., 2002). Other collocated instruments at Elkmont include a METEK Micro Rain Radar (MRR), operating

at 24 GHz (K band) with the range-gate resolution of 100 m up to 30 vertical levels in the atmosphere and sensitivity to rain rates of 0.01 mm $h^{-1}$; a tipping bucket rain gauge (RG) with measurement resolution of 0.1 mm $tip^{-1}$; a Vaisala weather station (WXT) recording local meteorological conditions (e.g., wind speed, wind direction, relative humidity, and temperature) every 1-s.

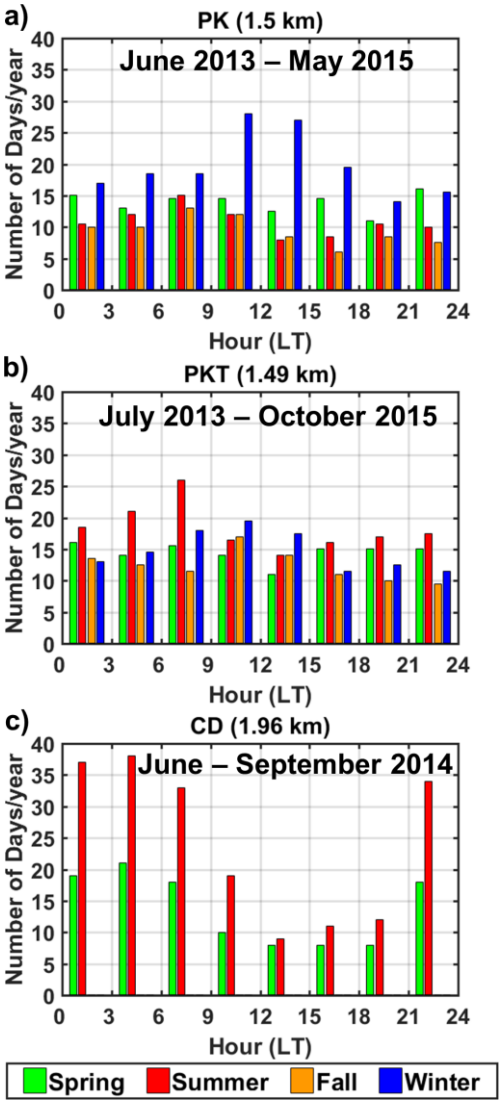

**Figure 3-2: Diurnal cycles of fog occurrences in each season (spring: April-May-June, summer: July-August-September, fall: October-November-December, and winter: January-February-March) sampled by fog collectors at PK (a), PKT (b), and CD (c). Note the elevation of each site is denoted in parentheses after its name and the corresponding observation period is indicated at the top of each plot.**

#### 3.2.2.2 Ceilometer Observations

The Automated Surface Observing System (ASOS) equipped with automated laser ceilometers is a valuable source of long-term cloud observations in the United States since 1992 (Sun et al., 2007). Routine observations generally report cloud cover, sky condition, cloud type, CBH, and visibility. There are currently more than 900 ASOS sites in the United States (ASOS Program Office Staff, 1998). The Automated Weather Observing System (AWOS) is operated and controlled by the Federal Aviation Administration (FAA), recording similar surface observations at a 20-minute interval. The 5-min ASOS and 20-min AWOS data are archived by the National Oceanic and Atmospheric Administration (NOAA) NCDC (http://www.ncdc.noaa.gov/).

At the ASOS/AWOS unit, the CBH is estimated from vertical profiles up to 3.6 km (~15 m vertical resolution) above the surface and calculated from every 30-second sample during the most recent 30-minute observational periods (with the last 10 minutes of data doubly weighted). Note three different layers can be detected at a time. The cloud height indicator sensor uses a vertical-pointing laser beam (0.9 μm) to track the time interval between pulse transmission and reception reflected from cloud base to determine the CBH. Moreover, local radiation fog is also reported by the co-located visibility instrument. Other surface observations such as surface temperature, dew point temperature, wind

speed, and precipitation are also included in 5-min Meteorological Terminal Air Report (METAR) weather reports (U.S. Air Force, 1998). Common issues with ceilometer CBH estimates are: (1) the algorithm cannot respond fast enough to detect rapidly changing sky conditions; (2) the laser is very sensitive and occasionally detects invisible moist layers before visible clouds form; and (3) sometimes sharp inversions in very cold winter weather, may cause false detection of clouds. Nevertheless, ceilometers provide well-qualified and consistent ground observations of cloud vertical structure at low altitude.

The region of study spans the SA (34° N − 37° N, 85°W − 81°W) as depicted in Figure 3-1. There are about 9 ASOS/AWOS stations available over the study region though only 3 stations (denoted by the green circle and pink triangles in Figure 3-1b) are located along or in the vicinity of the CALIPSO/CloudSat tracks (denoted by red/blue, and orange dots). For daytime overpasses, we employed the 5-min ASOS dataset from the Asheville Airport (KAVL) at an elevation of 654 m above mean sea level (MSL) and the 20-min AWOS dataset from the Jefferson Ashe County Airport (KGEV) at an elevation of 969 m MSL; for nighttime overpasses, the 20-min AWOS dataset from the Andrews Murphy Airport (KRHP) at an elevation of 520 m MSL was used. At these surface sites, CBH is the primary observation used in this study. First, we examined the seasonal distribution of the cloud cover using the ceilometer CBH at the first layer and the diurnal cycle of fog (in local time, LT) using visibility measurements during June 2006 − October 2016. Figure 3-3 displays the frequency distribution of CBH (in the left panel) and the diurnal cycle of fog

occurrences (in the right panel) at each site in each season. We can see that more frequent LLCF are observed at all three stations in the warm season (spring and summer) compared to the cold season (fall and winter). However, distinct features of cloud and fog regimes are also evident at the three ground observation stations. At the low-elevation sites (KAVL and KRHP), the CBH distribution peaks around 1−2 km above ground level (AGL). At the high-elevation site (KGEV), the frequency reaches the maximum around 0.5−1.5 km AGL. Thus, lower cloud bases tend to be formed over the ridge location compared to valley stations. In terms of fog occurrences, corresponding to a visibility range shorter than five eighth Statute Miles (SM), the two valley sites (KAVL and KRHP) experience persistent radiation fog in the early morning of all seasons, whereas the ridge station (KGEV) records more frequent morning fog in the warm season than the two valley sites and the diurnal cycle of fog in the cold season is uniformly distributed at KGEV. Despite a large spatial variability of LLCF over the SAM, these three stations serve as the ground truth for the multi-year climatology study using satellite measurements as described in Section 3.4.

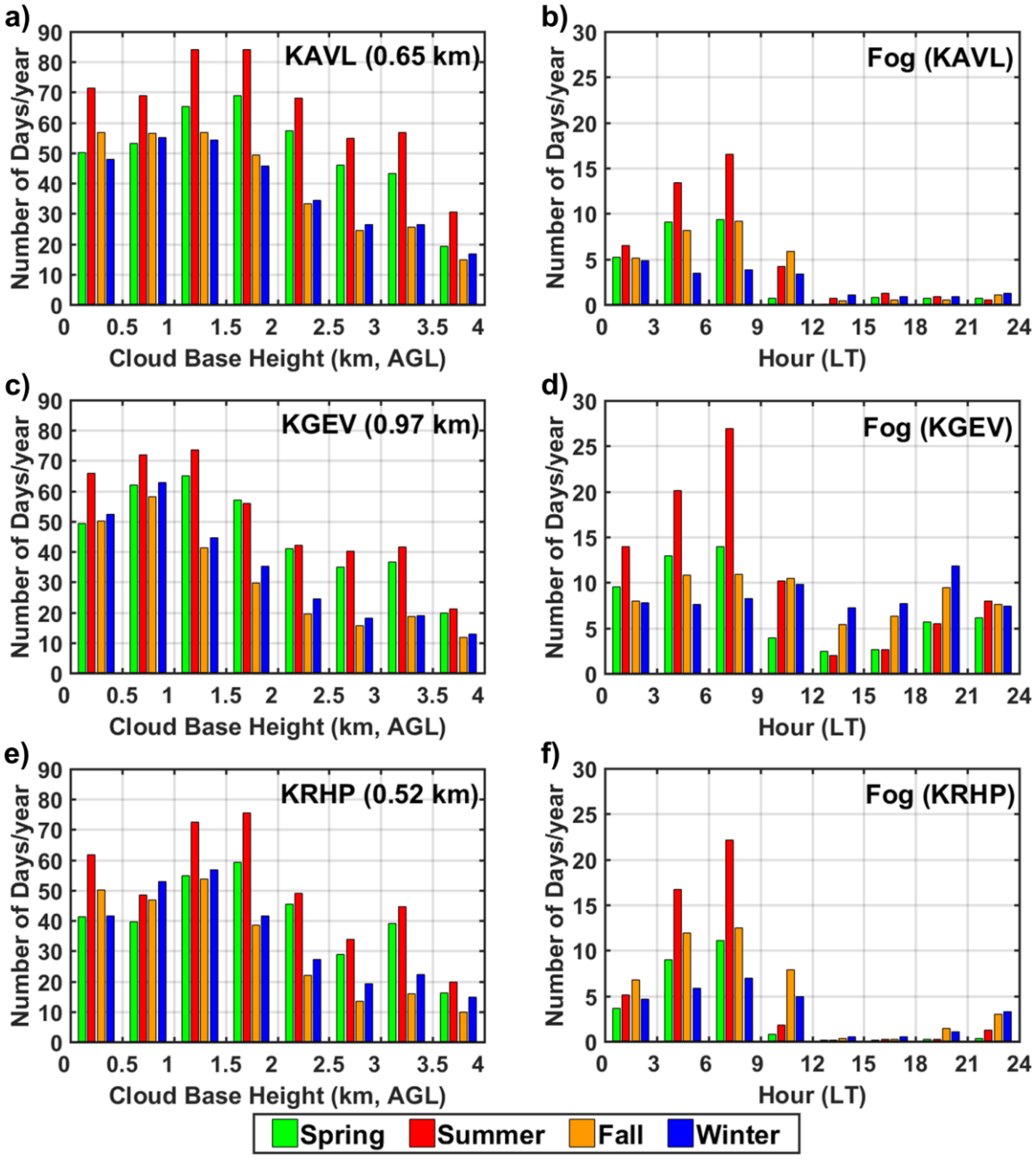


**Figure 3-3: (Left) Seasonal histograms of ceilometer cloud base heights (CBHs) at KAVL (a), KGEV (c), and KRHP (e) during June 2006 – October 2016. Note the elevation of each site is denoted in parentheses after its name; (Right) Seasonal and diurnal cycles of fog occurrences (visibility < 5/8 Statute Miles) at the corresponding ceilometer sites during the same period. Note the spring season represents April-May-June, the summer season represents July-August-September, the fall season represents October-November-December, and the winter represents January-February-March.**

## 3.3 Seeder-Feeder Interactions

As discussed in Section 3.1, the SAM experience mid-day light rainfall throughout the year that peaks before convective activity develops in the mid and late-afternoon (Duan et al., 2015;Wilson and Barros, 2014). Elsewhere, mid-day light rainfall does not reach the ground due to evaporation in the warm season (e.g. Himalayas) (Barros et al., 2000). By contrast, mid-day rainfall in the SAM can reach hourly rates similar to convective precipitation (i.e. > 10 mm/hr). Microphysical and radar observations indicate significant enhancement of number concentrations across the R-DSD spectrum, and in particular in the number of large drop sizes that reach the surface (2015, 2014). Light rainfall can potentially interact with LLCF (i.e., SFI) consequently leading to significantly enhanced surface rainfall as documented by Prat and Barros (2010a) and Wilson and Barros (2014, 2015). Wilson and Barros (2014) resorted to ground observations and modeling to demonstrate the importance of LLCF in amplifying precipitation in the inner SAM via SFI, including the mid-day peak and the evening ridge-valley gradients. They relied on typical values of fog distributions (droplet number concentrations, liquid water content) from the literature to define fog microphysics, as observations were not available at that time. In this study, the local fog DSD (F-DSD) observed by the MPS at ELK was used to investigate the physical mechanisms of low-level precipitation enhancement induced by the SFI on the western (upwind) slopes of the SAM under strong mountain-valley wind conditions.

### 3.3.1 Column Model Description

A dynamical microphysics bin model that simulates the evolution of raindrop microphysics between cloud base and the ground surface (rain shaft) for warm rainfall events is used to investigate the collisional drop-drop interactions between light seeder rainfall and local feeder fog (Prat and Barros, 2007b;Prat and Barros, 2007a). This column model explicitly solves the stochastic collection equation-stochastic break equation (SCE-SBE) using a number and mass conservative scheme on a discretized bin grid. The discrete formulation of the SCE-SBE equation in the $i^{th}$ bin ($i = 1, 2, \ldots, nbin$) is written as

$$\begin{aligned}\frac{dN_i(z,t)}{dt} + V_i\frac{dN_i(z,t)}{dt} &= S_i(z,t)\\ &= \sum_{\substack{j,k \\ x_{i-1}\le(x_j+x_k)\le x_{i+1}}}^{j\ge k} \left(1-\frac{1}{2}\delta_{j,k}\right)\eta C_{j,k}N_j(z,t)N_k(z,t)\\ &\quad - N_i(z,t)\sum_{k=1}^{nbin} C_{i,k}N_k(z,t)\\ &\quad + \frac{1}{2}\sum_{j=1}^{nbin}\sum_{k=1}^{nbin} N_j(z,t)N_k(z,t)B_{i,k}\kappa_{i,j,k}\\ &\quad - N_i(z,t)\sum_{k=1}^{nbin} B_{i,k}N_k(z,t)\end{aligned} \tag{3-1}$$

where the first term on the left-hand side of the equation describes time rate of change in the droplet number concentration $N_i(z, t)$ at height $z$ and time $t$, the second term accounts for the falling of drops at a velocity $V_i$. The source term $S_i(z, t)$ represents the net gain from coalescence-breakup dynamics, which is expressed by the four terms at the right-hand

side of the equation. From left to right, they are the production of droplets resulting from coalescence of smaller drops, the removal of droplets resulting from coalescence with other droplets, the gain of droplets due to breakup of larger drops, and the loss of droplets due to their breakup. One distinct aspect of the model is the explicit incorporation of bounce and distinct modes of breakup (neck/filament, sheet, crown and disk) (Testik and Barros, 2007;Barros et al., 2008;Wilson and Barros, 2014, 2015) using a *We-p* parameterization of regimes of collision outcomes after Testik et al. (2011) and Prat et al. (2012), where *We* is the Weber number and $p$ is the ratio of the small to the large diameter of two colliding raindrops (see Figure A1 in Appendix A).

Finally, the rain rate at height $z$ and time $t$ is expressed as

$$RR(z,t) = \frac{3600}{\rho_w} \sum_{i=1}^{nbin} N_i(z,t) m_i V_{rel}\,(z) \tag{3-2}$$

$$V_{rel}(z) = V_i - V_{air}(z) \tag{3-3}$$

where $m_i$ is the characteristic mass (g) of drops in the $i^{th}$ bin, the relative velocity $V_{rel}\,(z)$ is calculated as the difference of the fall velocity of drops in the $i^{th}$ bin $V_i$ and the mean air velocity $V_{air}\,(z)$ at height $z$ (downdrafts are denoted by positive signs and updrafts in negative signs), and $\rho_w$ is the density of water (= 1 g cm$^{-3}$).

The radar reflectivity (ZDBZ) is computed as

$$ZDBZ(z,t) = 10log_{10}\left(\sum_{i=1}^{nbin} N_i(z,t) D_i^6\right) \tag{3-4}$$

where $D_i$ is the characteristic diameter of drops in the $i^{th}$ bin. Note the dependence of reflectivity on $D^6$ corresponding to a factor of ~0.001 between 1 and 3mm drop diameters everything else being equal, which is illustrative of the strong nonlinear decrease in the sensitivity of radar measurements for small drop sizes.

## 3.3.2 Model Results

### 3.3.2.1 Evaluation

In the early morning of 01 October 2015, large number concentrations of small drops (12.5 – 37.5 μm) were recorded by the MPS at ELK, indicating the presence of radiation fog (Figure 3-4a). The droplet effective radius ($r_e$, see Eq. A1 in Appendix A), derived from the MPS droplet size distributions remained relatively constant (~ 25 μm) in the morning and suddenly increased up to 375 μm around mid-day (shaded area in Figure 3-4b) enhanced by low level moisture convergence (Wilson and Barros, 2017). The mean liquid water content (LWC, see Eq. A2) around the mid-day peak (11:00 – 14:00 LT) is 0.09 g/m$^3$ (not shown here). In the early afternoon, upper-level precipitation approached the site. Steeper reflectivity gradient toward the surface was observed by the MRR (Figure 3-4c), suggesting low-level amplification of the rainfall. This case is ideal to investigate SFI under light rainfall conditions representative of the persistent mid-day LLCF and rainfall in the Smoky Mountains on the western ridges of the SAM.

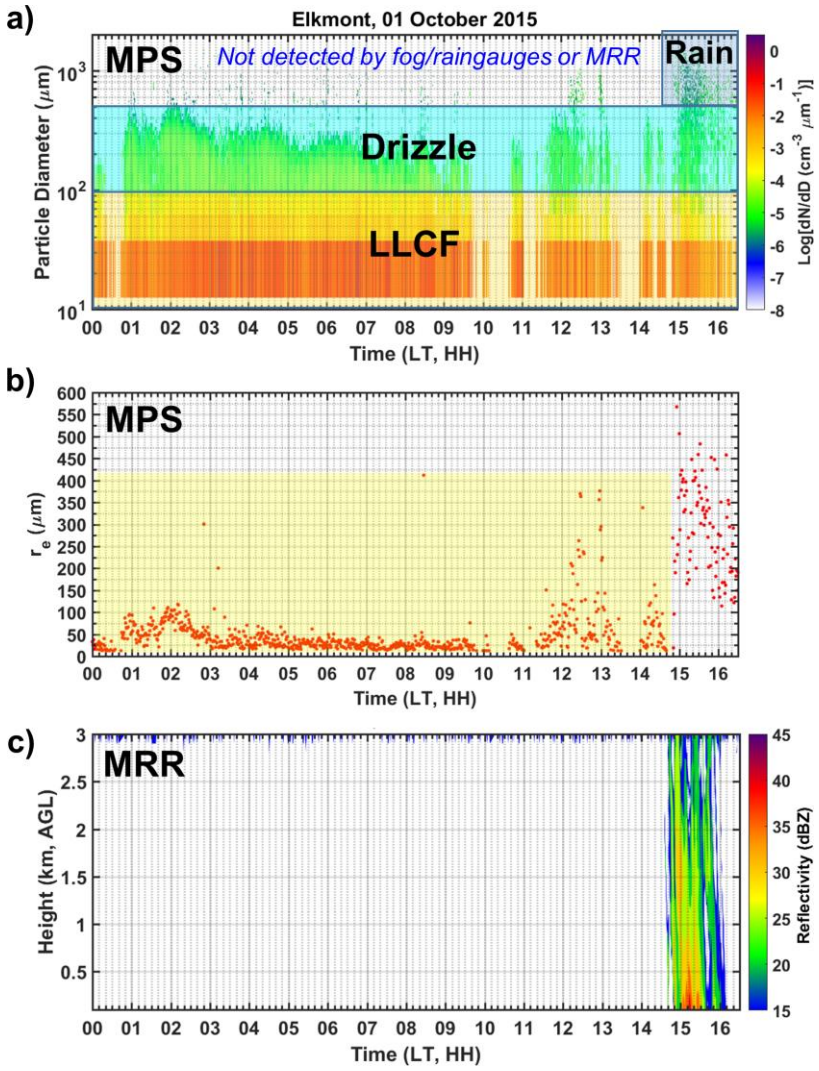


**Figure 3-4: Time series of drop size distributions (a) from the meteorological particle spectrometer (MPS), droplet effective radius ($r_e$; c) derived from the MPS spectra, and reflectivity profiles (c) from a collocated Micro Rain Radar (MRR) at Elkmont on 01 October 2015. Note the shaded area in (b) highlights the period of fog presence.**

The column microphysics model simulation for this event was set up from 14:50 – 16:00 LT and the model was run on an optimized irregular grid of 60 bins with diameters ranging from 10 μm to 6.2 mm (Wilson and Barros, 2014). The initial and top boundary conditions can be retrieved from the MRR observations. At the initial time, R-DSDs were

derived from 30 levels of MRR reflectivity (100-m resolution) and imposed at the corresponding positions in the simulated vertical column. The dynamic top boundary condition (TBC) was updated every 60 s introducing a new R-DSD based on the MRR reflectivity measurements at the column top. The time step (1 s) and vertical resolution (10 m) are maintained constant during the simulation period. The TBC height was prescribed at 1,300 m AGL based on the MRR profiles and to minimize lateral advection effects that are not represented in the model as well as ice microphysics that have a negligible influence on the rainfall evolution in the column. The selection of TBC height and the retrieval of R-DSDs from MRR reflectivity observations is detailed by Wilson and Barros (2014). In Wilson and Barros (2014), a comprehensive review of the literature was conducted toward selecting appropriate F-DSD, which were transferred and scaled to meet water budget requirements locally. Herein, we rely for the first time MPS observations to derive local F-DSDs just before the onset of a rainfall event. For six different periods (1, 10, 13, 15, 17, 20 mins) before 14:50 LT, the F-DSD was obtained by averaging the MPS droplet spectra below 50 μm (maximum diameter for a fog droplets) and fitted by a negative exponential distribution (see Eq. 3-5) using least-squares minimization.

$$\frac{dN}{dD} = N_0 e^{-\Lambda D} \tag{3-5}$$

wherein $N_0$ (cm$^{-3}$ μm$^{-1}$) represents the intercept and $\Lambda$ (μm$^{-1}$) represents the slope. The fitting parameters for six averaging periods and the corresponding LWC (see Eq. A2) are

summarized in Table 3-2 and the resulting F-DSD spectra are shown in Figure 3-5a. Note an additional run was conducted by including droplet sizes up to 100 μm in fog spectra #2a. Next, several simulations were conducted assuming a uniform fog distribution of 400-m depth in the atmospheric column from 15:00–15:30 LT. Note that the timing and depth of fog were determined based on the observed reflectivity profiles that indicate stronger reflectivity gradients toward the surface (bottom heavy reflectivity profiles) during 15:00–15:30 LT within 400 m above the ground (see Figure 3-4c). With each fog DSD (Figure 3-5a) as model input, the cumulative rainfall is evaluated against the precipitation observations from the surface instruments (RG and MRR) at ELK, as shown in Figure 3-5b. Herein "MOD-SFI" refers to model output with the presence of fog, thus activating SFI between the falling raindrops from an upper-level seeder source and small droplets in the feeder fog; "MOD-NO FOG" refers to the simulation without fog.

**Table 3-2: Fitting parameters of the negative exponential distribution characterizing the fog droplet spectra and their liquid water content (LWC) for different averaging periods before the onset of the rainfall event on 01 October 2015. Note $N_0$ represents the intercept and $\Lambda$ represents the slope.**

| | Avg. Period | $D_{max}$ (μm) | $N_0$ ($cm^{-3}$ $\mu m^{-1}$) | $\Lambda$ ($\mu m^{-1}$) | LWC ($g/m^3$) |
|---|---|---|---|---|---|
| FOG #1 | 1 min | 50 | 0.59 | 0.11 | 0.0104 |
| FOG #2a | 10 mins | 50 | 0.37 | 0.11 | 0.006 |
| FOG #2b | 10 mins | 100 | 0.37 | 0.11 | 0.0074 |
| FOG #3 | 13 mins | 50 | 2.15 | 0.17 | 0.0064 |
| FOG #4 | 15 mins | 50 | 4.37 | 0.18 | 0.0101 |
| FOG #5 | 17 mins | 50 | 3.75 | 0.19 | 0.0085 |
| FOG #6 | 20 mins | 50 | 2.95 | 0.18 | 0.0078 |

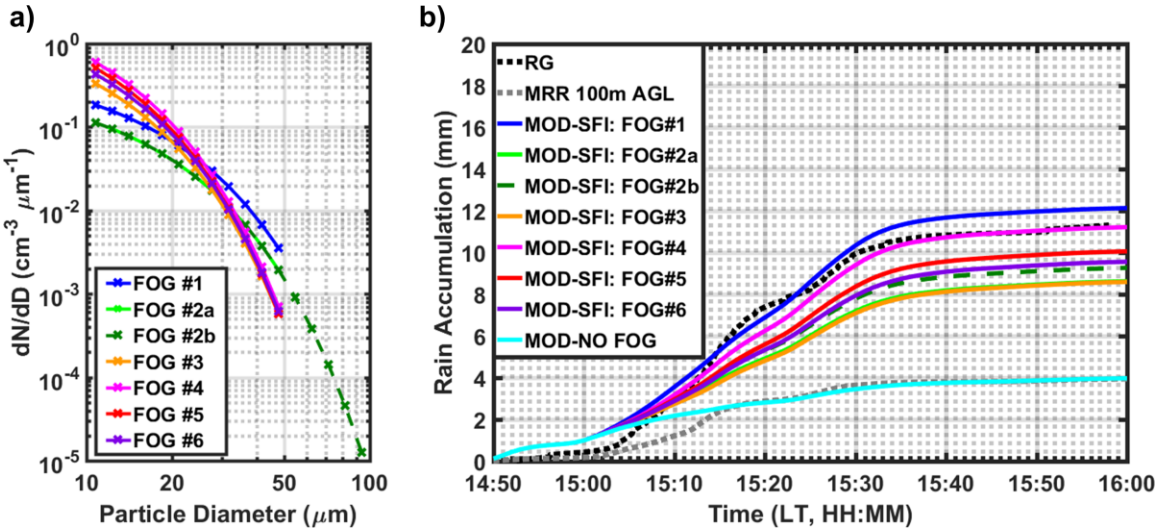


**Figure 3-5: a) Fog droplet spectra using six averaging periods of the MPS data before 14:50 LT (details about the spectra can be referred to Table 2); b) Simulated cumulative rainfall with each spectrum used as the fog input in the model, compared to observations from the raingauge (RG, black dotted line) and MRR (grey dotted line). "MOD-SFI" indicates model simulations with the presence of fog, thus activating seeder–feeder interactions (SFI). "MOD-NO FOG" indicates the model simulation without fog.**

When fog is taken into account, the simulated rain accumulation near the surface (10 m AGL) is comparable to the RG measurement (black dotted line in Figure 3-5b), which is considered as the ground truth. In particular, the simulation results with fog spectra #4 (15 mins averaging period and LWC = 0.01 g/m$^3$ in Table 3-2, pink lines in Figure 3-5) achieve the best agreement with the overall rainfall accumulation reported by the RG at the end of the simulation period (70 mins). As expected, the simulated rainfall using FOG #2b (with larger drops included in the fog spectra, indicated by the darker green dashed line) is slightly increased compared to the results from FOG #2a (indicated by the light green line). Note that the simulated rainfall accumulation without fog are consistent

with the corresponding MRR rainfall observations at the first gate (100 m AGL, grey dotted line in Figure 3-5b), and both of them fail to capture the enhanced rainfall measured at the surface induced by the SFI. This is because the MRR reflectivity-rainfall estimation software provided by the manufacturer relies on incorrect assumptions, and therefore we use reflectivity alone for subsequent analysis.

The rain accumulation at the beginning of the event (14:50 – 15:06 LT) is slightly overestimated by all the model simulations as compared to the surface observations from the RG and MRR. This overestimation error can be explained by comparing the reflectivity profiles from the MRR and the model results with the optimal fog input (MOD-SFI: FOG #4) in Figure 3-6. Within the height of TBC (1.3 km AGL, indicated by the thick black line in Figure 3-6a), a large amount of raindrops was falling through the simulation column around 14:52 LT, however, a discontinuity in the vertical structure of reflectivity profiles appeared around 15:00 LT below the TBC, which is likely caused by the advection of falling raindrops by the horizontal wind away from the MRR location (see surface wind speed in Figure 3-6c). By contrast, simulated reflectivity profiles (Figure 3-6b) show a continuous structure toward the surface around the same time, as horizontal wind is not taken into account in the column model. This results in stronger reflectivity in the simulation column during 15:00–15:06 LT as compared to the MRR observation.

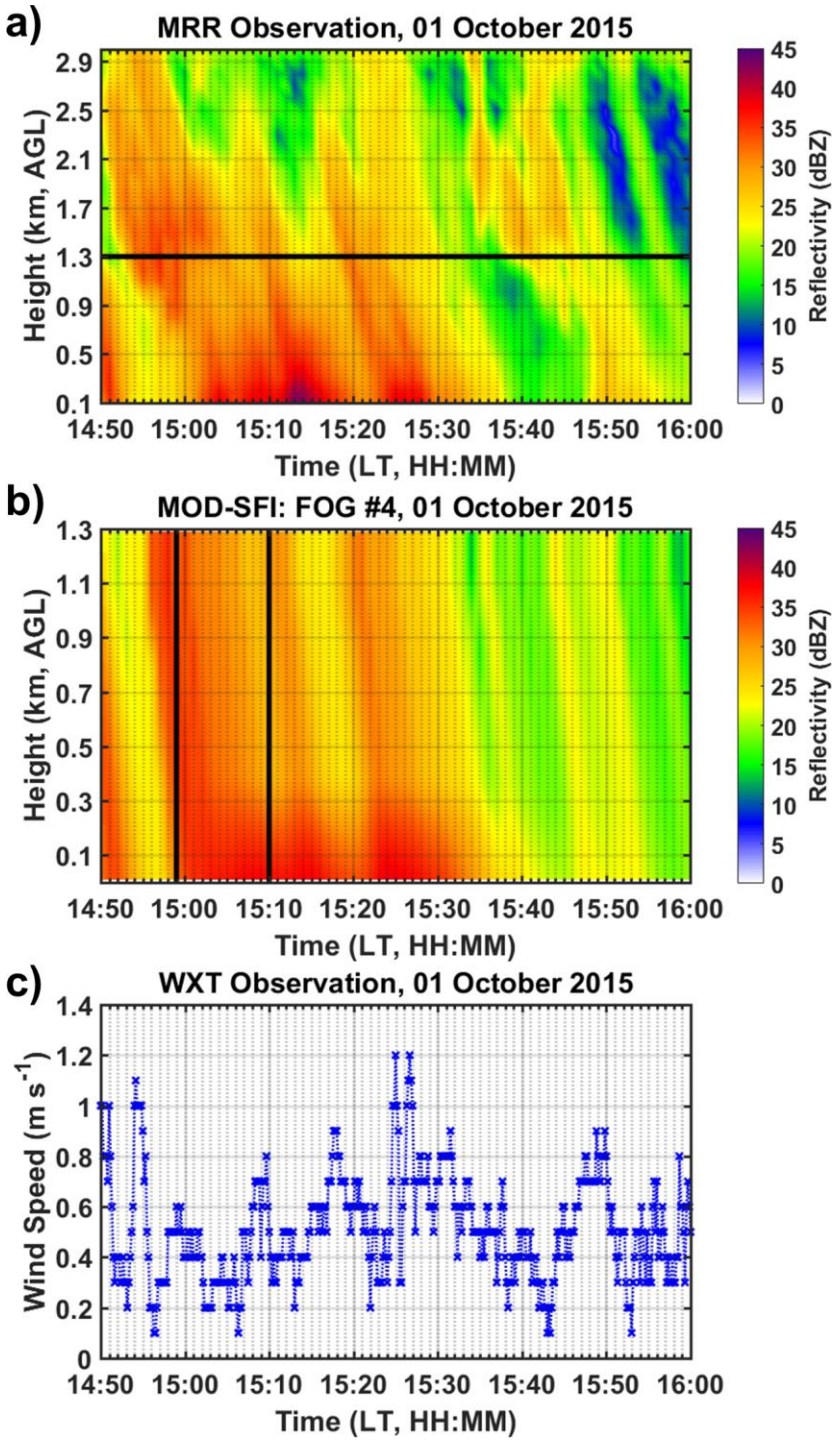


**Figure 3-6: Time series of observed reflectivity (a) from the MRR, simulated reflectivity (b) with the presence of fog (FOG #4, see its spectrum in Figure 3-5a) during 15:00–15:30 LT, and surface wind speed (c) observed by the weather station (WXT). The**

**black horizontal line in (a) marks the top boundary level at 1.3 km AGL. The black vertical lines in (b) mark 14:49 LT and 15:10 LT, which will be discussed in later figure.**

The model simulates a column with winds at rest, and the temporal variability of fog microphysics proper is not represented in the model. For example, one important low-level process absent from the model representation is turbulence, which can play a significant role in fog dynamics by increasing the collision rate of droplets, thus significantly enhancing the efficiency of collision-coalescence process in fog microphysical processes (Pinsky et al., 2000;Pinsky et al., 2008). Notwithstanding the approximations in the model and the limitations in the observations, the improved model prediction of rain accumulation (with fog spectra #4) against the simulation without fog is ~8 mm that is 65% of the total RG accumulation. Similar rainfall enhancement was captured in long-term paired fog and rainfall observations at all locations marked in Figure 3-1b as well as elsewhere across the SAM by contrasting paired high and low elevation observations (Angulo-Martínez and Barros, 2015;Wilson and Barros, 2014, 2015). These results highlight the remarkable contribution of LLCF to the enhanced rainfall intensity in agreement with the observations.

#### 3.3.2.2 SFI Microphysics

To probe the impact of SFI on drop microphysics, the quantitative contribution of coalescence (first two terms on the right-hand side of Eq. 3-1) and breakup (last two terms on the right-hand side of Eq. 3-1) to changes in droplet number concentrations at three different heights (350-, 150-, 10-m AGL) are shown at 14:59 LT (before the activation of

SFI) and at 15:10 LT (after the SFI have been going on for ten minutes) as illustrated in Figure 3-7. For light rainfall without "feeder" fog (14:59 LT, Figure 3-7a), coalescence dominates over breakup for drops smaller than 0.6 mm. At 15:10 LT (Figure 3-7b), the dominant role of coalescence over breakup shifts to small drop sizes ranging from 0.01 to 0.05 mm in diameter, indicating intensive interactions between feeder fog droplets (10–50 μm) and seeder rain drops (> 100 μm) at low-levels. Further, coalescence effectively behaves as a collection mechanism with the much larger seeder drops sweeping the small fog droplets in their path (Testik and Barros, 2007) as expressed by net losses in number concentrations at 15:10 LT that are substantially larger than at 14:59 LT by approximately six orders of magnitude. As expected, persistent coalescence leads to an increased production of small raindrops (0.2–0.7 mm in diameter, Figure 3-7d) at 10 m AGL. This effect is also manifest in the temporal evolution of the R-DSDs within the fog layer proper (400 m), as shown in Figures 3-8b-d. As a result of enhanced coalescence efficiency, the number concentrations of small raindrops (0.2–0.7 mm) at 15:10 LT (marked by the second vertical line in Figures 3-8a-d) are significantly higher than the ones at 14:59 LT (marked by the first vertical line in Figures 3-8a-d) by one to two orders of magnitude. This effect propagates across the spectrum, as the increase in the number of small raindrops later contributes to the increase in the number and efficiency of collisions between small diameter (d2 < 0.6 mm) and larger diameter drops (d1). As illustrated in Figure A1a, the large number of collisions for low $p = \frac{d2}{d1}$ moves the collision outcomes dynamics from

Regime II that is dominated by breakup dynamics to Regime I where coalescence and filament breakup compete. This results in a net decrease in breakup efficiency compared to light rainfall without SFI, and a significant increase in the number concentration of drops > 0.7 mm, corresponding to changes in raindrops between 1 and 2 mm by one order of magnitude (e.g. Figures 3-8e and 8f). Because the most significant differences in rainfall spectra with and without fog are found for small and intermediate size raindrops, this represents a significant detection challenge to radar measurements (Figure A1b).

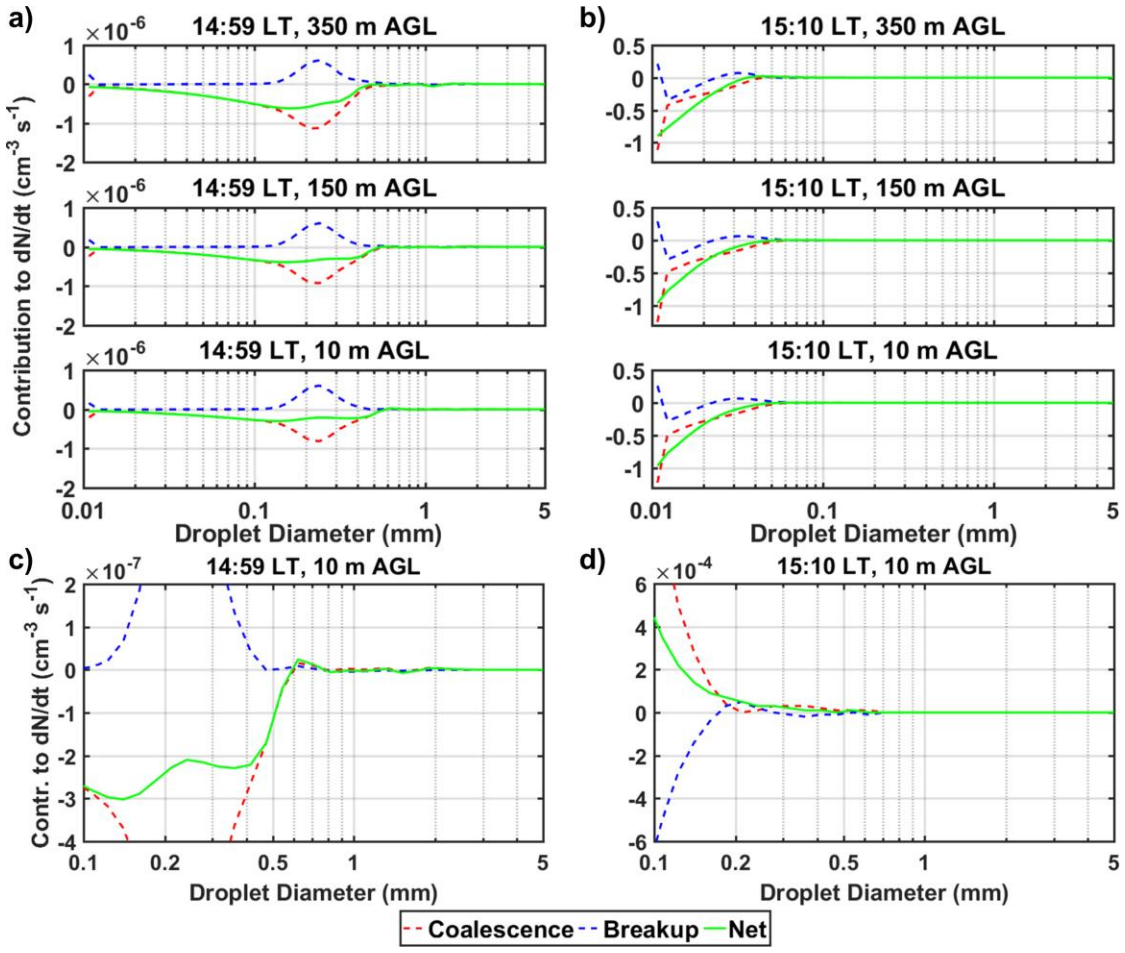


**Figure 3-7: (Top) Contribution of coalescence and breakup processes to changes in simulated droplet number concentrations at three different heights (350-, 150-, 10-m**

**AGL) in the simulation column before (14:59 LT; a) and after (15:10 LT; b) the activation of SFI in the model. (Bottom) Enlarged plots for 14:59 LT (c) and 15:10 LT (d) at 10 m AGL.**

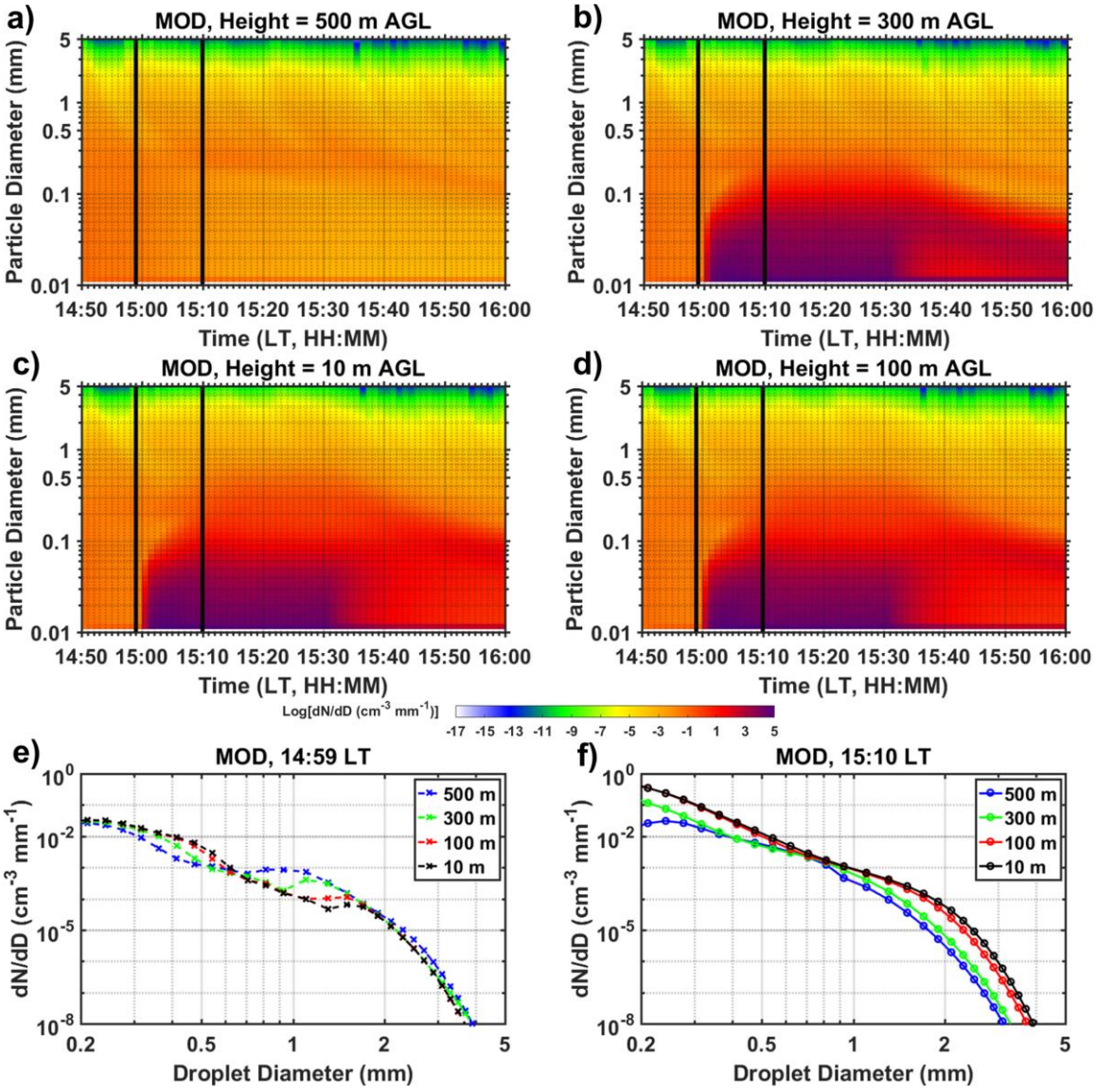


**Figure 3-8: (Top) Time series of simulated drop size distributions at four different heights (clockwise: 500-, 300-, 100-, 10-m AGL). The black vertical lines in (a-d) mark 14:49 LT and 15:10 LT. (Bottom) Simulated rain droplet spectra at 14:59 LT (e) and 15:10 LT (f) at 500-, 300-, 100-, 10-m AGL.**

By introducing the local LLCF observations in the model simulations of rainfall on the western slopes, this study adds to previous work in the inner region (Prat and Barros, 2010a;Wilson and Barros, 2014) demonstrates the importance of LLCF on modulating the diurnal cycle of orographic precipitation via SFI and illustrated the physical mechanisms of the low-level rainfall amplification due to enhanced coalescence efficiency across the spectrum and change in the breakup mode of larger drops. However, ground-based measurements in mountainous regions are severely lacking and limited by their short sampling duration and small spatial coverage. Over the past two decades, satellite remote sensing is widely utilized to provide a global view of cloud and precipitation distributions and enables long-term monitoring of the Earth's systems, in particular with the advent of active sensors (Stephens et al., 2002). The vertical enhancement in intermediate raindrop sizes results in moderate reflectivity with nonlinear steeper reflectivity gradients for moderate to heavy rainfall intensities (e.g. ~ 10 mm/hr in the present case study) at low levels and lower elevations as reported by Wilson and Barros (2014). This behavior is compounded with ground-clutter effects of satellite observations in complex terrain that account for the spatial and temporal characteristics in rainfall retrieval errors in the Tropical Rainfall Measurement Mission (TRMM) Precipitation Radar (PR) identified by Duan et al. (2015) and Prat and Barros (2010b). Next, multi-satellite observations will be applied to investigate the spatial and temporal variability of LLCF, and their optical and

microphysical properties in the SA, aiming at elucidating the role of LLCF in orographic precipitation at the regional scale.

## *3.4 Satellite-based Climatology of CBH using CALIOP and CPR*

Previous studies (Del Genio and Wolf, 2000;Doran and Zhong, 1995) have shown that variations in CBHs are correlated to key physical processes in the atmosphere. Changes in CBH directly influence cloud microphysics and optical properties and link to variations in surface fluxes, atmospheric circulation and planetary boundary layer structure. CBH is the most ambiguous cloud property in all available CALIPSO and CloudSat products, especially in complex terrain, and yet is critical to distinguish low-level clouds (LLC) relative to the topography. Over the study region, two daytime CALIOP tracks (indicated by red dotted lines in Figure 3-1b) overpassing KAVL and KGEV and one nighttime CALIOP track (indicated by blue dotted lines in Figure 3-1b) overpassing KRHP were analyzed. Due to the battery anomaly on 17 April 2011, only daytime CloudSat data are collected after October 2011. Thus, only daytime CPR observations (ground tracks denoted by orange lines) are employed in this study. CALIOP and CPR fly over the KAVL station around 18:50 UTC (14:50 LT) and the KGEV station around 18:45 UTC (14:45 LT) during the daytime, and the KRHP station around 7:45 UTC (3:45 LT) at night. The ceilometer observations summarized in Figure 3-3 provide a comprehensive view of the diurnal and seasonal cycles of ground-based observations of LLCF.

To assess the strengths and weaknesses of CALIOP and CPR sensors over this region, a direct and independent evaluation of satellite measurements for each sensor against near-simultaneous ground ceilometer observations at the KAVL and KGEV stations for the daytime overpasses was conducted first. As stated earlier, the CALIOP CBH is obtained from the Level 2 cloud layer product at 333-m horizontal resolution, and the CPR CBH is defined as the height of the lowest bin with cloud mask larger than 20 in each profile from the 2B-GEOPROF product. For pixel-to-point comparisons, satellite CBH estimates are matched with ceilometer CBHs at KAVL (KGEV) that are acquired within a 5-min (20-min) window centered over the satellite overpass time and located within the corresponding satellite footprints. Similar comparisons with ceilometer measurements were also conducted with the CALIOP Level 2 cloud layer product at coarser horizontal resolutions (1- and 5-km). To avoid introducing uncertainties of the sampling volume by collocating the CALIOP and CPR, the comparisons were conducted separately at their original pixel resolutions (333-m, 1-km and 5-km for CALIOP, 1.4 km for CPR). It should be noted that the revisit time of CALIPSO/CloudSat overpasses is 16 days, and the ground track of each overpass is not perfectly overlapped. Thus, the time- and space-collocated comparisons between the individual sensor and ceilometers are very limited (< 40) for the entire study period (June 2006 − October 2016), thus insufficient to render any conclusions with statistical significance (not shown here). Next a simple method to combine CPR and CALIOP products using 10-year observations is described

in Section 3.4.1, followed by evaluation of the combined CBH estimates against ground-based ceilometer measurements to demonstrate their performance in detecting LLCF in the SA in Section 3.4.2.

### 3.4.1 Merging Methodology Using CALIOP and CPR

Given the complementary nature of CALIOP and CPR, the synergistic use of these two sensors can potentially provide a complete vertical profile of cloud layering and work to minimize the deficiencies in detecting LLCF. A strategy to merge CALIOP and CPR measurements designed to extract maximum information regarding the occurrence of hydrometeor layers is outlined next. Because tenuous and broken clouds at low-levels are likely to be missed by the CALIOP due to its small sampling area and strong attenuation of Lidar signals, thereby decreasing the chance of LLCF detection, horizontal averaging of the CALIOP Level 2 CBH at 333-m resolution is necessary before merging the products of the two active sensors. Instead of simple averaging, the algorithm developed by Zhang et al. (2012) was adopted to account for clouds from different layers or different parts of the same layer. The schematic diagram in Figure 3-9 illustrates the algorithm workflow that starts with preprocessing the CALIOP data. The CALIOP CBH (CBH-L) is chosen as the smaller value of non-null CBHs determined using the following two approaches: 1) spatial and temporal geolocation match to the center of the sampling area within the CALIOP footprint (333-m), and 2) horizontal averaging was conducted over the sampling box following the procedure as described in Zhang et al. (2012). The CPR CBH (CBH-R)

is determined as the lowest bin height with cloud mask level greater than 20 and matched to the center of the sampling area within the CPR footprint (1.4 km). Finally, the merged CBH for the sampling area is chosen as the smaller value of CBH-L and CBH-R. Overall, this framework not only maintains the superior detection skill of each sensor when both measurements are available, but also enables detection when either signal is unavailable.

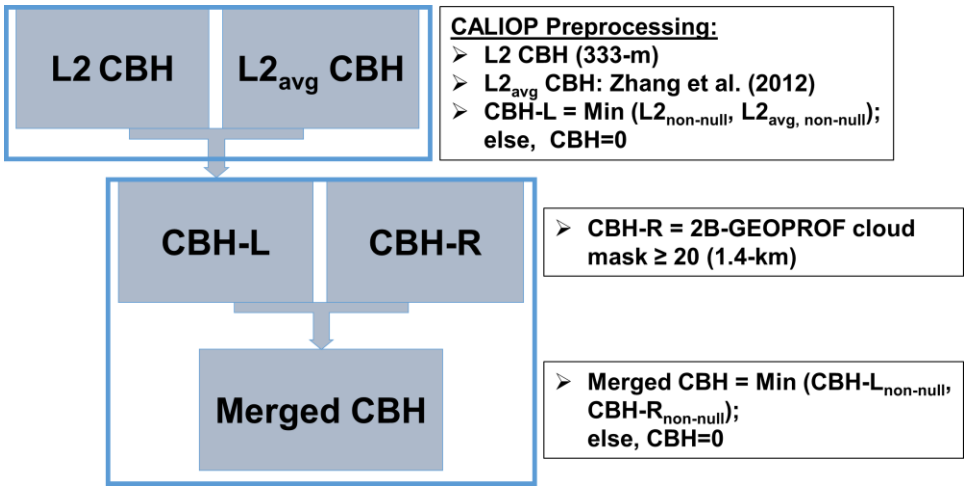


**Figure 3-9: Schematic of merging the CALIOP CBH using the L2 333-m cloud layer product and the CPR CBH from the 2B-GEOPROF product.**

As Lidar signals suffer stronger attenuation than the radar, the detection skill of the CALIOP is highly sensitive to sampling area. Thin scattered clouds are likely to be missed by CALIOP at its highest resolution (333 m × 70 m), thereby further decreasing the chance of LLCF detection. Thus, the CALIOP data at 333-m was first horizontally averaged and sampling boxes of different sizes were designed with the ground station at the center. Various values of averaging length-scales (i.e., 5-, 10-, 20-, 30-, 40-km) of CALIOP 333-m CBHs were assessed with the 5-min ASOS dataset from the KAVL station

for the 10-year study period, as summarized in Table 3-3a. At this site, ceilometer measurements within a 5-min window centered over the overpass time were used, amounting to 201 comparison pairs between CALIOP and the ceilometer. For the comparisons presented hereafter, simultaneous detections of CBH by the satellite and ceilometer are considered as correct detections; CBH detections by the satellite but not reported by the ceilometer are treated as false alarms (FA); CBH detections by the ceilometer when satellite observations are absent or exceed the upper limit of the ceilometer detection range (3.6 km AGL) are treated as missed detections (MD); CBH detections reported by neither of the satellite and the ceilometer are considered as correct rejections. The detectability statistics indicate the optimal averaging scale of 20 km as it achieves the highest correlation with the in situ measurements (Table 3-3a). This process was repeated for the two other AWOS sites (KGEV and KRHP) as reported in Table 3-3b and 3c. Note that 20-min ceilometer datasets are available at AWOS sites, thus a 20-min window centered over the overpass time is applied to obtain the matched ceilometer CBHs. This results in total comparison pairs of 211 and 209 for KGEV and KRHP, respectively. The results in Tables 3-3b and 3c show that the optimal scale is 30 km for both AWOS stations. We can see that the selection of the optimal averaging scale highly depends on the local climatology and available ground data sources (e.g., temporal resolution). Therefore, the optimal sampling size for other regions, especially

mountainous areas, can be determined from local ground observations if possible in a manner similar to the methodology applied in this study, or through careful iteration.

**Table 3-3a: Contingency tables and correlation coefficients (r) of ceilometer cloud base heights (CBHs) at KAVL and daytime satellite retrieved CBHs using the following products: averaged CALIOP Level 2 cloud layer product (333-m CBHs) at 5-, 10-, 20-, 30-, and 40-km horizontal scale; merged CALIOP-CPR CBHs using 10- and 20-km averaging scales for the CALIOP data, following the method outlined in Figure 3-9. Values in parentheses are expressed as a percentage of the total number of observation pairs (last column of the table). Note the 5-min window centered over the satellite overpass time is applied to obtain the matched ceilometer CBHs at KAVL.**

| | Correct Detection | False Alarm | Missed Detection | Correct Rejection | Corr. Coef. | Total Pairs |
|---|---|---|---|---|---|---|
| **CALIOP (5 km)** | 38 (19%) | 2 (1%) | 60 (30%) | 101 (50%) | 0.50 | 201 |
| **CALIOP (10 km)** | 47 (24%) | 2 (1%) | 51 (25%) | 101 (50%) | 0.52 | 201 |
| **CALIOP (20 km)** | 64 (32%) | 9 (4%) | 34 (17%) | 94 (47%) | 0.56 | 201 |
| **CALIOP (30 km)** | 66 (33%) | 15 (7%) | 32 (16%) | 88 (44%) | 0.51 | 201 |
| **CALIOP (40 km)** | 69 (34%) | 21 (11%) | 29 (14%) | 82 (41%) | 0.50 | 201 |
| **Merged (10 km)** | 70 (35%) | 5 (2%) | 28 (14%) | 98 (49%) | 0.61 | 201 |
| **Merged (20 km)** | 86 (43%) | 12 (6%) | 12 (6%) | 91 (45%) | 0.66 | 201 |

**Table 3-3b: Contingency tables and correlation coefficients (r) of ceilometer CBHs at KGEV and daytime satellite retrieved CBHs using the following products: averaged CALIOP Level 2 cloud layer product (333-m CBHs) at 5-, 10-, 20-, 30-, and 40-km horizontal scale; merged CALIOP-CPR CBHs using 20- and 30-km averaging scales for the CALIOP data, following the method outlined in Figure 3-9. Values in parentheses are expressed as a percentage of the total number of observation pairs (last column of the table). Note the 20-min window centered over the satellite overpass time is applied to obtain the matched ceilometer CBHs at KGEV.**

| | Correct Detection | False Alarm | Missed Detection | Correct Rejection | Corr. Coef. | Total Pairs |
|---|---|---|---|---|---|---|
| **CALIOP (5 km)** | 58 (28%) | 4 (2%) | 70 (33%) | 79 (37%) | 0.38 | 211 |
| **CALIOP (10 km)** | 61 (29%) | 6 (3%) | 67 (32%) | 77 (36%) | 0.36 | 211 |
| **CALIOP (20 km)** | 77 (36%) | 6 (3%) | 51 (25%) | 77 (36%) | 0.49 | 211 |
| **CALIOP (30 km)** | 90 (43%) | 12 (6%) | 38 (18%) | 71 (33%) | 0.52 | 211 |
| **CALIOP (40 km)** | 95 (45%) | 18 (9%) | 33 (15%) | 65 (31%) | 0.47 | 211 |
| **Merged (20 km)** | 100 (47%) | 8 (4%) | 28 (13%) | 75 (36%) | 0.59 | 211 |
| **Merged (30 km)** | 110 (52%) | 14 (7%) | 18 (8%) | 69 (33%) | 0.63 | 211 |

**Table 3-3c: Contingency tables and correlation coefficients (r) of ceilometer CBHs at KRHP and nighttime satellite retrieved CBHs using different horizontal averaging scales (5-, 10-, 20-, 30-, and 40-km) of CALIOP Level 2 cloud layer product (333-m CBHs). Values in parentheses are expressed as a percentage of the total number of observation pairs (last column of the table). Note the 20-min window centered over the satellite overpass time is applied to obtain the matched ceilometer CBHs at KRHP.**

| | Correct Detection | False Alarm | Missed Detection | Correct Rejection | Corr. Coef. | Total Pairs |
|---|---|---|---|---|---|---|
| **CALIOP (5 km)** | 41 (20%) | 8 (4%) | 70 (33%) | 90 (43%) | 0.22 | 209 |
| **CALIOP (10 km)** | 44 (21%) | 8 (4%) | 67 (32%) | 90 (43%) | 0.32 | 209 |
| **CALIOP (20 km)** | 63 (30%) | 31 (15%) | 48 (23%) | 67 (32%) | 0.38 | 209 |
| **CALIOP (30 km)** | 76 (36%) | 43 (21%) | 35 (17%) | 55 (26%) | 0.47 | 209 |
| **CALIOP (40 km)** | 77 (37%) | 47 (22%) | 34 (16%) | 51 (25%) | 0.43 | 209 |

### 3.4.2 Combined Sensor Analysis

The merging methodology (see the diagram in Figure 3-9) was applied to combine the CPR data and two resolutions of the CALIOP data at KAVL (10- and 20-km) and KGEV (20- and 30-km) sites, based on the averaging scales examined above. As shown in the last two rows of Tables 3-3a and 3-3b, the merged estimates during daytime show improved skill over the averaged CALIOP alone. Combining the CPR data and the optimal averaging of CALIOP data at KAVL (20-km, last row of Table 3-3a) and KGEV (30-km, last row of Table 3-3b) sites, respectively, the merged results indicate higher probabilities of correct detections (43% for KAVL and 52% for KGEV), fewer occurrences of MD (6% KAVL and 8% for KGEV), and larger correlation coefficients (0.66 for KAVL and 0.63 for KGEV). It is expected that slightly more FA (6% for KAVL and 7% for KGEV) are resulted in the merged estimates. At nighttime, the merging method is not applicable as no CPR data is recorded after October 2011, and the sample size prior to that date is

small. Thus, only the CALIOP measurements were used and averaged for nighttime comparisons at KRHP. As expected, the detectability statistics are not as notable as the merged estimates but the averaging of CALIOP pixels shows clear advantages over the original Level 2 layer products because of sample size. It is important to keep in mind the uncertainties associated with the sampled cloud-volume agreement when averaged ground-based measurements over a certain temporal resolution are directly compared to fast-moving space-based observations, especially at coarse horizontal resolutions and/or different temporal scales (Kim et al., 2011). Therefore, the discrepancies between satellite estimates and ground observations may be in part due to large temporal averaging intervals (e.g., 5-min, 20-min) of the ground ceilometers, which lack representativeness of rapidly changing clouds over mountainous regions. In particular, LLCF typically have short lifetimes and even shorter spatial correlation scales in complex terrain, and there are inherent inconsistencies between the observing strategies used by ceilometers (bottom-up) and satellites (top-down) due to severe attenuation of the latter especially when multilayer clouds are present, which stands as a critical challenge for the validation of satellite products. A close examination of the vertical profiles of radar and Lidar observations for the FA and MD cases reveals distinct observational deficiencies of the merged estimates of CALIOP and CPR. For FA, the error is attributed to large horizontal averaging of Lidar signals under scattered cloudiness conditions. For MD, both sensors are limited in detecting LLCF in the presence of thick upper clouds and/or in unfavorable

weather conditions (e.g., mist, rain) due to significant attenuation of CALIOP signals and low sensitivity of the CPR, in addition to ground clutter effects of both sensors.

Even though twice-daily satellite observations (around 3:45 LT and 14:45−14:50 LT) cannot capture the full diurnal range in the SAM, they provide a useful illustration of nighttime-daytime contrasts over the study region. Figure 3-10 displays the seasonal histograms of satellite CBH estimates (bottom panel) compared to the first layer CBHs detected from the ground ceilometers at the satellite overpass time from June 2006 to October 2016 (top panel). The total number of observation days is denoted in parentheses after each season. Note the merged products (CALIOP-CPR) at KAVL and KGEV sites at daytime are derived from the CPR data and averaged CALIOP data at their corresponding optimal scales (KAVL: 20-km, KGEV: 30-km) and the nighttime CALIOP data averaged at 30-km horizontal scale are used for comparisons at KRHP site. For daytime cases at KAVL (see Figures 3-10a and d), the occurrence frequencies of the combined satellite observations, and the ceilometer in summer are in good agreement with both peaking at 1.5−2 km MSL, though CBH values below 1.5 km are still missed by the merged satellite estimates for all seasons. These MDs again point out the limitation of both active sensors in detecting LLCF when surface clutter and low sensitivity to small drops hinder detection by the CPR and the CALIOP signals suffer strong attenuation due to optically thick clouds aloft. At KGEV (see Figures 3-10b and e), the merged satellite CBHs during daytime capture well the variations in the spring, summer and fall seasons, with distributions

peaking at 1.5–2 km, 2–2.5 km, and 1.5–2 km, respectively. Similarly, both satellite sensors missed daytime clouds detected by the ceilometer near the surface (below 1.5 km). At KRHP (see Figures 3-10c and f), nighttime CALIOP succeeds to detect frequency maxima of LLCF below 1 km in summer and fall, likely associated with nocturnal fog often recorded by the ceilometer in these seasons (see Figure 3-3d). The superior performance of nighttime CALIOP detections can be explained by that Lidar signals are less noisy during nighttime as compared to daytime observations that are subject to solar radiation contamination in the background (Young and Vaughan, 2009). In winter, both satellite and ceilometer distributions peak around 1–1.5 km, however, the maximum in nighttime LLCF occurrences is underestimated by the CALIOP.

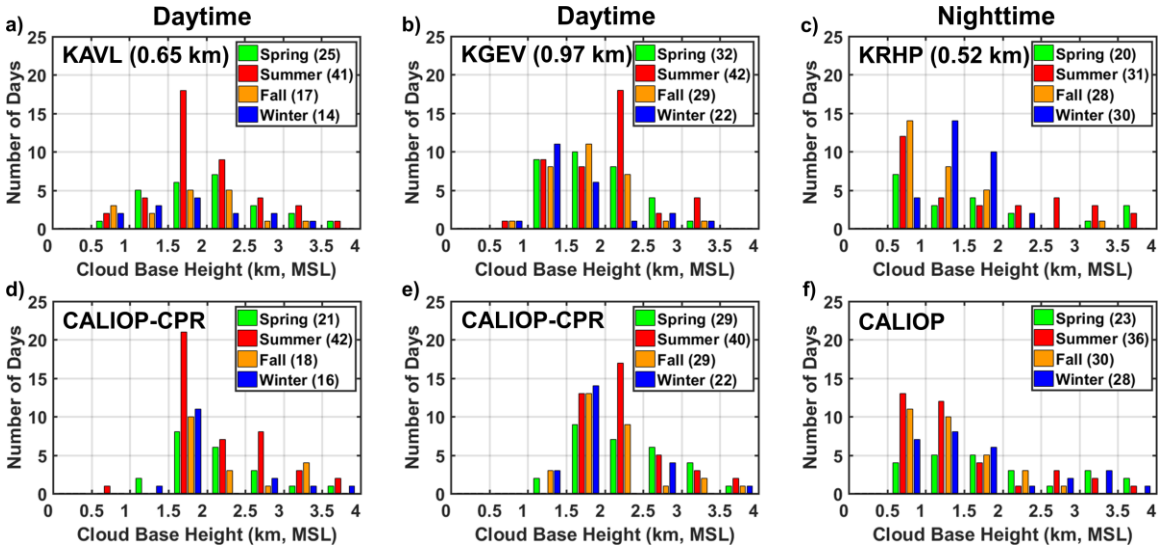


**Figure 3-10: Probability distributions using 10-year (June 2006 – October 2016) observations of CBHs from: (a) the ground ceilometer at KAVL (elevation: 0.65 km) around daytime overpass (~14:50 LT); (b) the ground ceilometer at KGEV (elevation: 0.97 km) around daytime overpass (~14:45 LT); (c) the ground ceilometer at KRHP (elevation: 0.52 km) around nighttime overpass (~3:45 LT); (d) the merged CALIOP-CPR CBHs for daytime cases at KAVL; (e) the merged CALIOP-CPR CBHs for daytime cases**

**at KGEV; (f) the averaged CALIOP CBHs at 30-km horizontal scale for nighttime cases at KRHP. Note the total number of observation days is denoted in parentheses after each season (spring: April-May-June, summer: July-August-September, fall: October-November-December, and winter: January-February-March) and the elevation of each site is denoted in parentheses after its name in (a)-(c).**

In order to investigate the spatial variability of LLCF along the entire satellite tracks, we define 0.1° × 0.1° (10 km × 10 km) grid boxes over the entire study region. As shown in Figure 3-1b, three daytime and four nighttime satellite orbits are mapped in this region with overpass times between 14:40−15:10 LT and 3:30−4:00 LT, respectively. For each daytime overpass, the merged CALIOP-CPR CBH retrieval at each grid cell is determined from the CALIOP and CPR observations within the grid box, using the methodology discussed in Section 3.4.1. For each nighttime overpass, the CBHs from CALIOP 333-m cloud layer products are averaged horizontally within each sampling box following the algorithm from Zhang et al. (2012) to derive CALIOP CBH at each grid cell. Figure 3-11 displays the spatial distribution of LLCF along CALIPSO/CloudSat tracks over the study region. Here, only grid cells with at least 30 overpasses and satellite observed CBH below 4 km MSL (consistent with the upper detection limit of ground ceilometers) are used to calculate the mean and coefficient of variance (CV) values at each grid cell. Satellite CBHs relative to MSL are converted to AGL. It is apparent that variations in CBH show a pronounced spatial pattern linked to the topography variability (terrain elevation denoted by contour lines: 500 m-solid grey, 1000 m-solid black, and 1500 m-dotted black) in this region.

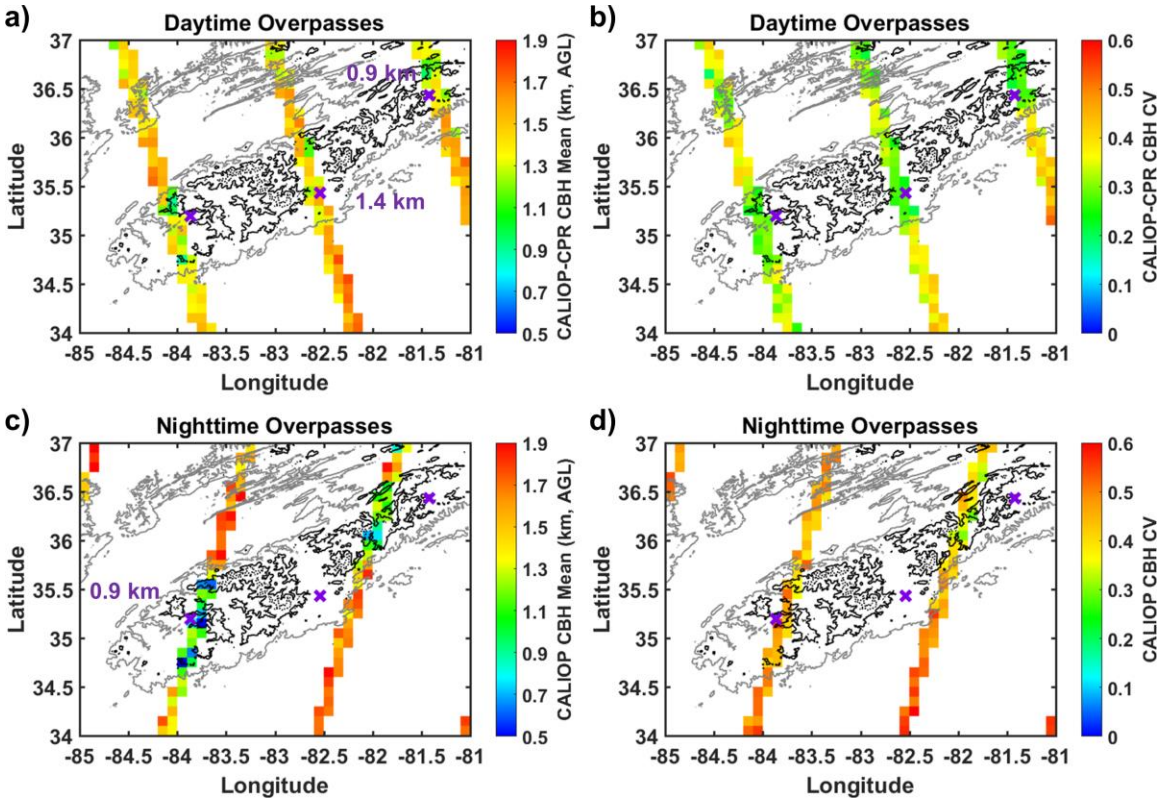


**Figure 3-11: (Top) Mean of CALIOP-CPR CBHs (km, AGL) for low-level clouds and fog (LLCF, merged CBH < 4 km MSL) and the corresponding coefficient of variance (CV) in each grid box (0.1° × 0.1°) for daytime overpasses. (Bottom) Mean of CALIOP CBHs (km, AGL) for LLCF (CALIOP CBH < 4 km MSL) and the corresponding CV in each grid box (0.1° × 0.1°) for nighttime overpasses. Contour lines denote terrain elevation of 500 m (solid grey), 1000 m (solid black) and 1500 m (dotted black). Note the three ground ceilometer sites (from left to right: KRHP, KAVL, KGEV) are marked by purple crosses and the numbers next to them represent mean ceilometer CBHs around satellite overpass time.**

The merged estimates during daytime indicate relatively shallower bases of LLCF persistently observed over the mountainous area than the adjacent plains, as suggested by the smaller CV values over high terrain (see Figure 3-11b). The nighttime CALIOP observations exhibit generally lower cloud bases than daytime CBHs over the SAM, illustrating a more significant contrast of cloud base levels between mountainous regions

and lowland area. We can also note that relatively larger variations over time are evident for nighttime retrievals compared to daytime merged estimates (Figures 3-11b and d). For comparison, the ceilometer observations at KRHP, KAVL, and KGEV sites (marked by the purple crosses from left to right in Figure 3-11) around the satellite overpass time are also present. The mean values of ceilometer CBHs (see their histograms in Figures 3-10a-c) are used to evaluate the corresponding satellite CBH mean at the grid boxes where ground ceilometers are located. The ceilometer CBHs at KAVL (1.4 km AGL) and KGEV (0.9 km AGL) during daytime are overestimated by the merged CBHs by 200 m and 500 m, respectively while the ceilometer CBH at KRHP (0.9 km AGL) during nighttime is slightly underestimated by the CALIOP CBH. The former are located on the Blue Ridge along which persistent shallow clouds and fog banks form on the eastern slope of the SAM (e.g. Black Mountains and Blue Ridge).

Overall, the synergy of the combined CALIOP and CPR observations enables us to conduct statistically significant analysis of LLCF over the study region and demonstrates improved detection skills in mapping LLCF over the individual sensor. The daytime results of merged satellite observations are in general agreement with in situ measurements at KAVL and KGEV, especially for the summer season. Nighttime CALIOP observations suffice to capture LLCF below 1 km, in agreement with persistent nocturnal fog observed by the ground ceilometer at KRHP. In the presence of optically thick clouds at upper levels, challenges in detecting daytime shallow boundary clouds with bases

lower than 1.5 km still remain for the merged satellite observations, which are attributed to physical limitations of low sensitivity of CPR, strong extinction of CALIOP signals, and ground clutter effects of both sensors. Spatial analysis along satellite tracks illustrates that persistent LLCF are detected over the mountains with relatively lower cloud bases than adjacent plains in the SA, especially during nighttime.

## *3.5 Evaluating low-level processes using a column model*

Although CALIOP and CPR demonstrate great potential to resolve the vertical structure of LLCF, previous discussions have also revealed limitations in the application of active sensors over the study region due to long revisit times and narrow satellite swaths. The passive sensor MODIS onboard the Aqua satellite maintains a close formation with CALIPSO and CloudSat satellites. The wide viewing swath of MODIS (2330-km cross-track) can extend the spatial coverage beyond narrow swaths of active sensors and compensate for the sparse temporal sampling that is inadequate to reflect spatial variations in seasonal cycles. The revisit frequency of MODIS over this study region is about one to two days because of its wide viewing swath. Next MODIS observations will be explored to characterize the top, optical, and microphysical properties of LLCF over the SA.

### 3.5.1 Spatial Patterns of LLCT CTH

MODIS provides high-spectral resolutions of cloud properties at 1-km resolution and significant refinements in its retrieval algorithm are implemented in C6 by evaluating

against near-coincident cloud-top observations from the CALIOP (Baum et al., 2012). Figure 3-12 shows the density-colored scatterplots of MODIS CTH at 1-km pixel and the collocated CALIOP CTH for daytime and nighttime observations over the study region. The CALIOP CTH is calculated as the average of CALIOP 333-m CTHs within the MODIS 1-km footprint. There are approximately 3 Lidar profiles within the 1-km field-of-view (FOV) of MODIS. Due to the narrow beam width (~ 70 m) of CALIOP, only a small fraction of the entire MODIS FOV (1-km) at the Earth's surface is sampled by CALIOP. Thus, uncertainties resulted from the differences in sampling area between MODIS and CALIOP should be kept in mind when interpreting the comparison of their collocated CTH measurements. The viewing angles for all the MODIS pixels in comparison are in the range of 13.6° − 16.9°, as the nadir-viewing track of Aqua does not follow the CALIPSO flight track. This results in a parallax effect on the CTH dependence of the collocation (Holz et al., 2008), which are not taken into account in this study. For daytime cases, we only consider single layer clouds, as determined by the cloud multilayer flag in MODIS. As indicated in Figure 3-12a, MODIS CTHs agree well with CALIOP CTHs, in particular for low clouds with tops < 5 km. This is likely attributed to the new lapse-rate approach applied in C6 to retrieve MODIS CTH of low clouds (Holz et al., 2008). The underestimation of daytime CTHs by MODIS is likely associated with its lower sensitivity to small droplets near the cloud top as compared to CALIOP, which is superior in detecting tenuous and geometrically thin clouds. With multi-layer profiles included

during nighttime, a systematic high CTH bias of 0.2−1.2 km is found in the MODIS results (Figure 3-12b). The overestimation by MODIS could be explained by the possible ambiguities induced by its viewing geometry as a longer path through the atmosphere is observed by MODIS at an angle than CALIOP with only nadir view. Overall, the cloud-top product from MODIS demonstrates consistent detections of low clouds (CTH < 5 km MSL) with near-simultaneous measurements from CALIOP.

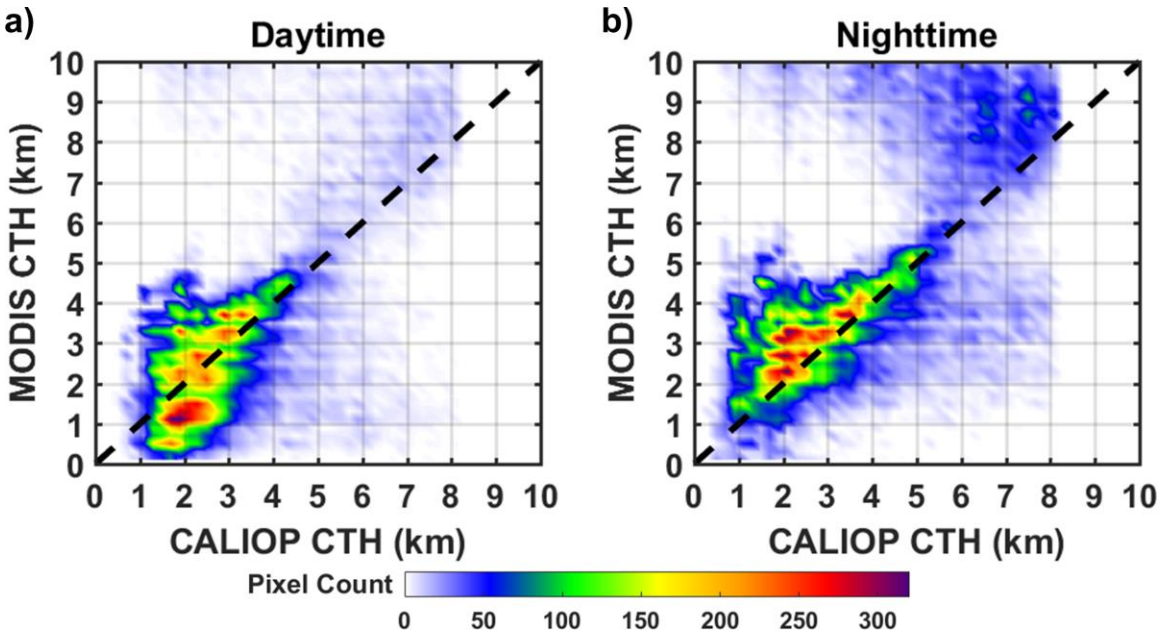


**Figure 3-12: Density-colored scatterplots of MODIS cloud top heights (CTHs) at 1-km pixel and the collocated CALIOP CTHs for daytime (a; single-layer clouds only) and nighttime (b) observations. The dashed black line represents the 1:1 line.**

To further probe LLCF distributions using MODIS observations, grid cells of 0.05° × 0.05° (5 km × 5 km) are defined over the entire study region (map in Figure 3-1b). For each season, the spatial variability of LLCF (CTH < 5 km MSL) observed by MODIS for daytime (~ 14:00 − 15:30 LT) and nighttime (~ 3:00 − 4:30 LT) overpasses during the 10-

year study period are exhibited in Figures 3-13 and 3-14, respectively. If there are at least 5 pixels (1-km) with MODIS CTH < 5 km within the grid cell, one day is counted in this cell. Only single-layer clouds are considered for daytime overpasses. Inspection of Figure 3-13 reveals more frequent daytime low-clouds are evident in the warm season (spring and summer) as compared to the cold season (fall and winter). In particular, mountain ridges experience persistent cover of low clouds at daytime in spring and summer. Note that LLCF occurrences in summer are over 50 days/year over the mountains at elevations above 1,500 m MSL (dotted black contour lines in Figure 3-13b). One interesting feature of the LLCF distributions for the warm season is that relatively fewer clouds form above large lakes or artificial reservoirs (indicated by the white dots based on 30-arcsec gridded data from the USDA-NRCS State Soil Geographic Database) impounded by major dams in this region while higher frequencies of cloud occurrences are found over the adjacent lands (Figures 3-13a and b). Specifically, note the organization of cloudiness between major lakes part of the Tennessee Valley Association (TVA) system of dams to the west of the SAM and away from the large dams in the upper Savannah and Catawba-Pee Dee rivers in the east, which are indicative of the robust role of lake breeze circulations in the organization of LLC formed along southerly and easterly low level moisture convergence patterns (Wilson and Barros, 2017). To be specific, the lake breeze refers to thermally driven winds blowing from a large body of open water toward the surrounding lands due to the pressure gradient of the air over the water (high pressure) and dry land (low

pressure) produced by differences in their heat capacities during daylight with solar heating. The moisture supply from open water evaporation transported to adjacent lands creates favorable conditions for cloud formation, and even trigger thunderstorms when the atmosphere is unstable in the warm season. By contrast, synoptic winds from west-northwest dominate in the fall and winter, leading to extensive formation of low clouds on the windward side of the SAM. Due to the mountain barrier effect, forced orographic lifting of incoming air masses results in enhanced formation of low-level orographic clouds along the windward slopes but significantly reduced occurrences of low clouds on the leeward side (Barros and Lettenmaier, 1994;Barros and Kuligowski, 1998). Further, the lake breeze flow is hindered in the cold season as the required pressure gradient is unlikely to form under strong regional winds.

Figure 3-14 displays the seasonal spatial distribution of nighttime LLCF observed by MODIS. As information from visible wavelength is not available at night, we only consider clouds with the confidence level of "confident cloudy" as determined by the cloud mask product (MYD35). In the spring and summer season, high frequencies of nocturnal LLCF occurrences are present in the mountain valleys consistent with regional-scale stability at low levels resulting in the pooling of cold moist air in the inner SAM (Wilson and Barros, 2017). At nighttime, this region experiences the highest frequency of LLCF coverage in the winter season compared to other seasons, especially along the windward slopes of the SAM, consistent with forced orographic lifting of westerly and

northwesterly winds as noted above. Due to the inherent dependence of cloud properties on viewing geometry, care should be taken when using MODIS products observed over a wide range of sensor zenith angles (Maddux et al., 2010). Additional spatial distributions of MODIS pixel counts with viewing angles less than 20° for each season during the 10-year study period are provided in Figures A2 and A3. These maps highlight the areas in the study domain with larger fraction of near-nadir observations, which are less prone to the sensor zenith angle biases and likely lends credence to the corresponding observational findings of LLCF detection.

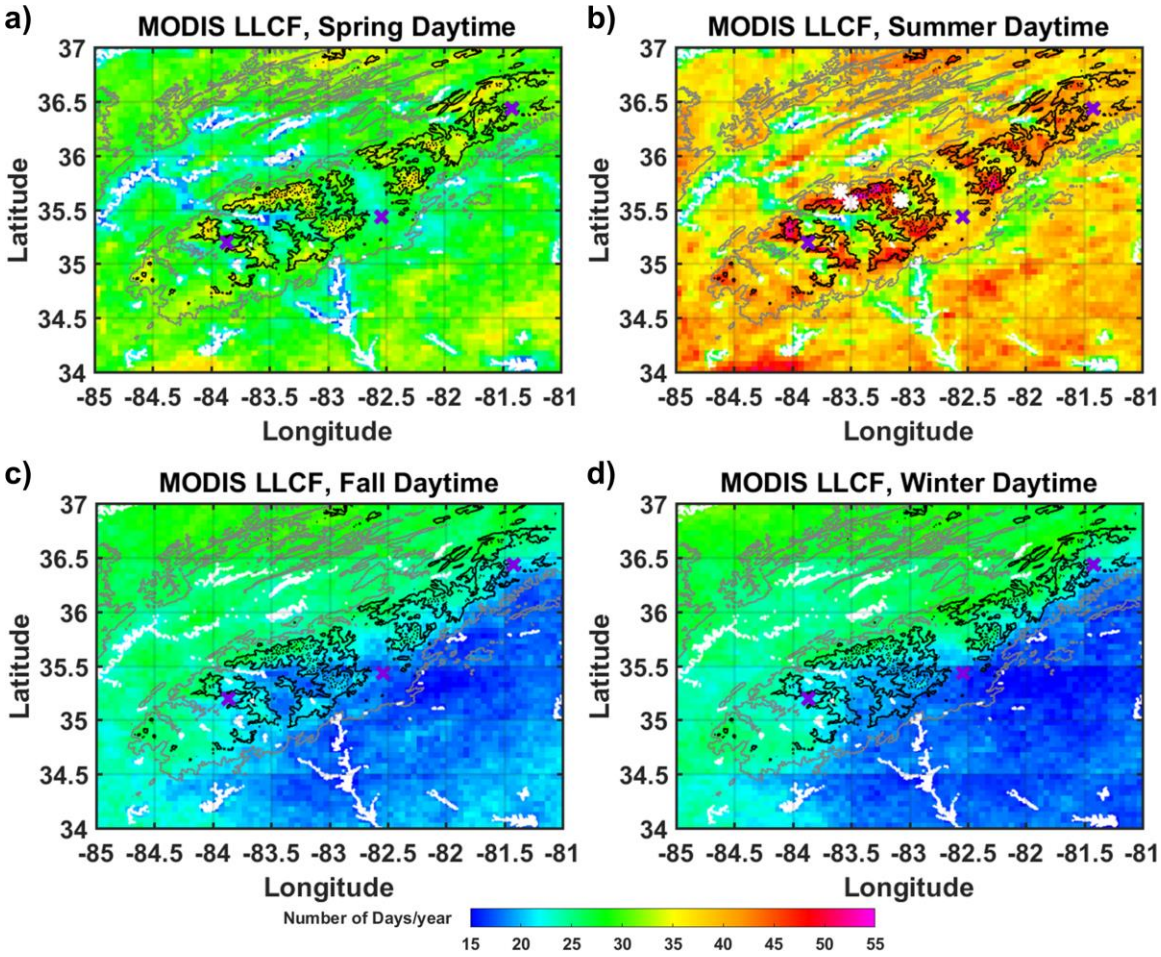

**Figure 3-13: Spatial distributions of MODIS LLCF (CTH < 5 MSL, single-layer clouds only) occurrences in each grid box (0.05° × 0.05°) during daytime overpasses for each season (spring: April-May-June, summer: July-August-September, fall: October-November-December, and winter: January-February-March). Contour lines mark terrain elevation of 500 m (solid grey), 1000 m (solid black) and 1500 m (dotted black) and water surface is delineated by white dots. Note the three ground ceilometer sites (from left to right: KRHP, KAVL, and KGEV) are marked by purple crosses and white asterisks in (b) denote the four ground fog collectors (from left to right: ELK, CD, PK, and PKT).**

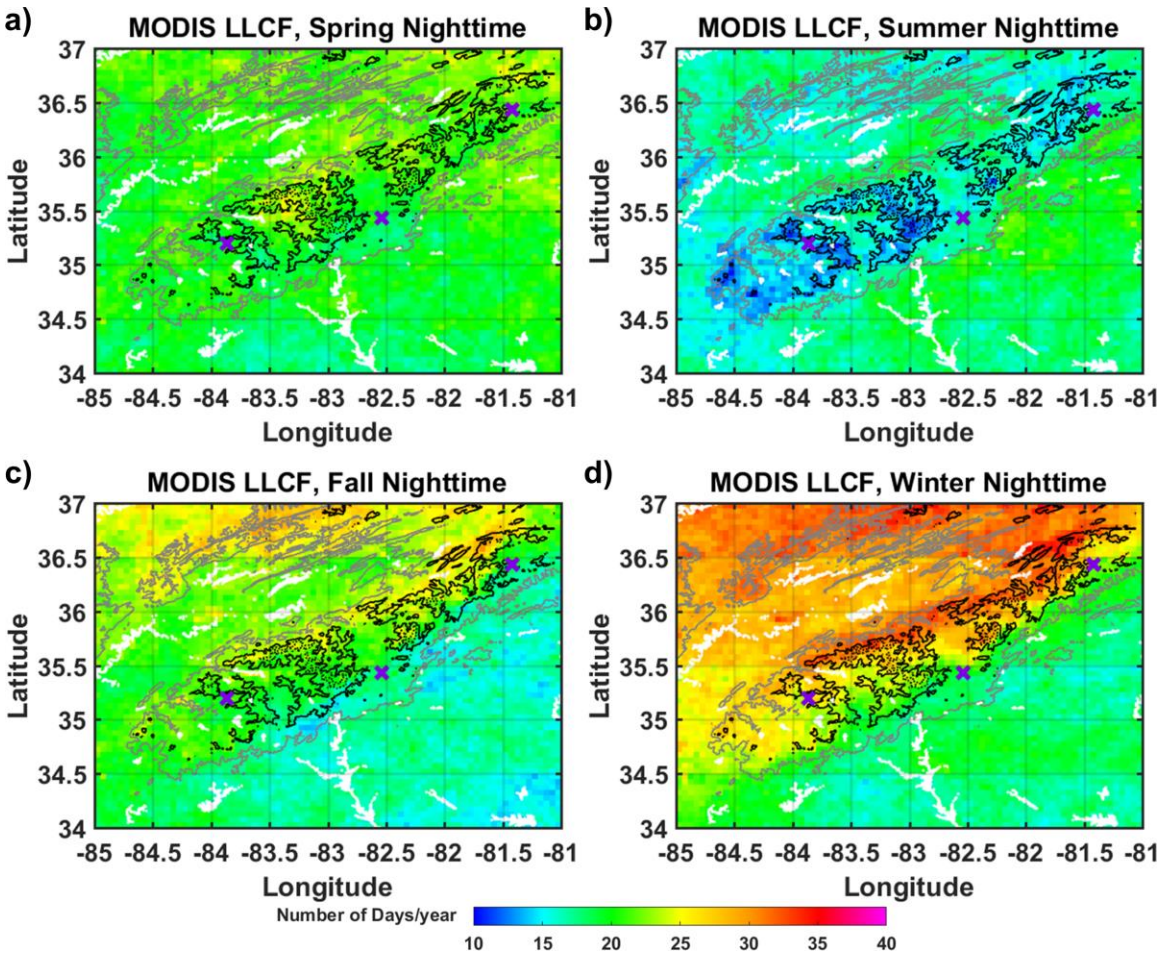


**Figure 3-14: Spatial distributions of MODIS LLCF (CTH < 5 MSL, confident cloudy only) occurrences in each grid box (0.05° × 0.05°) during nighttime overpasses in each season (spring: April-May-June, summer: July-August-September, fall: October-November-December, and winter: January-February-March). Contour lines mark terrain elevation of 500 m (solid grey), 1000 m (solid black) and 1500 m (dotted black)**

**and water surface is delineated by white dots. Note the three ground ceilometer sites (from left to right: KRHP, KAVL, and KGEV) are marked by purple crosses.**

### 3.5.2 Optical and Microphysical Properties of LLCF

Next we focus on characterizing the climatology of optical and microphysical properties of daytime LLCF using the MODIS observations and ground ceilometer measurements. During June 2006 − October 2016, the optical and microphysical properties retrieved from MODIS combined with the CBH information obtained from ground ceilometers are utilized to evaluate LLCF properties at these ceilometer sites during daytime overpasses. The analysis is limited to low clouds with top heights less than 5 km MSL when single layer is detected by MODIS. Figure 3-15 shows the fractional occurrence density maps of collocated MODIS top, optical, and microphysical properties as a function of ceilometer CBHs (AGL) at KRHP, KAVL, and KGEV sites. The ceilometer CBHs are obtained within 5 (20) minutes of the MODIS overpass time at KAVL (KRHP and KGEV) and are matched with the MODIS pixel within its footprint (1 km). This corresponds to 194 observation pairs at KRHP, 206 pairs at KAVL, and 253 pairs at KGEV for the 10-year study period. LLCF with lower CBHs are more frequent observed at the ridge site (KGEV) compared to the two valley sites (KRHP and KAVL), which is consistent with the previous analysis of 10-year ceilometer observations (Figure 3-3) and combined CBHs from CALIOP and CPR (Figure 3-11). Conditional on ground ceilometer detections from bottom-up, the distributions of CWP-CBH and COT-CBH indicate frequent LLCF occurrences at these sites (CBH < 2 km AGL for KRHP and KAVL, CBH < 1.5 km AGL for

KGEV), which are associated with small values of vertically integrated cloud properties (CWP < 100 g/m² and COT < 15). Although CER exhibits large variability, similarities can be found in the lower-left corner of the diagrams showing a prominent feature of LLCF composed of small liquid water droplets with effective radius around 5–15 μm near cloud tops.

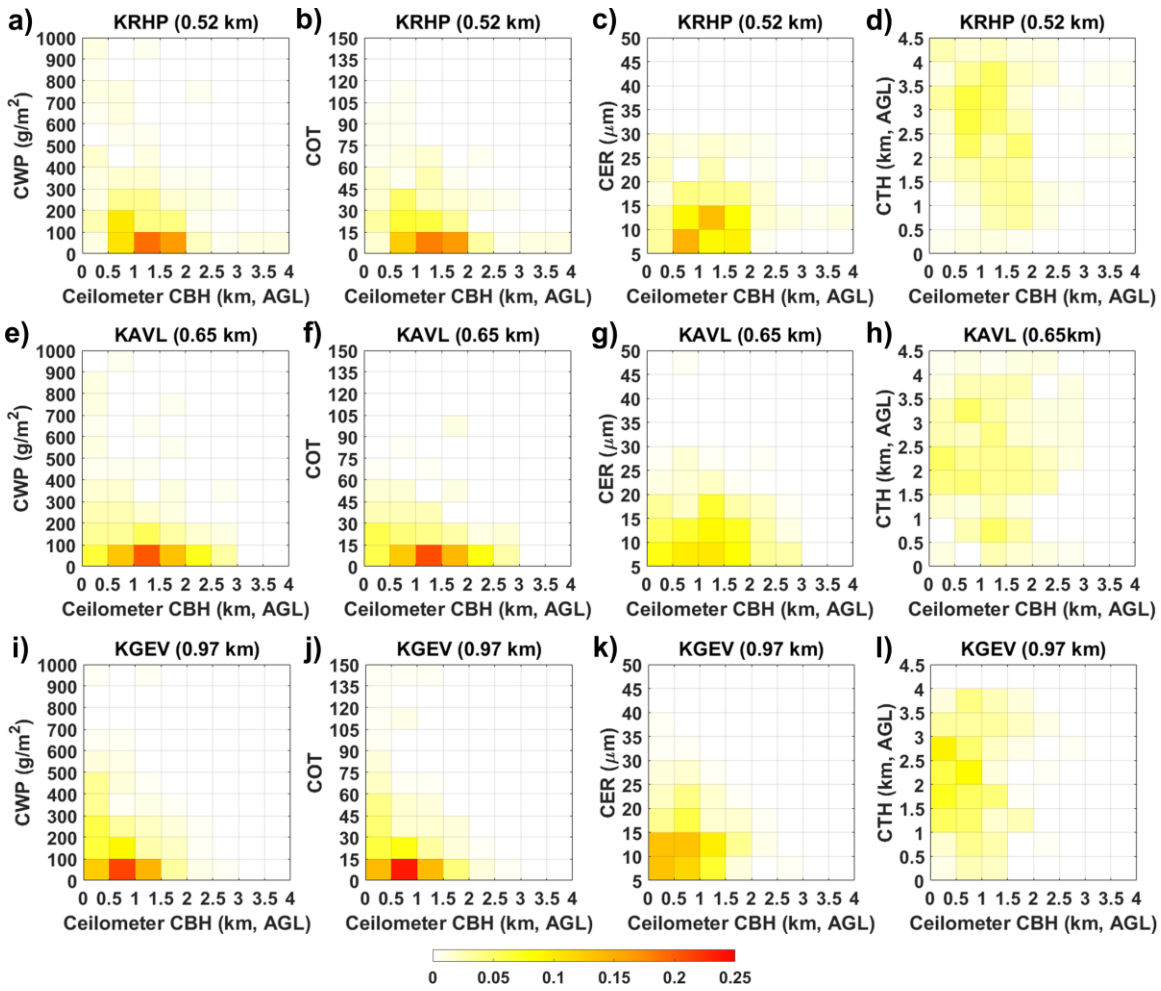


**Figure 3-15: Fractional occurrences of collocated MODIS cloud properties of LLCF (single-layer clouds with CTH < 5 km MSL) as a function of ceilometer CBHs at KRHP (a-d), KAVL (e-h), and KGEV (i-l) during June 2006 – October 2016 (daytime overpasses only). Note the elevation of each site is denoted in parentheses after its**

**name. In each panel, CWP represents cloud water path, COT represents cloud optical thickness, and CER represents cloud particle effective radius.**

Figure 3-4b shows the ground-based MPS observations of LLCF immersion in the absence of rainfall with CER values around 25 μm in the early morning until 11:00 LT. After 11:00 LT, surface CER values (50−150 μm) are significantly higher than the MODIS CER estimates (5−15 μm) near cloud tops by a factor of 3−10 because the number of drizzle sized drops increases relative to the LLCF sized drops (< 100 μm) that is one to two orders of magnitude lower at mid-day (Figure 3-4a). This indicates there is significant vertical stratification of the microstructure of LLCF from cloud top to the ground surface, suggesting DSD evolution in the LLCF column proper, thus conditioning the environment for enhanced SFI when the "seeder" light rainfall arrives in the afternoon.

Similar analyses were conducted for 10-year MODIS observations sampled around the ground sites with fog collectors (see Table 3-1). Within the grid box (5 km × 5 km, as defined in Section 3.5.1) where each ground station is located, Figures A4-A7 present the joint frequency histograms of MODIS CTH and the optical and microphysical properties (CWP, COT, and CER) for each season. Note that only single-layered LLCF measurements with tops below 5 km MSL and near-nadir viewing angles (< 20°) are considered in the analysis. As PK and PKT are located at the same grid box, only results for PK are shown here. The system of reference for the MODIS CTHs was converted from MSL to AGL. In the warm season (spring and summer), it is evident that more clouds with lower tops are present over higher elevation sites (CD and PK & PKT) as compared to the

valley station (ELK). Regardless of differences in terrain elevation, similar ranges of CWP (~ 0–200 g/m$^2$) and COT (0–30) values are observed for LLCF at all ground locations in the warm season (Figures A4 and A5) while larger CWP and COT values are found in the cold season (Figures A6 and A7). Interestingly, despite low CWP and COT in summer, the corresponding CER values are higher on average and exhibit higher variability (right panel in Figure A5) compared against narrow distributions of low CER values (~ 5–15 μm) in spring, fall, and winter (right panels in Figures A4, A6, and A7).

## *3.6 Conclusion*

Remote sensing observations of orographic precipitation exhibit large underestimation errors from sub-daily to annual scales tied to landform and topographic complexity generally (e.g.,Barros et al., 2000;Barros, 2013a;Duan et al., 2015;Prat and Barros, 2010a). In the SAM, which are representative of middle mountains in the tropics and mid-latitudes that are hosts to high biodiversity cloud forests and generally humid ecosystems, nearly a decade of ground-based rainfall accumulation and rainfall microphysics, show that the diurnal cycle of rainfall exhibits an all-season mid-day peak that explains a large fraction of the regional annual freshwater input, and it is critical to regional drought resilience (Wilson and Barros, 2015, 2017). Over roughly the last decade, independent field observations of vertical structure of rainfall, rainfall microphysics, and rainfall intensity and accumulation in the SAM show evidence of low-level enhancement of R-DSDs with rainfall intensities up to one order of magnitude and rainfall

accumulations on the order of 200–300% at daily, seasonal and annual time-scales (Angulo-Martínez and Barros, 2015;Wilson and Barros, 2014, 2015). These observations are indicative of space-time distributions of rainfall that do not fit the classical orographic precipitation model with strong upslope enhancement characteristic of high-mountain ranges, consistent with the lack of a rain-shadow region in the SE US.

The objective of this study is to understand the physical basis of the observed mid-day peak in rainfall that is also observed in humid mountain regions rich in biodiversity elsewhere (e.g. Central Andes) from local to regional scales and from case-study to climate time-scales. Following Wilson and Barros (2014) and Angulo-Martínez and Barros (2015) who demonstrated the impact of SFI in amplifying rainfall over the inner mountain region, here the modeling was extended to the western slopes of the SAM using in situ observations and modeling. First, a rainfall column microphysics model constrained by fog observations was used first to investigate how SFI modify the R-DSD to reveal that fast SFI (2–5 min time-scales) modify the R-DSD by increasing coalescence efficiency in the small drop range (< 0.7 mm diameter), whereas competition between coalescence and breakup dominates for larger drop (3–5 mm diameter). Detailed analysis of the collision dynamics reveals that the presence of high number concentrations of small drops in LLCF changes the collision dynamics of breakup to the filament-only mode, which results in the balance of coalescence and breakup effects for large drops. The net result is a large increase in the concentration numbers of intermediate size raindrops in the 0.7–3 mm

range and up to a ten-fold increase in rainfall intensity, with very large changes in the number concentrations between 1–2 mm and up to 3 mm. Second, the focus turned to satellite observations with an eye in building evidence of the role of LLCF in modulating the observed space-time diurnal cycle of precipitation at the regional scale. A 10-year climatology of LLCF habits was developed based on combined CBH estimates from CALIOP and CPR, and on MODIS observations of CTHs, as well as cloud properties including LWP, COT, and cloud-top CER. The climatology shows high-frequency daytime LLCF over mountain ridges in the warm season (especially in summer) shifts to river valleys at nighttime, consistent with previous modeling studies of regional patterns of warm season moisture convergence. In fall and winter, the spatial patterns of LLCF define a cloud-shadow region to the east of the continental divide in the SAM, consistent with cold-season weather patterns. Optical and microphysical properties of LLCF from collocated MODIS and ground ceilometers observations indicate small values of vertically integrated CWP (< 100 g/m$^2$), COT (< 15), and CER (< 15 μm) at cloud top that increases up to 150 μm near the surface at mid-day before rainfall onset based on the observations. The significant vertical stratification of LLCF microphysics and SFI pose a challenge to satellite-based remote sensing of precipitation in mountainous regions. Further, despite high rainfall rates and LWC, this study shows that, the underestimation of low-level enhancement of precipitation induced by the SFI has a physical basis that is explained by collision dynamics with dominant preference for filament breakup when large numbers

of small drops are present, in contrast with microphysics of similar rainfall rates under different rainfall regimes (e.g. deep convection, Figure A1). Thus, the microphysics of SFI pose a critical challenge to radar detection which is further complicated in mountainous regions by ground clutter artifacts (Duan et al., 2015).

The modeling results in this study evaluated the role of SFI in surface precipitation enhancement. However, the dynamic evolution of fog microphysics and fog intermittency are not available in the study region and are not represented in the current model. Future research efforts will focus on incorporating enhanced turbulent collision rate to the collision-coalescence process (Pinsky et al., 2008) in the column model as well as exploring other contributing physical processes including integration with Large-Eddy Simulations (LES) to better represent winds fields. The combination of models and observations can lead toward physically-based representation of LLCF and SFI in remote-sensing retrieval algorithms. Further observations and modeling studies are needed to achieve a comprehensive synthesis for global scale applications.

# 4. Understanding aerosol-cloud interactions in the development of orographic cumulus congestus during IPHEx

Note this chapter appeared as reference (Duan et al., 2017).

## *4.1 Introduction*

Atmospheric aerosols produced by dramatically increased industrialization and urbanization exert a large impact on the climate system and the hydrological cycle (Koren et al., 2008;Ramanathan et al., 2001;Tao et al., 2012). Aerosols influence the earth-atmosphere system primarily via two mechanisms: a radiative (direct) effect and a microphysical (indirect) effect (Rosenfeld et al., 2008). The direct effect on the Earth's energy budget occurs via scattering and absorbing of shortwave and longwave radiation in the atmosphere, hence modulating the net radiation and climate (Haywood and Boucher, 2000;Ramanathan et al., 2001). The indirect effect is related to aerosols as cloud condensation nuclei (CCN) or ice nuclei (IN) that alter microphysical properties and consequently affect cloud radiative properties and precipitation efficiency (Jiang et al., 2008;Lohmann and Feichter, 2005;McFiggans et al., 2006). In particular, an increase in aerosol concentration results in enhanced cloud droplet number concentration (CDNC), smaller average drop size, and increased cloud albedo (Twomey, 1977). Smaller cloud droplets are associated with lower collection and coalescence efficiency, slower drop growth and reduced precipitation, thus leading to longer cloud lifetimes (Albrecht, 1989;Andreae and Rosenfeld, 2008;Khain et al., 2005). Over complex terrain in California

and Israel, Givati and Rosenfeld (2004) attributed a reduction in annual precipitation of 15–25% to air-pollution aerosols from upwind urban areas. Such local effects can translate into large spatial shift in clouds and precipitation in that aerosol-cloud interactions (ACI) inducing suppression of precipitation upwind could give rise to the enhancement of precipitation downwind, thus shifting the spatial distribution of orographic precipitation which can strongly influence the hydrological cycle at local scales as shown by Muhlbauer and Lohmann (2008).

Observations collected over complex terrain during IPHEx (Integrated Precipitation and Hydrology Experiment; Barros et al., 2014) provide a great opportunity to investigate ACI in an orographic context of the Southern Appalachian Mountains (SAM, see Fig. 4-1). Previous research (Wilson and Barros 2014) showed that seeder-feeder interactions among multilayer clouds generally, and between locally initiated or propagating convective clouds and low-level boundary layer clouds in particular, can increase the intensity of rainfall by one order of magnitude in the SAM and explain the observed peak mid-day peak in rainfall. Thus, the ability to predict the evolution of cloud formation and the vertical structure of droplet size distribution (DSD) in this region is of paramount interest.

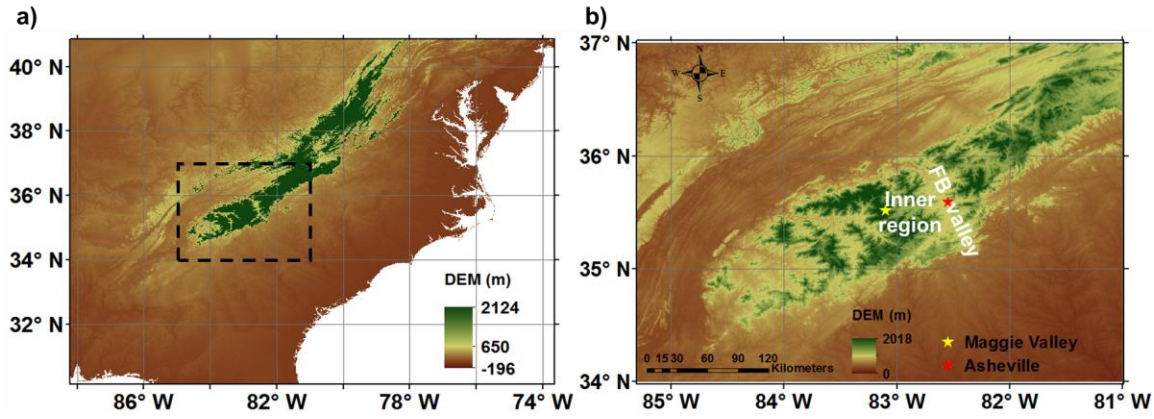


**Figure 4-1: a) Study region of the IPHEx campaign in the SAM (highlighted in the black box), as shown in context of a large scale map of the southeastern United States. (b) Topographic map of the SAM including the two ground-based IPHEx observation sites referred to in this study. FB valley denotes French Broad valley.**

Because of their multiscale nature and complex physics, the representation of physical and chemical processes related to clouds and precipitation in numerical models relies on parameterizations with varying degrees of uncertainties depending on space-time model resolution (Khairoutdinov et al., 2005;Randall et al., 2003). For example, the characteristic time-scale of condensational growth of submicron-size droplets is on the order of 1 ms, and length scales of individual drops range from μm to cm (Pinsky and Khain, 2002), that is a scale gap of five to nine orders in magnitude with respect to the spatial resolution of cloud-resolving models (kms). Although detailed 2-D and 3-D models that explicitly resolve cloud formation and microphysical evolution to varying degrees of completeness have been developed for applications in deep convective clouds including both warm- and ice-phase processes (Fan et al., 2009;Leroy et al., 2009), relatively large time steps and coarse spectral resolution of aerosols and cloud droplets

are employed for computational efficiency, and these processes are highly parameterized. Analysis of high resolution (~ 1 km) numerical weather prediction (NWP) simulations in the SAM for various hydrometeorological regimes using different Weather Research and Forecasting (WRF) physical parameterizations concluded that the prediction of cloud development and cloud vertical microphysical structure are inadequate to capture the spatial and temporal resolution of precipitation rate and precipitation microphysics at the ground (Wilson and Barros, 2015, 2017).

An alternative modelling approach to investigate ACI is the cloud parcel model (CPM) that simulates aerosol activation and cloud droplet growth, as well as thermodynamic adaptation of ascending air parcels at μm and ms scales (Abdul-Razzak et al., 1998;Cooper et al., 1997;Flossmann et al., 1985;Jacobson and Turco, 1995;Kerkweg et al., 2003;Nenes et al., 2001;Pinsky and Khain, 2002;Snider et al., 2003). A synthesis of model formulation including spectral binning strategy, principal physical processes (i.e., condensational growth, collision-coalescence, entrainment), and key aspects of their numerical implementation is presented in Table 4-1 for CPMs frequently referred to in the peer-reviewed literature. In the past, process studies using CPMs targeted principally aerosol-CDNC closure between model simulations and field observations. For example, Conant et al. (2004) conducted an aerosol-cloud droplet number closure study against observations from NASA's Cirrus Regional Study of Tropical Anvils and Cirrus Layers–Florida Area Cirrus Experiment (CRYSTAL-FACE) using the adiabatic CPM by Nenes et

al. (2001;2002) that solves activation and condensation processes only (see Table 4-1 for details). Using a condensation coefficient ($a_c$) value of 0.06, they reported that predicted CDNC was on average within 15% of the observed CDNC in adiabatic cloud regions. Fountoukis et al. (2007) used the same CPM as Conant et al. under extremely polluted conditions during the 2004 International Consortium for Atmospheric Research on Transport and Transformation (ICARTT) experiment. They found that the optimal closure of cloud droplet concentrations was achieved when the condensation coefficient was about 0.06. For marine stratocumulus clouds sampled during the second Aerosol Characterization Experiment (ACE-2), Snider et al. (2003) applied the UWyo parcel model (http://www.atmos.uwyo.edu/~jsnider/parcel/) to simulate condensation processes in adiabatic ascent (see Table 4-1) and experimented with various condensation coefficients in the range of 0.01–0.81. They hypothesized that the lower CDNC overestimation errors (20 to 30% for $a_c$ = 0.1) in their CPM simulations could be mitigated by varying the condensation coefficient as a function of dry particle size instead of using one value for the entire distributions, but did not actually demonstrate this was the case.

**Table 4-1: Cloud parcel models with detailed microphysics from the literature and in this study (Duke CPM). NA denotes information is not described in the reference paper.**

| Parcel model | Binning | Condensation | Coalescence | Entrainment | Numerics |
|---|---|---|---|---|---|
| **Abdul-Razzak et al. (1998)** | Discrete | Leaitch et al. (1986) | Not included | No included | LSODE solver (Hindmarsh, 1983) |
| **Cooper et al. (1997)** | Moving discrete | Fukuta and Walter (1970) | Modified Kovetz and Olund (1969) | Not included | Fifth-order Runge-Kutta (adaptive-size) |
| **Flossmann et al. (1985)** | Discrete | Pruppacher and Klett (1978) | Berry and Reinhardt (1974) | Lateral homogeneous bubble model | NA |
| **Jacobson and Turco (1995)** | Hybrid discrete | Jacobson and Turco (1995) | Jacobson et al. (1994) | Not included | SMVGEAR (Jacobson and Turco, 1994) |
| **Kerkweg et al., (2003)** | Discrete | Pruppacher and Klett (1997) | Bott (2000) | Lateral homogeneous bubble model | NA |
| **Nenes et al. (2001; 2002)** | Moving discrete | Pruppacher and Klett (1997); Seinfeld and Pandis (1998) | Not included | Not included | LSODE solver (Hindmarsh, 1983) |
| **Pinsky and Khain (2002)** | Moving discrete | Pruppacher and Klett (1997) | Bott (1998); turbulent effect on drop collision | Not included | NA |
| **Snider et al. (2003)** | Discrete | Zou and Fukuta (1999) | Not included | Not included | NA |
| ***Duke CPM*** | Moving discrete | Pruppacher and Klett (1997); Seinfeld and Pandis (2006) | Bott (1998); turbulent effect on drop collision | Lateral homogeneous bubble/jet model | Fifth-order Runge-Kutta (adaptive-size) |

The condensation coefficient of water is a key ACI physical parameter in parcel models and has a strong influence on activation and droplet growth by condensation as it expresses the probability that vapour molecules impinge on the water droplet when they strike the air-water interface (McFiggans et al., 2006). Experimental measurements reviewed by Marek and Straub (2001) exhibit a strong inverse relationship between pressure and $a_c$ values ranging from 1000 hPa to 100 hPa and from 0.007 to 0.1, respectively (their Fig. 4). Chodes et al. (1974) measured condensation coefficients in the range of 0.02–0.05 with a mean of 0.033 from measurements of individual droplets grown in a thermal diffusion chamber for four different supersaturations. Ganier et al. (1987) repeated Chodes et al.'s experiments and found that the average condensation coefficient is closer to 0.02 after correcting their supersaturation calculations. Shaw and Lamb (1999) conducted extensive simultaneous measurements of the condensation coefficient and thermal accommodation coefficients ($a_T$) for individual drops in a levitation cell and reported values for $a_c$ and $a_T$ in the ranges of 0.04–0.1 and 0.1–1 with most probable values of 0.06 and 0.7, respectively.

In this study, a new spectral CPM was developed aiming to replicate independently aircraft microphysical observations during IPHEx, which solves explicitly the cloud microphysics of condensation, collision-coalescence, and lateral entrainment processes. The focus of this study is also on the spatial evolution the droplet spectra as a function of height that determines the vertical microstructure of clouds against airborne

observations. Numerical experiments were conducted with the objective of elucidating the quantitative impact on cloud formation at early developments of key ACI modelling parameters (e.g., condensation coefficient, entrainment strength), as well as initial conditions (e.g. aerosol properties, thermodynamic conditions in the atmosphere). Surface aerosol measurements sampled during IPHEx and sounding profiles from WRF simulations were used to initialize the parcel model. Predicted cloud droplet spectra and vertical profiles of thermodynamic variables are evaluated against airborne measurements for a cumulus congestus case-study to elucidate determinant factors in the microphysical evolution of clouds, at early stages in particular. Model sensitivity experiments were conducted to provide insight into possible ranges of major ACI modelling parameters in the SAM, which were not available before or during IPHEx. Multi-parcel simulations were performed to examine the realistic evolution and vertical development of cumulus clouds, which are formed by multiple air parcels rising in succession (Roesner et al., 1990).

The manuscript is organized as follows. The mathematical formulation of the cloud parcel model is briefly described in Sect. 4.2. Section 4.3 presents the IPHEx measurements relevant for the modelling study. In Sect. 4.4, model sensitivity tests against *in situ* observations are conducted focusing on exploring physically-meaningful ranges of key parameters of ACI and identifying major contributors to cloud formation over the complex terrain of the SAM. Results from multi-parcel simulations highlight the

importance of coupled thermodynamics-microphysics to replicate the realistic formation of cumulus clouds. Finally, a discussion of the main findings and a brief outlook of ongoing and future research are presented in Sect. 4.5.

## 4.2 Model description

To investigate the evolution of cloud droplet spectra originating from aerosol distributions of uniform chemical composition, a new cloud parcel model (hereafter DCPM, or Duke CPM for specificity) was developed to explicitly solve key cloud microphysical processes (see the last row of Table 4-1 for details). The model synthesizes well-established theory and physical parameterizations in the literature. In particular, condensation and lateral homogeneous entrainment follow the basic formulations of Pruppacher and Klett (1997) and Seinfeld and Pandis (2006) albeit modified to incorporate the single parameter representation of aerosol hygroscopicity (Petters and Kreidenweis, 2007). The representation of collision-coalescence processes takes into account the variation of collision efficiencies with height (Pinsky et al., 2001), and the effects of turbulence on drop collision efficiency as per Pinsky et al. (2008). The model discretizes the droplet spectra on a finite number of bins (*nbin*) using a discrete geometric volume-size distribution, spanning a large size range with fewer bins and very fine discretization in the small droplet sizes to improve computational efficiency (Kumar and Ramkrishna, 1996;Prat and Barros, 2007b). The characteristic single-particle volumes in adjacent bins are expressed as $v_{i+1} = V_{rat}\, v_i$, where $V_{rat}$ is a constant volume ratio (Jacobson, 2005). When

condensation and coalescence are solved simultaneously, a traditional stationary (time-invariant) grid structure often introduces artificial broadening of the droplet spectrum by reassigning droplets to fixed bins through interpolation, that is numerical diffusion (Cooper et al., 1997;Pinsky and Khain, 2002). To eliminate numerical diffusion artefacts, a moving grid structure is implemented so that an initial size distribution based on a fixed grid discretization can change with time according to the condensational growth. This approach allows particles in each bin to grow by condensation to their exact transient sizes without partitioning between adjacent size bins. Subsequently, collision and coalescence are resolved on the moving bins that evolve from condensation. The DCPM predicts number and volume concentrations of cloud droplets and interstitial aerosols, liquid water content (LWC), effective drop radius, reflectivity and other moments of DSD. It also tracks thermodynamic conditions (e.g., supersaturation, temperature, pressure) of the rising air parcel. The flowchart in Fig. 4-2 graphically describes the key elements and linkages in the parcel model, including microphysical processes, and main inputs and outputs. A detailed description of the formulation of key processes in presented next. A glossary of symbols as well as additional formulae are summarized in Appendix B. The performance of the DCPM was first evaluated by comparing its dependence on different parameters with the results from the numerical simulations reported by Ghan et al. (2011) as shown in Appendix D1.

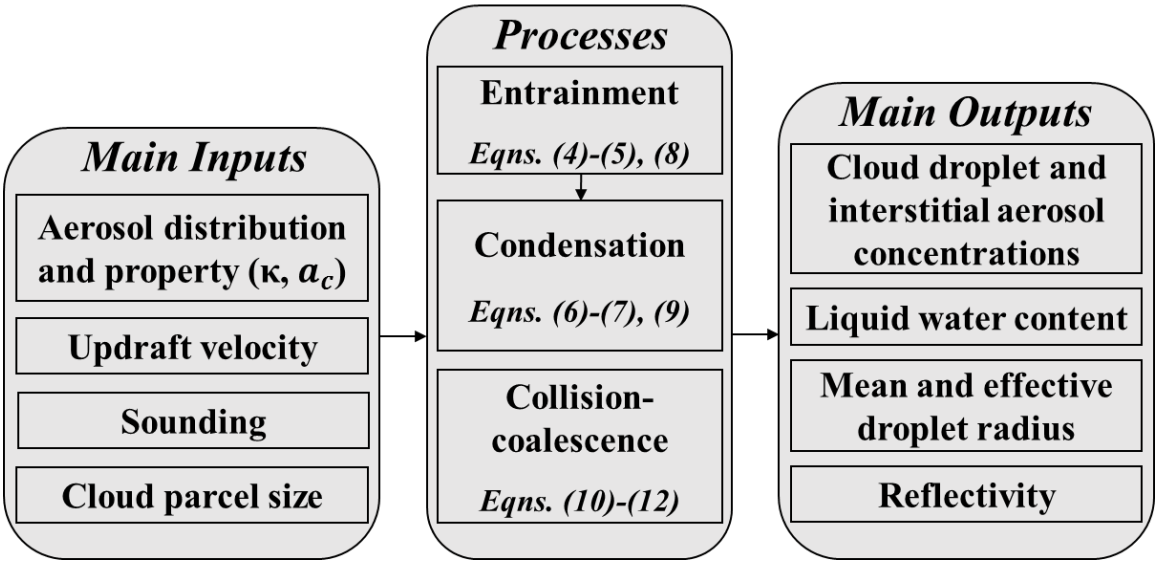


**Figure 4-2: Flowchart of the main inputs, microphysical processes, and main outputs of the DCPM. Equation numbers refer to formulae in Sect. 4.2.**

### 4.2.1 Condensation growth with entrainment

The time variation of the parcel's temperature ($T$) can be written as

$$-\frac{dT}{dt} = \frac{gV}{c_p} + \frac{L}{c_p}\frac{dw_v}{dt} + \mu\left[\frac{L}{c_p}(w_v - w_v{}') + (T - T')\right]V \tag{4-1}$$

where the first two terms on the right-hand side represent adiabatically cooling of a rising parcel and the third term describes the modulation by entraining ambient dry air. The vertical profiles of ambient temperature ($T'$) and water vapour mixing ratio ($w_v'$) can be interpolated from input sounding data from atmospheric model simulations or radiosonde observations.

The change of the water vapour mixing ratio ($w_v$) in the parcel over time is described by

$$\frac{dw_v}{dt} = -\frac{dw_L}{dt} - \mu(w_v - w_v' + w_L)V \tag{4-2}$$

The change of the parcel's velocity ($V$) is given by

$$\frac{dV}{dt} = \frac{g}{1+\gamma}\left(\frac{T-T'}{T'} - w_L\right) - \frac{\mu}{1+\gamma}V^2 \quad (4\text{-}3)$$

where $\gamma \approx 0.5$ to include the effect of induced mass acceleration introduced by Turner (1963).

Due to significant uncertainties and complexities of entrainment and turbulent mixing (Khain et al., 2000), only lateral entrainment that mixes in ambient air instantaneously and is homogeneous in the parcel is considered in the DCPM. Based on observations from McCarthy (1974), the entrainment rate ($\mu$) is represented by an empirical relationship that describes the influx of air and ambient particles into the parcel as varying inversely with cloud radius. To describe the lateral entrainment, the bubble model (Scorer and Ludlam, 1953) and the jet model (Morton, 1957) are both incorporated in the parcel model.

For the bubble model, the change of the radius of a thermal bubble ($R_B$) over time is given as

$$\frac{dlnR_B}{dt} = \frac{1}{3}\left(\mu_B V - \frac{dln\rho_a}{dt}\right) \quad (4\text{-}4)$$

where $\mu_B = C_B/R_B$ and $C_B \approx 0.6$ (McCarthy, 1974).

For the jet model, the time variation of the radius of a jet plume ($R_J$) is expressed by

$$\frac{dlnR_J}{dt} = \frac{1}{2}\left(\mu_J V - \frac{dln\rho_a}{dt} - \frac{dlnV}{dt}\right) \quad (4\text{-}5)$$

where $\mu_J = C_J/R_J$ and $C_J \approx 0.2$ (Squires and Turner, 1962).

The condensational growth rate of droplets in the $i^{th}$ bin ($i = 1, 2, \ldots, nbin$) is represented as

$$\frac{dr_i}{dt} = \frac{G}{r_i}\left(S - S_{eq}\right) \tag{4-6}$$

where droplet growth via condensation is driven by the difference between the ambient supersaturation ($S$) and the droplet equilibrium supersaturation ($S_{eq}$, see Eq. B4 in Appendix B). The growth coefficient (G) depends on the physicochemical properties of aerosols (see Eq. B1 in Appendix B).

Assuming $S \ll 1$, then $(1+S) \approx 1$, thus the time variation of the supersaturation in the parcel can be expressed as

$$\frac{dS}{dt} = \alpha V - \gamma\left(\frac{dw_L}{dt} + \mu V w_L\right) + \mu V\left[\frac{LM_w}{RT^2}(T - T') - \frac{pM_a}{e_s M_w}(w_v - w_v')\right] \tag{4-7}$$

where $\alpha$ and $\gamma$ depend on temperature and pressure (see Eq. B5 and B6 in Appendix B). During the parcel's ascent, entrainment mixes out cloud droplets and interstitial aerosols inside the parcel and brings in dry air and aerosol particles from the environment. Entrained aerosols are exposed to supersaturated conditions in the parcel. Some of them become activated and continuously grow into cloud droplets. The rate of change in droplet number in the $i^{th}$ bin ($i = 1, 2, \ldots, nbin$) due to entrainment is

$$\left(\frac{dN_i}{dt}\right)_{ent} = -\mu V(N_i - N_i') \tag{4-8}$$

where the number concentration of ambient aerosol particles at a certain altitudinal level $N'(z)$ is calculated based on the assumption that the initial aerosol distribution at the

surface $N(0)$ decays exponentially with height: $N'(z)=N(0)exp(-z/H_S)$, where $z$ is the height above ground level (AGL) and $H_S$ is the scale height, depending on aerosol types (Kokhanovsky and de Leeuw, 2009).

The rate of change in liquid water mixing ratio ($w_L$) in the parcel is calculated as follows

$$\frac{dw_L}{dt} = \frac{4\pi\rho_w}{3\rho_a}\sum_{i=1}^{nbin}\left(3N_i r_i^2\frac{dr_i}{dt} + r_i^3\frac{dN_i}{dt}\right) \tag{4-9}$$

### 4.2.2 Collision-coalescence growth

To describe droplet growth by collision-coalescence process, the stochastic collection equation (SCE) that solves for the time rate of change in the number concentration is written following Hu and Srivastava (1995)

$$\frac{\partial N(v)}{\partial t} = \frac{1}{2}\int_0^v N(v-v',t)N(v',t)C(v-v',v')dv' - N(v,t)\int_0^\infty N(v',t)C(v,v')dv' \tag{4-10}$$

where the first integral on the right-hand side of the equation describes the production of droplets of volume $v$ resulting from coalescence of smaller drops, and the second integral accounts for the removal of droplets of volume $v$ due to coalescence with other droplets. The continuous SCE is discretized and numerically solved by a linear flux method as outlined by Bott (1998). This method is mass conservative, introduces minimal numerical diffusion, and is highly computationally efficient (Kerkweg et al., 2003;Pinsky and Khain, 2002). As noted before, the collision-coalescence process is calculated on a moving grid with bins modified by condensational growth at each time step.

For two colliding drops of volume of $v$ and $v'$, the coalescence kernel $C(v, v')$ in Eq. (4-10) is computed as the product of the gravitational collision kernel $K(v, v')$ and the coalescence efficiency $E_{coal}(v, v')$,

$$C(v, v') = K(v, v')E_{coal}(v, v') \tag{4-11}$$

$$K(v, v') = (9\pi/16)^{1/3}\left(v^{1/3} + v'^{1/3}\right)^2|V - V'|E_{coll}(v, v') \tag{4-12}$$

where $V$ $(V')$ is the terminal velocity of drop volume $v$ $(v')$ and $E_{coll}$ $(v, v')$ is the corresponding collision efficiency.

The terminal velocity of cloud drops is estimated following Beard (1976) in three ranges of the particle diameter (0.5 μm–19 μm, 19 μm–1.07 mm, 1.07 mm–7 mm). Another approximation by Best (1950) is also available as an option in the model. The table of drop-drop collision efficiencies at 1-μm resolution developed by Pinsky at al. (2001) is used for $E_{coll}$. This table was created based on simulations of hydrodynamic droplet interactions over a broad range of droplet radii (1–300 μm), including collisions among small cloud droplets as well as between small cloud droplets and small raindrops. Moreover, $E_{coll}$ was derived at three pressure levels of 1,000-, 750-, and 500-mb and can be interpolated at each level of a rising cloud parcel, thus taking the increase of $E_{coll}$ with height into account. Turbulence can significantly enhance collision rates especially for small droplets (below 10 μm in radii) as it increases swept volumes and collision efficiencies, and influences the collision kernels and droplet clustering (Khain and Pinsky, 1997;Pinsky et al., 1999;Pinsky et al., 2000). Considering different turbulent intensities for typical stratiform, cumulus,

and cumulonimbus clouds, detailed tables of collision kernels and efficiencies in turbulent flow, created by Pinsky et al. (2008) for cloud droplets with radii below 21 μm, are also incorporated in the model. $E_{coal}$ is parameterized following Seifert et al. (2005), who applied Beard and Ochs (1995) for small raindrops ($d_s < 300$ μm), Low and List (1982) for large raindrops ($d_s > 600$ μm), and used an interpolation formula for intermediate drops (300 μm < $d_s$ < 600 μm) where $d_s$ is the diameter of the small droplet. A simpler and faster option suggested by Beard and Ochs (1984) is also available in the model.

### 4.2.3 Numerical formulation

The equations in Sect. 4.2.1 constitute a stiff system of non-linear, first-order ordinary differential equations and involve state variables at very different scales. For the numerical integration of condensation growth, a fifth-order Runge-Kutta scheme with Cash-Karp parameters (Cash and Karp, 1990) using adaptive time steps (Press et al., 2007) is employed. At each time step, the error is estimated using the fourth-order and the fifth-order Runge-Kutta methods. Because dependent variables differ by several orders of magnitude, a fractional error (ε) is defined to scale the error estimate by the magnitude of each variable. Specifically, the step size is adaptively selected to satisfy a fractional tolerance of $10^{-7}$ for all variables. The initial time step to calculate condensational growth is $5\times10^{-4}$ s. The maximum time step is set as $10^{-3}$ s to ensure the diffusional growth of drops is precisely simulated and non-activated particles reach equilibrium with the parcel supersaturation at each time step. For the collision-coalescence processes in Sect. 4.2.2, a

simple Euler method is applied to integrate forward in time. A time increment of 0.2 s is chosen to assure that the available mass in each bin is much larger than the change of mass in the bin during the redistribution of the mass at one time step. Relying on separate numerical integration methods for calculating condensation and collision-coalescence allows us to either include or exclude each process easily to examine its role individually in cloud formation.

## *4.3 IPHEx observations*

The intense observing period (IOP) of the IPHEx field campaign took place during 01 May–15 June, 2014. The study region was centred on the SAM extending to the nearby Piedmont and Coastal Plain regions of North Carolina (see maps in Fig. 4-1). IPHEx was one of the ground validation campaigns after the launch of NASA's Global Precipitation Mission (GPM) core satellite, and details about this campaign can be found in the science plan (Barros et al. 2014). During the IPHEx IOP, measurements of aerosol concentrations and size distributions ranging from 0.01 to 10 μm were collected at the ground level. Collocated with aerosol instruments, the ACHIEVE (Aerosol-Cloud-Humidity Interaction Exploring & Validating Enterprise) platform was also deployed, equipped with W-band (94 GHz) and X-band (10.4 GHz) radars, a ceilometer, and a microwave radiometer. Two aircraft were dedicated to the IPHEx campaign. The NASA ER-2 carried multi-frequency radars (e.g., a dual-frequency Ka-/Ku-, W-, X-band) and radiometers, and functioned as the GPM core-satellite sampling simulator from high altitude. The University of North

Dakota (UND) Citation aircraft was instrumented to characterize the microphysics and dynamical properties of clouds, including LWC and DSDs from cloud to rainfall drop sizes. Therefore, this data set offers a great opportunity to perform modelling studies of warm season cloud formation in complex terrain. A detailed description of the specific measurements relevant to this study is provided below.

### 4.3.1 Surface measurements

Aerosol observations were carried out at the Maggie Valley (MV) supersite (marked as the yellow star in Fig. 1b) in the inner mountain region during the IPHEx IOP. The elevation of the MV site is 925 m mean sea level (MSL). This data set provides a clear characterization of the size distribution and hygroscopicity of surface aerosols in this inner mountain valley, which was not available previously. Nominal dry aerosol size distributions at the surface were measured by a scanning mobility particle counter system (SMPS) for particles from 0.01 to 0.5 μm in diameter, and a passive cavity aerosol spectrometer (PCASP; manufactured by Droplet Measurement Technologies, Inc., Boulder, CO, USA) for particle diameters in the size range of 0.1–10 μm. The SMPS consists of an electrostatic classifier (TSI Inc. 3081) and a condensation particle counter (CPC, TSI 3771). Note that the relative humidity (RH) of the differential mobility analyser (DMA) column is well controlled and the average RH (± one standard deviation) of the sheath and sample flows are 2.0±0.8% and 3.2±0.5%, respectively. In addition, a co-located ambient CPC (TSI 3772), which measures aerosol particles greater than 10 nm without

resolving their size distributions, shows very close agreement with the SMPS measurements with regard to total number concentrations of aerosol particles ($N_{CN}$). Size-resolved CCN concentrations ($N_{CCN}$) were sampled by a single column CCN counter (manufactured by Droplet Measurement Technologies, Inc., Boulder, CO, USA) that was operated in parallel to the SMPS-CPC. The CCN instrument cycles through 6 levels of supersaturation (S) in the range of 0.09–0.51%. At a given S level, each CCN measurement cycle took approximately 8 min, corresponding to one SMPS-scan and buffer time to adjust supersaturation. On average 178 measurement cycles were collected daily during the IPHEx IOP, except for occasional interruptions due to instrument maintenance. CN and CCN distributions were inverted as described previously (Nguyen et al., 2014;Petters and Petters, 2016). Supersaturation was calibrated using dried ammonium sulfate and a water activity model (Christensen and Petters, 2012;Petters and Petters, 2016). The midpoint activation diameter ($D_{50}$) is derived from the inverted CN and CCN distributions (Petters et al., 2009). The hygroscopicity parameter ($\kappa$) is obtained from $D_{50}$ and instrument supersaturation (Petters and Kreidenweis, 2007). In addition, a co-located Vaisala weather station (WXT520) was continuously recording local meteorological conditions (e.g., wind speed, wind direction, relative humidity, temperature, and pressure) at 1-s interval. Diurnal cycles of these local meteorological variables during the IPHEx IOP are displayed in Fig. D7. The average meteorological conditions at the sampling site are 0.8±0.6 m $s^{-1}$ in wind speed, 172±115° in wind direction, 77±18% in

relative humidity, 19±4 °C in ambient temperature (arithmetic mean ± one standard deviation).

Figure 4-3 presents a general overview of the temporal variability in aerosol size distributions and total number concentrations from the SMPS and PCASP, respectively during the entire sampling period. To avoid episodic intrusion of long-range transport or local pollution, aerosol measurements with $N_{CN,SMPS} > 10{,}000$ cm$^{-3}$ were removed from the analysis in order to isolate inherent properties of aerosol particles in the pristine forest environment of the SAM. The average total number concentration (± one standard deviation) of dry aerosol particles with diameters between 0.01 to 0.5 μm is 2,487±1,239 cm$^{-3}$, as sampled by the SMPS during the campaign (see Figs. 4-3a and b). Strong local fluctuations in number concentrations, in particular around midnight, are due to the presence of Aitken mode particles as indicated in Fig. 4-3a. These sharp increases in small particles are likely produced by the power engine in the Maggie Valley Sanitary District adjacent to the sampling site. The average total number concentration (± one standard deviation) of dry aerosol particles in accumulation and coarse modes (0.1–10 μm in diameter) is 1,106±427 cm$^{-3}$ as sampled by the PCASP during the campaign (see Figs. 4-3c and d). As expected, large particles from the PCASP show a much lower temporal variability in number concentrations as compared to small particles from the SMPS. Similarly, their diurnal cycles (see Figs. D8a and b) exhibit relatively large temporal variations in $N_{CN,SMPS}$ while $N_{CN,PCASP}$ remain relatively stable throughout the day. Rainfall

occurrences result in steep decreases in aerosol number concentrations, as shown in Figs. 4-3b and d.

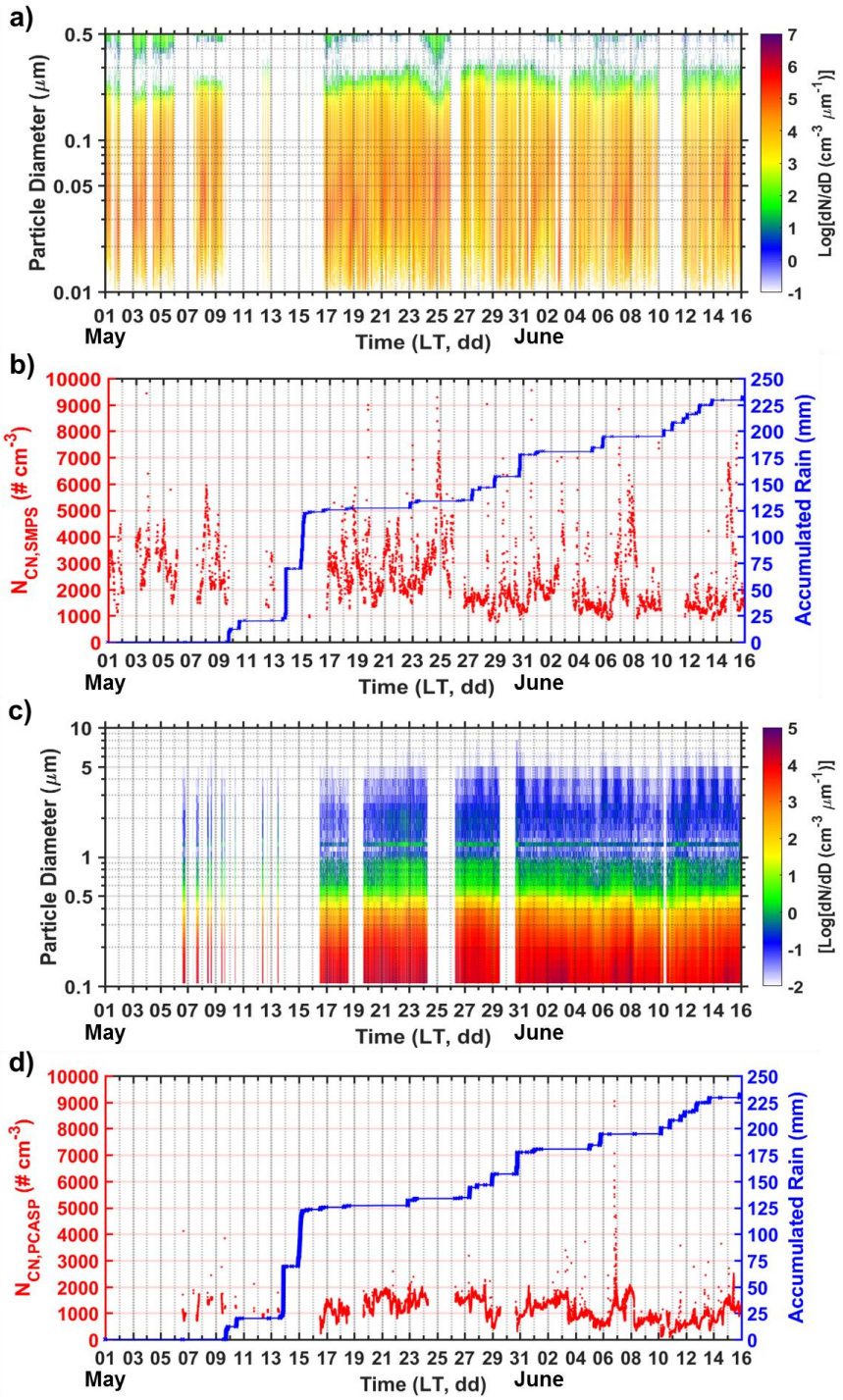

**Figure 4-3: Time series of dry aerosol size distribution and total number concentration ($N_{CN}$) from the SMPS (a, b) and PCASP (c, d), respectively, measured at MV during the IPHEx IOP. Discontinuities in the data are associated with delayed installation (PCASP), rainfall occurrences, and occasional instrument malfunction.**

As discussed before, κ and $N_{CCN}$ were derived at six different supersaturation levels. In this study, we only show measurements collected at relatively high supersaturations (0.19–0.51%) as poor fits to $D_{50}$ are often resulted due to low number concentration at S = 0.09% and 0.12% and thus no kappa value was reported. Figure 4-4 shows that both κ and $N_{CCN}$ exhibit large temporal variabilities during the campaign. In Fig. 4-4a, the average value of κ (± one standard deviation) is 0.28±0.09 at S = 0.19%, 0.22±0.08 at S = 0.38%, 0.18±0.07 at S = 0.51%. In spite of local fluctuations in κ at each supersaturation level, larger κ values are generally obtained at lower supersaturation (Fig. 4-4a). A higher value of κ is derived from a larger $D_{50}$ due to the fact that only large particles can be activated at a low supersaturation. Therefore, aerosol particles of different sizes are characterized with different hygroscopic properties. This is consistent with the finding from an earlier study in the Amazon rainforest showing that accumulation mode particles are more hygroscopic than Aiken mode particles (Gunthe et al., 2009). Note that the average κ values at each supersaturation level are comparable to subsaturated κ (0.14–0.46) measured in the southeastern United States (Nguyen et al., 2014) and the approximate global average (κ ~ 0.3) for continental aerosols (Andreae and Rosenfeld, 2008). At this surface site, the average $N_{CCN}$ (± one standard deviation) is 569±208 $cm^{-3}$ at S = 0.19%, 1,022±387 $cm^{-3}$ at S = 0.38%, 1,210±505 $cm^{-3}$ at S = 0.51% (see Fig. 4-4b). The

diurnal cycles in Fig. D8d indicate that $N_{CCN}$ at S = 0.19% is remarkably stable while $N_{CCN}$ at higher supersaturations (0.38% and 0.51%) exhibit pronounced variations throughout the day, likely linked to the changes in small particle concentrations (see Fig. D8a). In general, no evident diurnal cycles in κ and $N_{CCN}$ are noted from the observations in Figs. D8c and d.

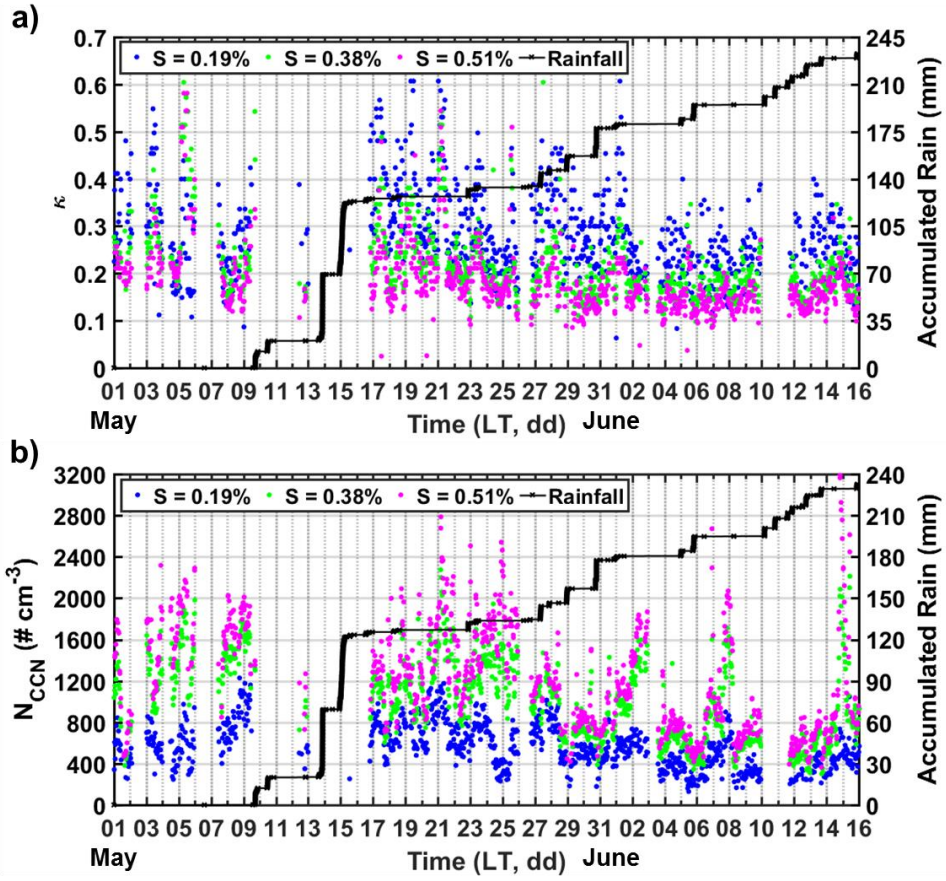


**Figure 4-4: Time series of hygroscopicity parameter (κ, a) and CCN concentration ($N_{CCN}$, b) at three supersaturation levels, measured at MV during the IPHEx IOP. Discontinuities in the data are associated with rainfall occurrences and occasional instrument malfunction.**

### 4.3.2 Aircraft measurements

Airborne observations from the UND Citation, equipped with meteorological (e.g., temperature, pressure, humidity) sensors and microphysical instruments, are used in this study (Poellot, 2015). Vertical velocity was obtained from a gust probe and bulk LWC values were retrieved from two hot-wire probes (a King-type probe and a Nevzorov probe). Size-resolved concentrations were measured from three optical probes, covering droplet diameter from 50 μm to 3 cm: a PMS two-dimensional cloud probe (2D-C), a SPEC two-dimensional stereo probe (2D-S), and a SPEC high volume precipitation spectrometer 3 probe (HVPS-3). The cloud droplet probe (CDP) measures cloud drop concentrations and size distributions for small particles with diameters from 2 to 50 μm in 30 bin sizes. The droplet sizes are determined by measuring the forward scattering intensity when droplets transit the sample area of the CDP. Coincidence errors have been found to cause measurement artefacts, which tend to underestimate droplet concentrations and broaden droplet spectra. This type of error occurs when two or more droplets pass through the CDP laser beam simultaneously, and is highly dependent on droplet concentrations (Lance et al., 2010).

Bulk LWC measurements from hot-wire probes can serve as independent observations to identify and correct coincidence-related sizing errors in the CDP. For example, during the flight on 12 June 2014, bulk LWC values from the King and Nevzorov probes are used to evaluate the CDP-derived LWC integrated from its droplet size

distribution (see Eq. B7 in Appendix B). In this study, bulk LWC data with air temperature greater than 0 °C are considered in order to eliminate erroneous attribution of ice- or mix-phase particles to liquid water by hot-wire probes. In Fig. 4-5a, we can notice that CDP LWC produces a positive bias compared to LWC from the two hot-wire probes, whereas the King and Nevzorov probes demonstrate general agreement with each other. The CDP instrument aboard the UND Citation was modified by adding an optical mask, which has been proven to resolve the underestimation of droplet concentrations (Delene, 2016;Lance, 2012). Herein, we assume that the bias in CDP LWC is caused by the oversizing error rather than the undercounting error. Thus, we applied a correction to the CDP size distributions, as introduced by Painemal and Zuidema (2011). This bias can be removed based on the linear correlation revealed by the comparison between the King- and CDP-LWC using data collected during the first horizontal leg of the 12 June flight (see Fig. 4-5b). In the correction procedure, King LWC data between 0.05 and 0.6 g $m^{-3}$ are taken into account. Thus, a linear regression with coefficient of determination $R^2$ = 0.80 is fitted between the CDP- and King-LWC and the derived slope (= 1.26 as denoted in Fig. 4-5b) is used to adjust CDP droplet size distributions. The modified droplet size in each bin is calculated by dividing the original size by $1.26^{1/3}$ (~ 1.08) to attain consistent LWC between the CDP and the King probe. The corrected droplet size distributions slightly shift the measured spectra to smaller drop sizes (not shown here), thus providing confidence in the performance of the CDP probe during the campaign.

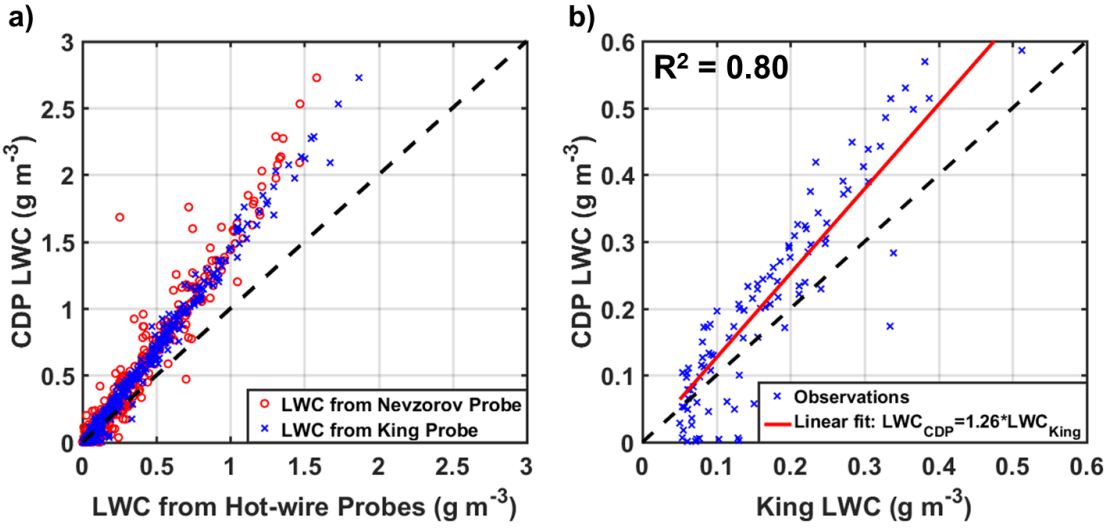


**Figure 4-5: a) Scatterplot for for LWC from the CDP and two hot-wire probes (the King and Nevzorov probes), sampled during the 12 June flight. b) LWC observations from the CDP and the King probe during the first horizontal cloud transect on the same day are fitted by a linear regression (represented by the red line) with coefficient of determination $R^2 = 0.80$.**

### 4.3.3 Cumulus congestus case-study

On 12 June 2014, the W-band radar observations at MV (see Fig. D9) indicate the formation of cumulus congestus clouds before 12:30 local time (LT) and further growth into cumulonimbus clouds. Near the MV site, a coordinated aircraft mission of both the UND Citation and NASR ER-2 was conducted from 12:14 to 15:51 LT on 12 June. Cloud droplet concentrations and size distributions were sampled by conducting successively higher constant-altitude flight transects through clouds. Droplet spectra were sampled at 1-Hz resolution (corresponding to approximately 90 m in flight distance) by the CDP and coincidence errors were taken into account by applying the correction as described in Sect. 4.3.2. In particular, the lowest horizontal leg (see the flight track in Fig. 4-6a, altitude

around 2,770–2,800 m MSL) through the cloud is investigated to avoid the influence of substantial mixing in the upper portion of the cloud, which is not treated in the DCPM currently. In rising updrafts, in-cloud samples (white plus signs in Fig. 4-6a) are defined with a minimum LWC of 0.25 g $m^{-3}$ from the CDP. Along the first leg, three cloudy regions are identified near the eastern ridges (ER, highlighted in the blue dashed box), over the inner valley region (IC, highlighted by the blue circle), and near the Eastern Cherokee Reservation (ECR, highlighted in the blue dashed box).

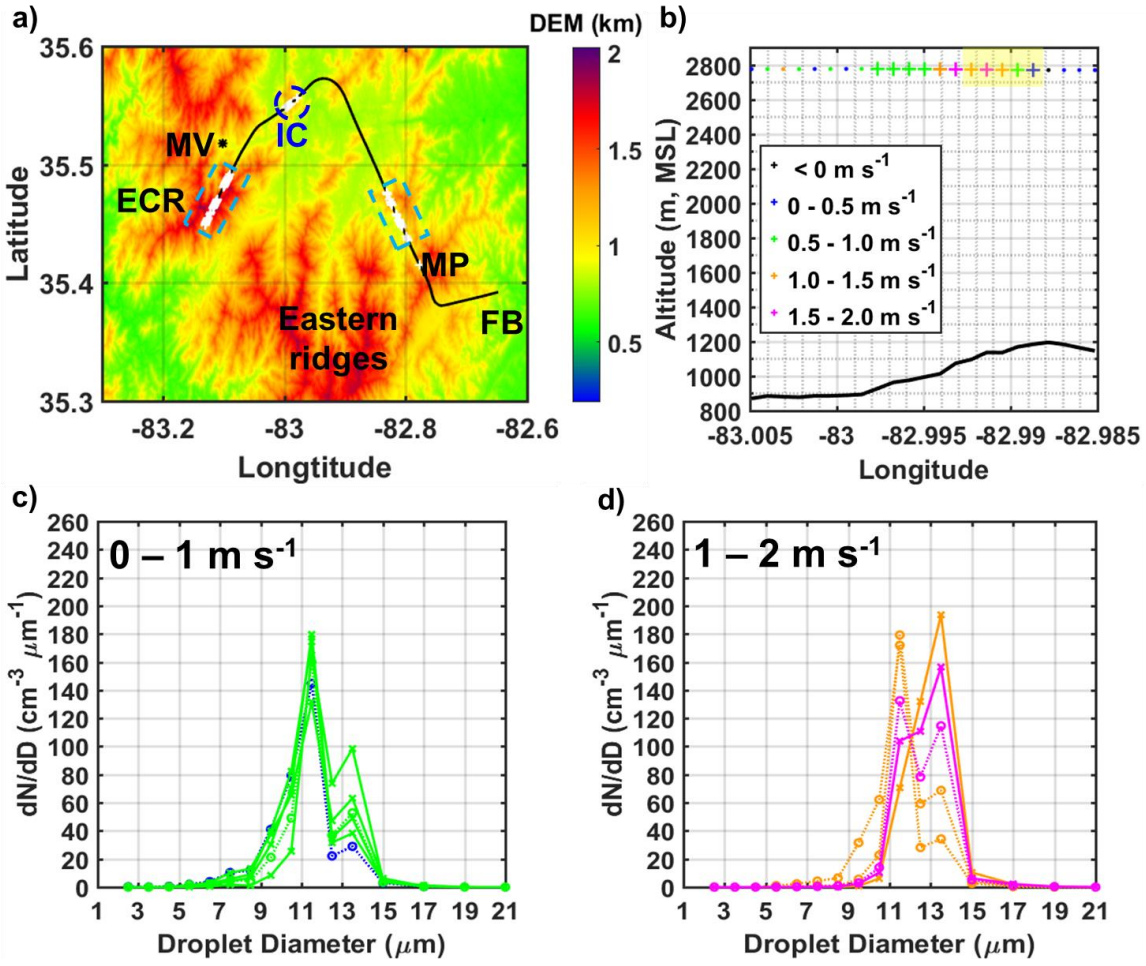

**Figure 4-6: a) Lowest cloud transect of the UND Citation flight track on 12 June 2014. The in-cloud observations are identified as white plus signs, and MV is marked by the black asterisk. For left to right in the map, ECR denotes Eastern Cherokee reservation, MP denotes Mount Pisgah, and FB denotes French Board valley. b) Velocity variations of the targeted in-cloud region, denoted by IC in (a). Coloured plus signs indicate updraft velocities of the in-cloud samples, collected at 1-Hz (~ 90 m in flight distance) resolution. Cloud droplet concentrations of the in-cloud samples in IC (b) with low (0–1 m s-1) and high (1–2 m s-1) updrafts are shown in (c) and (d), respectively. The updraft velocity of each sample is indicated by its colour, referring to the range in the legend of (b). Dotted lines with circle markers represent the droplet spectra in the reference sub-region within IC, as shaded in (b).**

In these cloudy regions, strong updrafts, and higher values of cloud drop numbers and LWC from the CDP are evident as shown in Fig. 4-7. The drop number concentrations from the 2-DC probe (measuring hydrometeors with diameter between 105 μm and 2 mm) indicate negligible amount of precipitation-sized drops in these cloudy regions (Fig. 4-7d), indicating the sampling of cumulus congestus clouds development by the aircraft. To further eliminate regions influenced by mixing and other unresolved mechanisms, cloud segments to perform the modelling study are carefully selected by screening the cloud droplet spectra observed by the CDP. Following criteria 2 and 3 listed in Conant et al. (2004), measurements with effective droplet diameter greater than 2.4 μm and geometric standard deviation less than 1.5 are used in the analysis. During the first cloud transect, only one in-cloud region (IC, circled in Fig. 4-6a) satisfies Conant et al.'s requirements with 11 cloudy samples collected over approximately 1 km flight distance (plus signs in Fig. 4-6b). Significant topographic heterogeneity (see terrain transect in Fig. 4-6b) can exert a considerable influence on cloud formation across this region. As shown in Figs. 4-6c and

d, a pronounced variability in drop number distributions is manifest in the in-cloud samples clustered by low (0–1 m $s^{-1}$) and high (1–2 m $s^{-1}$) updrafts. As expected, the droplet spectra in stronger updrafts at the core (see Fig. 4-6d) have higher number concentrations and narrower size range compared to the samples at the edge of the cloud (see Fig. 4-6c). Observed variations in vertical velocities and droplet number concentrations in complex terrain are indicative of challenges in the application of parcel models as homogeneity is assumed for aerosol concentrations below cloud base and within the microstructure of the air parcel.

Moreover, droplet spectra measured within updraft core of two other cloudy regions in the inner SAM (highlighted in dashed light blue boxes in Fig. 4-6a) as well as IC are shown in the top panel of Fig. 4-8. Fig. 4-8d displays the background aerosol concentrations measured by the CPC (lower cut-off diameter 10 nm) aboard the UND Citation along the complex terrain of the SAM (elevation along the flight transect is indicated by the black line) during the first horizontal leg (see flight track in Fig. 4-6a). From east to west (flight direction as indicated by the blue arrow), it is noticeable that the three cloud regions (shaded in Fig. 4-8d) are linked to considerable drops in the aerosol concentrations. In particular, clouds form over the foothills of the eastern ridges (ER, see location in Fig. 4-6a) in the inner region are associated with low-level moisture convergence from the east (Wilson and Barros, 2017). The cloud core sampled in this convergence zone is formed in intense updrafts (~ 8 m $s^{-1}$, see Fig. 4-8c) and it exhibits

wide droplet spectra with heavier tails (larger drops) than the observations in the IC core (updrafts ~ 1–2 m $s^{-1}$, see Fig. 4-8b). The in-cloud samples over high terrain elevations near the ECR (see location in Fig. 4-6a) also exhibit wide spectra but smaller number concentrations due to the formation of drizzle in clouds (Fig. 4-7d). As noted in Fig. 4-8d, significant increases (~ 1,000 $cm^{-3}$) in aerosol number concentrations are evident when the aircraft flew from the French Board (FB) valley into the inner SAM region that includes the Pisgah National Forest and the Great Smoky Mountains National Park (Figs. 4-1b and 4-7a). Generally, there is a close agreement between salient topographic features and variations in aerosol number concentrations. As size distributions are not resolved in the CPC measurements, we resort to the surface sampling of aerosol concentrations at MV (indicated by the dashed vertical line in Fig. 4-8d and marked as the black asterisk in Fig. 4-6a) as the input for modelling study at IC. Moderate vertical velocities measured in IC region (Fig. 4-6b) and analysis of the radar profiles at MV (Fig. 4-6) suggest that the early development phase of the cumulus congestus observed in the inner SAM was sampled by the aircraft on June 12 during IPHEx.

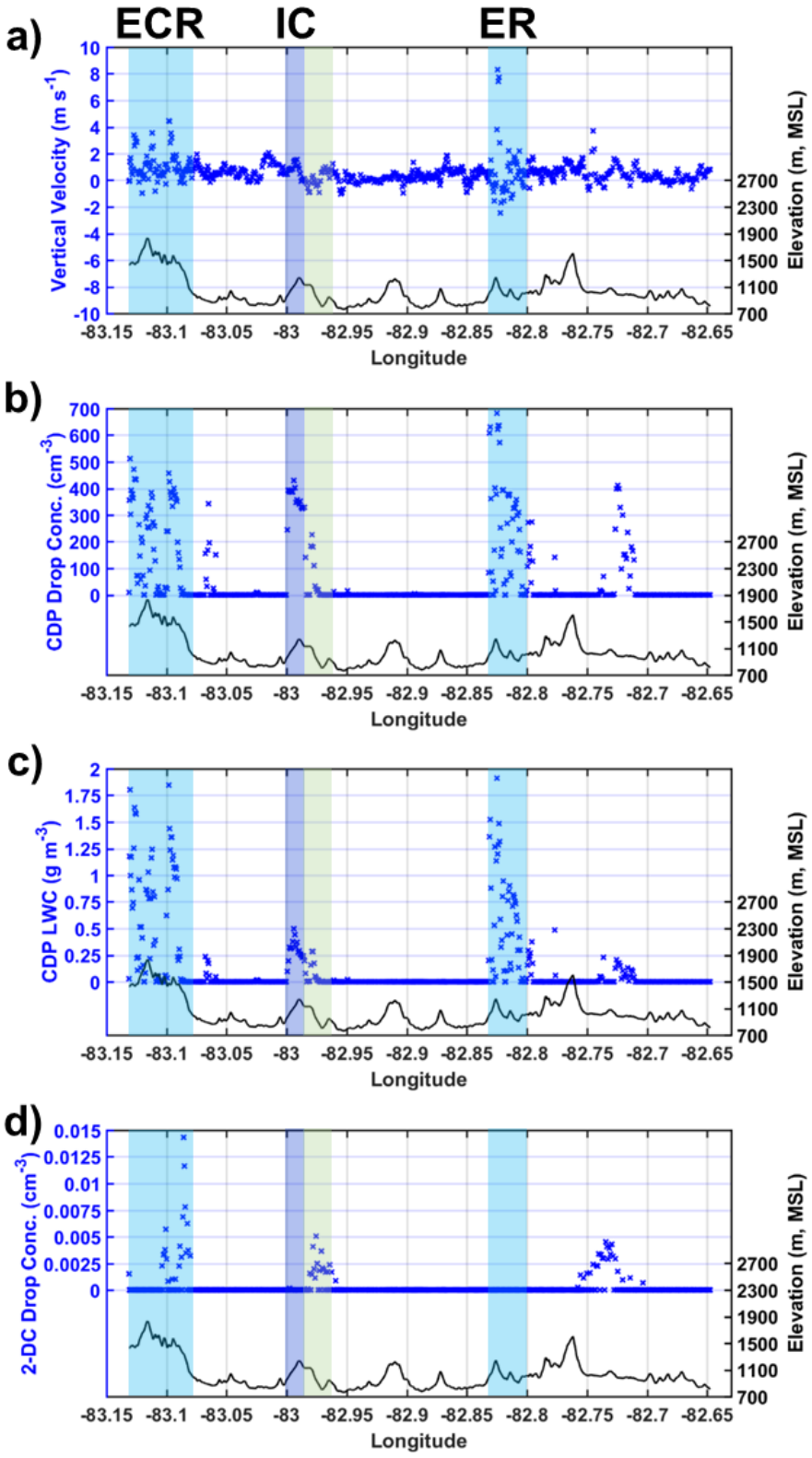
a)
ECR
IC
ER
Vertical Velocity (m s-1)
10
8
6
4
2
0
-2
-4
-6
-8
-10
-83.15 -83.1 -83.05 -83 -82.95 -82.9 -82.85 -82.8 -82.75 -82.7 -82.65
Longitude
Elevation (m, MSL)
2700
2300
1900
1500
1100
700
b)
CDP Drop Conc. (cm-3)
700
600
500
400
300
200
100
0
Longitude
Elevation (m, MSL)
c)
CDP LWC (g m-3)
2
1.75
1.5
1.25
1
0.75
0.5
0.25
0
Longitude
Elevation (m, MSL)
d)
2-DC Drop Conc. (cm-3)
0.015
0.0125
0.01
0.0075
0.005
0.0025
0
Longitude
Elevation (m, MSL)

**Figure 4-7: Airborne observations of vertical velocity (a), drop concentrations (b) and LWC (c) from the CDP, and drop concentrations from 2-DC probe (d) abroad the UND Citation during the first horizontal leg (see flight track in Fig. 4-6a). The blue shaded areas correspond to three cloudy regions (from left to right: ECR-Eastern Cherokee reservation, IC-targeted in-cloud region, and ER-eastern ridges), as highlighted in the dark blue circle and light blue boxes in Fig. 6a. The terrain elevation is represented by the black line.**

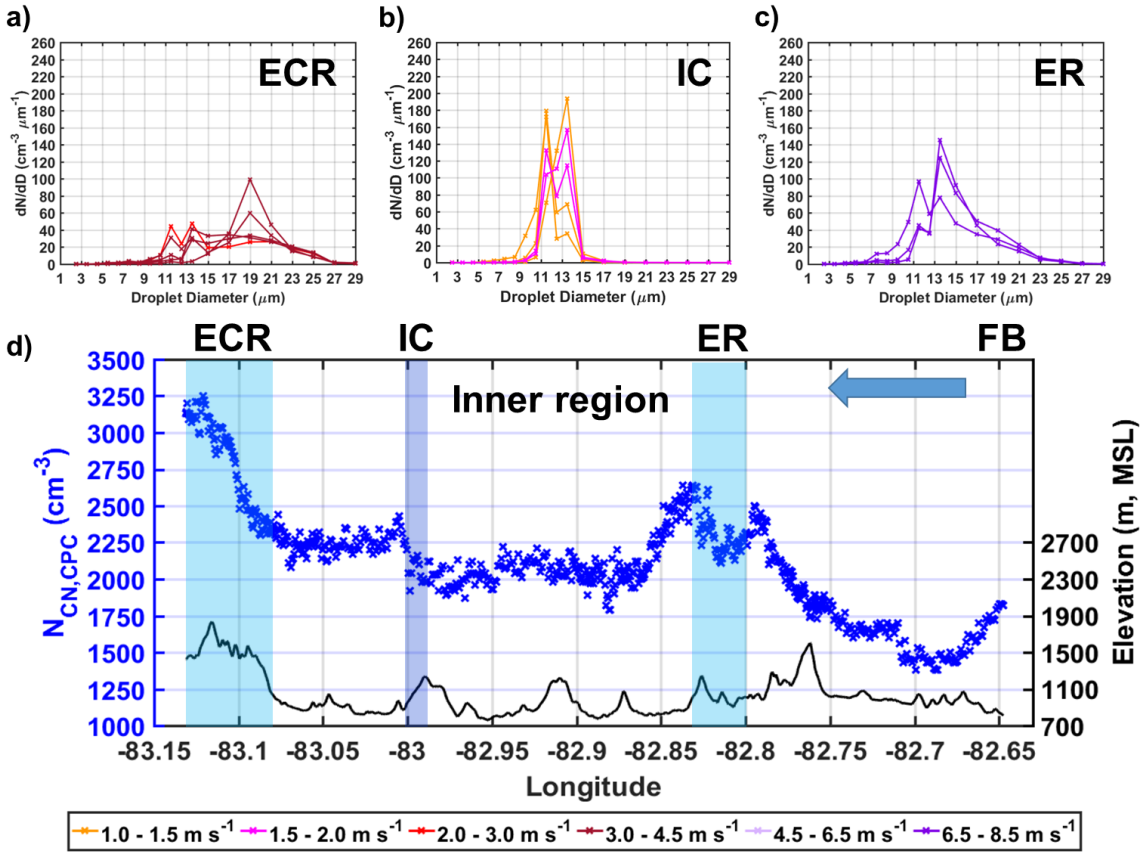


**Figure 4-8: Cloud droplet concentrations at the updraft core of clouds near the Eastern Cherokee reservation (ECR, a), within the targeted in-cloud region (IC, b), and near the foothills of the eastern ridges (ER) over the inner region (c), respectively. Their locations can be referred to Fig. 4-6a. The updraft velocity of each sample is denoted by its colour. d) Background aerosol concentrations from the CPC abroad the UND Citation during the first horizontal leg (see flight track in Fig. 4-6a, and the flight direction is indicated by the blue arrow here). The blue shaded areas correspond to cloudy regions in (a)–(c), also as highlighted in the dark blue circle and light blue boxes in Fig. 4-6a. The terrain elevation is represented by the black line and FB denotes French Board valley.**

## *4.4 Modelling experiments*

### 4.4.1 Model initialization and reference simulation

Dry aerosol concentrations measured by the SMPS and PCASP at MV were averaged over the first 10 mins (averaging interval: 12:14 LT–12:24 LT) of the 12 June flight, and then merged into a single size distribution as shown in Fig. 4-9. The combined aerosol distribution at the surface is fitted by the superimposition of four lognormal functions using least-squares minimization. Table 4-2 summarizes parameters (total number concentration, geometric mean diameter, and geometric standard deviation) that characterize the four lognormal distributions. We can notice that aerosol number concentrations below 0.03 μm are greatly underestimated by the fitted cumulative distribution (cyan curve in Fig. 4-9). These particles in such small sizes mostly remain non-activated under the supersaturated condition typical of the atmosphere, thus, underestimation of their concentrations does not significantly affect our modelling results of cloud formation. At the cloud base of IC, aerosol size distributions are estimated by assuming that total number concentrations at the surface decay exponentially with a scale height ($H_s$) of 1,000 m, and geometric mean diameters and corresponding geometric standard deviations remain constant with height. The dry aerosol distribution at cloud base is calculated as the sum of four lognormal distributions with fitted parameters indicated in the last three columns of Table 4-2 and is taken as initial input to the model. The aerosol distribution is discretized into 1,000 bins, covering the size range of 0.01–10

μm. The bins are spaced geometrically with a volume ratio of 1.026. The bin grid at such a high resolution is sufficient to precisely simulate the partitioning of growing droplets and interstitial aerosols in the parcel. It is also assumed that the aerosol is internally mixed so that the hygroscopicity does not vary with particle size. Thus, we prescribe a κ value of 0.14 for each aerosol bin, deriving from the average κ during the first 10 mins of the 12 June flight.

**Table 4-2: Lognormal fit parameters characterizing the aerosol number distribution of four modes. Note N = total number of aerosol particles per cm³; Dg = geometric mean diameter (μm); $\sigma_g$ = geometric standard deviation for each mode. $N_{surf}$ and $N_{CBH}$ represent total aerosol number concentrations at the surface and cloud base height (CBH: 1,270 m), respectively.**

| Mode # | $N_{surf}$ ($cm^{-3}$) | $N_{CBH}$ ($cm^{-3}$) | $D_g$ (μm) | $\sigma_g$ |
|---|---|---|---|---|
| **1** | 1401.9 | 393.7 | 0.076 | 1.63 |
| **2** | 415.7 | 116.8 | 0.195 | 1.35 |
| **3** | 0.3 | 0.084 | 0.75 | 1.3 |
| **4** | 0.3 | 0.084 | 2.2 | 1.4 |

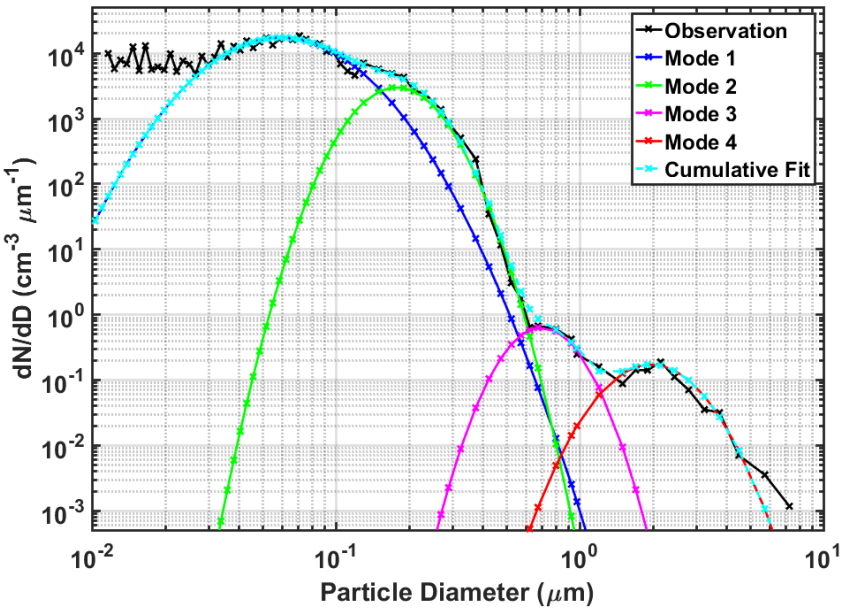

**Figure 4-9: Mean surface aerosol size distribution fitted by four lognormal functions. Observations are merged from the SMPS and PCASP, and are averaged during the first 10 mins (12:14 LT – 12:24 LT) of the 12 June flight. Fitted parameters (total number concentration, geometric mean diameter, and geometric standard deviation) for each mode are summarized in Table 4-2.**

During the IPHEx IOP, daytime radiosondes were launched every 3-hour at Asheville, NC (see the red star in Fig. 4-1b). Not only is this location very far away from the targeted cloudy region (IC), but the timing of the sounding (11 LT) is also much earlier than the flight take-off on 12 June 2014. At 11 LT, the sounding at Asheville shows a relatively dry atmosphere especially at low levels (not shown here). In this study, we resort to high-resolution WRF model simulations to provide vertical profiles of air temperature, RH, and pressure as sounding input to the parcel model. Detailed domain configuration of the WRF simulation (see Fig. 4-10a) can be found in Appendix D2. WRF-simulated sounding columns from the grid cells (0.25-km resolution) in the IC region (highlighted in Fig. 4-6a) are averaged to estimate vertical profiles of ambient temperature and RH for the case-study as shown in Fig. 4-10b. The cloud base height (CBH) is chosen as the level where simulated RH is approximately 100%. As marked by the horizontal black line in Fig. 4-10b, CBH = 1,270 m AGL at 12:15 LT when the parcel is released from cloud base. The temperature excess of the air parcel over the environment is initialized as 1.0 K, and the initial pressure and RH of the parcel at cloud base adapt to cloud surroundings. As vertical velocities were not sampled at cloud base, the initial updraft velocity ($V_0$) is assumed to be uniformly distributed and equal to 0.5 m $s^{-1}$, consistent with

vertical velocities observed by the W-band radar (see Fig. D9b) around the same altitude (2.5 km MSL). Therefore, the air parcel is launched at cloud base with an initial parcel radius (R) of 500 m, an initial updraft of 0.5 m $s^{-1}$, and initial aerosol particles that are in equilibrium with the humid air at cloud base. When the parcel is rising, the lateral entrainment is treated as the bubble model parameterization with the characteristic length scale R = 500 m (see Eq. 4-4 in Sect. 4.2.1). Ambient aerosol particles penetrate through lateral parcel boundaries and their number concentrations also decrease exponentially with height ($H_S$ = 1,000 m). The turbulent kinetic energy dissipation rate is chosen as 200 $cm^2s^{-3}$, typical of cumulus clouds at early stages. The parcel reaches cloud top when vertical velocity is near zero. Note that despite specified as stated above for the reference simulation, sensitivity to parcel radius R and scale height Hs will also be explored in Sect. 4.4.2.

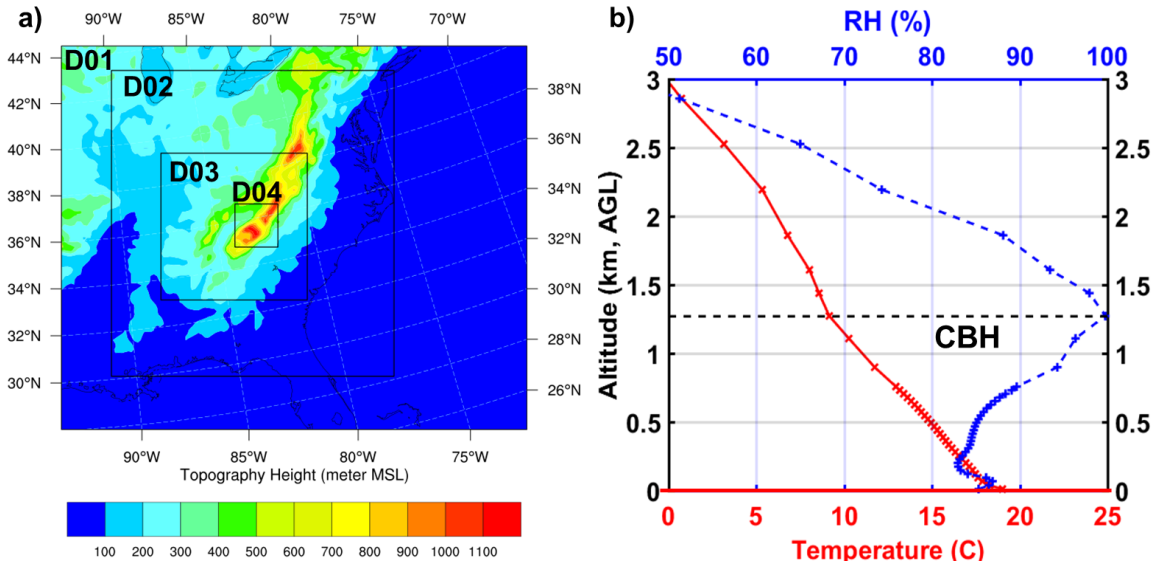

**Figure 4-10: a) WRF model configuration of four one-way nested domains at 15-, 5-, 1.25-, 0.25-km grid resolution, respectively. b) Vertical profile of temperature (red solid line) and relative humidity (dashed blue line) from the spatially-averaged WRF sounding columns at IC (see its location in Fig. 4-6a). The horizontal dashed line depicts CBH = 1,270 m AGL.**

## 4.4.2 Parameter sensitivity analysis

In this section, sensitivity tests are conducted to probe the range of unavailable measurements in light of in-cloud observations from the aircraft and assess the role of individual state variables and processes on the microphysics of the cumulus congestus case-study on 12 June during IPHEx. Selected parameters are perturbed one at a time while other assumptions and input parameters remain as specified in Sect. 4.4.1.

### 4.4.2.1 Condensation coefficient

Condensation plays a dominant role in the early stages of cloud formation and one key factor in this process is the condensation coefficient ($a_c$) that governs activation and condensational growth. A laboratory study by Chuang (2003) reported $a_c$values ranging from $4\times10^{-5}$–1, and experimental values from field campaigns and from chamber studies of individual droplet growth also differ over a wide range (0.007–0.1) as reviewed in Sect. 4.1. To determine an optimal value of the condensation coefficient that achieves a close agreement with the IPHEx airborne observations, $a_c$ was made to vary in the range [0.001, 1.0] on the basis of Fountoukis and Nenes (2005). For the targeted in-cloud region (IC), Fig. 4-11 shows simulated profiles of updraft velocity, supersaturation, total CDNC, LWC, and their sensitivity to selected $a_c$ values in comparison with the airborne observations

(different symbols indicate the ranges of measured updraft velocities triangles: 0–0.5 m $s^{-1}$, squares: 0.5–1.0 m $s^{-1}$, pentagrams: 1–1.5 m $s^{-1}$, hexagrams: 1.5–2.0 m $s^{-1}$). Measurements from the IC region along the lowest cloud transect (highlighted in the blue circle in Fig. 4-6a) are used to evaluate model performance, since no observations are available in the upper unmixed cloudy areas to assess the entire vertical profiles simulated by the CPM. Only simulations with reasonable agreement with the observations are presented, thus results with $a_c$ from 0.06 to 1.0 are not shown here. Particles above 1 μm in diameter are considered cloud droplets and are included in the integration to calculate LWC. Note that ground elevations under the IC region vary from 928 m to 1,184 m MSL (see Fig. 4-6b), and the region is on a small hill in the middle of the valley and surrounded by much higher ridges (terrain elevation ~ 1,500 m MSL). Hereafter, aircraft measurements are expressed as AGL to facilitate their comparisons with the model results.

Simulated updraft velocities at the observation levels (Fig. 4-11a) are consistent with the general trend of airborne measurements, which decrease with height. It is apparent that $a_c$ has a significant impact on the simulated supersaturation profiles (Fig. 4-11b). Low values of $a_c$ strongly inhibit the phase transfer of water vapour molecules onto aerosol particles, slowing the depletion of water vapour available in the parcel, and thus substantially increasing maximum supersaturation ($S_{max}$). Consequently, smaller aerosol particles with high concentrations are activated due to a higher $S_{max}$, resulting in a direct increase in cloud droplet numbers with lower values of $a_c$ (Fig. 4-11c). Overall, the

results are in agreement with earlier studies (Nenes et al., 2002;Simmel et al., 2005) that investigated the dependence of cloud droplet number concentrations on the condensation coefficient.

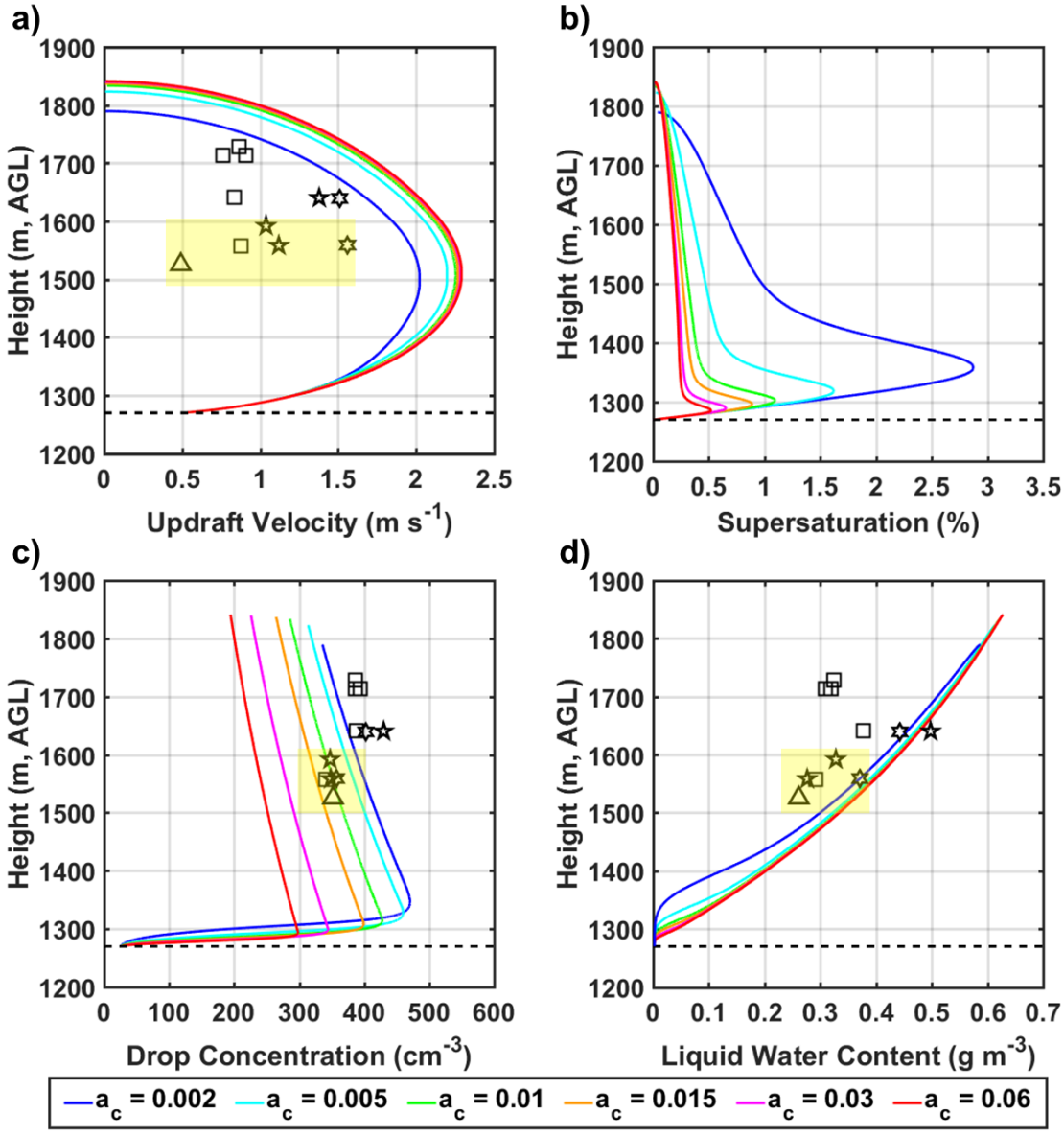


**Figure 4-11: Sensitivity of the updraft velocity (a), supersaturation (b), total drop concentration (c), and LWC (d) to the variations in the condensation coefficient ($a_c$) as compared to the airborne observations, marked by the different black symbols**

**denoting the ranges of their updraft velocities (triangles: 0–0.5 m s-1, squares: 0.5–1.0 m s-1, pentagrams: 1–1.5 m s-1, hexagrams: 1.5–2.0 m s-1). The horizontal dashed line depicts CBH. In (b), the observed supersaturation is not shown for comparison as large uncertainties are associated with airborne measurements of temperature in clouds, thus rendering the derivation of supersaturation unreliable.**

Moreover, Fig. 4-11c shows that the simulation with $a_c$ = 0.01 (green line) captures well the observed drop concentrations between 1,500 m and 1,600 m AGL (highlighted in yellow shade), whereas a condensation coefficient that is one order of magnitude lower (blue line) yields better results for the observations above 1,600 m. As summarized in Table 4-3, the simulated CDNC for the region between 1,500 m and 1,600 m AGL along the hillslope (shaded in Fig. 4-6b, reference sub-region within IC) for $a_c$ = 0.01 attains an average CDNC of 354 $cm^{-3}$, which is only ~1.3% higher than the observed average between 1,500 m and 1,600 m (349.4 $cm^{-3}$). The corresponding LWC is also in reasonable agreement with the range of observed values (Fig. 4-11d). The observed CDNC for the upper cluster between 1,600 m and 1,750 m (397.5 $cm^{-3}$) is underestimated by all simulations with different $a_c$ values and the averaged CDNC using a much lower condensation coefficient (0.002) is ~ 8% lower than the averaged observation. Inspection of Fig. 4-11c suggests that within IC there are two clusters of air parcels at different levels above ground associated with different condensation coefficients. Interestingly, the higher cluster (above lower elevation, Fig. 4-6b) is better matched by a lower condensation coefficient, whereas a higher condensation coefficient achieves the best agreement in the reference region that includes the updraft core near the hilltop.

**Table 4-3: Evaluation of the predicted CDNC from simulations using various condensation coefficients against the averaged observation from the CDP.**

| Condensation coefficient | Prediction[a] ($cm^{-3}$) (1,500 – 1,600 m) | Difference[b] (%) (1,500 – 1,600 m) | Prediction[a] ($cm^{-3}$) (1,600 – 1,750 m) | Difference[b] (%) (1,600 – 1,750 m) |
|---|---|---|---|---|
| 0.002 | 402.7 | 15.3 | 365.9 | -7.9 |
| 0.005 | 385.8 | 10.4 | 350.5 | -11.8 |
| 0.01 | 354.0 | 1.3 | 321.6 | -19.0 |
| 0.015 | 328.5 | -6 | 298.5 | -24.9 |
| 0.03 | 281.0 | -19.6 | 255.3 | -35.7 |
| 0.06 | 242.1 | -30.7 | 219.9 | -44.6 |

[a]The averaged CDNC in the predictions for the indicated altitudes.
[b]Difference (%)= 100×(Prediction - Observation)/Observation. Note observation between 1,500 m and 1,600 m AGL (349.4 $cm^{-3}$) is calculated by averaging the five CDNC measurements and observation between 1,600 m and 1,750 m AGL (397.5 $cm^{-3}$) is calculated by averaging the five CDNC measurements.

The sensitivity of predicted spectra at 1,500 m (in solid lines, Fig. 4-12a) to $a_c$ varying from 0.002 to 0.06 is very high. The observed spectrum (black dotted line) is the average from five individual CDP measurements (dotted lines with circle markers in Figs. 4-7c and d, also highlighted in the yellow shaded area in Fig. 4-6b) between 1,500 m and 1,600 m AGL (see Fig. 4-11d for their LWC in shade). Generally, spectra simulated with lower values of $a_c$ are broader with higher numbers of small droplets, while simulations with large values of $a_c$ yield narrower spectra shifted to larger droplet sizes. The differences in drop size range and spectra shape can be explained by inspecting the vertical profiles of the parcel supersaturation and $S_{eq}$ for six illustrative aerosol particle diameter ($D_{aero}$) depicted in Fig. D10. Growth by water vapour condensing on different sizes of cloud droplets is determined by the difference between S and $S_{eq}$ (Eq. 4-6 in Sect. 4.2.1). At low S, small particles become interstitial aerosols, and their corresponding $S_{eq}$ remains in equilibrium with the parcel supersaturation ($S - S_{eq} = 0$). At high S, as a result

of low $a_c$, activation of small aerosols contributes to significant spectra broadening, produces larger CDNC, and shifts the droplet size distribution toward smaller diameters due to slower condensational growth. This is consistent with Warner (1969b) who found that low condensation coefficients (< 0.05) were required to capture the observed dispersion of droplet spectra in natural clouds, especially for small sizes (i.e. left-hand side of the spectra). Figure 4-12b displays the simulated droplet number distributions at different levels for $a_c$ = 0.01 in comparison with the individual droplet spectra measured by the CDP. The spectrum at 1,559 m AGL (black dotted line) and its CDNC (357 $cm^{-3}$) and LWC (0.37 g $m^{-3}$) are closely replicated by the DCPM, and the simulated spectra are representative of the evolution of cloud droplet distributions in one parcel at different cloud development stages. Simulated spectra at 1,500 m and 1,600 m altitude show very good agreement with the observed number concentration and drop size range. Below 1,600 m, a shift of the unimodal spectra to larger drop sizes suggests that the condensation process currently dominates the growth of cloud droplets. Larger drops above 1,700 m could be produced by coalescence growth, leading to the formation of a second mode at larger sizes in the upper portion of the cloud. For the analyses presented hereafter, we consider $a_c$ = 0.01 together with other initial conditions as prescribed in Sect. 4.4.1, as the reference simulation (denoted by the grey line in the following figures).

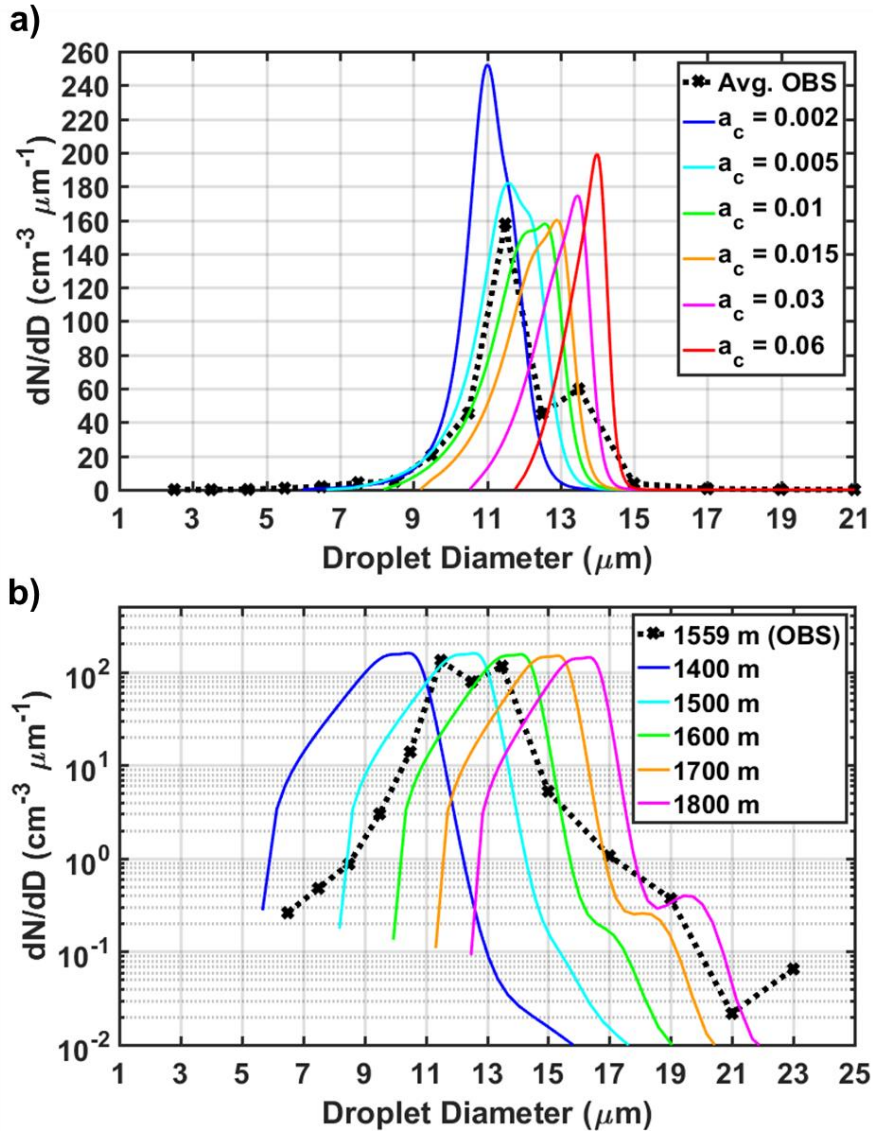


**Figure 4-12: a) Sensitivity of simulated droplet spectra at 1,500 m (solid lines) to the variations in $a_c$. The black dotted line reflects the average of five droplet spectra observed by the CDP (dotted lines with circle markers in Figs. 4-6c and d) between 1,500 m and 1,600 m AGL. b) Simulated evolution of cloud droplet spectra at 1,400 m, 1,500 m, 1,600 m, 1,700 m, and 1,800 m altitude assuming $a_c$= 0.01. The black dotted line denotes the observed droplet spectrum at 1,559 m that has similar total CDNC and LWC as the simulation with $a_c$ = 0.01 at the same altitude.**

Further examination using data from other cloud and precipitation probes suggests that concentrations of droplets larger than 30 μm in diameter are negligible

during the first horizontal leg. Considering that droplets with diameters larger than 30–32 μm are required to trigger effective droplet collisions (Pinsky and Khain, 2002), we conclude that the collision-coalescence process is not important in the sampled IC region, and it is unlikely that it contributes to the wide bimodal spectra observed at early stages of cloud growth. It is noteworthy that small drops are absent in the simulated spectra, in contrast to the observed spectrum that exhibits a broad drop size range and two distinct modes (see Fig. 4-12b). One possible explanation is that the moving bin grid determined by the condensation process tends to widen the spectral gap between the growing droplets and non-activated aerosol particles in the ascending parcel. Thus, a geometric size distribution with 1,000 bins is utilized herein to further refine the discretization for small particle sizes. Another explanation relates to the uncertainties of the input sounding extracted from the WRF simulation. Even though ambient aerosols are continuously entrained through lateral boundaries, most of them remain as interstitial aerosol particles because the low supersaturation in the parcel is insufficient to enable activation (see Fig. 4-11b). The WRF sounding in Fig. 4-10b exhibits a lapse rate of -4.1 °C $km^{-1}$ from 1,270 m (CBH) to 2,200 m, corresponding to stable atmospheric conditions unfavourable for cloud development. Additional model simulations were performed by altering lapse rates and humidity profiles at lower levels (see Appendix C1). The results point out that uncertainties of the assumed environmental thermodynamic conditions (e.g., temperature, humidity) impose significant constraints in reproducing wider bimodal

spectra present in natural clouds, thus posing as a significant challenge in cloud modelling study.

#### 4.4.2.2 Entrainment strength

To access the influence of entrainment on cloud drop concentrations and LWC, different strengths of lateral entrainment are examined by altering the initial cloud parcel size R at the cloud base. Figure 4-13 displays the vertical profiles of total CDNC and LWC, and cloud droplet spectra formed at three altitudinal levels (1,500 m: solid line, 1,600 m: dotted line, and 1,700 m: dashed line) for simulations using different initial parcel radii as compared to the CDP observations in the IC region (denoted by black symbols in Figs. 4-13a and b and the black dotted line in Fig. 4-13c). Entrainment appears to have a dominant influence on the cloud vertical structure as small rising parcels associated with higher entrainment dissipate faster by intensive mixing of dry ambient air through lateral cloud boundaries. Stronger entrainment strength results in a direct decrease in drop concentrations and LWC, while it has little influence on the droplet size range. The best agreement on droplet numbers is between the reference simulation (R = 500 m, $a_c$ = 0.01; grey line in Fig. 4-13a) and the reference sub-region within IC (between 1,500 m and 1,600 m AGL), whereas results for R = 1,500 m better replicate the higher cluster of cloudy samples (above 1,600 m AGL). Recall that previously, when R was held constant the higher cluster is better replicated using $a_c$ values one order of magnitude smaller than the reference value. Thus, the sensitivity analysis does suggest there is a trade-off with weaker

entrainment for a higher condensation coefficient (R = 1500 m and $a_c$ = 0.01, the orange line in Fig. 4-13a) when other parameters in the reference simulation remain the same.

Given R = 500 m, an additional test was conducted using the jet model parametrization of lateral entrainment (Eq. 4-5 in Sect. 4.2.1). The comparison of two entrainment parameterizations indicates that the bubble model (the grey line) has stronger entrainment strength than the jet model (red line) given the same initial parcel size (500 m). Nevertheless, continuous increases in simulated LWC in the upper portion of the cloud (see Fig. 4-13b) for both parameterizations are unrealistic in real clouds (Paluch, 1979). This problem can be likely ascribed, at least in part, to the uncertainties in the environmental conditions associated with the WRF sounding. As noted in Fig. B-1, decreases in LWC are manifest at the upper portion of the cloud, as indicated in the simulations with modified sounding inputs. The lack of sufficient mixing with dry ambient air near cloud top is an inherent deficiency in the simple parameterization of lateral homogenous entrainment, assuming decreasing entrainment strength with height, but this assumption does not significantly affect our conclusions for in-cloud regions below cloud top.

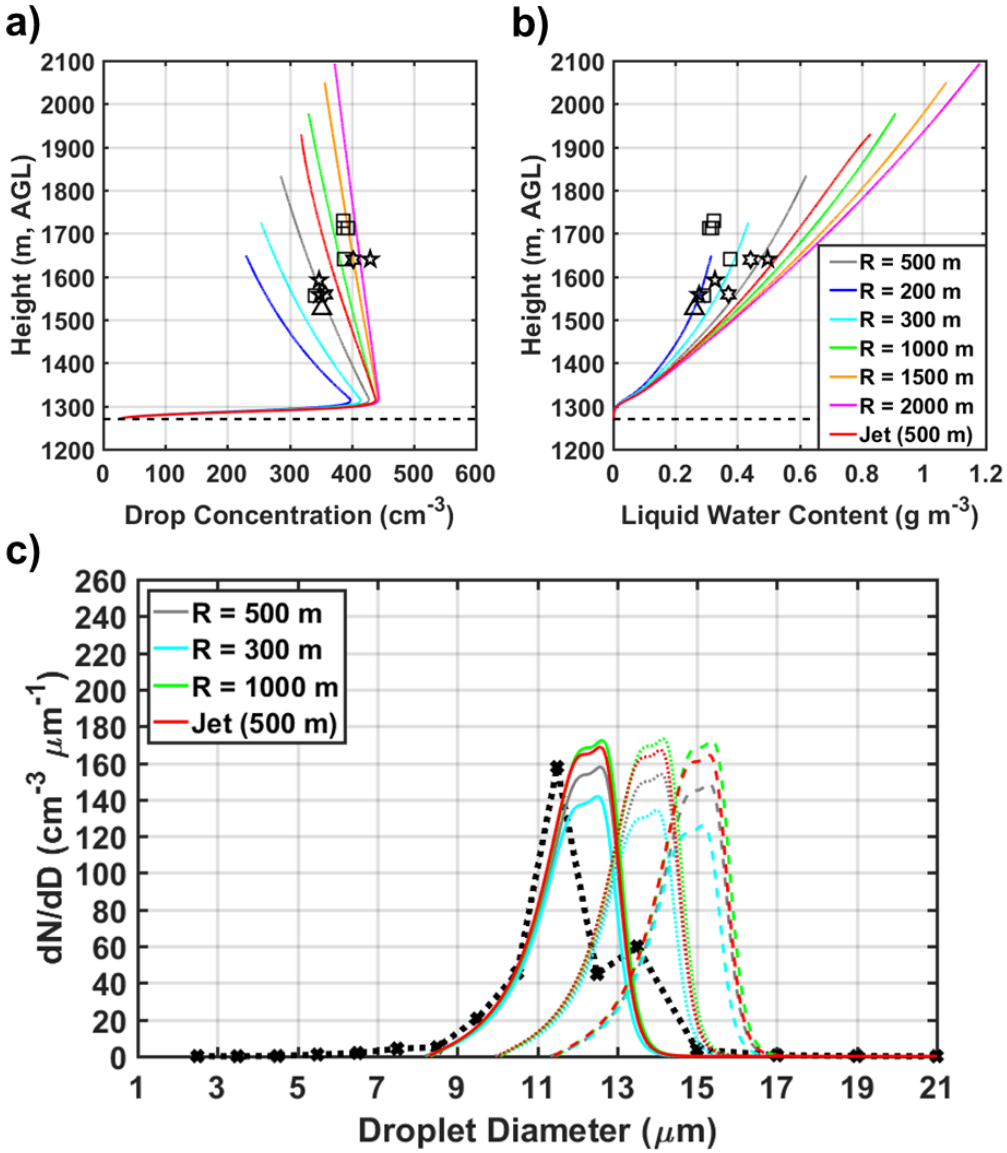


**Figure 4-13: Sensitivity of the total drop concentration (a) and LWC (b) to the variations in the initial parcel radius (R) considering lateral entrainment as a bubble model and a jet model. In (a) and (b), the airborne observations are marked by different black symbols, denoting the ranges of their updraft velocities (triangles: 0–0.5 m $s^{-1}$, squares: 0.5–1.0 m $s^{-1}$, pentagrams: 1–1.5 m $s^{-1}$, hexagrams: 1.5–2.0 m $s^{-1}$), and the horizontal dashed line depicts CBH. c) Predicted droplet spectra at three altitudinal levels (1,500 m: solid line, 1,600 m: dotted line, and 1,700 m: dashed line) using two parameterization schemes for lateral entrainment: the bubble model with R = 500 m (base case, grey lines), R = 300 m (cyan lines), and R = 1,000 m (green lines); the jet model with R = 500 m (red lines). The black dotted line reflects the average of five droplet**

**spectra observed by the CDP (dotted lines with circle markers in Figs. 4-7c and d) between 1,500 m and 1,600 m AGL.**

#### 4.4.2.3 Initial aerosol concentration

The initial aerosol concentration at cloud base can also have significant effects on cloud development. Because aerosol size distributions were not sampled by the aircraft during IPHEx, they are estimated by extrapolating surface aerosol number concentrations according to an exponential decay with a given scale height ($H_S$). To probe and characterize the dependence of droplet formation on aerosol concentrations available at cloud base, sensitivity to $H_S$ was explored by varying its values from 800 m to 1,200 m. Figure 4-14 shows the simulated profiles of the total CDNC and LWC, and cloud droplet spectra formed at three altitudinal levels (1,500 m: solid line, 1,600 m: dotted line, and 1,700 m: dashed line). It is not surprising that aerosol concentrations at cloud base have a substantial influence on the resulting droplet concentrations. Higher aerosol concentrations, inferred from larger $H_S$ lead to larger drop numbers with smaller average droplet sizes, which is known as the first indirect effect of aerosols (Twomey, 1977). Yet, here, LWC appears insensitive to the initial aerosol concentration as it is limited by moisture content available in the parcel.

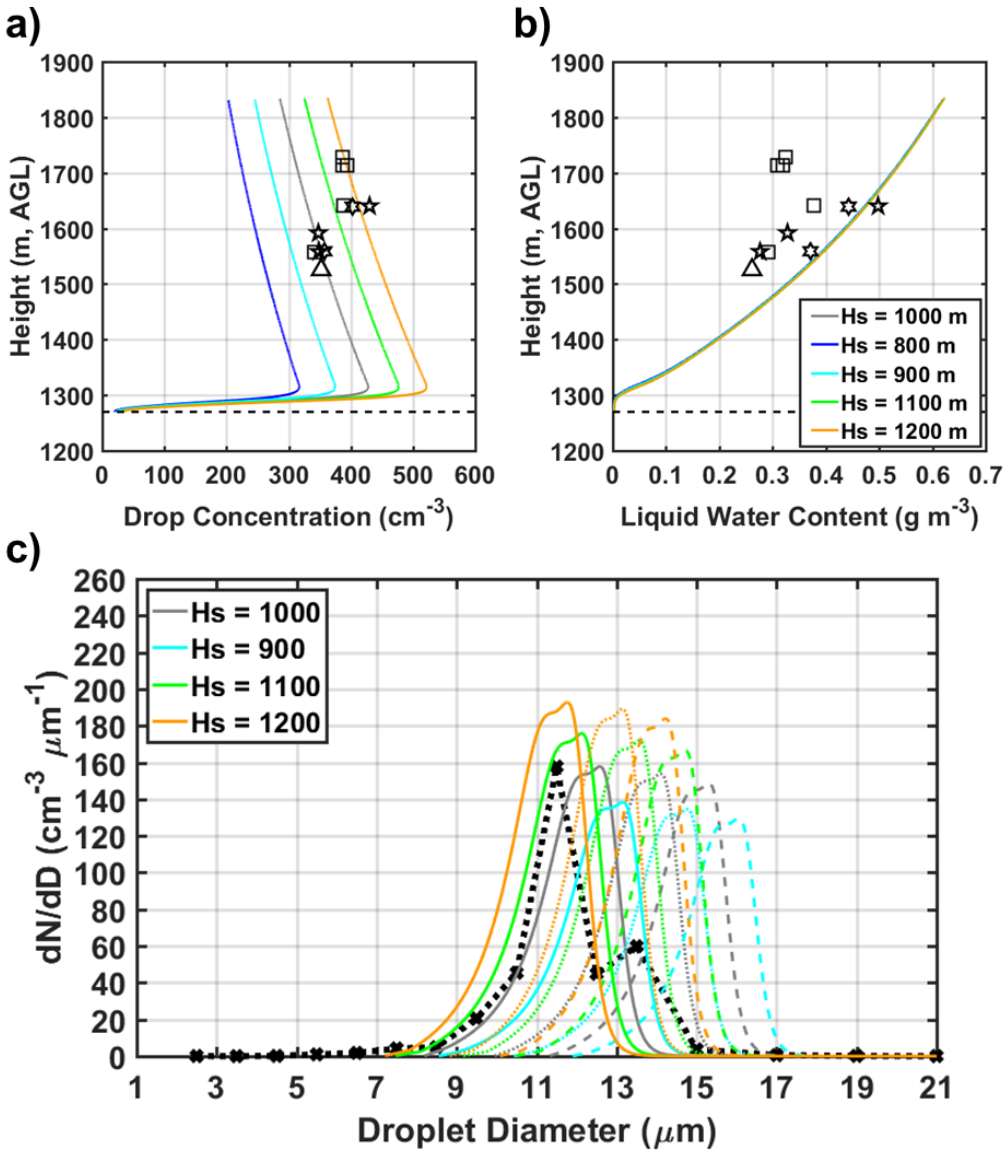


**Figure 4-14: Sensitivity of the total drop concentration (a), LWC (b), and droplet spectra (c) at three altitudinal levels (1,500 m: solid line, 1,600 m: dotted line, and 1,700 m:dashed line) to the variations in initial aerosol concentrations at cloud base, as represented by different values of the scale height ($H_S$). In (a) and (b), the airborne observations are marked by different black symbols, denoting the ranges of their updraft velocities (triangles: 0–0.5 m $s^{-1}$, squares: 0.5–1.0 m $s^{-1}$, pentagrams: 1–1.5 m $s^{-1}$, hexagrams: 1.5–2.0 m $s^{-1}$), and the horizontal dashed line depicts CBH. The black dotted line reflects the average of five droplet spectra observed by the CDP (dotted lines with circle markers in Figs. 4-7c and d) between 1,500 m and 1,600 m AGL.**

The optimal value of $H_S$ = 1,000 m yields the best agreement on CDNC between the DCPM simulations and the average droplet spectra observed by the CDP (black dotted line in Fig. 4-14c, see reference sub-region within IC shaded in Fig. 4-6b), which lies within the typical $H_S$ range (550–1,100 m) of aerosol number concentration measurements for remote continental type (Jaenicke, 1993). As noted before, aerosols in the atmosphere exhibit a significant space-time variability especially in regions of complex terrain, which can contribute to the diverse cloud droplet spectra observed across the cloud transect (see Fig. 4-8). We should recognize that this feature cannot be captured by current model simulations that assume a homogenous aerosol distribution at cloud base.

#### 4.4.2.4 Summary of sensitivity analysis

Sensitivity tests by changing $a_c$ in the range of 0.001–1.0 suggest that the predicted CDNC, LWC, and thermodynamic conditions are highly dependent on the condensation coefficient with $a_c$ = 0.01 achieving the best agreement with the total number concentration and size distributions from the airborne observations. At early stages of cloud development, the condensation coefficient plays a key role in the simulated spectra width and shape that increases in $a_c$ lead to a shift towards larger droplet sizes and narrower spectra widths. Entrainment has a substantial impact on the cloud depth, droplet numbers, and LWC, whereas initial aerosol concentrations have a strong effect on number concentrations and size distributions of cloud droplets, but induce little effects on LWC. Additional tests regarding the hygroscopicity and initial updraft velocity were

conducted and discussed in Appendix C2 and C3, respectively. We should keep in mind the uncertainties associated with the CBH level, which is estimated from the WRF model simulations as concurrent soundings are not available during IPHEx. If the CBH is lifted by 100 m, simulations using different $a_c$ values (0.002 – 0.06) are in better agreement with the measurements and the observed CDNC in the reference region (yellow shade, Fig. 4-11c) is better captured with a higher $a_c$ value (0.015) whereas narrower spectra is predicted in the simulation with a higher $a_c$ value, inconsistent with the observed spectra (not shown here). Due to the limited dataset from the campaign, a specific set of initial conditions are inferred from surface and airborne observations and reasonable assumptions are made based on the literature in this study.

Based on the sensitivity tests, the cloud spectra observed in the inner region of the SAM for early development of cumulus congestus on 12 June are better replicated by a relatively low value of $a_c$ (0.01). Previous field campaigns, as discussed in Sect. 4.1, have applied $a_c = 0.06$ for wam cumulus during CRYSTAL-FACE (Conant et al., 2004), $a_c$ = 0.042 for stratocumulus during Coastal Stratocumulus Imposed Pertubation Experiment (CSTRIPE, Meskhidze et al., 2005), and $a_c$ = 0.06 for cumuliform and stratiform clouds during ICARTT (Fountoukis et al., 2007), which are typical values for aged atmospheric droplets (Fountoukis and Nenes, 2005;Shaw and Lamb, 1999). It is noteworthy that the aforementioned closure studies assume adiabatic conditions in the parcel and some were only evaluated near cloud base. In our study, the vertical strucuture of cloud microphysics

is simulated by the DCPM with entrainment included and comparisons against the observations are performed several hundred meters above cloud base. Exploratory simulations assuming a higher aerosol number concentration at cloud base ($H_S$ = 1,200 m, Fig. C4b) show a highly nonlinear response to changes in $a_c$ and R that the best agreement in CDNC is achieved with higher $a_c$ values (0.03 and 0.06) for weak entrainment (R = 1500 m) consistent with the trade-off between entrainment (stronger) and condensation coefficient (lower) discussed in Sect. 4.4.2.2. However, the corresponding spectra simulated with higher $a_c$ values show large discrepancies in width and shape with the observed spectra within IC (not shown here), and thus predictions of inferior skill regarding vertical development of clouds.

Besides entrainment, one possible explanation for the lower condensation coefficients in IPHEx can be the presence of organic film-forming compounds (FFCs) on the surface of natural aerosol particles (Feingold and Chuang, 2002). Organic films can strongly impede the uptake of moisture by atmospheric aerosol particles, thus reducing the value of $a_c$ (Gill et al., 1983;Mozurkewich, 1986). Nenes et al. (2002) conducted a parcel model study to investigate the impact of aerosol coating with organic FFCs using a constant $a_c$ and concluded that the initial condensational growth is impeded, leading to higher supersaturations in the parcel, and increasing the cloud droplet number by a substantial amount due to a higher number of activated CCN. Without the characterization of the organic speciation in this campaign, the presence of organic coating

on local aerosols remains an open question. Nevertheless, results from laboratory experiments of direct contact condensation on aerosols in cloud chambers with horizontal or vertical moist flows, point to $a_c$ values around 0.01 (Garnier et al., 1987;Hagen et al., 1989) in contrast with the most probable value (0.06) found in the levitation cell by Shaw and Lamb (1999).

### 4.4.3 Multi-parcel simulations

In the previous section, it is demonstrated that single parcel simulations provide reasonable first estimates of key parameters in cloud formation, and their results agree well with the observed ranges of in-cloud measurements during IPHEx. The formation of cumulus clouds proper can be further described as the ensemble of multiple individual rising thermals of different sizes and vertical velocities (Cooper, 1989;Warner, 1969a). In order to simulate the realistic evolution of cumulus clouds with multiple air parcels rising in succession, Mason and Jonas (1974) and Roesner et al. (1990) pursued a multi-parcel modelling strategy such that a new parcel ascends within an environment established by its predecessors. However, when a series of parcels is rising, complicated interactions may occur under the Lagrangian framework of the parcel model, and they are difficult to resolve unless a more complex formulation of in-cloud parcel interactions is implemented (Khain et al., 2000). To examine the impact of antecedent conditions on individual cloud parcels, a simple solution is to impose a time delay for the launch of the next parcel to prevent it from overtaking the previous parcel during its ascent. As illustrated in Fig. 4-

15, the second parcel rises through the environment modified by the first parcel ($\Gamma_1$) and entrains interstitial aerosols left behind by the first parcel. After the second parcel ascends above the maximum height of the first parcel, it continues to rise through the undisturbed environment ($\Gamma_{env}$) and entrains ambient aerosol particles.

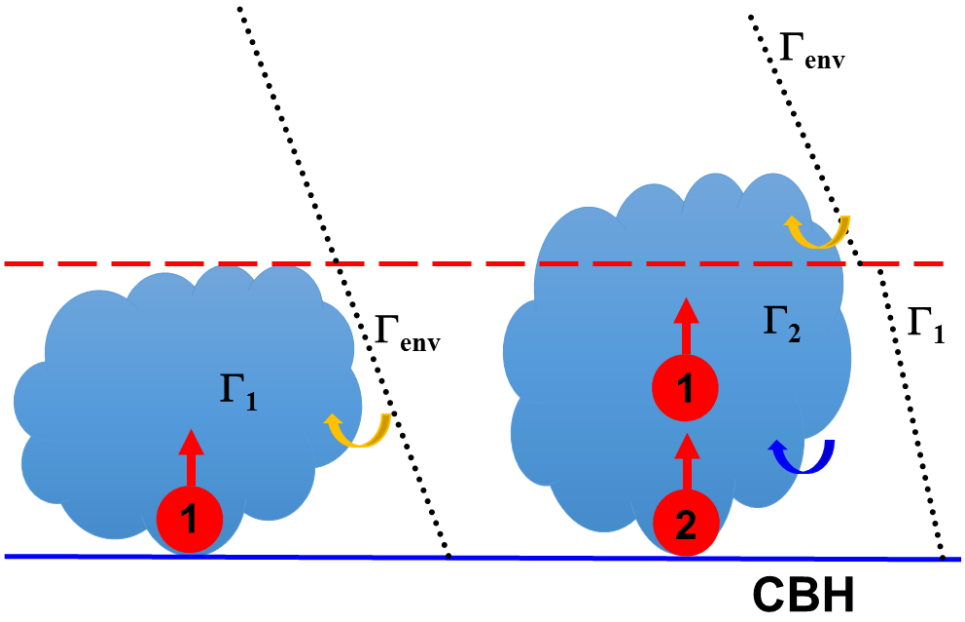


**Figure 4-15: Conceptual representation of the double-parcel simulations. The behaviour of the second parcel is determined by the new environment ($\Gamma_1$) established by the first parcel. During the ascent of the second parcel, interstitial aerosols left behind by the first one are entrained (indicated by the blue curved arrows). When the second parcel rises above the maximum height that the first parcel has reached (indicated by the red dashed line), its behaviour is determined by the initial environment ($\Gamma_{env}$) and aerosol particles from the environment are entrained (indicated by the yellow curved arrows). The order of each parcel is denoted inside the red circle and the blue solid line marks CBH.**

For the cumulus congestus clouds on 12 June 2014, a time-delay was adopted in the multi-parcel simulations so that the current parcel only passes its predecessor when it comes to rest. Results from the multi-parcel simulations show that the second parcel

attains a slightly higher maximum supersaturation (1.17%) than the previous parcel (1.16%), and rises with a higher updraft velocity (not shown here). After the second parcel emerges from the environment modified by the first parcel, no further increases in the supersaturation were produced in our simulation (not shown here), which is different from the results in Roesner et al. (1990). This is attributed to the initial environmental conditions obtained from the WRF sounding for this case-study (absolutely stable atmosphere with slow cooling below 2,200 m). Vertical profiles of drop concentrations and LWC, and droplet spectra of the first and second parcels are displayed in Fig. 4-16. Within the maximum height reached by the first parcel, the second parcel experiences a steeper decrease of droplet number concentration compared to the first one because only interstitial aerosol particles are entrained and most of them remain non-activated due to only slightly increased maximum supersaturation in the second parcel. In the new environment established by the first parcel, the second parcel achieves a higher LWC value and its cloud droplet spectra (represented by the solid lines in Fig. 4-16c) is slightly broader extending to larger size ranges compared to the first parcel (represented by the dotted lines in Fig. 4-16c). Above the maximum height of the first parcel, a pronounced secondary mode develops in the second parcel, resulting from coalescence growth tied to faster condensational growth. In addition, a third parcel simulation was conducted and its results only show slightly changes as compared to the second parcel, again likely explained by the unfavourable environmental conditions from the WRF sounding.

Nevertheless, each successive air parcel can create a new thermodynamic condition for the subsequent parcels and lead to deeper vertical development and faster droplet growth, thus conducive to convective cloud formation.

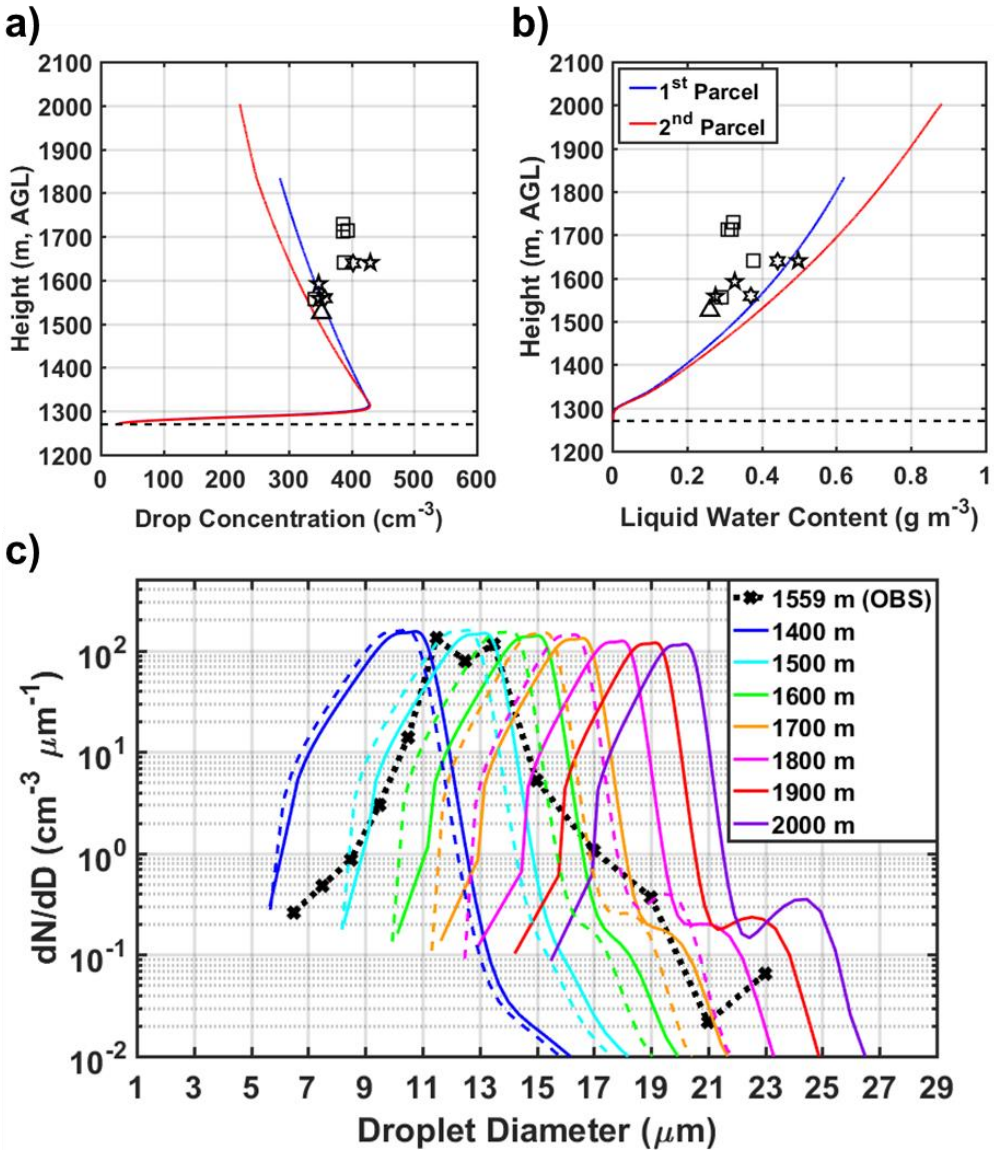


**Figure 4-16: Vertical profiles of the simulated total drop concentration (a) and LWC (b) for the first and second parcels. In (a) and (b), the airborne observations are marked by different black symbols, denoting the ranges of their updraft velocities (triangles: 0–0.5 m s$^{-1}$, squares: 0.5–1.0 m s$^{-1}$, pentagrams: 1–1.5 m s$^{-1}$, hexagrams: 1.5–2.0**

**m $s^{-1}$), and the horizontal dashed line depicts CBH. c) Simulated evolution of cloud droplet spectra for the first (represented by the dashed lines) and second (represented by the solid lines) parcels at different altitudinal levels. The black dotted line denotes the observed droplet spectrum at 1,559 m that has similar total CDNC and LWC as the simulated spectrum in the first parcel at the same altitude.**

## *4.5 Summary and discussion*

In this study, an entraining cloud parcel model (DCPM) with explicit bin microphyscis is used to explore the vertical structure of cloud development and evaluated against extensive data collected during the IPHEx campaign during May–June 2014 in the complex terrain of the SAM (Barros et al. 2014). Because measurements of key input parameters are not available from the campaign, or cannot be resolved by current sampling techniques, there is a pressing need to investigate the physical space of such parameters (e.g., condensation coefficient, entrainment, and scale height) and their interdependencies, which ultimately govern ACI in cloud formation and development. The study specifically focuses on the development of a mid-day cumulus congestus case on 12 June 2014 when aircraft measurements are available. Although this flight sampled three distinct cloud regions during the lowest cloud transect, the IC region and the MV supersite are closely located in the inner valley region of the SAM and thus a detailed modelling study could be conducted leveraging ground based aerosol measurements, ceilometer, and multi-frequency radar profiles available at MV to inform model initialization (Figs. D9 and 4-9). Given the specific set of initial conditions inferred from MV observations and initial parameters from the literature, sensitivity analysis was first

conducted to determine the possible ranges of key ACI modelling parameters that achieved good agreement with the observed CDNC and droplet spectra collected roughly 300–500 m above cloud base in the cloud updraft core. Albeit a large variability in cloud microphysical properties was observed at sub-km scale (~ 90 m is the spatial resolution of the measurements along the flight track) over the complex terrain of the inner SAM even within IC, the modelling results for the reference simulation demonstrate good agreement with the measured LWC and droplet size spectra of the cumulus congestus cloud.

In the framework of the physically based cloud parcel model, sensitivity of the simulated cloud microphysical characteristics to variations in key parameters was investigated within the context of *in situ* measurements. Results from sensitivity tests show that condensation coefficient exerts a profound influence on the droplet concentration, size distribution, LWC, and thermodynamic conditions inside the parcel, with a decrease in $a_c$ leading to an increase in cloud droplet number, a broader droplet spectra, and a higher maximum supersaturation above cloud base. The case-study during IPHEx reveals that the observed cloud features in the inner mountain region of the SAM are better replicated by a low value of $a_c$ (0.01), achieving a minimum error of ~1.3% of the observation. As expected, entrainment is found to be a major process controlling the vertical structure, CDNC, and LWC of the cloud. Further, it was shown that with other input parameters remain the same as reference simulation conditions, there is a trade-off between entrainment and the condensation coefficient: strong entrainment (meaning the

characteristic scale R in the bubble parameterization is small) is compensated by lower $a_c$ values, and vice-versa. This explains higher values found in previous aerosol-CDNC closure studies assuming adiabatic cloud conditions (zero entrainment) in the CPMs. Initial aerosol concentrations at cloud base also have a large impact on droplet numbers but negligible influence on LWC. Nevertheless, analysis of the effect of the interdependence of initial aerosol concentration, condensation coefficient and entrainment strength on the CDNC revealed ambiguous behavior that could only be resolved by assessing the properties of the simulated droplet spectra (shape, range) against the aircraft measurements at different altitudes throughout the clouds (i.e., well above cloud base). Overall, these findings provide a better picture of dominant factors in modelling cloud formation and provide some insight into key parameters of ACI processes in this region. This further highlights the need to have a constraining set of observational inputs in order to validate our findings over the SAM.

Finally, model and data limitations should be acknowledged. First, realistic entrainment and mixing with cloud surroundings have been found to contribute significantly to droplet spectrum broadening. It is important to recognize the limitations of the lateral homogeneous entrainment employed in the model. Its concept is based on a simple assumption that entrained aerosols are mixed instantly across the parcel, which neglects the inhomogeneous supersaturation and microphysical structure inside the cloud associated with discrete entrainment events on different spatial scales (Baker et al.,

1980;Khain et al., 2000). Turbulent mixing (Krueger et al., 1997) can break down entrained blobs of air into smaller scales and subsequently form small adjacent regions with uniform properties on account of molecular diffusion, thus leading to considerable spectrum broadening. In addition, the parameterization of entrainment through lateral boundaries neglects entrainment with dry air at cloud top that is expected to be an important element to cloud vertical development (Telford et al., 1984). Downdrafts induced by the penetration of dry air at cloud top can sink and mix with updrafts, effectively diluting number concentrations and broadening droplet spectra in clouds (Telford and Chai, 1980).

The multi-parcel approach was adopted to explore the impact of thermodynamic conditions on cloud vertical development, and consequently cloud microphysical structure. The new environment created by its predecessors enables the following air parcel to reach a higher altitude and develop larger droplets, thus facilitating the formation of convective clouds even under unfavourable environmental conditions (i.e., WRF sounding). When atmospheric soundings representative of local conditions are available, one could envision multiple parcels being lifted from cloud base at different times with different velocities over a duration sufficient to grow cloud droplets to the observed sizes. For cloud layers with thermal instability, complexity of in-cloud vertical velocity fields with localized areas of much stronger updrafts has been found to support the formation of wide bimodal spectra in cumulus clouds due to in-cloud nucleation of new droplets from interstitial aerosols when the parcel supersaturation higher up in the

cloud exceeds the cloud base maximum (Pinsky and Khain, 2002). As a result, this mechanism can lead to the formation of a secondary mode of small droplets in individual spectra, different from our observed spectra with a second mode centred at a larger droplet size (Figs. 4-7 and 4-12). High supersaturations in the range of 1.7–3.2% are indeed measured in the lower portion of the cloud in the IC region (marked as black symbols in Fig. 4-11b). However, lower supersaturation is predicted by the parcel model at the observation levels and no further rise of supersaturation is present above the cloud base maximum under the conditions of the original and modified environments, likely attributed to the ambiguities in the sounding input from WRF. Therefore, the uncertainties of ambient thermodynamic conditions significantly constrain the modelling study of the observed clouds in our case. Another limitation in the current approach is the assumption of uniform hygroscopic properties for all particle sizes. In reality, the aerosol distribution is an aggregate of particles with different physicochemical properties, including different shapes, solubility, and chemical species (Kreidenweis et al., 2003;Nenes et al., 2002). Even if specified initial aerosol characteristics were to capture the variation of $\kappa$ with size, how to track the evolution of $\kappa$ as particles among different bins undergo coalescence and breakup remains a challenge. Nevertheless, the sensitivity analysis indicates that the cloud droplet growth is generally insensitive to hygroscopicity (Appendix C2), thus the constant $\kappa$ value used in this study does not significantly affect our modelling results.

The present study underlines the importance of the relationhsip between entrainment processes that determine the local- (microscale) and cloud-scale thermodynamic environment around individual particles, and the aerosol condensation coefficient that measures the effectiveness of condensation processes in the same thermodynamic environment. Given the multiscale thermodynamic structure of clouds, these interactions suggest that realistically the condensation coefficients in the natural environment are transient and spatially variable. Therefore, further research to arrive at representative ensemble estimates are necessary to reduce the associated uncertainties of the aerosol indirect effect. In the present study, the local sensitivity of selected model parameters are assessed individually over certain ranges based on IPHEx data and the literature, which ignores non-linear interactions among ACI modelling parameters as discussed above. Future work will focus on exploring the sensitivity of the DCPM in a multi-dimentional parameter space to quantify multiple parameter interactions (Gebremichael and Barros, 2006;Yildiz and Barros, 2007) on ACI processes using the fractorial design method (Box et al., 1978).

# 5. Interpreting aerosol-cloud interactions on low-level clouds formation and warm season precipitation in mountainous regions

## *5.1 Introduction*

Long-term observations from a high-altitude ground raingauge (RG) network in the Southern Appalachian Mountains (SAM) reveal a distinct seasonal variability in the diurnal cycle of rainfall occurrences. As expected, the diurnal cycle of warm season (spring and summer) precipitation is characterized by late afternoon peaks, attributed to isolated thunderstorms and mesoscale convective systems dominant in the warm season (Duan et al., 2015). Nevertheless, most precipitation in this region is associated with stratiform systems with hourly rainfall intensity less than 3 mm/hr, contributing to 30–50% of annual rainfall accumulation in the SAM (Wilson and Barros, 2014). Another regional feature in the SAM is the persistent occurrence of low-level clouds and fog (LLCF) in all seasons. As illustrated in the satellite climatology study in Sect. 3, high frequencies of LLCF are found over mountain ridges at daytime and in mountain valleys at nighttime. In the absence of large-scale forcing, the diurnal cycle of LLCF in the SAM can be explained by organized atmospheric moisture mesoscale convergence patterns, modulated by the topography. In particular, predominantly easterly and south-easterly low-level moisture convergence is associated with early afternoon low-level clouds (LLC) formation in the inner mountainous regions of the SAM (Wilson and Barros, 2017).

However, the linkages of low-level cloudiness and consequently precipitation patterns to cloud condensation nuclei (CCN) availability and local processes remains elusive.

Previous work using a cloud parcel model demonstrated that variations in aerosol properties have a major impact on the microphysical characteristics and thermodynamic state of orographic cumulus congestus at early stages (see Sect. 4). Considering the feedback mechanisms in the atmosphere, the response of cloud microphysics to aerosol changes can influence the dynamic structure of cloud systems, which in turn affects the microphysical processes of clouds and subsequently precipitation evolution. Furthermore, the complex feedbacks among radiation, microphysics, convection, and surface fluxes in complex terrain cannot be resolved in the simplistic representation of cloud microphysical processes in an air parcel. Thus, mesoscale modeling of regional processes is required to unveil the indirect effects of aerosols on the microphysical pathways of cloud formation and precipitation evolution in mountainous regions, and to elucidate the interplay between microphysical and dynamical processes of clouds and precipitation in the warm season. Here, an exploratory study is presented to investigate the indirect effects of aerosols on the space-time variability of cloud formation and rainfall evolution, especially at low-levels. For this purpose, the Advanced Weather Research and Forecasting (WRF) model will be used to investigate the CCN sensitivity of summer rainfall events (10–12 June 2014) during the Integrated Precipitation and Hydrology Experiment (IPHEx), leveraging the comprehensive measurements of aerosol, cloud, and

precipitation measurements collected in the SAM. Specifically, CCN spectra sampled during this field campaign will be incorporated in the model simulations to quantitatively assess the impacts on cloud formation and precipitation development to changes in CCN characteristics, focusing on the influence on the spatial distribution and diurnal cycle of LLC, and the microphysical and dynamic evolution of precipitation processes on local (ridge-valley) and regional scales, as well as hydrometeorological impacts and feedbacks.

The IPHEx field campaign took place in two phases: a long-term Extensive Observing Period (EOP, one-year period of collecting ground measurements) and an Intensive Observing Period (IOP), including large-scale radars and aircraft observations during 01 May – 15 June 2014. With airborne and ground-based measurements of the vertical structure of precipitation microstructure and cloud microphysical properties in the lower 2 – 3 km of the troposphere and information on surface aerosol/CCN characteristics, this campaign provides an unprecedented opportunity for the detection and attribution studies of aerosol-cloud interactions (ACI) on cloud formation and precipitation processes in the SAM. The airborne measurements include high altitude sampling of multi-frequency radar reflectivity, cloud and precipitation microphysics (e.g., droplet spectra and liquid water content). The ground observation network, including micro rain radar (MRR), Partical Size and Velocity (PARSIVEL) disdrometer, and raingauge, provides low-level vertical profiles of radar reflectivity and surface precipitation characteristics (e.g., rain rate and drop size distribution) widely available in

the SAM (see Fig. 5-1). In particular, surface aerosols/CCN measurements were collected at the Maggie Valley (MV) supersite (same location as P22 in Fig. 5-1). Collocated with aerosol instruments, the ACHIEVE (Aerosol-Cloud-Humidity Interaction Exploring & Validating Enterprise) platform was equipped with W-band (94 GHz) and X-band (10.4 GHz) radars, a ceilometer, and a microwave radiometer.

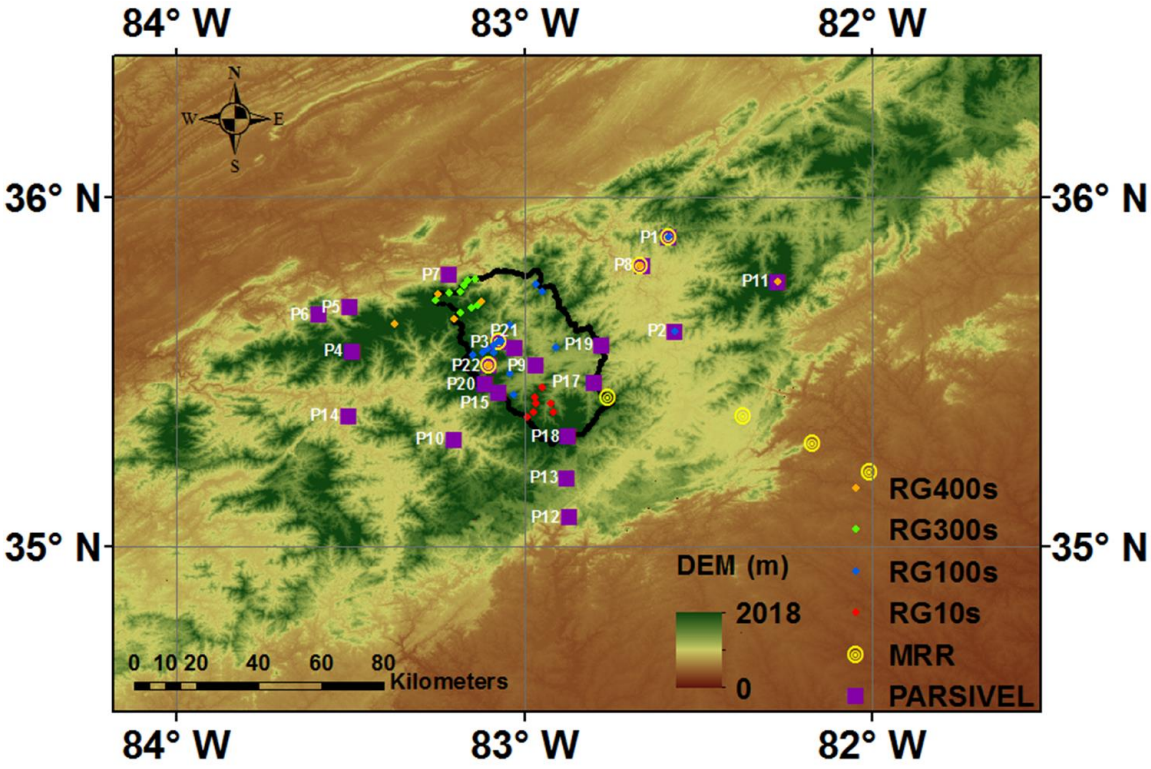


**Figure 5-1: Topographic map of the study region with ground instruments during the IPHE IOP. Raingauges (RG) are marked by colored dots, representing different regions over the inner SAM (red: eastern region; blue: inner region; green: western region, inner-western region: orange). PARSIVEL disdrometers are marked by purple squares and their names (Px, in white) are indicated next to the symbols. Micro rain radars (MRRs) are marked by yellow circles. Note the Pigeon River Basin (PRB) over the inner region is delineated by the black line and the location of the Maggie Valley supersite is the same as P22.**

This chapter is organized as follows: Section 5-2 describes the setup of the WRF model, the initialization procedures of the simulations, and the experiment design for sensitivity tests. Modeling results are discussed in Section 5-3, and a summary of the findings and the conclusions drawn are present in Section 5-4 as well as a brief outlook for future work.

## *5.2 Model and experiment setup*

### 5.2.1 WRF model setup

The focus of this study is the Pigeon River Basin (PRB, see Fig. 5-1), where the most comprehensive observations are available during IPHEx and will be used to perform diagnostic studies of numerical simulations using WRF. Built on previous modeling experiences (see Sect. 4.4), the Advanced WRF Version 3.8.1 (Skamarock et al., 2008) was used to conduct 5-day simulations over the SAM from 00:00 UTC 08 June for the first domain (06:00 UTC for second, and third domains) to 06:00 UTC 13 June 2014 for all three domains (see domains in Fig. 5-2a). The model configuration was set up similar to Sect. 4.4.1 and Wilson and Barros (2017). One-way nested domains are configured with horizontal grid spacings of 9-, 3-, and 1-km. This corresponds to grid sizes of 190×190, 352×352, and 355×355 for the first (D01), second (D02), and third (D03) domains, respectively. In order to better resolve the low-level processes, a terrain-following vertical grid with 90 layers is constructed with 30 levels in the lowest 1 km AGL and the model top is at 50 hPa.

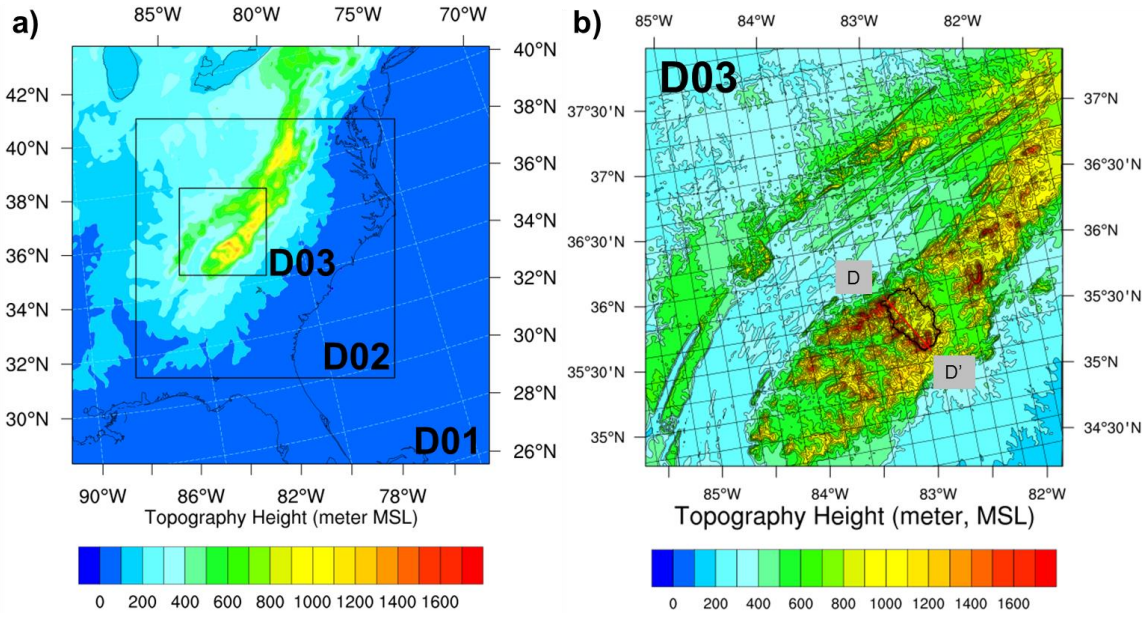


**Figure 5-2: a) Model configuration of three one-way nested WRF domains at 9-, 3-, 1-km resolution, respectively. b) Topographic map of Domain 3 (D03), marked with cross section D-D' along the ridgelines in the PRB where the long term raingauge network (Fig. 5-1) is located.**

Initialization and lateral boundary conditions are updated every 6-hour using the National Centers for Environmental Prediction (NCEP) Final Operational Global Analysis (FNL) with 1°×1° horizontal resolution (Kalnay et al., 1996). The Kain-Fritsch cumulus parameterization scheme (Kain, 2004) is used in the first domain (9 km), and convection is resolved explicitly in the second (3 km) and third (1 km) domains. Other physics options include Milbrandt and Yau (2005b) double moment microphysics, a new version of the Rapid Radiative Transfer Model radiation scheme for longwave and shortwave (Iacono et al., 2008), and the unified Noah land-surface model (Tewari et al., 2004) applied for all four domains. The Mellor-Yamada-Nakanishi-Niino (MYNN) planetary boundary layer scheme (Nakanishi and Niino, 2004) is selected together with the Monin-Obukhov (Janjic

Eta) surface layer scheme. The soil temperature and moisture fields are also initialized from the NCEP FNL data.

### 5.2.2 Modelling experiments with Milbrandt-Yau microphysics

To investigate the effects of aerosol properties on the sensitivity of aerosol-cloud-precipitation interactions (ACPI), the double moment Milbrandt-Yau microphysics scheme (total number concentration and mixing ratio), hereinafter MY05 was selected. Number concentrations of nucleated cloud droplets ($N_{CCN}$) in MY05 are calculated based on a four-parameter CCN activation spectrum (Eq. 5-1), which is a more realistic representation of CCN populations for supersaturation greater than 0.01% as compared to a single power law expression in Twomey (1959). This CCN activation scheme (Cohard et al., 1998; hereafter CPB98) has demonstrated improved estimation of cloud droplet numbers as it accounts for the limited availability of small-sized condensation nuclei with increasing supersaturation.

$$N_{CCN}(s_{v,w_{max}}) = C s_{v,w_{max}}^{k} F\left(\mu, \frac{k}{2}, \frac{k}{2}+1; -\beta s_{v,w_{max}}^{2}\right) \quad (5\text{-}1)$$

where $s_{v,wmax}$ is the maximum water vapor supersaturation and F(a, b, c; x) is the hypergeometric function. For the four parameters of the fit, C is a scaling factor, k can be estimated as the slope for a small supersaturation region in a log-log plot of $N_{CCN}$ and $s$, β indicates the location of the slope break, and μ represents the flat aspect of the curves at high supersaturation (see Fig. 1 in CPB98).

The CCN activation spectra fitted for continental and maritime aerosol types, obtained from CPB98 are implemented in MY05, but the formula Eq (5-1) and corresponding fitting parameters for each aerosol type are not directly employed for computing $N_{CCN}$ in the microphysics scheme. Instead, maximum supersaturation is first expressed as a function of updraft speed $w$, temperature $T$, and pressure $p$ using an iterative method, as outlined by Cohard and Pinty (2000). To reduce computational cost, non-linear least-square fits are applied to $s_{v,wmax} = f(w, T, P)$ and $N_{CCN} = f(w, T, P)$ for specified CCN spectra. Details of the non-linear regression fits can be found in Milbrandt and Yau (2005a) and Shrestha (2011). Using the Milbrandt-Yau microphysics in WRF, we adopted the same method as stated above to incorporate the CCN spectra sampled at MV, representative of the inner SAM for the simulations in Domain 3 (D03, see Fig. 5-2b). Figure 5-3 displays the CCN spectra collected on the day before the rainfall events (09 June 2014) and the day after (13 June 2014), compared with the continental and marine types from CPB98. The four fitted parameters for each CCN spectrum are summarized in Table 5-1. The Jun09 CCN spectrum was estimated based on measurements collected after three days of dry air conditions and before the precipitation onsite in the early morning of 10 June, which is representative of the regional background level of aerosol characteristics. The Jun13 CCN spectrum describes the relatively clean atmospheric conditions as aerosol particles are mostly scavenged after several rainfall events during 10 – 12 June. Compared to the continental type from CPB98, the Jun09 spectrum shows

lower number concentrations of CCN for supersaturation < 0.1% whereas the CCN number concentrations at supersaturation > 0.1% are remarkably high by up to three times greater in magnitude. This can be ascribed to high number concentrations of small aerosol particles available in the SAM that are activated at high supersaturation.

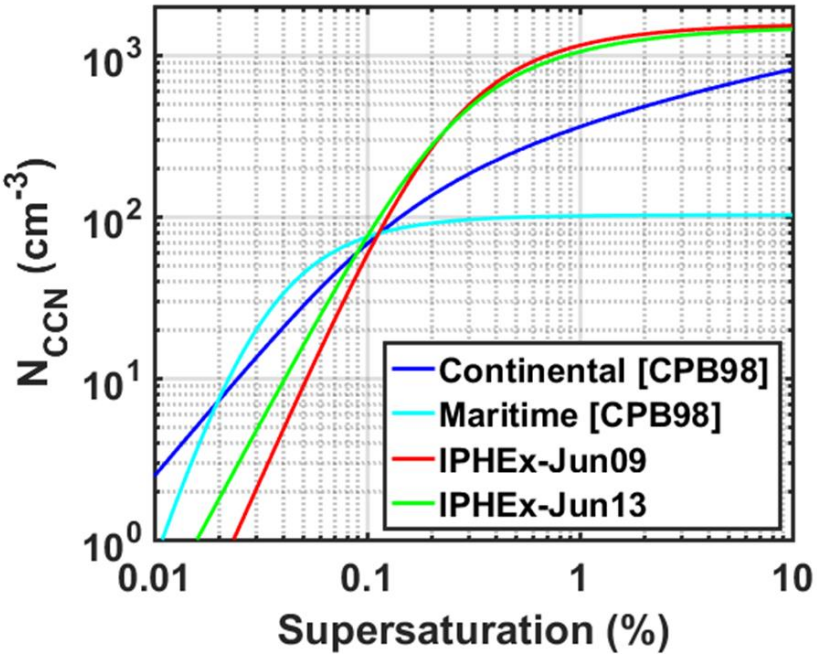


**Figure 5-3: CCN spectra estimated from surface measurements at MV on 09 June and 13 June during IPHEx, as compared to the continental and maritime CCN spectra from CPB98 (default CCN types in MY05).**

**Table 5-1: Fitted parameters of the analytical estimate of $N_{CCN}$ (Eq. 5-1, developed by CPB98) for the corresponding CCN spectra in Fig. 5-3.**

| | C ($cm^{-3}$) | k | β | μ |
|---|---|---|---|---|
| **Continental [CPB98]** | 3270 | 1.56 | 136 | 0.7 |
| **Maritime [CPB98]** | $1.93 \times 10^8$ | 4.16 | 1370 | 2.76 |
| **IPHEx-Jun09** | 68824 | 2.97 | 23.46 | 1.96 |
| **IPHEx-Jun13** | 24935 | 2.44 | 22.66 | 1.62 |

To probe the sensitivity of microphysical and dynamical processes in cloud formation and precipitation evolution to the aerosol indirect effect, we conducted two experimental WRF simulations in D03 for the rainfall events during 10–12 June 2014: a control run (hereafter, CONTL) with the continental CCN type (default continental aerosol in MY05 microphysics scheme in WRF3.8.1), and a sensitivity test (hereafter, IPHEx) with the Jun09 CCN spectrum measured during IPHEx. The other setup in these two model simulations for D03 remains the same as specified in Sect. 5.2.1. It should be noted that the change made in the sensitivity test only modified the cloud nucleation scheme in MY05. Aerosols' indirect effects as ice nuclei also play a significantly role in cloud dynamics and precipitation development (Diehl et al., 2007;Hoose et al., 2010), but this is beyond the scope of this study.

### 5.2.3 Rainfall case-study

The case study of interest is a long-duration precipitation event with enhanced convective activity on 11 and 12 June 2014, resulting in widespread showers and thunderstorms over this region. Herein, rainfall events on 11 June and 12 June are the focus of this study. Daily weather maps for these two days were obtained from the National Center for Environmental Prediction, Weather Prediction Center (http://www.wpc.ncep.noaa.gov/dailywxmap) as shown in Fig. E3. On 11 June, an upper-level trough was approaching the southeastern US and large areas of moisture were transported to this region under southerly/southwesterly flows (Fig. E3a). On 12

June, the influence of the trough weakened as it moved away from this region (Fig. E3b). The rainfall accumulation during 11–12 June is recorded by a high-density raingauge network (see locations in Fig. 5-1) in the SAM as displayed in Fig. 5-4. As expected, early afternoon and evening rainfall was consistently observed among all gauges in different regions for these two days. A strong spatial variability of precipitation is also manifest in different regions over the SAM. In particular, several gauges at high elevation (denoted by darker colored lines) over the inner region (blue circles in Fig. 5-1 and blue lines in Fig. 5-4b) and inner-western region (orange circles in Fig. 5-1 and orange lines in Fig. 5-4d) report significantly higher rainfall accumulation than gauges over the eastern (red circles in Fig. 5-1 and red lines in Fig. 5-4a) and western regions (green circles in Fig. 5-1 and green lines in Fig. 5-4c). We also note light precipitation in the early afternoon of 11 June and 12 June over the inner region (Fig. 5-4b) and heavy precipitation in the early afternoon of 12 June over the western region (Fig. 5-4c) and inner-western region (Fig. 5-4d).

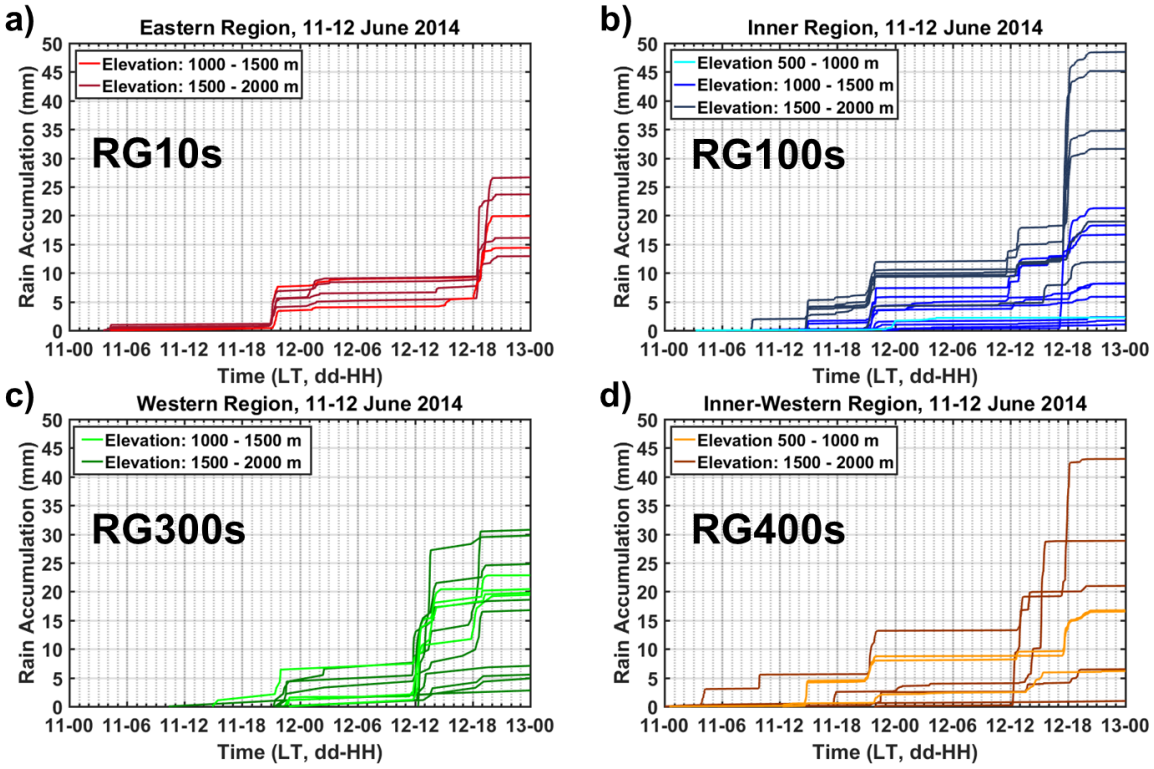


**Figure 5-4: Accumulated rainfall recorded by the raingauge (RG) network during 11–12 June 2014. Gauges in eastern, inner, inner-western, and western regions correspond to RG10s, RG100s, RG300s, and RG400s, respectively in Fig. 5-1. RG at higher elevation are represented in darker colored lines.**

The precipitation events during 11–12 June were also recorded by the collocated ground instruments (MRR, RG, and disdrometers in Fig. E1 and W-band radar in Fig. E2, See Appendix E) at the MV supersite (elevation: 925 m, same location as P22 in Fig. 5-1), located in the inner region. For the early afternoon rainfall events on 11 June and 12 June, stronger reflectivity gradients toward the surface are shown in the MRR profiles on 11 June, resulting in higher rain rates up to 30 mm/hr (left column in Fig. E1) whereas high reflectivity values consistently throughout the vertical column are observed on 12 June (right column in Fig. E2) with rain rates up to 10 mm/hr. Similar reflectivity features with

steeper gradients toward the surface also appear in the late afternoon event on 12 June with a longer duration. During the intermittent rain showers, shallow cumulus clouds (cloud tops < 4 km) were formed as noted in the W-band reflectivity profiles in Fig. E2.

## *5.3 Modeling results*

### 5.3.1 Evaluation against observations

To examine whether the rainfall events during 11–12 June are well replicated in the WRF simulations, the rainfall accumulation across D-D′ (see cross section in Fig. 5-2b) is evaluated against raingauge observations (see Fig. 5-4). D-D′ cuts northwest to southeast along the ridgelines in the PRB where most of the raingauges are located (Fig. 5-1). Fig. 5-5 presents a modified version of a time-longitude plot, first introduced by Hovmöller (HovmÖller, 1949) and will be referred to as Hovmöller diagram hereafter. As the low-level moisture convergence patterns are similar in two simulations, only the IPHEx results are shown in Fig. 5-5 for illustration. On 11 June, the observed precipitation onset in the early afternoon around 1430 LT (local time) is captured well by both simulations although a slight overestimation of precipitation initiation is predicted over the eastern region in CONTL. Distinct spatial distributions of rainfall accumulation are manifest in the two simulations for the early afternoon event on 11 June. Heavier rainfall is produced over the eastern region in CONTL, whereas more precipitation is estimated over the inner region in IPHEx, which is in better agreement with the spatial variability of rainfall observed by raingauges across the PRB (Fig. 5-4). For the late evening event

(2100 LT – 2200 LT) on 11 June, strong low-level convergence was also predicted in both simulations (see Fig. 5-5c). As shown in Figs. 5-5d and e, the timing of the early afternoon (~ 1200 LT) and early evening (~ 1800 LT) events on 12 June are well replicated in both simulations while large amounts of rainfall (up to about 30 mm, Fig. 5-4b) reported by raingauges over the inner region are significantly underestimated in both simulations.

The rain microphysics in the WRF simulations are assessed by calculating the mass-weighted mean diameter ($D_m$) using the total number concentration ($N_T$) and mixing ratio ($q$) from the two-moment Milbrandt-Yau scheme in a manner similar to Wilson and Barros (2017). As the information on the exact distribution of rain drops is not available, $D_m$ is computed as

$$D_m = \left(\frac{\rho q}{c N_T}\right)^{1/3} \tag{5-2}$$

where air density ϱ is obtained from pressure and temperature outputs from the model and the coefficient $c = (\pi/6)10^3$. Fig. E4 and Fig. 5-6 display the Hovmöller diagrams of estimated rain Dm at two low altitudes (2 km and 2.5 km MSL) along the D-D′ cross section for 11 June and 12 June, respectively. For comparison, Fig.5-6e shows the observed $D_m$ at the surface level, which is derived from drop size distribution (DSD) measurements by ground PARSIVEL disdrometers (P3, P7, and P21, see their locations in Fig. 5-1). In both simulations, relatively large $D_m$ values are predicted at the peak of the early afternoon events for both days (11 June: ~ 1500 LT in Fig. E4; 12 June: 1200 LT in Fig. 5-6). For the afternoon event on 11 June, the simulated $D_m$ maxima in both runs approach 1.2

mm near the surface (2 km MSL, Figs. E4a and b), comparable to the observed sizes by the valley disdrometers over the inner (P21, blue circles in Fig. 5-6e) and western (P7, green circles in Fig. 5-6e) regions. On 12 June, $D_m$ maxima in both simulations are predicted near the surface over the western region around 1200 LT (2km MSL, Figs. 5-6a and b) and the corresponding values reach 1.3 mm, which are about half of the largest size recorded by the valley disdrometer in the western region (P7, green circles in Fig. 5-6e). It is noteworthy that significant differences in $D_m$ distributions are evident between the ridge (P3) and valley (P7 and P21) disdrometers on 12 June, in particular in the afternoon. The large $D_m$ values (up to ~ 5 mm) observed at valley locations can be likely explained by the reverse orographic enhancement observed over the inner region of the SAM with significantly increased rainfall intensity at low elevations as compared to adjacent ridge locations due to seeder-feeder interactions (SFI) between LLCF and incoming precipitating systems (Wilson and Barros, 2014, 2015). However, the well-documented surface precipitation enhancement is not captured in either model simulation. The modeled $D_m$ profiles in both simulations are generally uniform in the lower 2 km AGL on both days, indicating small variations in the vertical structure of rain drop sizes (not shown here) in disagreement with the ground radar observations that report stronger gradients in reflectivity toward the surface (Figs. E1a and b).

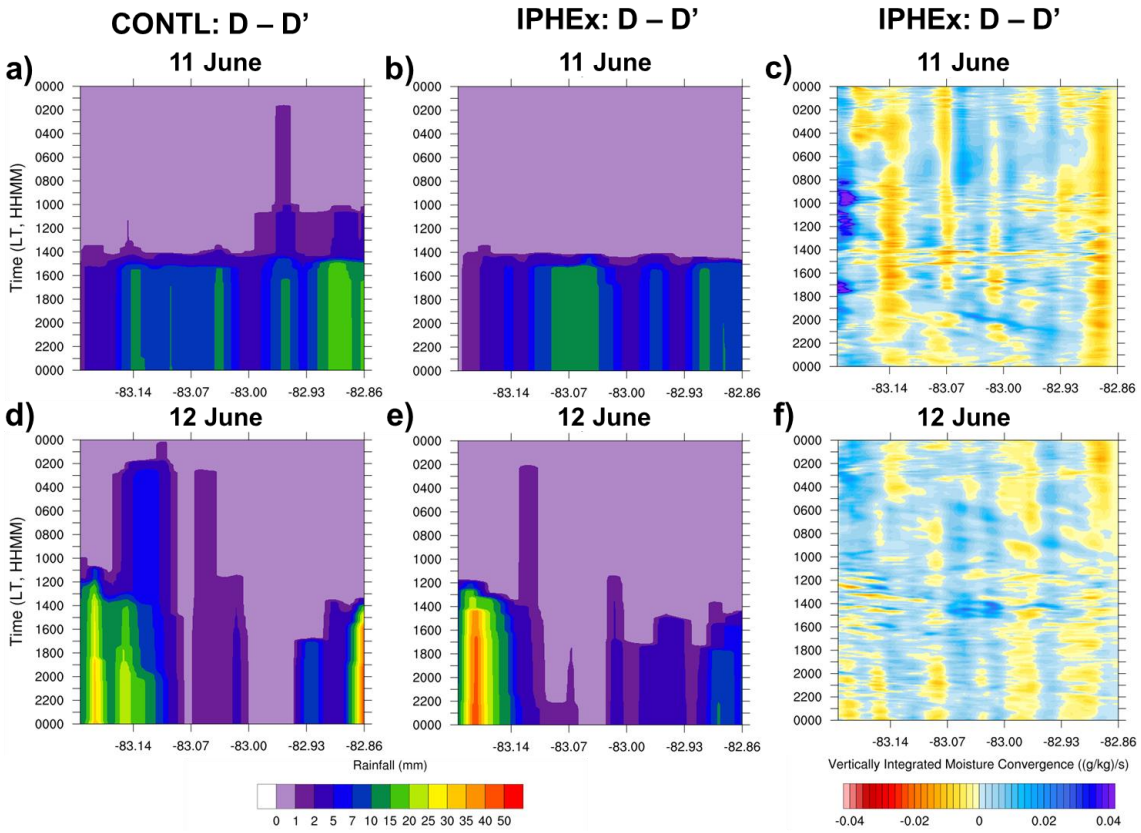


**Figure 5-5: Model results along the D-D′ cross section for 11 June (top panel) and 12 June (bottom panel) cases, with columns from left: Hovmöller diagrams of predicated rainfall accumulation from the CONTL (left column) and IPHEx (middle column) simulations; Hovmöller diagrams of predicted vertically integrated moisture convergence within 500 m AGL from the IPHEx simulation (right column). Note x-axis represents longitude and is read from left to right (west to east). Y-axis represents time progressing from top to bottom.**

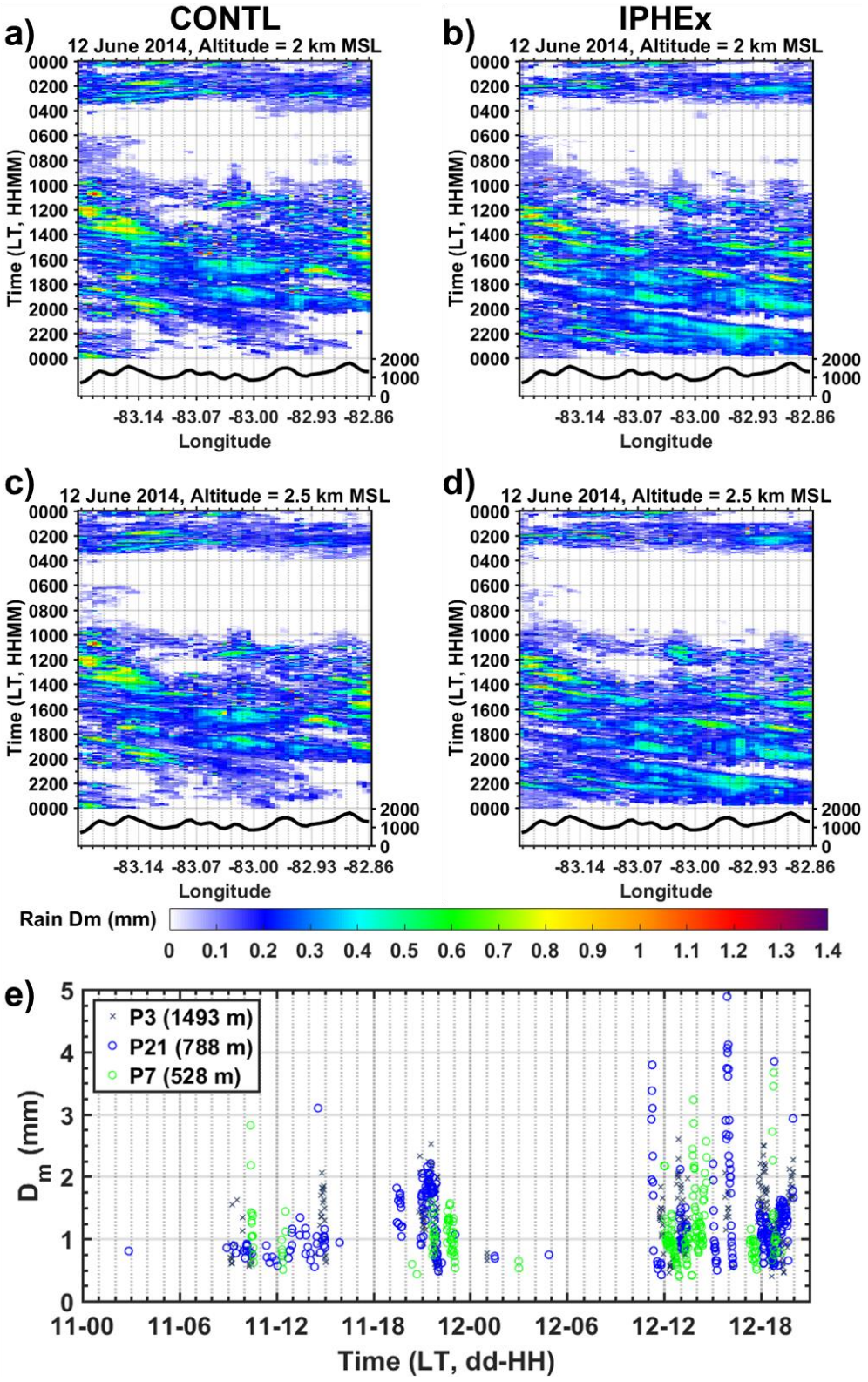
a)
CONTL
12 June 2014, Altitude = 2 km MSL
b)
IPHEx
12 June 2014, Altitude = 2 km MSL
c)
12 June 2014, Altitude = 2.5 km MSL
d)
12 June 2014, Altitude = 2.5 km MSL
Time (LT, HHMM)
0000
0200
0400
0600
0800
1000
1200
1400
1600
1800
2000
2200
0000
2000
1000
0
-83.14 -83.07 -83.00 -82.93 -82.86
Longitude
Rain Dm (mm)
0 0.1 0.2 0.3 0.4 0.5 0.6 0.7 0.8 0.9 1 1.1 1.2 1.3 1.4
e)
P3 (1493 m)
P21 (788 m)
P7 (528 m)
D_m (mm)
0
1
2
3
4
5
11-00
11-06
11-12
11-18
12-00
12-06
12-12
12-18
Time (LT, dd-HH)

**Figure 5-6: Hovmöller diagrams of the modeled rain $D_m$ at different altitudes (2 km and 2.5 km MSL) along the D-D' cross section from the CONTL (a, c) and IPHEx (b, d) simulations for 12 June event in comparison with ground observations from PARSIVEL disdrometers (see locations in Fig. 5-1). In (e), the elevation of each disdrometer is specified in the parentheses in the legend.**

To examine the sensitivity of cloud microphysics to changes in CCN types, the Hovmöller diagrams of cloud droplet number concentrations (CDNC) at different altitudes above the D-D' cross section for 11 June and 12 June are displayed in Fig. E5 and Fig. 5-7, respectively. As noted in Figs. E5a and b, persistent LLC are present throughout the day over the eastern ridge (elevation ~ 1760 MSL, denoted by the thick black line at the bottom of each plot) in both simulations. The cloud cover appears to be less frequent at a higher altitude (2.5 km MSL, Figs. E5c and d). It is also noteworthy that number concentrations of cloud droplets in IPHEx are approximately two to four times higher than the values in CONTL (100 – 200 $cm^{-3}$) on both days. As shown in the right column of Fig. 5-7, widespread low-level cloudiness around mid-day of 12 June is simulated in IPHEx especially over the inner region (highlighted in shade), consistent with the W-band radar observations at the MV supersite (Fig. E2, see its location over the inner region in Fig. 5-1).

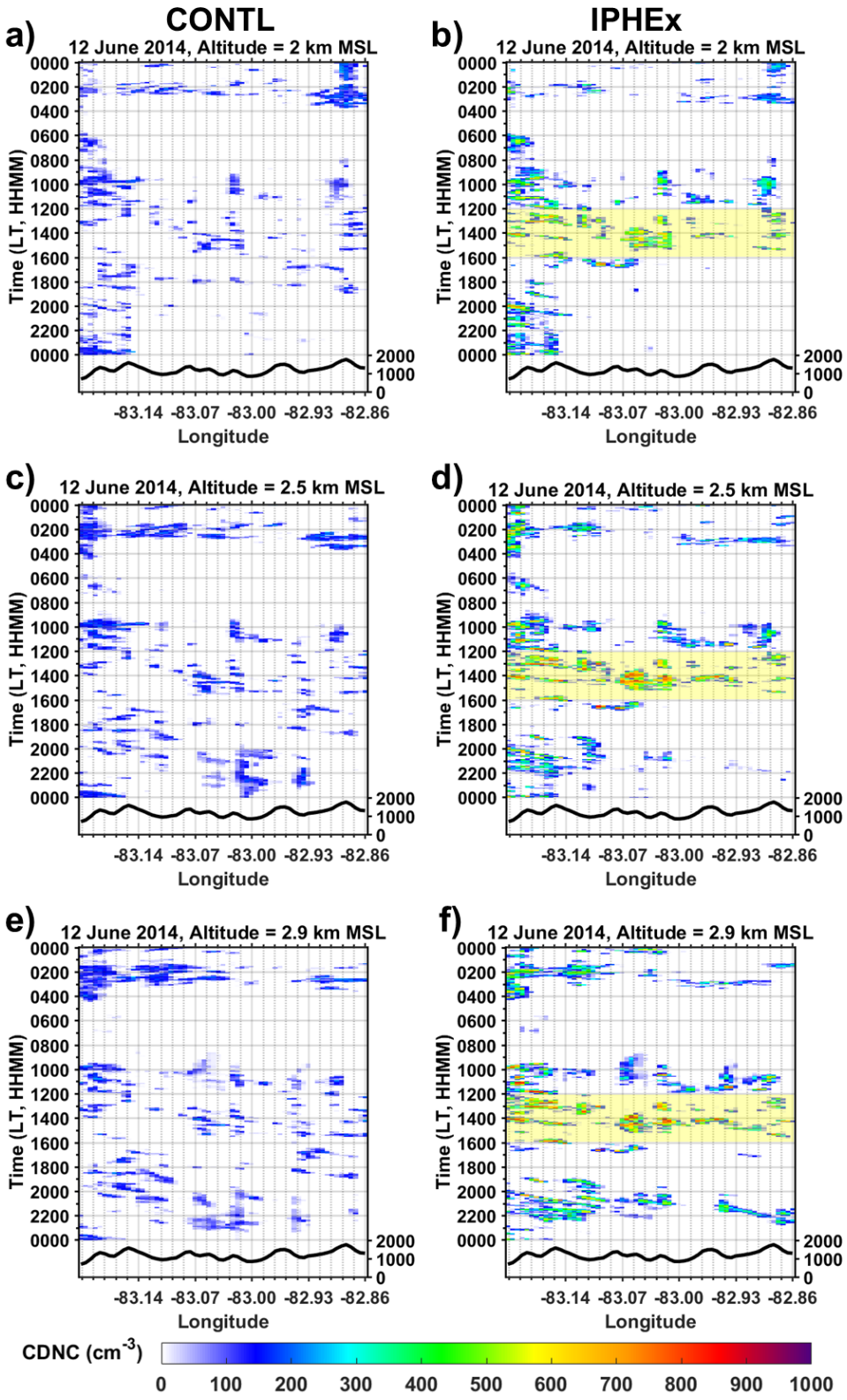
CONTL
IPHEx
a)
b)
c)
d)
e)
f)
12 June 2014, Altitude = 2 km MSL
12 June 2014, Altitude = 2.5 km MSL
12 June 2014, Altitude = 2.9 km MSL
Time (LT, HHMM)
0000
0200
0400
0600
0800
1000
1200
1400
1600
1800
2000
2200
2000
1000
0
-83.14 -83.07 -83.00 -82.93 -82.86
Longitude
CDNC (cm-3)
0 100 200 300 400 500 600 700 800 900 1000

**Figure 5-7: Hovmöller diagrams of simulated cloud droplet number concentration (CDNC) at different altitudes (2 km, 2.5 km, and 2.9 km MSL) along the D-D′ cross section from the CONTL (left column) and IPHEx (right column) runs for 12 June event.**

The early afternoon event on 12 June was also sampled by the UND Citation aircraft, which flew over the PRB from 1214 LT to 1551 LT. Cloud concentrations and size distributions were collected by conducting successively higher constant-altitude flight transects through clouds. Fig 5-8a depicts the Citation flight tracks (in red continuous lines) over the PRB and in-cloud regions (blue dots in Fig. 5-7a) are identified with minimum liquid water content (LWC) of 0.25 g $m^{-3}$ from the cloud droplet probe (CDP) aboard the UND Citation. The LWC is derived by integrating the size-resolved concentrations of cloud droplets measured by the CDP, which covers droplet diameter from 2 to 50 μm. As seen in Fig. 5-8b, the in-cloud samples (blue dots in Fig. 5-8a) exhibit pronounced vertical variations in total number concentrations, indicating a general decreasing trend of drop numbers with height. Along the first horizontal leg (~ 2.8 km MSL), droplet number concentrations vary from 100 to 700 $cm^{-3}$, highlighting a large spatial variability in cloud characteristics over this region. At a similar altitude (~ 2.9 km MSL, Fig. 5-7f), the IPHEx prediction captures well the observed variability and is in good agreement with the airborne measurements. On the other hand, significantly underestimated CDNC with small spatial variations by CONTL fail to represent persistent LLC observed in this region, as reported by campaign measurements and the satellite-based climatology study discussed in Sect. 3.

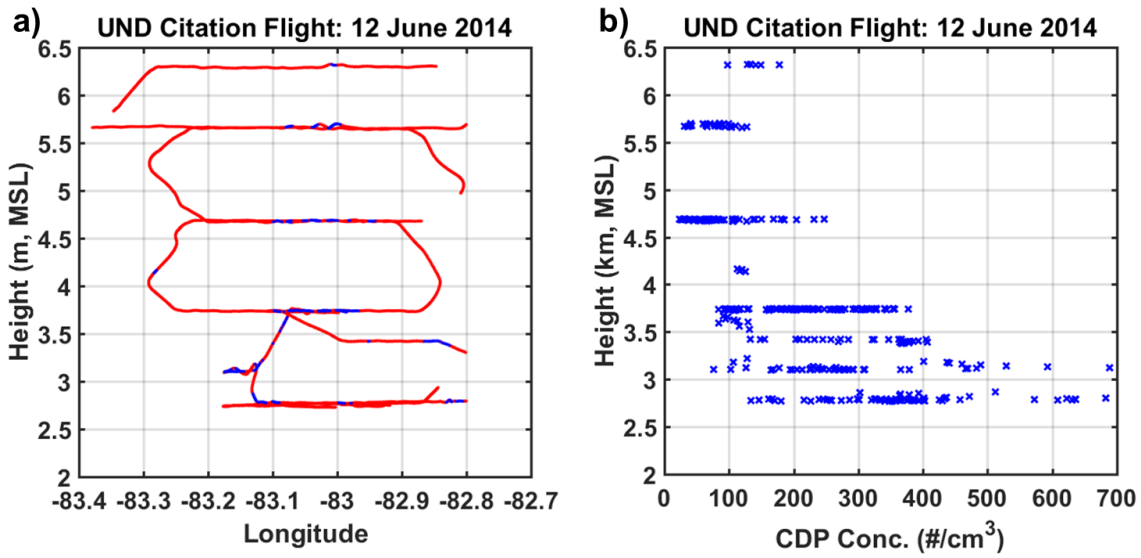


**Figure 5-8: a) UND Citation flight track over the PRB on 12 June 2014 with cloudy regions indicated by blue dots. b) Cloud droplet concentrations measured by the CDP onboard the Citation aircraft.**

### 5.3.2 Effects of aerosol-cloud interactions on regional precipitation

With the confidence in the performance of the WRF simulations as evaluated against *in situ* observations from the campaign, we can explore the larger picture of aerosol effects on clouds and precipitation on the regional scale. The comparisons of the 24-hr accumulated precipitation for 11 June and 12 June between CONTL and IPHEx simulations in D03 are displayed in Fig. 5-9 as well as the difference between two runs for each day. Due to the approaching trough on 11 June, a substantial amount of rainfall is yielded on the western side of the SAM as indicated in the left column of Fig. 5-9. Under such strong synoptic forcing conditions on 11 June (see Fig. E3a), similar spatial patterns in precipitation are produced in both simulations but significantly lower amounts in rainfall accumulation are apparent in the IPHEx run.

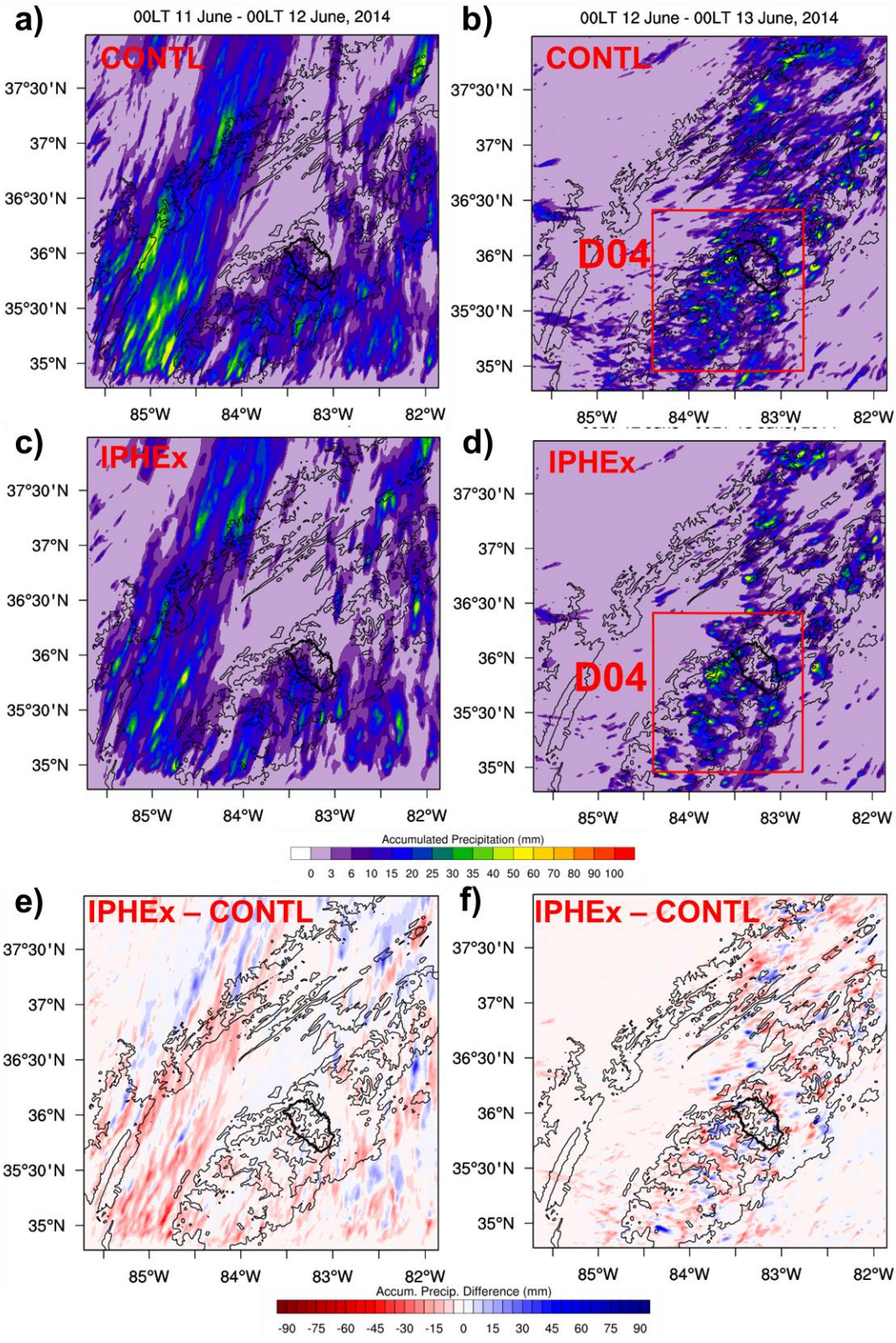
a)
00LT 11 June - 00LT 12 June, 2014
CONTL
b)
00LT 12 June - 00LT 13 June, 2014
CONTL
D04
c)
IPHEx
d)
IPHEx
D04
37°30'N
37°N
36°30'N
36°N
35°30'N
35°N
85°W
84°W
83°W
82°W
Accumulated Precipitation (mm)
0 3 6 10 15 20 25 30 35 40 50 60 70 80 90 100
e)
IPHEx – CONTL
f)
IPHEx – CONTL
Accum. Precip. Difference (mm)
-90 -75 -60 -45 -30 -15 0 15 30 45 60 75 90

**Figure 5-9: Total accumulated precipitation and the corresponding differences between the CONTL and IPHEx simulations (difference = IPHEx - CONTL) on 11 June (left column) and 12 June (right column). In (b) and (d), the D04 box bounding the region of rainfall maxima on 12 June will be used in later discussion.**

On 12 June (right column of Fig. 5-9), the rainfall maxima shift eastward to the mountainous areas in both simulations. Under weak synoptic forcing conditions on 12 June (see Fig. E3b), mesoscale processes modulated by the topography play a dominant role in redistributing the precipitation in this region, resulting in rainfall "hot-spots" with accumulation up to 100 mm in high terrain. We can also note that the difference in total accumulated rainfall between CONTL and IPHEx (difference = IPHEx - CONTL) on 12 June is considerably greater than 11 June over the mountainous regions, suggesting that CCN characteristics have a larger influence on local precipitation processes in complex topography on 12 June. This highlights the contrast between the 11 June event that are controlled by the large-scale forcing and the 12 June event in which local aerosols play a more significant role under weak synoptic forcing conditions.

To examine the aerosol effects on cloud formation, the time series of cloud cover in D03 between the CONTL and IPHEx simulations are shown in Fig 5-10. The cloud fraction is calculated as the ratio of model grids with cloud liquid water path (LWP) > 0.1 $kg/m^2$ to the total grid numbers in D03. Generally speaking, larger areas of clouds are developed in IPHEx especially during the afternoon. The changes in cloud cover can have further implications on radiative forcing and surface heat budget as the increase in cloudiness due to aerosol indirect effects can reduce the amount of solar radiation

reaching the ground, and therefore less heat is available for evaporation (Ramanathan et al., 2001;Wilson and Barros, 2017). For example, significant differences in cloud cover fraction is estimated between two simulations during 14−16 LT on 11 June (highlighted by the yellow shade in Fig. 5-10a). The corresponding temporal mean and coefficient of variance (CV = standard deviation/mean) of the differences in surface shortwave radiation and surface temperature between CONTL and IPHEx (difference = IPHEx - CONTL) are shown in Figs. 5-10b-e, Although large variations are present in D03 due to the fast-moving nature of clouds, changes in surface shortwave radiation and temperature between two simulations indicate robust spatial patterns with positive/negative mean values with small absolute values of CV ($|CV|<1$, indicated by cyan or green colors in Figs. 5-10c and e). In particular, high number concentrations of fine CCN in IPHEx result in decreased solar radiation (average values down to ~ -100 $W/m^2$) and consequently cause surface cooling (average values down to ~ -2 K) over the PRB (indicated by the black thick line in Fig. 5-2b) whereas large temporal variations (CV~ -2 − -1) are evident over the basin. Similar analysis was also performed for the early afternoon (12−15 LT) on 12 June (highlighted by the yellow shade in Fig. 5-10a) as shown in Fig. E6. Due to changes in synoptic forcing conditions, a larger spatial variability of differences in surface shortwave radiation and temperature between two simulations is manifest on 12 June when mesoscale processes with topography modulation govern the formation and evolution of clouds, consequently influencing radiative forcing and surface heat budget in this region.

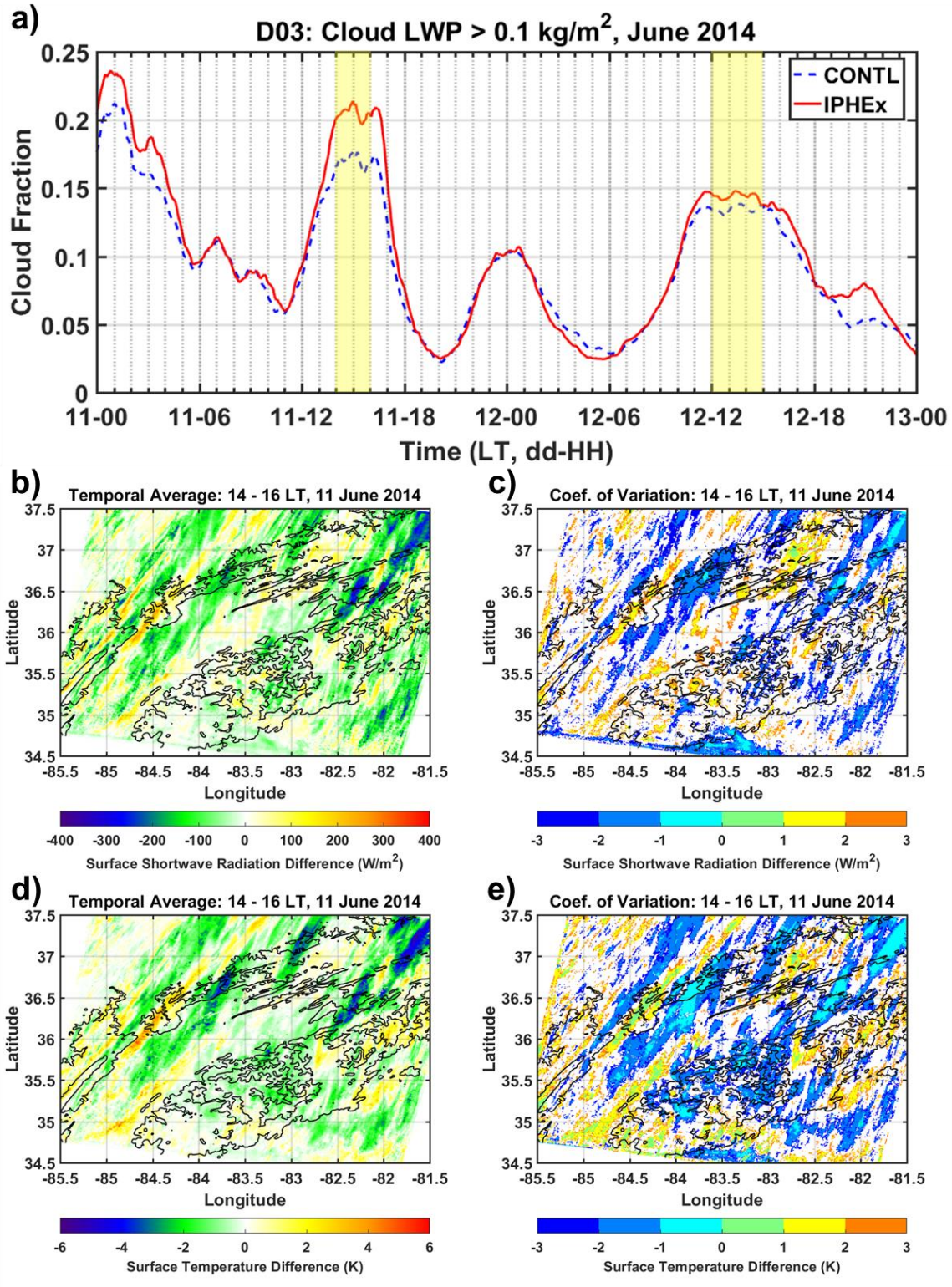
a)
D03: Cloud LWP > 0.1 kg/m2, June 2014
CONTL
IPHEx
Cloud Fraction
0.25
0.2
0.15
0.1
0.05
0
11-00
11-06
11-12
11-18
12-00
12-06
12-12
12-18
13-00
Time (LT, dd-HH)
b)
Temporal Average: 14 - 16 LT, 11 June 2014
Latitude
Longitude
Surface Shortwave Radiation Difference (W/m2)
c)
Coef. of Variation: 14 - 16 LT, 11 June 2014
Latitude
Longitude
Surface Shortwave Radiation Difference (W/m2)
d)
Temporal Average: 14 - 16 LT, 11 June 2014
Latitude
Longitude
Surface Temperature Difference (K)
e)
Coef. of Variation: 14 - 16 LT, 11 June 2014
Latitude
Longitude
Surface Temperature Difference (K)

**Figure 5-10: a) Time series of cloud coverage (defined as cloud liquid water path > 0.1 kg/m$^3$) fraction in D03 for the CONTL and IPHEx simulations. Bottom panel: Temperature average and coefficient of variance (CV) of differences in surface shortwave radiation (b, c) and surface temperature (d, e) during 14–16 LT on 11 June 2014, as highlighted by the yellow shade in (a).**

To examine the microphysical impacts of the CCN characteristics on the spatiotemporal evolution of cloud and precipitation, further analysis was conducted in a smaller domain 4 (D04, red box in Fig. 5-9) where rainfall maxima are predicted at high elevation on 12 June in both simulations. Figure 5-11 shows time series of rainfall rate, cloud LWP, ice water path (IWP), and rain LWP averaged over the area with terrain elevation above 500 m MSL in D04. The modeled LWP is integrated from vertical profiles of cloud and rain mixing ratios and the modeled IWP accounts for ice, snow, graupel and hail hydrometeors. Although both simulations exhibit similar timing for the onset of the afternoon rainfall event on 11 June, the rainfall on 12 June in the IPHEx run is suppressed in the initial stage of the afternoon event as compared to CONTL, and a second peak is produced in the evening around 1930 LT for IPHEx. It is also noteworthy that the cloud LWP in IPHEx is significantly enhanced throughout the events compared to CONTL (Fig. 5-11b). This can be attributed to the fine CCN characteristics (high number concentrations at high supersaturation) observed during IPHEx. As a result of high CCN concentrations, decreases in rain LWP in the IPHEx run are evident on both days whereas increases in IWP are observed in the late afternoon and evening of 12 June in IPHEx. The suppression of rain LWP and enhancement of IWP under high-CCN conditions can be likely explained

by reduced sizes of cloud droplets in the IPHEx simulation. This reduction in drop sizes can result in decreased efficiency of coalescence and warm rain processes, hence allowing more cloud particles to be transported above the freezing level and subsequently forming more ice-phase particles (Rosenfeld and Woodley, 2000;Tao et al., 2007). Note that more significant indirect effects due to changes in CCN types are demonstrated in the rainfall events on 12 June, and they will be the focus of our discussion henceforth.

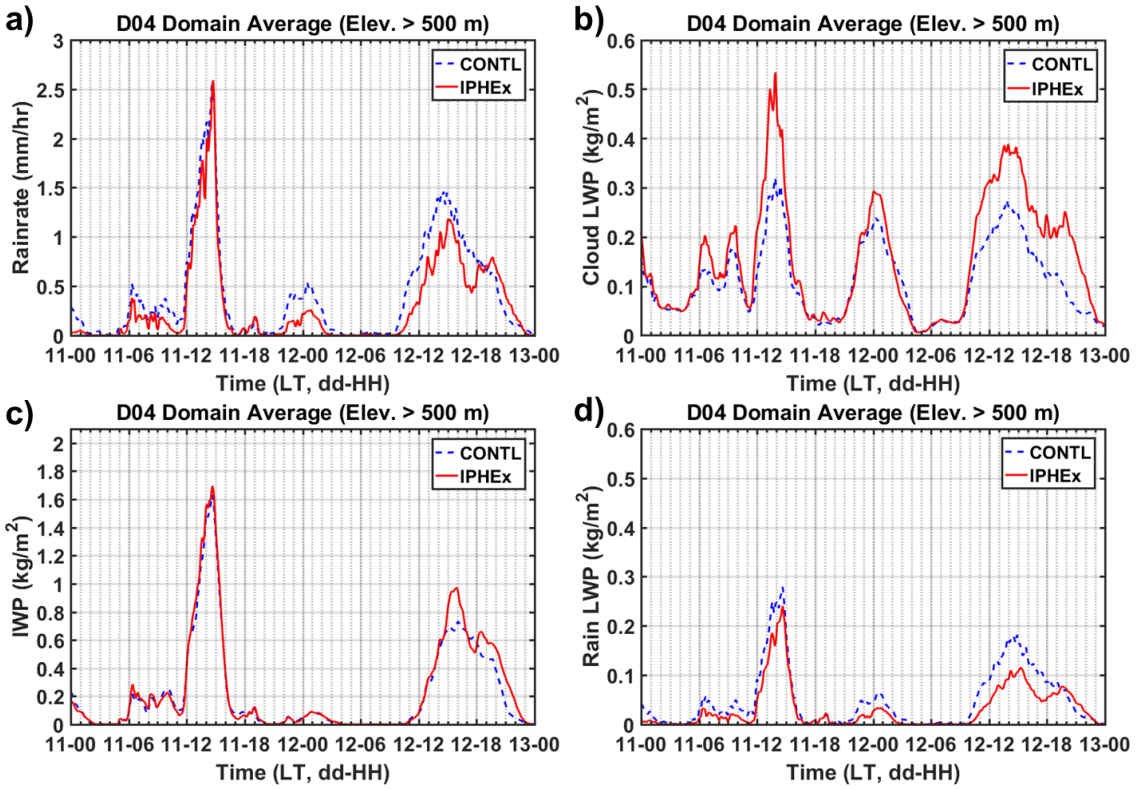


**Figure 5-11: Time series of rainrate (a), cloud liquid water path (LWP, b), ice water path (IWP, c) and rain LWP (d) averaged over area with terrain elevation above 500 m MSL in D04 (red boxes in Figs. 5-9b and d) for two simulations. Cloud and rain hydrometeors are included in the LWP. Ice, snow, graupel and hail particles are counted in the IWP.**

For the afternoon and evening events on 12 June, the changes in spatial variability of vertically integrated LWP and IWP to different CCN characteristics from the two simulations are also manifest and their distributions averaged during 1200 – 1600 LT and 1800 – 2100 LT are shown in Fig. 5-12 and Fig. E7, respectively. As noted in Figs. 5-12a and b, the cloud LWP over the entire D03 in the IPHEx simulation is remarkably higher than CONTL and a wider extent of cloud cover with high LWP is evident in IPHEx. It should be pointed out that maxima in cloud LWP are predicted over the mountain ridges, consistent with previous findings of frequent daytime occurrences of LLC over the ridgelines of the SAM based on long-term satellite observations (see Sect. 3.4). The rain LWP in IPHEx is generally suppressed and the precipitation distribution is organized to be more concentrated over the mountainous area (Figs. 5-12c and d). Although ice hydrometeors are produced over a broader area in CONTL, larger core areas of the storm cells with higher values of IWP are estimated in the IPHEx run. This suggests enhanced formation of ice particles aloft, hence fostering cold rain processes. Similar features of increased IWP are also present in the main structure of the storm during 1800 – 2100 LT on 12 June (see Figs. E7e and f), likely contributing to the early evening rainfall peak in the IPHEx simulation (Fig. 5-11a). To distinguish microphysical processes involved in the afternoon and evening rainfall events, total rainfall accumulations during 1200 – 1700 LT and 1700 – 2400 LT are shown in Fig. 5-13. The cross section A-A' marked in Figs. 5-13a

and b passes through major storm cells of the afternoon event and cross section E-E′ marked in Figs. 5-13c and d spans the main storm structure of the evening event.

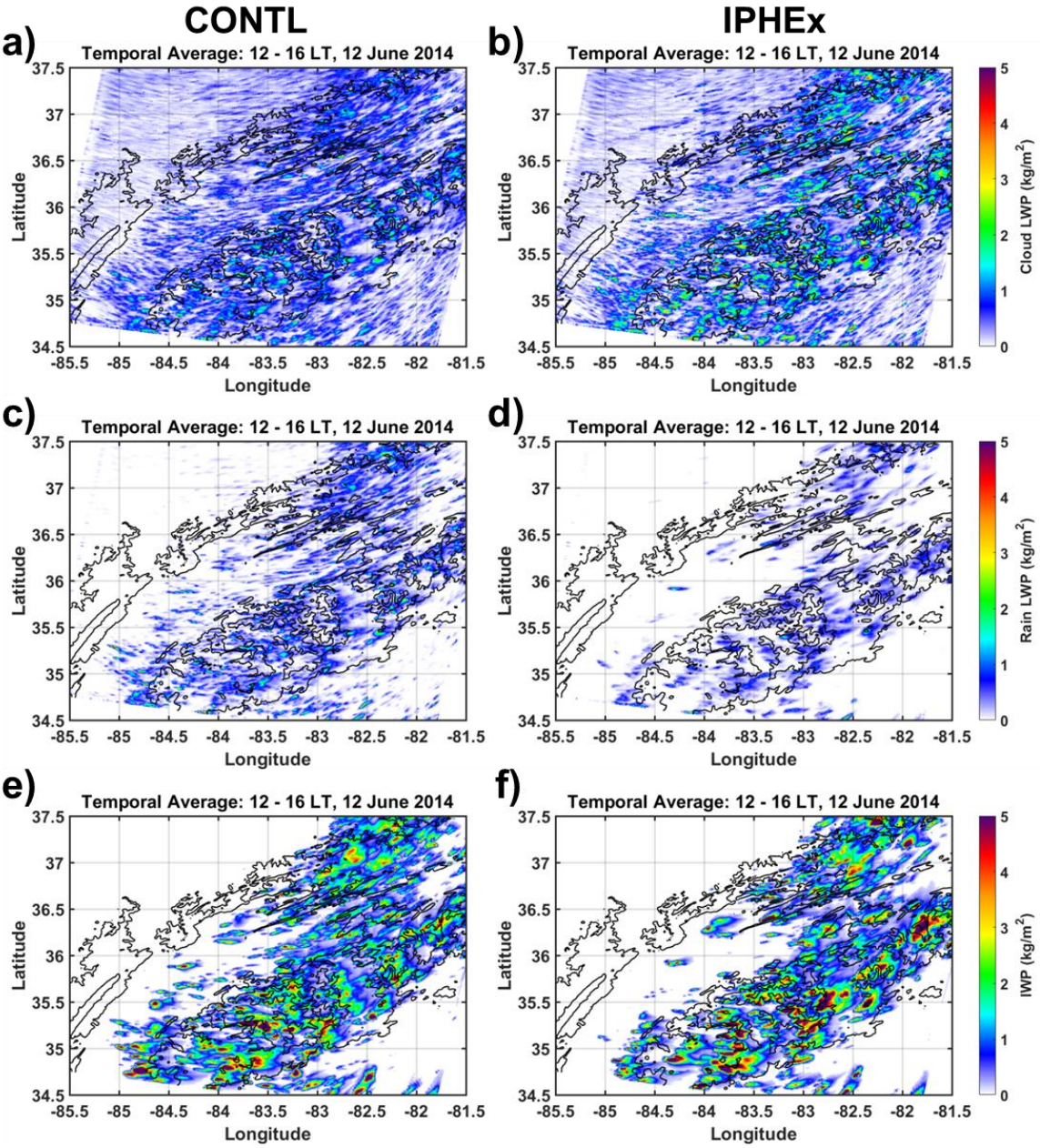


**Figure 5-12: Spatial variations of cloud LWP (a, b), rain LWP (c, d), and IWP (e, f) averaged over 1200 – 1600 LT on 12 June 2014 for the CONTL (left column) and IPHEx (right column) simulations.**

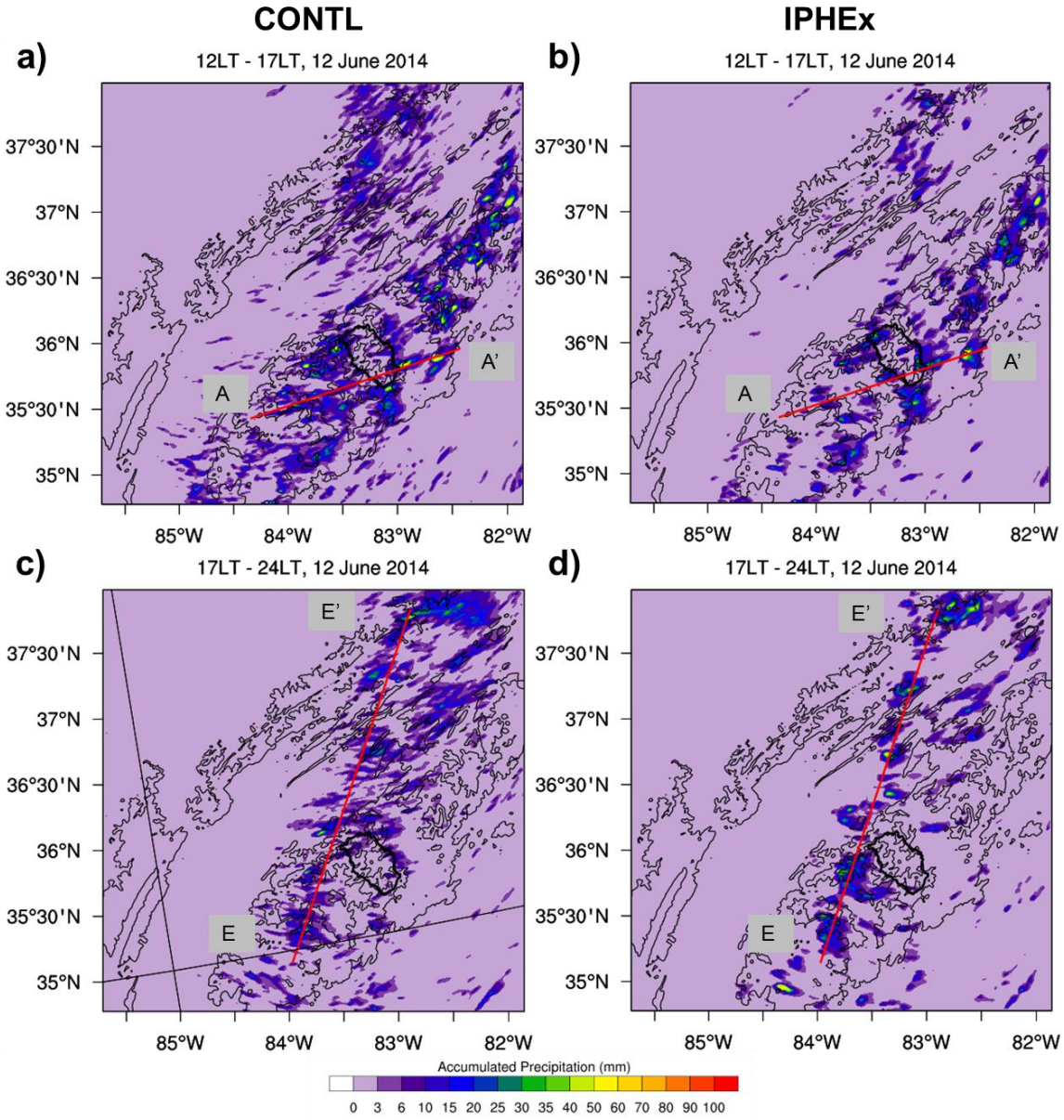


**Figure 5-13: Accumulated precipitation during 1200 – 1700 LT (top panel) and 1700 – 2400 LT (bottom panel) on 12 June 2014 for the CONTL (left column) and IPHEx (right column) simulations. Cross sections A-A′ and E-E′ marked in each plot will be used in later analysis.**

The temporal and spatial progression of rainfall across A-A′ and E-E′ for the CONTL and IPHEx simulations on 12 June are shown in Fig. 5-14 and Fig. E8, respectively.

Distinct from rainfall propagation associated with strong frontal passage, scattered showers in the afternoon are present along the cross section with localized rainfall propagating eastward in both simulations as indicated in Fig. 5-14. Over the western and inner segments of A-A', the precipitation initiation is delayed in IPHEx and less amount of light to moderate rainfall is produced as compared to CONTL. In both simulations, heavy precipitation (~ 90 mm/hr) is estimated at the eastern side as a result of strong convective activity in the early afternoon (1200 – 1400 LT). A second rainfall peak around 1530 LT in IPHEx contributes to larger rainfall accumulation by the end of the event over the eastern side. For the evening event on 12 June, more widespread showers are observed along the E-E' cross section in both simulations and much higher rainfall accumulation is predicted in IPHEx as compared to CONTL (Fig. E8).

To investigate the interplay between microphysics and dynamics of the afternoon precipitation at different phases, the vertical structure of the major storm cells (averaged over longitude in the red box) was examined here. The temporal evolution of the key hydrometeors and vertical component of wind speed, and the mass-weighted mean diameter ($D_m$) of cloud and rain droplets are presented in Fig. 5-15 and Fig. 5-16, respectively. As indicated in the left column of Fig. 5-15, the mixing ratios of various hydrometeors are plotted as contour lines with the minimum value of 0.25 g/kg for all hydrometeors but set at different intervals (Hail, cloud, and graupel: 0.5 g/kg; rain: 0.25 g/kg). In Fig. 5-16, number concentrations of cloud droplets (with the minimum value of

100 $cm^{-3}$ and an increment interval of 100 $cm^{-3}$) and number concentrations of rain drops (with the minimum value of 0.001 $cm^{-3}$ and an increment interval of 0.001 $cm^{-3}$) are represented as black contour lines in the left column and right column, respectively.

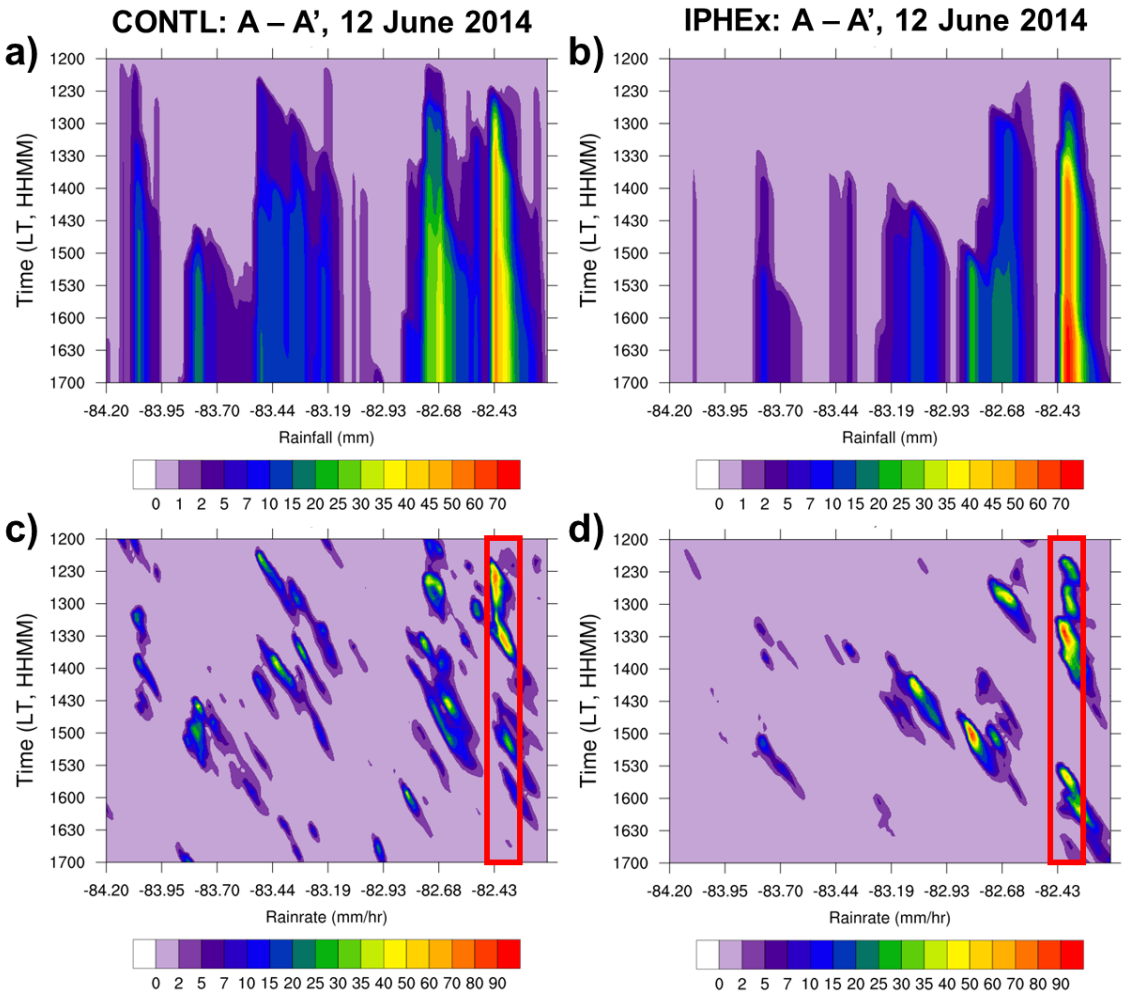


**Figure 5-14: Simulated rainfall accumulation (a, b) and rainrate (c, d) along the A-A' cross section from the CONTL (left column) and IPHEx (right column) runs for the afternoon event on 12 June 2014. The red boxes in (c) and (d) highlight key storm cells predicted in both simulations.**

As noted in Fig. 5-15, the timing of the early afternoon rainfall event in both simulations is consistent, however suppressed precipitation is evident at the initial stage

(1200 – 1300 LT) of the IPHEx simulation. During 1200 – 1300 LT, the IPHEx simulation predicts smaller sizes of cloud and rain droplets as well as significantly higher concentrations of cloud droplets compared to CONTL (Fig. 5-16). On the contrary, heavier rainfall with longer duration is produced by IPHEx in the late afternoon event although precipitation is delayed by half an hour compared to CONTL (Fig. 5-15). The likely explanation for the IPHEx simulated results of the early afternoon event is that the larger amount of smaller cloud droplets diminishes the autoconversion efficiency of cloud droplets to rain drops and hence it allows more evaporative cooling of these increased cloud droplets. This further leads to accelerated downdrafts intensity and consequently enhanced updrafts at higher altitudes (Fig. 5-15d) as a result of strengthened gust front (Lee et al., 2010;Tao et al., 2007).

Due to changes in cloud dynamic structure, the response of cloud microphysical processes to aerosols is further enhanced. With increased gustiness in the IPHEx simulation, more small cloud drops are uplifted above the supercooled levels and freeze onto ice particles, yielding a larger amount of graupel (blue contours, Fig. 5-15c). This leads to the release of additional latent heat of freezing aloft and absorption of heat at lower levels when falling ice particles melt, thus enhancing local circulations and subsequently invigorating deeper convective clouds (Rosenfeld et al., 2008). During the intermission of rainfall, low-level clouds (top < 5 km) are developed in the IPHEx simulation, consistent with the W-band radar observations at MV (Fig. E2).

For the late afternoon event, the simulated precipitation structure in IPHEx suggests a deep system with the cloud top extending above 10 km, which allows intensive interactions between the microphysics and dynamics of the cloud. Due to the changes in evaporative cooling and the vertical structure of latent heating as discussed above, the vertical velocity and upward advection of moist air is stronger in IPHEx, thus favoring graupel production and subsequently yielding a large amount of rainfall. Although delayed precipitation is estimated in IPHEx, rain formation via the ice phase becomes more efficient and offsets the suppressed warm rain processes.

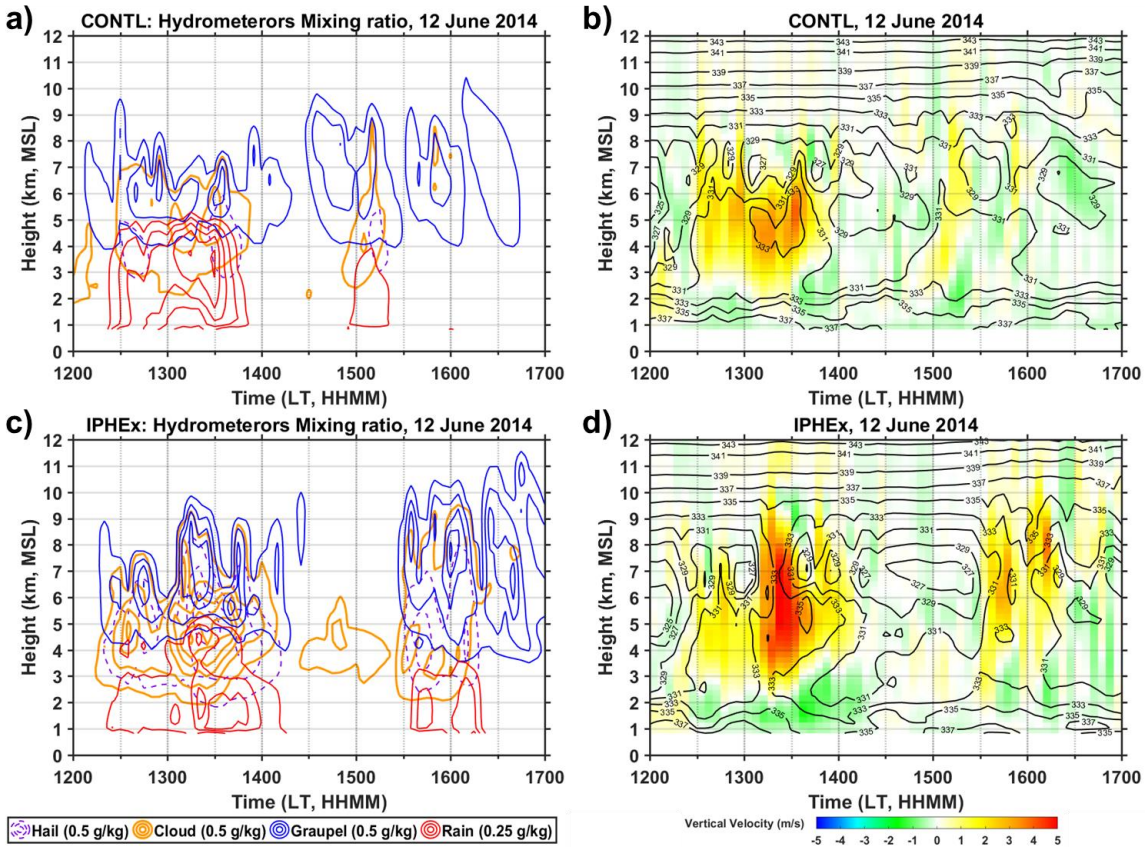


**Figure 5-15: Temporal evolution of the averaged vertical profiles of the primary hydrometeors (a, c) and vertical velocity (b, d) for the major convective cells identified**

in Fig. 5-14 (averaged along longitude in the red box) in CONTL (top panel) and IPHEx (bottom panel). In (a) and (c), the minimum value of colored contours is set at 0.25 g/kg for all hydrometeors. Hail, cloud, graupel are increased at an interval of 0.5 g/kg and rain at an interval of 0.25 g/kg. In (b) and (d), equivalent potential temperature is denoted by black contours with its values indicated in text.

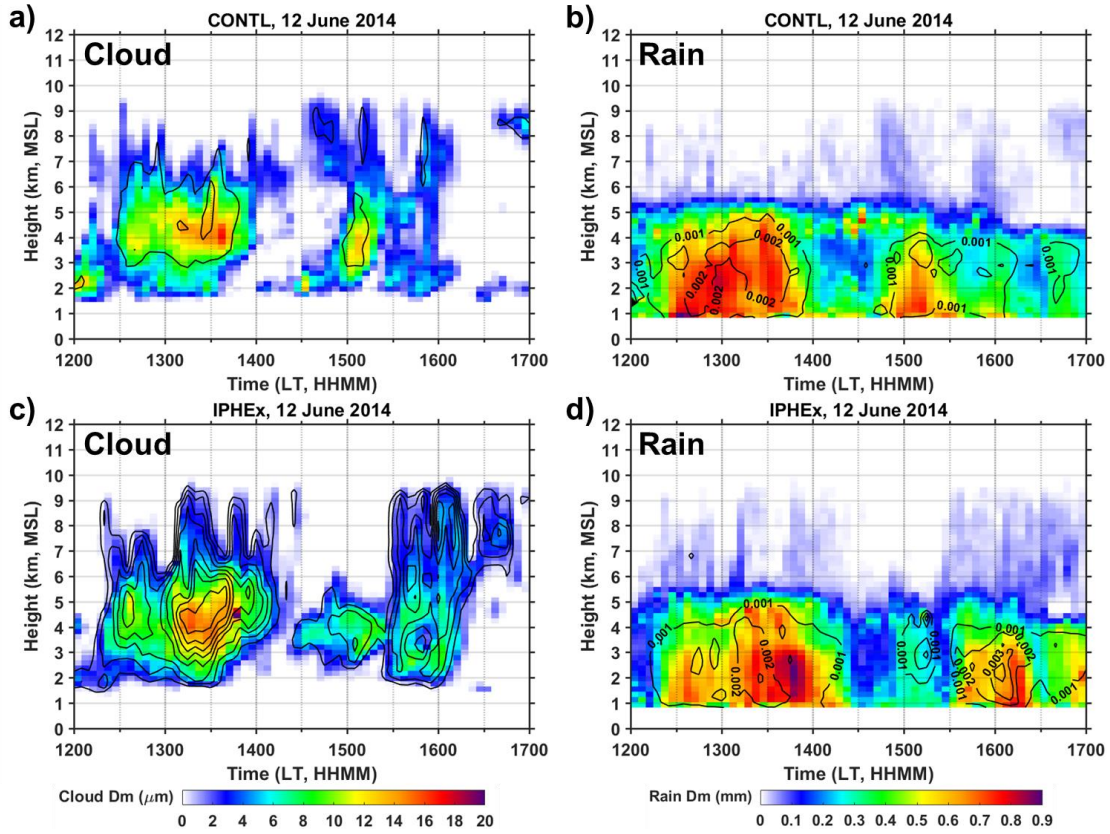


Figure 5-16: Temporal evolution of the averaged vertical profiles of the cloud Dm (a, c) and rain Dm (b, d) for the major convective cells identified in Fig. 5-14 (averaged along longitude in the red box) in CONTL (top panel) and IPHEx (bottom panel). In (a) and (c), cloud droplet number concentrations are denoted by black contours with the minimum value of 100 $cm^{-3}$ and an increment interval of 100 $cm^{-3}$. In (b) and (d), rain droplet number concentrations are denoted by black contours with its values indicated in text.

## 5.4 Conclusions and discussion

To investigate the sensitivity of cloud formation and warm season precipitation in the SAM to variations in aerosol properties, two WRF simulations using different CCN types were conducted in this study and the modeling results presented here demonstrate that changes in CCN characteristics have a significant impact on both microphysical and dynamical processes of summer precipitation events in the SAM, as well as on the spatial distributions of LLC and surface precipitation. To better represent local aerosol characteristics in the SAM, the CCN spectrum estimated from the *in situ* measurements in the inner SAM during the IPHEx campaign was incorporated to the model microphysics scheme MY05. Thus, sensitivity tests were performed by using the standard continental CCN spectrum in MY05 and the local CCN spectrum from IPHEx with high concentrations of fine aerosols.

The case study presented here is a two-day precipitation event (11–12 June 2014) during the IPHEx IOP, when extensive measurements of aerosol/CCN, cloud, and precipitation are made available in the complex topography of the SAM. Different synoptic environments are associated with the rainfall events on 11 June (strongly synoptically forced) and 12 June (locally forced). In both model simulations, the onset and timing of predicted rainfall events are in general consistent with raingauge observations. The IPHEx simulation on 11 June better replicates the afternoon rainfall patterns recorded by the surface raingauge network in the PRB with heavier precipitation observed over the

inner region. On 12 June, the modeling results in both simulations underestimate the large amount of rainfall accumulated in the raingauges over the inner region. In both runs, the simulated $D_m$ profiles show small variations in the vertical structure within the lower 2 km AGL. The modeled $D_m$ values near the surface for both simulations are significantly lower than ground measurements from disdrometers in particularly for valley locations. This suggests the model deficiency in representing the surface precipitation enhancement induced by SFI, which are often observed at low elevations over the inner SAM as documented in Wilson and Barros (2014) and Sect. 3.5.

As expected, different CCN features have a direct influence on the microphysical characteristics of LLC and their temporal and spatial variability in the SAM. Compared to the CONTL, a broader coverage of clouds associated with high LWP is estimated in the IPHEx simulation, which is attributed to the activation of fine aerosol particles with high concentrations. The results from the IPHEx predictions also suggest daytime maxima in cloud LWP occurring over mountain ridges, which agrees with long-term satellite measurements over the SAM as described in Sect. 3. At low-levels, the estimated number concentrations of cloud droplets in the IPHEx simulation are remarkably higher than the values in CONTL by approximately two to four times and better agreement of cloud droplet numbers is achieved between the IPHEx predictions and the airborne measurements collected around the same altitude. Moreover, the IPHEx run well captures the spatial variations in droplet numbers of LLC observed by the aircraft and accurately

replicates widespread low-level cloudiness around mid-day especially over the inner region, consistent with ground radar observations in the inner SAM.

This study also demonstrated further effects on the microphysical and dynamical characteristics of cloud systems and precipitation fields as a result of variations in aerosol properties. The rainfall events on 11 June and 12 June illustrate the contrast of aerosol effects on surface precipitation under strong and weak synoptic forcing conditions. Although suppression of surface rainfall accumulation is resulted in the IPHEx simulation for both days, a larger impact induced by changes in CCN characteristics is evident on 12 June when local processes play a dominant role in redistributing precipitation over the mountainous regions. Model results on both days show that the high concentrations of fine CCN in IPHEx cause a delay in convection initiation and precipitation onset due to decreased efficiency of converting numerous cloud droplets of smaller sizes to precipitation-sized drops, and hence hinder warm rainfall processes. The microphysical characteristics of simulated clouds are further affected by changes in CCN properties by virtue of allowing more small cloud drops to be uplifted above the freezing level, thus releasing additional latent heat of freezing aloft by freezing on ice hydrometeors and resorbing heat at lower levels by melting ice particles (Rosenfeld et al., 2008). Therefore, rainfall formation via the ice phase becomes more active and produces a large amount of graupel, contributing to significantly enhanced IWP in the storm cells. The variations in CCN characteristics also influence the dynamical structure of the storm through

accelerating evaporative cooling of small cloud droplets at low-levels and hence altering the vertical velocity field (intensified downdrafts at low altitudes and stronger updrafts at high altitudes) due to strengthened gust front (Lee et al., 2010;Tao et al., 2007).

The findings in this study emphasize the importance of specifying regional-representative CCN to provide a realistic description of local cloud features and subsequently conduct detection and attribution studies of aerosol-cloud interactions on precipitation initiation and evolution. To interpret the preliminary results between the two simulations in this work, we presented two possible explanations that additional release (absorption) of latent heat is caused by freezing (melting) of hydrometeors and evaporative cooling of small cloud droplets is enhanced due to the delay of early warm rain based on previous modeling studies (Lee et al., 2010;Rosenfeld et al., 2008;Tao et al., 2007). In future work, we will focus on quantifying the contribution of these potential processes by examining the latent heat cooling due to melting ice particles and evaporation, and the riming rate. We are also aware of the complex and highly nonlinear processes of ACPI and the findings of a particular precipitation event may not be applicable for other synoptic conditions or different cloud systems. Therefore, more case studies representing distinct precipitation systems will be conducted systematically in order to achieve a comprehensive understanding of ACPI in complex terrain.

# 6. Summary and conclusions

This section will provide a summary of the dissertation (Section 6.1), outline major research findings (Section 6.2), and discuss limitations in this work and suggestions for future research (Section 6.3).

## *6.1 Research summary*

The overarching objective of this dissertation is to advance the quantitative understanding of the indirect effect of aerosols on the diurnal cycle of low-level clouds and fog (LLCF) and warm-season precipitation in mountainous regions generally, and in the Southern Appalachian Mountains (SAM) in particular, for the purpose of improving the representation of orographic precipitation processes in remote sensing retrievals and physically-based models. The focus of this dissertation research in the SAM stems from the opportunity to leverage the existing wealth of data and modeling experience. Findings from this research can be transferable to other regions of complex topography with high biogenic aerosol loading and persistent LLCF, such as cloud forests, low- and mid-mountains in the humid tropics and extra-tropics.

The SAM is an invaluable hot-spot of biodiversity with old-growth, temperate forest ecosystems. The Great Smoky Mountains National Park (GSMNP) located in this region is recognized as an International Biosphere Reserve and World Heritage Site by UNESCO. The GSMNP is also one of the most visited national parks in the United States, which drew more than eleven million visitors in 2016 (NPS 2016). However, the SAM is

vulnerable to anthropogenic influences such as land use/land cover change and climate change due to its proximity to accelerated population growth in the southeastern United States. If reduced cloudiness and rising cloud ceilings persist in this region as a result of global warming, the mountain-top spruce-fir forests in the SAM that are strongly reliant on cloud immersion, may shift upward in elevation, thus severely threatening the existence of this relic forest (Berry and Smith, 2013). In the SAM, light rainfall (≤ 3mm/hr) accounts for 30–50% and higher of annual freshwater input to headwater catchments (Barros, 2013; Wilson and Barros, 2014, 2015). Orographic precipitation captured by headwater catchments is major freshwater resource for downstream areas (Barros, 2013). For example, headwater catchments in the SAM provide freshwater supply for more than 20 million people in adjacent lowlands (Wilson, 2016). Thus, light rainfall detection and estimation over complex terrain is critical in water cycle studies and regional water budgets, yet it still stands as a grand challenge in satellite precipitation retrievals. During the summer of 2014, this region was chosen as the core domain of the first field campaign of the Global Precipitation Mission (GPM) ground validation-IPHEx (Integrated Precipitation and Hydrology Experiment), which provides a comprehensive dataset of cloud and precipitation observations in the SAM. The GPM core satellite was launched in February 2014. The primary goal of the Dual-frequency Precipitation Radar (DPR) aboard the GPM is to provide improved measurements of light precipitation and solid

precipitation compared to its predecessor TRMM Precipitation Radar (PR), which is capable of observing moderate and heavy rainfall (Hamada and Takayabu, 2016).

Because of the long-standing historical presence of haze and fog in the SAM, this area is known as the "Smoky Mountains" due to high biogenic aerosol loading (Fink 1934; Spira 2011). The hypothesis in this dissertation is that the low-level cloudiness and precipitation features observed in this region are governed by the availability of aerosols, mostly likely originating from the dense forest in the SAM. Multiple aerosol characterization studies have been conducted in the SAM over the past decade. Measurements from the Southeastern Aerosol and Visibility Study (SEAVS) collected at the GSMNP in rural Tennessee during the summer of 1995 indicate that degraded visibility in the Great Smoky Mountains (GSM) is associated with high concentrations of biogenic aerosols emitted from the forest and anthropogenic aerosols produced from major combustion sources (Ames et al., 2000;Hand et al., 2000;Lowenthal et al., 2009). The 2013 Southern Oxidant and Aerosol Study (SOAS) sampled aerosol chemical properties at a ridge-top site on the north-western edge of the GSMNP (Look Rock, TN) aiming at examining the anthropogenic influences on biogenic secondary organic aerosol (SOA). Greatly benefited from the extensive observations of aerosol, cloud and precipitation collected in the SAM during IPHEx in 2014, this dissertation work provided the first quantitative assessment of the effects of aerosol characteristics on cloud formation and precipitation processes in the SAM, in particular at low-levels. In this study, an integrated

approach was adopted to analyze *in situ* observations from long-term observation networks (e.g., GSMNP raingauge, ASOS/AWOS), comprehensive measurements from the IPHEx campaign (e.g., aerosol/CCN instruments, large-scale ground-based radars, and aircraft), multi-satellite data (TRMM, CloudSat, CALIPSO, and MODIS), and modeling studies (parcel, column and numerical weather prediction models).

The dissertation research started by diagnosing the space-time structure of errors in precipitation measurements from the TRMM precipitation radar (PR). The satellite estimates were evaluated against a long-term raingauge network at high elevation in the SAM in order to elucidate the physical basis of retrieval errors over complex terrain. This study identified the underestimation of low-level rainfall enhancement by the satellite retrievals and this highlighted the detectability challenge of satellite observations in mountainous regions due to coarse horizontal resolutions and ground clutter effects. Because of these limitations, satellite measurements is unable to capture low-level processes between LLCF and upper precipitation systems (i.e., SFI), thus significantly underestimating low-level enhancement of precipitation recorded by ground raingauges (Duan et al., 2015; Chapter 2).

Recent research (Wilson and Barros, 2014, 2015) also suggests that LLCF amplify the diurnal cycle of orographic precipitation via SFI, leading to increased surface rainfall intensity by as much as one order of magnitude. However, this low-level rainfall enhancement is severely underestimated by TRMM observations due to its physical

limitations in complex terrain as indicated in Chapter 2. To address this, a spectral raindrop dynamics model was employed together with microphysical observations of LLCF immersion in the SAM. The modeling results illustrated how fast SFI can modify the rainfall drop size distribution near the surface and demonstrated the physical mechanisms of rainfall amplification by LLCF at local scales. To elucidate the role of LLCF at regional-scale, 10-year satellite observations from active (CALIPSO and CloudSat) and passive (MODIS) sensors were used to demonstrate the spatial co-organization of the diurnal cycle of LLCF and orographic precipitation. Cloud base height (CBH) products from CALIPSO and CloudSat were merged and evaluated against ground ceilometer measurements in the SAM. MODIS observations over the Southern Appalachians (SA) were utilized to map the spatial variability of LLCF at regional-scale and further characterize the optical and microphysical properties of daytime LLCF (Chapter 3).

To explain the persistent low-level cloudiness observed in this region, this study hypothesized that the microphysical properties and space-time distribution of LLCF in the SAM are governed by local aerosol characteristics. Thus, a spectral cloud parcel model was developed to explicitly solve activation, condensation, collision-coalescence, and lateral entrainment processes. This parcel model was applied to investigate the early development of cumulus congestus observed during the IPHEx campaign. Surface aerosol measurements sampled during IPHEx were used to initialize the parcel model and airborne observations from the campaign were used to evaluate modeling results of

cloud microphysics. This study found that variations in aerosol characteristics play a key role in the microphysical properties and thermodynamic state of orographic cumulus clouds at early stages prior to rainfall onset (Duan et al., 2017; Chapter 4).

However, considering the simplistic representation of cloud microphysical processes in a parcel model, mesoscale modeling simulations were used to probe the indirect effects of aerosols on cloud formation and precipitation evolution at local and regional scales, focusing on the impact on spatial distribution and diurnal cycle of low-level clouds (LLC) and the microphysical and dynamical processes of precipitation especially at low-levels. For this purpose, CCN spectra collected over the inner SAM during IPHEx were incorporated to the microphysics scheme in the WRF model and sensitivity tests were conducted by using the standard continental CCN spectrum in the model (CONTL) and the local CCN spectrum with high concentrations of fine aerosol particles (IPHEx). Exploratory WRF simulations were performed for summer precipitation events sampled by aircraft during IPHEx. Modeling results from the sensitivity study illustrate that different CCN features have a direct influence on the microphysical characteristics of LLC and their spatial variability in the SAM. This study also demonstrate further impacts on the microphysical and dynamical structure of the simulated storm and surface precipitation accumulation affected by changes in CCN characteristics. Moreover, this work underscores the importance of specifying regional-

based CCN to depict local cloudiness and conduct the associated modeling studies of aerosol-cloud interactions (ACI) on precipitation initiation and evolution (Chapter 5).

## 6.2 Major research findings

The major findings in this dissertation are recapitulated below along with the corresponding science questions (SQs) addressed in this research.

SQ1: What is the error structure of satellite precipitation estimates in the SAM? What is the satellite-based climatology of LLCF in the SA using multi-satellite measurements from the A-Train? What is the contribution of LLCF to the observed surface precipitation enhancement induced by SFI?

- The diagnostic error analysis of TRMM PR 2A25(V7) precipitation products reveals that detection errors are linked to persistent stratiform light rainfall in the SAM, which explains the high occurrence of false alarms throughout the year, as well as the diurnal maximum of missed detections at mid-day in the cold season (fall and winter) especially in the inner region.
- The TRMM PR product underestimates low-level orographic enhancement of rainfall associated with fog, cap clouds and cloud to cloud feeder–seeder interactions over ridges and in the valleys.
- Precipitation associated with small-scale systems (< 25 $km^2$) and isolated deep convection tends to be underestimated, which are attribute to non-uniform beam-filling effects due to spatial averaging of reflectivity at the PR resolution.

- The merged CBH estimates of CALIPSO and CloudSat demonstrate improved skills and reliable utility in detecting LLCF persistently observed in the SA, featuring with lower bases over mountainous regions than adjacent lowland areas especially at nighttime.
- 10-year MODIS observations reveal a profound seasonal pattern under the influences of topography variations and synoptic forcing over the SA. In the warm season (spring and summer), frequent daytime LLCF over mountain ridges shift to low elevations along river valleys at nighttime. In the cold season (fall and winter), the spatial patterns of LLCF delineate a cloud-shadow region to the east of the continental divide of the SAM.
- Collocated MODIS observations with ground ceilometers capture the optical and microphysical properties of LLCF, indicating low values of vertically integrated cloud water path (CWP < 100 $g/m^2$), cloud optical thickness (COT < 10), and cloud particle effective radius (CER < 15 μm).
- Ground-based CER estimates of LLCF immersion using the meteorological particle spectrometer (MPS) observations range between 25 and 400 μm at mid-day, which are higher than the MODIS cloud-top estimates by one order of magnitude.
- The present SFI case study showed increased surface precipitation by three-fold as a result of enhanced coalescence efficiency. Model results indicate that

number concentrations of small raindrops (up to 0.7 mm) increase by factors of 10-100 due to enhanced coalescence efficiency at time-scales of 2-5 min concurrent. Enhanced coalescence handicaps the collision-breakup efficiency of larger drops (> 1 mm diameter) resulting in increased numbers of large drops toward the surface, thus establishing a vertical gradient in rainfall microstructure (and radar reflectivity) in agreement with measurements.

SQ2: How do variations in aerosol properties and key physical processes (e.g., condensation, coalescence, and entrainment) influence the microphysical evolution and thermodynamic state of cumulus clouds developed in the inner SAM?

- Parcel modeling results indicate that simulated spectra with a low value of condensation coefficient (0.01) are in good agreement with IPHEx aircraft observations around the same altitude. This is in contrast with high $a_c$ values reported in previous studies assuming adiabatic conditions.
- Entrainment is shown to govern the vertical development of clouds and the change of droplet numbers with height. The sensitivity analysis suggests that there is a trade-off between entrainment strength and condensation process.
- Simulated CDNC also exhibits high sensitivity to variations in initial aerosol concentration at cloud base, but weak sensitivity to aerosol hygroscopicity.

SQ3: How do changes in aerosol characteristics affect the spatial distribution of LLC and subsequently the dynamical and microphysical processes of warm-season

precipitation? What is the role of local aerosols in controlling the diurnal cycle of LLC and rainfall?

- WRF simulations of summer precipitation events during IPHEx were conducted and model results from the numerical sensitivity tests show that the onset and timing of estimated rainfall events from both simulations (CONTL and IPHEx) are consistent with surface raingauge observations.
- The predicted number concentrations of cloud droplets in the IPHEx simulation are two to four times higher than the ones in CONTL. The estimated droplet number in IPHEx are in better agreement with the airborne observations and better replicate the widespread low-level cloudiness around mid-day over the inner region.
- Although suppression of early precipitation is resulted in the IPHEx simulation, rainfall formation via the ice phase becomes more efficient and produces a large amount of graupel, contributing to significantly enhanced ice water path (IWP) in the storm cells.
- The variations in CCN characteristics also influence the dynamical structure of the storm by altering the vertical velocity field, resulting in intensification of downdrafts at low altitudes and updrafts at high altitudes in the IPHEx simulation as compared to CONTL.

- The simulated $D_m$ (mass-weighted mean diameter) profiles in both simulations show small variations in the vertical structure within the lower 2 km AGL and the modeled $D_m$ values near the surface significantly underestimate the ones from ground disdrometer measurements especially at valley locations. This points out the model deficiency in representing the SFI, which contribute to large raindrops near the surface and the resulted surface precipitation enhancement observed at low elevations.

## *6.3 Limitations and suggestions for future research*

The findings in Chapter 5 are limited as they are concluded from one case study of summer rainfall events during IPHEx. In order to achieve a comprehensive assessment of ACPI in this region, more case studies need to be conducted in a systematic manner to assess aerosols' effects on different cloud systems and precipitation regimes. Modeling results from Chapter 5 also suggest large amount of ice particles produced in the storm cells, highlighting a strong need to investigate the variations in ice nucleation efficiency, ice microphysics, and riming processes due to changes in CCN characteristics.

Another model limitation in the WRF simulations is its inability to represent the SFI at such coarse horizontal and vertical resolution. Although 90 vertical layers with 30 levels in the lowest 1 km AGL were used in the current modeling structure, the model still cannot explicit solve the nonlinear stochastic coalescence-breakup dynamics that govern the vertical microstructure of clouds and rainfall. This presents a critical modeling

challenge in capturing the variations in vertical velocity profiles of hydrometeors at high vertical resolution (~ 10 m, used in the column model). In future work, WRF simulated profiles will be compared with column model results (Section 3.5) to provide insight on developing parameterization to represent the vertical stratification of low-level processes that are relevant for explaining surface precipitation enhancement induced by SFI.

For further investigation of modeling studies beyond the observation period of the IPHEx campaign, multi-satellite observations (e.g., CALIPSO, CloudSat, MODIS, GPM) can be exploited to evaluate model results via the Goddard Satellite Data Simulator Unit (G-SDSU;Matsui et al., 2014). G-SDSU can translate WRF model outputs into satellite-consistent observations and eliminate inconsistency problems resulting from viewing geometry effects, sensor sensitivity and retrieval algorithm assumptions. Therefore, with consistent assumptions of microphysical properties, simulated signals from model outputs can be readily compared to satellite observations and be easily linked to the relevant precipitation processes and cloud microphysical parameterizations for model diagnostic purposes.

Challenges still exist in the satellite measurements of the lower troposphere especially in mountainous regions due to ground clutter effects and coarse spatial resolutions of spaceborne sensors. Herein detailed model simulations will be used to fill the gaps of satellite observations in the lower troposphere over complex terrain. The parcel model described in Chapter 4 will be coupled to the Duke Rain Microphysics

Column Model (Prat and Barros, 2007b), and then this aerosol-cloud-rainfall column model will be further coupled with a Lidar and radar profiling simulator (Arulraj and Barros, 2017, in preparation) to characterize the signature of the vertical structure of low-level rainfall on multi-frequency radar observations. This can help interpret IPHEx observations and identify sources of ambiguity in the observations from the satellite-based sensors (e.g., CALIPSO CALIOP, CloudSat CPR, GPM DPR). For example, in the June 12 case study during IPHEx, simulated reflectivity from model outputs will be compared with "GPM-proxy" observations from the instrument suite on the ER-2 aircraft. This will contribute to error characterization of GPM core-satellite products and provide insight on the improvement of satellite precipitation retrievals over complex terrain.

In summary, the approach for future research will continue to integrate modeling studies (parcel, column, and WRF models), ground measurements, and satellite observations towards developing physical-based precipitation retrievals in mountainous regions and improving the representation of orographic precipitation processes in numerical predication models, in particular at low-levels.

# Appendix A

The droplet effective radius ($r_e$) is calculated as

$$r_e = \frac{\sum_{i=1}^{bins} r_i^3 n_i}{\sum_{i=1}^{bins} r_i^2 n_i} \tag{A1}$$

The liquid water content (LWC) is computed as

$$LWC = \frac{4\pi}{3}\rho_w \sum_{i=1}^{bins} n_i r_i^3 \tag{A2}$$

where $n_i$ is the number concentration of droplet in the $i^{th}$ bin ($i = 1, 2, \ldots, bins$) and $r_i$ is the radius of droplet in the $i^{th}$ bin. In Eq. (A2), $\rho_w$ is the density of water.

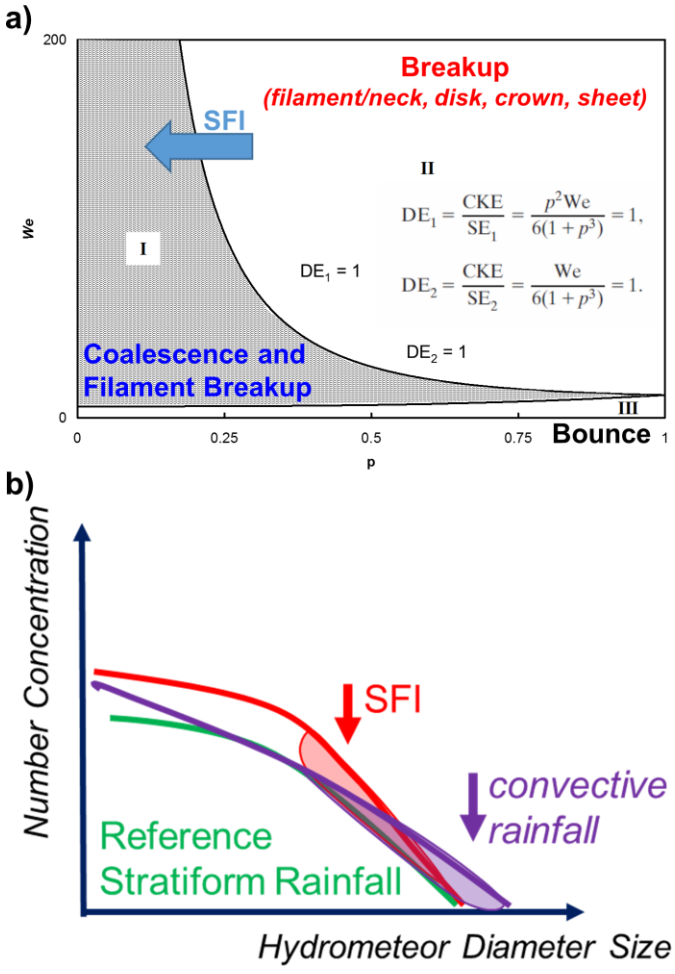

**Figure A1: (a) Regimes of drop collisions delineated according to DE1 and DE2: I-Coalescence and Filament Breakup dominate; II-Breakup dominates; III-Drops collide and bounce. Note SE is the surface tension energy neglecting viscosity, CKE is the collision kinetic energy, p is the diameter ratio between the small and larger diameters of two colliding hydrometeors, and We is the Weber number. This figure is adapted from Testik et al. (2011). For details see Testik (2009), Testik et al. (2011), Prat et al. (2012); (b) Conceptual synthesis of seeder-feeder interactions (SFI) impacts on rain drop size distribution (R-DSD) vis-à-vis convective rainfall of the same intensity with respect to a reference light stratiform rainfall.**

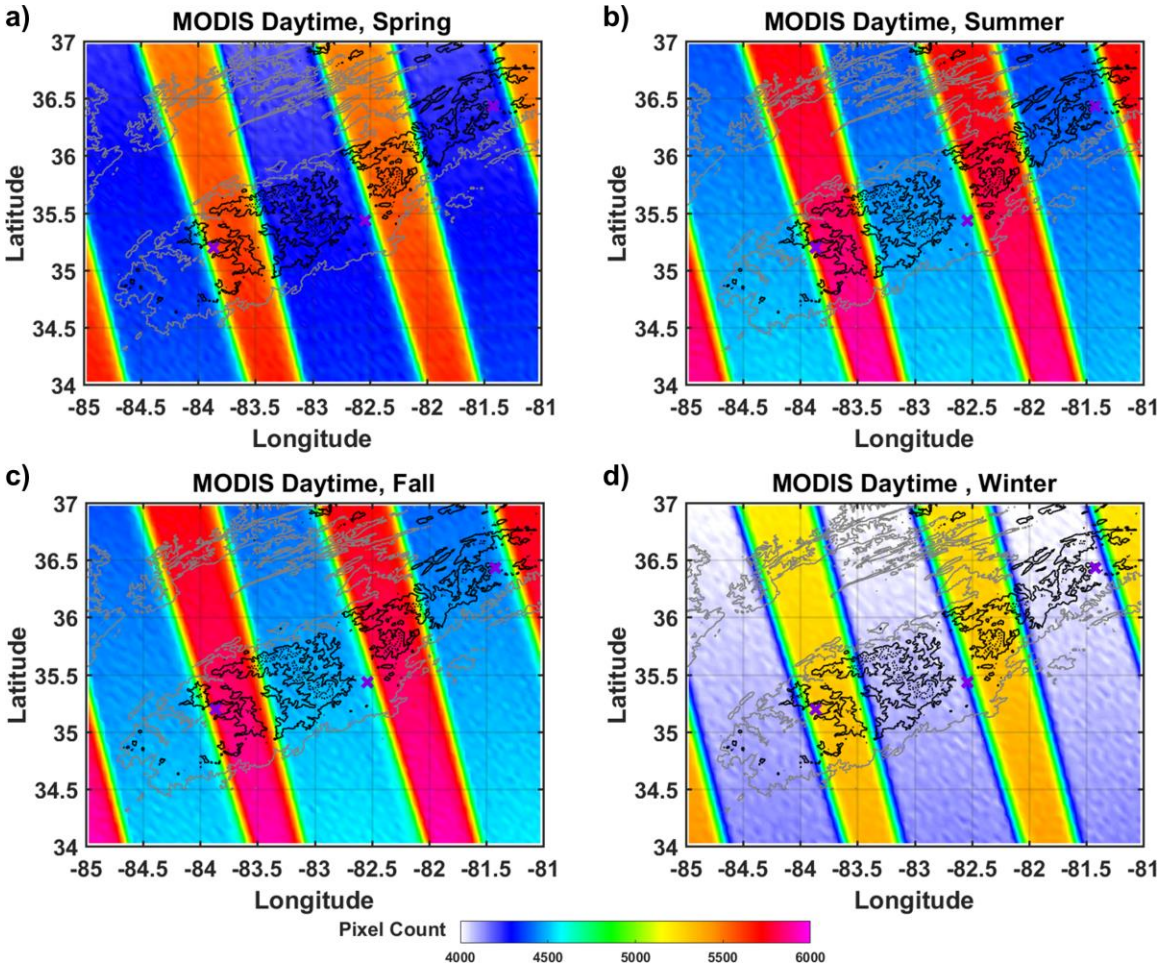


**Figure A2: Spatial distributions of MODIS pixel counts with viewing angle less than 20° in each season (spring: April-May-June, summer: July-August-September, fall: October-November-December, and winter: January-February-March) during daytime overpasses of June 2006 – October 2016. Note the three ground ceilometer sites (from left to right: KRHP, KAVL, and KGEV) are marked by purple crosses.**

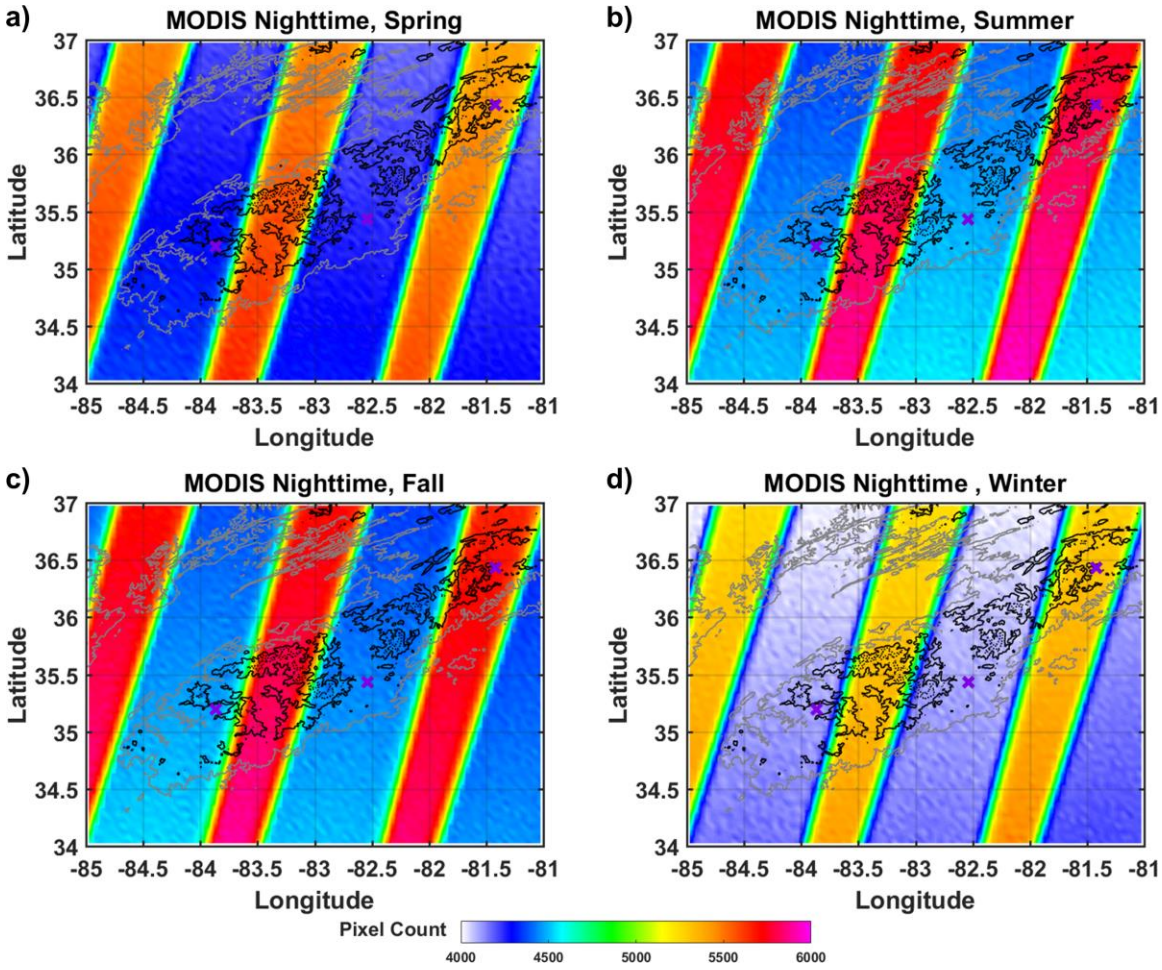


**Figure A3: Spatial distributions of MODIS pixel counts with viewing angle less than 20° in each season (spring: April-May-June, summer: July-August-September, fall: October-November-December, and winter: January-February-March) during nighttime overpasses of June 2006 – October 2016. Note the three ground ceilometer sites (from left to right: KRHP, KAVL, and KGEV) are marked by purple crosses.**

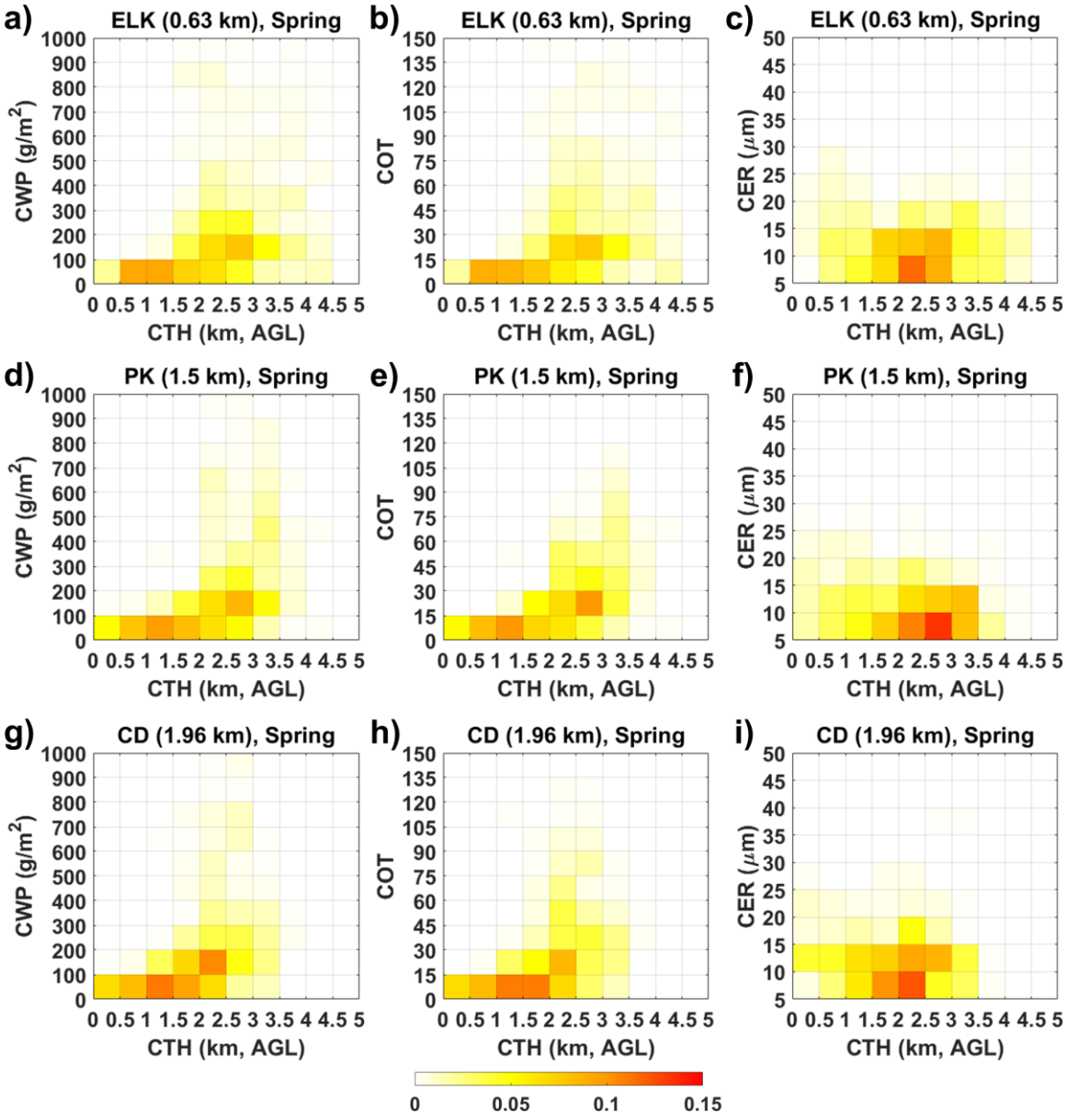


**Figure A4: Fractional occurrences of MODIS optical and microphysical properties (CWP, COT, and CER) for single-layered LLCF (CTH < 5 km MSL and viewing angle < 20°) as a function of MODIS CTH (AGL) observed in the grid box (0.05° × 0.05°) where each fog collector is located (ELK: a-c, PK: d-f, and CD: g-i) during the spring of June 2006 – October 2016 (daytime overpasses only). Note the elevation of each site is denoted in parentheses after its name.**

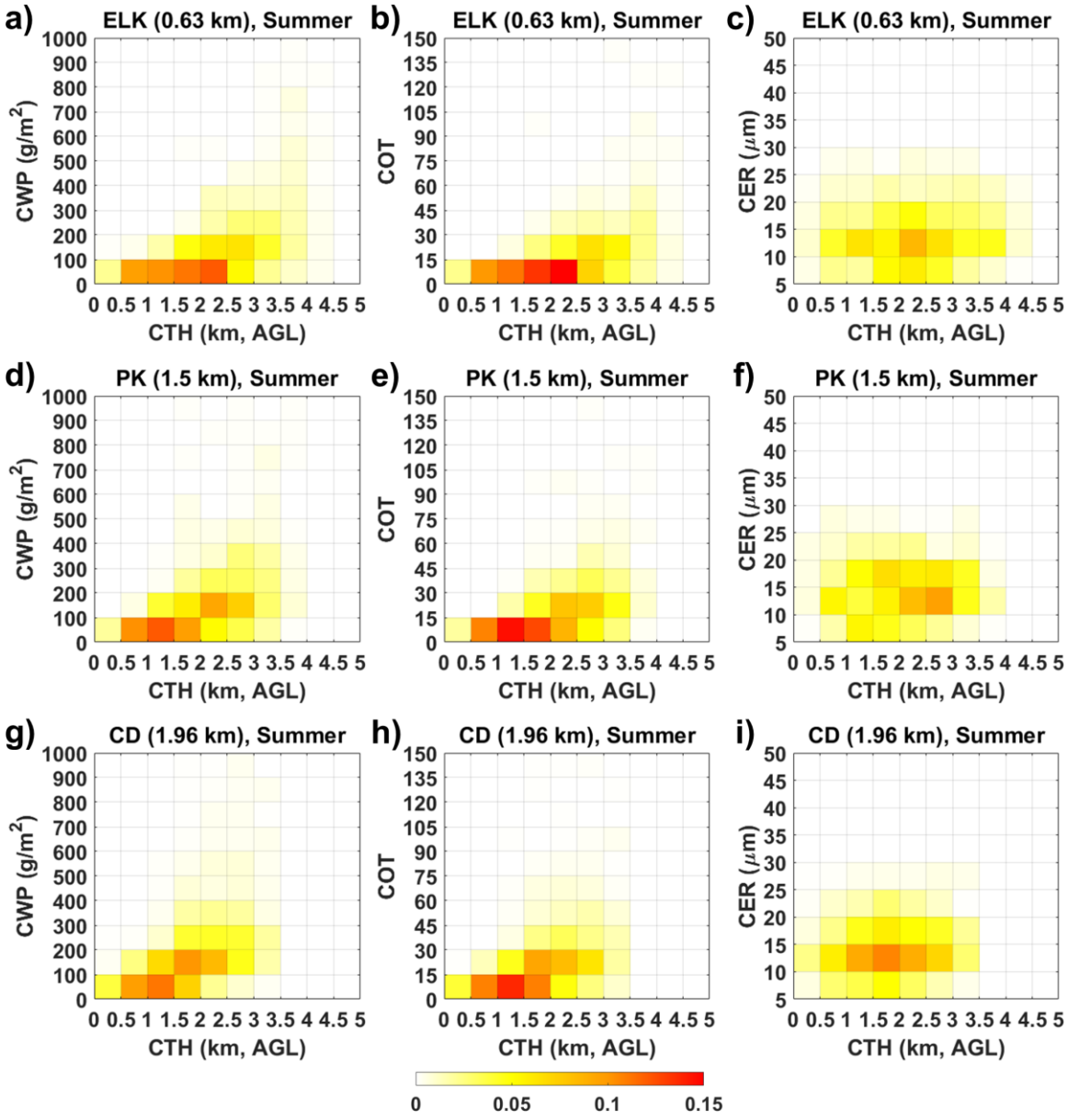


**Figure A5: Fractional occurrences of MODIS optical and microphysical properties (CWP, COT, and CER) for single-layered LLCF (CTH < 5 km MSL and viewing angle < 20°) as a function of MODIS CTH (AGL) observed in the grid box (0.05° × 0.05°) where each fog collector is located (ELK: a-c, PK: d-f, and CD: g-i) during the summer of June 2006 – October 2016 (daytime overpasses only). Note the elevation of each site is denoted in parentheses after its name.**

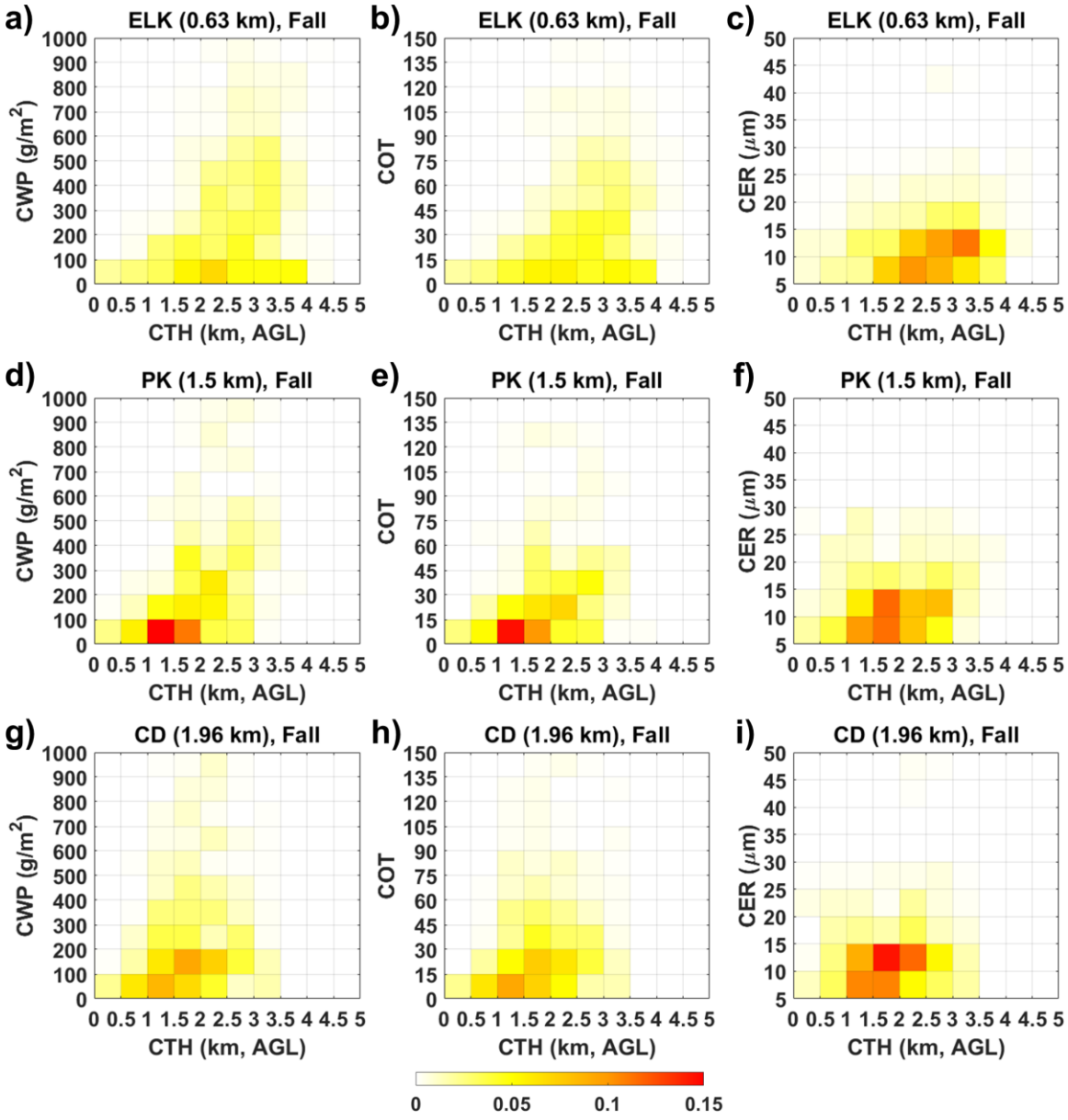


**Figure A6: Fractional occurrences of MODIS optical and microphysical properties (CWP, COT, and CER) for single-layered LLCF (CTH < 5 km MSL and viewing angle < 20°) as a function of MODIS CTH (AGL) observed in the grid box (0.05° × 0.05°) where each fog collector is located (ELK: a-c, PK: d-f, and CD: g-i) during the fall of June 2006 – October 2016 (daytime overpasses only). Note the elevation of each site is denoted in parentheses after its name.**

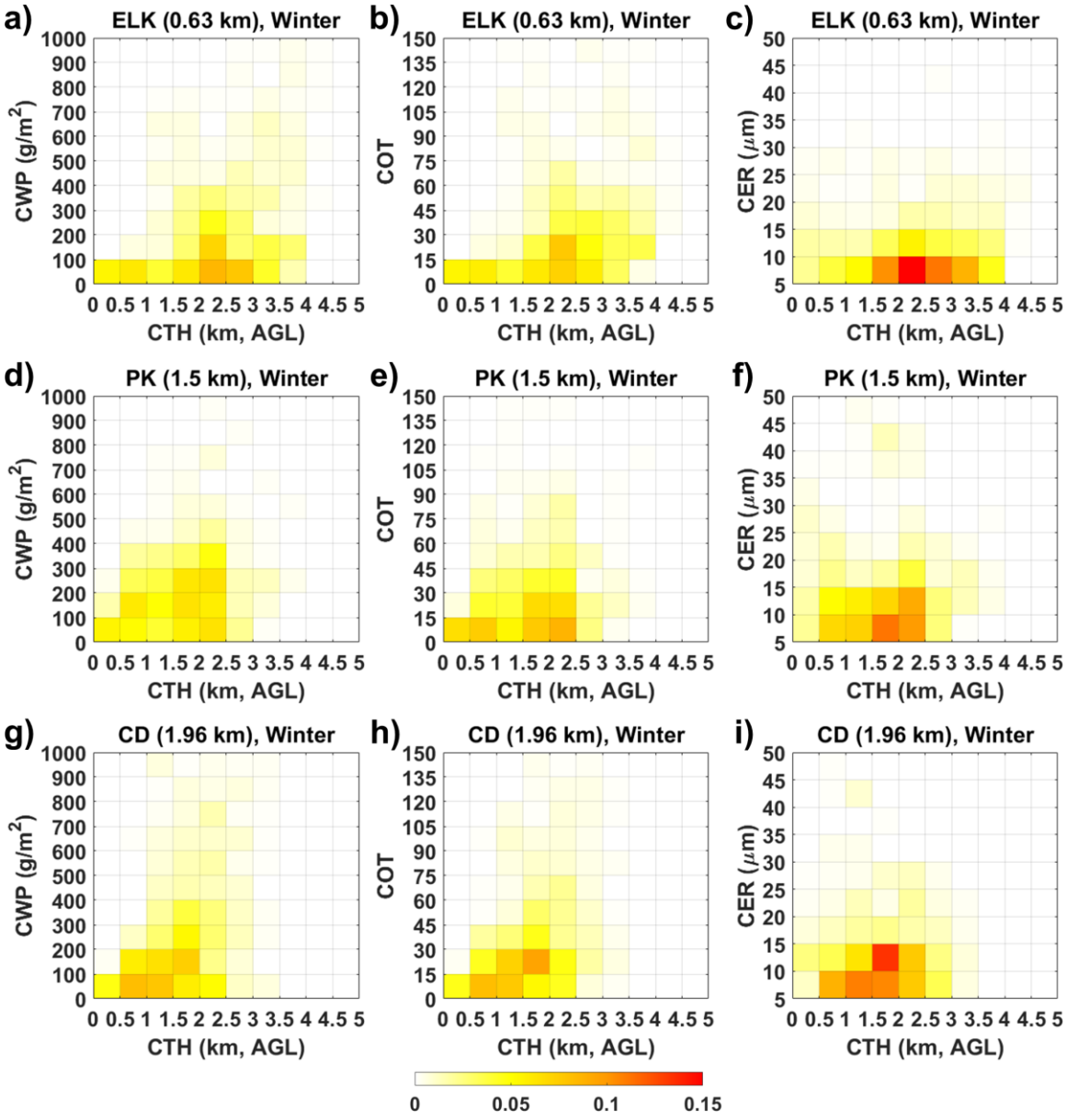


**Figure A7: Fractional occurrences of MODIS optical and microphysical properties (CWP, COT, and CER) for single-layered LLCF (CTH < 5 km MSL and viewing angle < 20°) as a function of MODIS CTH (AGL) observed in the grid box (0.05° × 0.05°) where each fog collector is located (ELK: a-c, PK: d-f, and CD: g-i) during the winter of June 2006 – October 2016 (daytime overpasses only). Note the elevation of each site is denoted in parentheses after its name.**

# Appendix B

*Glossary of Symbols*

| | |
|---|---|
| $a_c$ | condensation coefficient |
| $a_T$ | thermal accommodation coefficient |
| $c_p$ | specific heat of dry air |
| $D_v$, $D_v'$ | diffusivity of water vapor in air, modified diffusivity of water vapor in air |
| $e_s$ | saturation vapor pressure |
| $g$ | gravitational constant |
| $G$ | growth coefficient |
| $H_S$ | scale height |
| $k_a$, $k_a'$ | thermal conductivity of air, modified thermal conductivity of air |
| $L$ | latent heat of evaporation |
| $M_a$, $M_w$ | molecular weight of dry air, of water |
| $N$, $N'$ | number concentration of cloud droplets, of ambient aerosol particles |
| $p$ | pressure |
| $r$, $r_c$ | radius of cloud droplet, of dry aerosol particle |
| $R$ | universal gas constant |
| $R_B$, $R_J$ | radius of air bubble, of convective jet |
| $S$ | supersaturation |
| $S_{eq}$ | droplet equilibrium supersaturation |
| $T$ ($T'$) | temperature of air parcel (ambient air) |
| $V$ | parcel updraft velocity |
| $v$, $v'$ | droplet volumes |
| $w_L$ | mixing ratio of liquid water in parcel |
| $w_v$ ($w_v'$) | mixing ratio of water vapor in parcel (in environment) |
| $\kappa$ | hygroscopicity parameter |
| $\mu$ | entrainment rate |
| $\rho_a$, $\rho_w$ | density of dry air, of water |
| $\sigma_w$ | droplet surface tension |

*Additional Formulae*

$$G = \left[\frac{\rho_w RT}{e_s D_v' M_w} + \frac{L\rho_w}{k_a' T}\left(\frac{LM_w}{RT} - 1\right)\right]^{-1} \tag{B1}$$

where the modified diffusivity ($D_v'$) and thermal conductivity ($k_a'$) of water vapor in air account for non-continuum effects (Seinfeld and Pandis, 2006) and are described as follows

$$D_v' = \frac{D_v}{1 + \frac{D_v}{a_c r}\sqrt{\frac{2\pi M_w}{RT}}} \tag{B2}$$

$$k_a{}' = \frac{k_a}{1 + \frac{k_a}{a_T r \rho_a c_p}\sqrt{\frac{2\pi M_a}{RT}}} \tag{B3}$$

where the thermal accommodation coefficient ($a_T$) is taken as 0.96 (Nenes et al., 2001). Additional sensitivity tests of CDNC to $a_T$, ranging from 0.1 to 1 (Shaw and Lamb, 1999), were conducted and the resulting droplet concentrations indicate little sensitivity to this input parameter (not shown here).

The hygroscopicity parameter (κ) is adopted to characterize aerosol chemical composition on CCN activity according to κ-Köhler theory (Petters and Kreidenweis, 2007). $S_{eq}$ for droplets in the $i^{th}$ bin ($i = 1, 2, \ldots, nbin$) can be written as

$$S_{eq} = \frac{r_i^3 - r_{c,i}^3}{r_i^3 - r_{c,i}^3(1-\kappa_i)} exp\left(\frac{2M_w\sigma_w}{RT\rho_w r_i}\right) - 1 \tag{B4}$$

where $r_{c,i}$ and $r_i$ are the radius of the dry aerosol particle and the corresponding growing droplet, respectively. Droplet surface tension ($\sigma_w$) is a function of the parcel temperature (Pruppacher and Klett, 1997).

$$\alpha = \frac{gM_w L}{c_p RT^2} - \frac{gM_a}{RT} \tag{B5}$$

$$\gamma = \frac{pM_a}{e_s M_w} + \frac{M_w L^2}{c_p RT^2} \tag{B6}$$

Liquid water content (g $m^{-3}$):

$$LWC = \frac{4\pi}{3}\rho_w \sum_{i=1}^{bins} N_i r_i^3 \tag{B7}$$

# Appendix C

**1. Sensitivity to environmental conditions**

To account for the uncertainties associated with the environmental condition from WRF and examine its impact on cloud formation, two additional simulations were conducted with modified profiles of temperature and humidity at the lowest 2 km above CBH (1,270 m), as displayed in Fig. C1. In the first simulation, we adjusted the original lapse rate (-4.1 °C $km^{-1}$ from the WRF sounding, Fig. 4-10b) to -7 °C $km^{-1}$ ($\Gamma_1$) for 1,270–2,200 m. In the second one, specific humidity (q) in the environment was increased by 5% for 1,270–3,200 m together with the adjusted temperature profile in the first run. In both simulations, the lapse rate for 2,200–3,200 m was changed to -4 °C $km^{-1}$ to keep the ambient temperature below CBH and above 3,200 m unchanged. As expected, deeper clouds are formed in modified environments representing conditionally unstable atmosphere. A slight increase in specific humidity has little influence on the maximum supersaturation formed near cloud base. Consequently, its effect on droplet concentrations is also negligible due to the slightly increased maximum supersaturation (not shown here). It is expected that LWC is significantly enhanced and droplet growth is faster under the environmental condition of fast cooling and moist air.

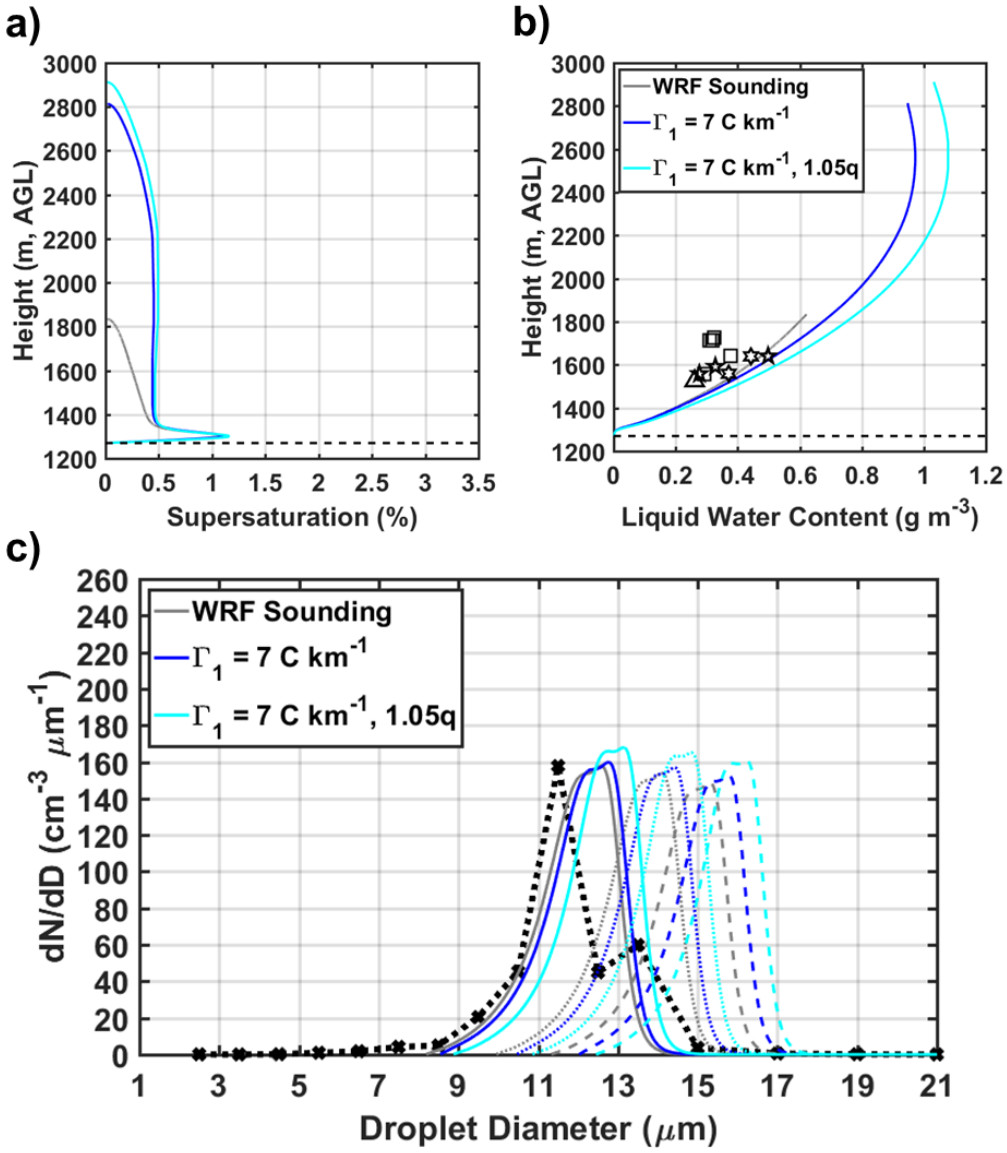


**Figure C1: Vertical profiles of the supersaturation (a) and LWC (b) for simulations with the original WRF sounding (grey lines), modified ambient temperature (blue lines), and modified ambient temperature and humidity (cyan lines). In (a) and (b), the airborne observations are marked by different black symbols, denoting the ranges of their updraft velocities (triangles: 0–0.5 m $s^{-1}$, squares: 0.5–1.0 m $s^{-1}$, pentagrams: 1–1.5 m $s^{-1}$, hexagrams: 1.5–2.0 m $s^{-1}$), and the horizontal dashed line depicts CBH. c) Predicted droplet spectra at three altitudinal levels (1,500 m: solid line, 1,600 m: dotted line, and 1,700 m: dashed line) to the variations in the environmental conditions modified from the WRF sounding. The black dotted line reflects the average**

**of five droplet spectra observed by the CDP (dotted lines with circle markers in Figs. 4-7c and d) between 1,500 m and 1,600 m AGL.**

**2. Sensitivity to hygroscopicity**

Another key element in the condensation process is the hygroscopic property that governs the influence of aerosol chemical composition on CCN activity. To account for its temporal variability observed during IPHEx, a $\kappa$ value varying from 0.1–0.4 (within the typical range measured at the surface site, see Figs. 4-4a and D8c) is applied uniformly for all particle sizes. As noted from Fig. C2, simulated profiles of supersaturation and total CDNC exhibit a weak dependence on the hygroscopicity that a slightly decrease in maximum supersaturation and a slightly increase in total CDNC are associated with more hygroscopic aerosols. Predicted droplet spectra at three altitudinal levels (1,500 m: solid line, 1,600 m: dotted line, and 1,700 m: dashed line) also show little sensitivity to the variations in $\kappa$. As discussed in Sect. 3.1, hygroscopic properties of aerosols have been found to vary with particle sizes. Potential uncertainties might remain by assuming a constant $\kappa$, but its variation with droplet sizes is not addressed in the current study. We should also note the hygroscopicity derived from surface measurements may not be representative for aerosols beneath the cloud (Pringle et al., 2010). However, the vertical variability of aerosol hygroscopicity is not taken into account in this study.

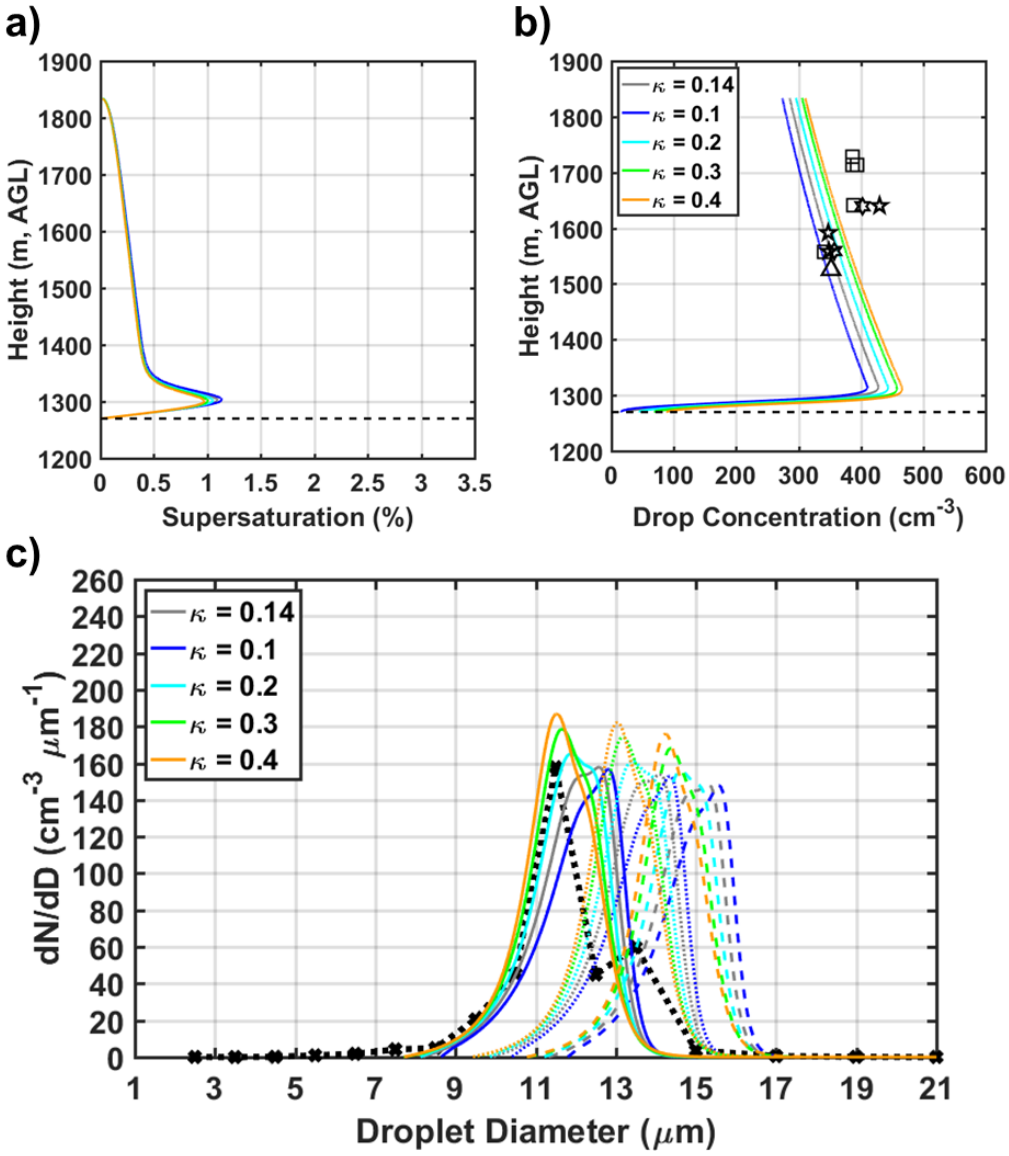


**Figure C2: Sensitivity of the supersaturation (a) and total drop concentration (b) to variations in hygroscopicity parameter (κ). In (a) and (b), the airborne observations are marked by different black symbols, denoting the ranges of their updraft velocities (triangles: 0–0.5 m $s^{-1}$, squares: 0.5–1.0 m $s^{-1}$, pentagrams: 1–1.5 m $s^{-1}$, hexagrams: 1.5–2.0 m $s^{-1}$), and the horizontal dashed line depicts CBH. c) Predicted droplet spectra at three altitudinal levels (1,500 m: solid line, 1,600 m: dotted line, and 1,700 m: dashed line) to the variations in κ. The black dotted line reflects the average of five droplet spectra observed by the CDP (dotted lines with circle markers in Figs. 4-7c and d) between 1,500 m and 1,600 m AGL.**

### 3. Sensitivity to initial updraft velocity

Cloud dynamics also play a crucial role in the microphysical evolution of cumulus clouds. One major parameter in the cloud dynamical field is the updraft velocity. In accordance with the observed vertical velocities from the aircraft and the W-band radar (see Fig. D9b), a reasonable variability in the initial updraft velocity at cloud base is introduced to assess its effects on the parcel supersaturation and cloud droplet concentrations, as shown in Fig. C3. By varying the initial updraft in a range of 0.1–1.5 m $s^{-1}$, simulated results display similar vertical velocities at the observation levels, which are still higher than the measured range (not shown here). As expected, slight increases in maximum supersaturation are resulted from larger initial updraft velocities, thus leading to slight enhancement of total droplet numbers. The simulated spectra show a slightly shift towards larger drop sizes due to weaker updrafts, which allow more time for cloud droplets to grow in a rising parcel.

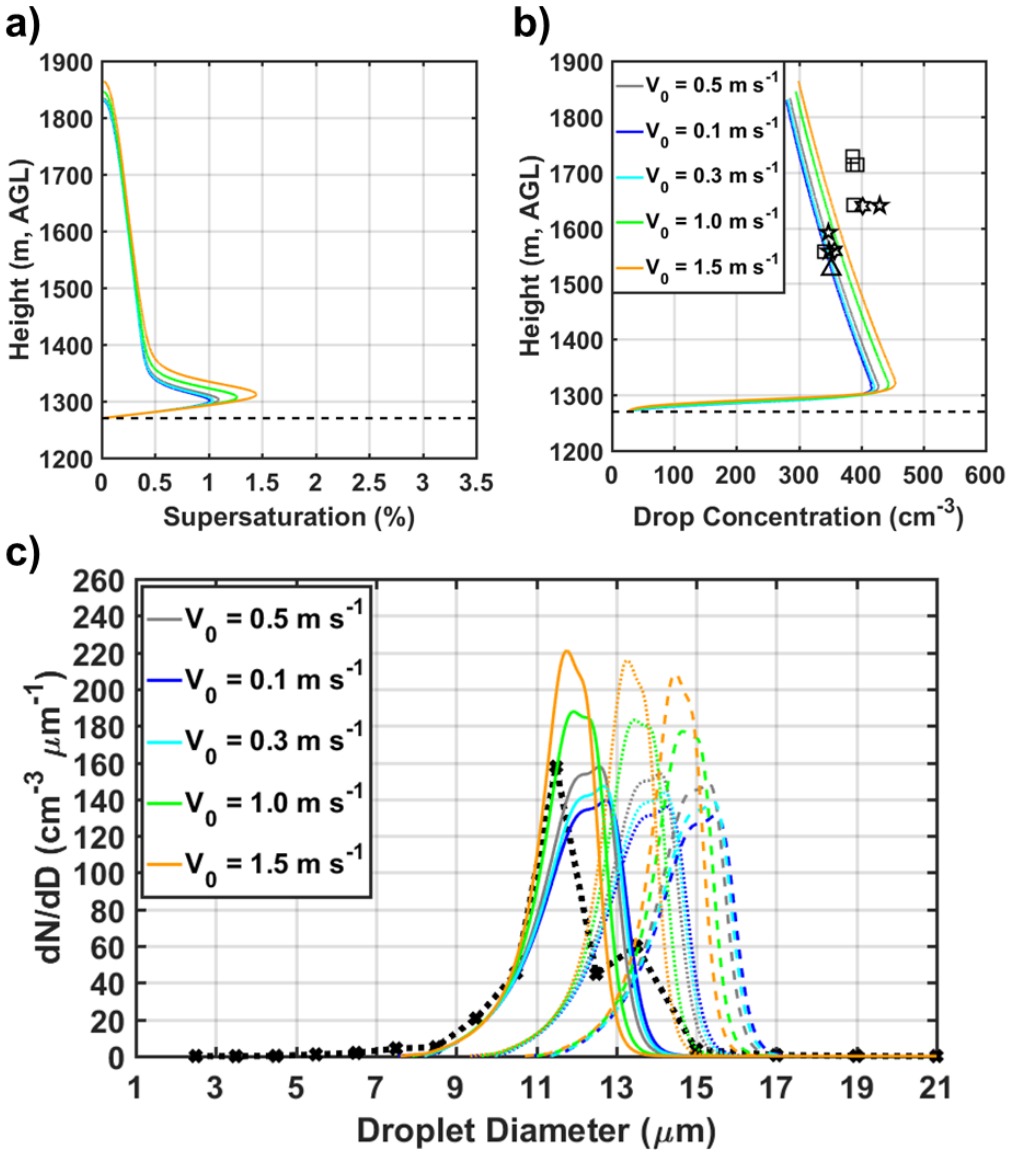


**Figure C3: Sensitivity of the supersaturation (a), total drop concentration (b), and droplet spectra (c) at three altitudinal levels (1,500 m: solid line, 1,600 m: dotted line, and 1,700 m:dashed line) to the variations in the initial updraft velocity ($V_0$) at cloud base. In (a) and (b), the airborne observations are marked by different black symbols, denoting the ranges of their updraft velocities (triangles: 0–0.5 m $s^{-1}$, squares: 0.5–1.0 m $s^{-1}$, pentagrams: 1–1.5 m $s^{-1}$, hexagrams: 1.5–2.0 m $s^{-1}$), and the horizontal dashed line depicts CBH. The black dotted line in (c) reflects the average of five droplet spectra observed by the CDP (dotted lines with circle markers in Figs. 4-7c and d) between 1,500 m and 1,600 m AGL.**

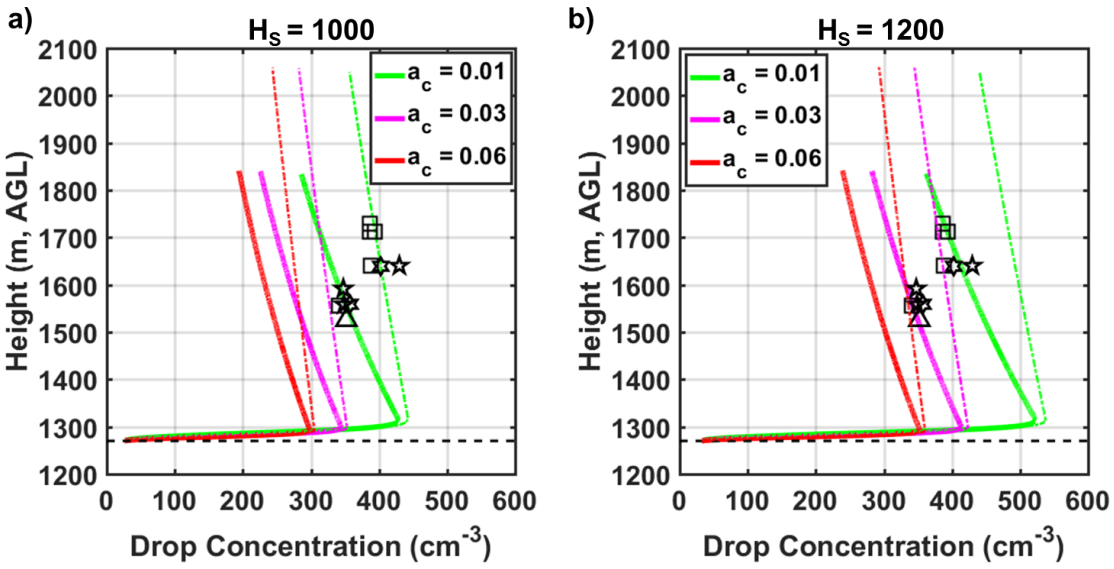


**Figure C4: Sensitivity of the total cloud drop concentration to the variations in condensation coefficient and entrainment strength (strong: R = 500 m, solid thick lines; weak: R = 1,500 m, dash-dot thin lines) assuming different initial aerosol concentrations at cloud base (a: $H_S$ = 1,000 m; b: $H_S$ = 1,200 m). The airborne observations are marked by different black symbols, denoting the ranges of their updraft velocities (triangles: 0–0.5 m $s^{-1}$, squares: 0.5–1.0 m $s^{-1}$, pentagrams: 1–1.5 m $s^{-1}$, hexagrams: 1.5–2.0 m $s^{-1}$). The horizontal dashed line depicts CBH.**

# Appendix D

**1 Comparison against another parcel model with condensation process**

The details of the numerical model used in Ghan et al. (2011) can be found in Abdul-Razzak et al. (1998) describing the condensation process in an air parcel rising adiabatically at uniform speed. For comparison here, the DCPM is tested with a constant updraft velocity ($dV/dt$ = 0, see Eq. 3 in Sect. 4.2.1) and both collision-coalescence and entrainment ($\mu$ = 0) processes excluded. Hence, the condensation process determines activated particle numbers and corresponding maximum supersaturation in both numerical models. We also applied the same initial conditions and the same baseline case with a single lognormal aerosol distribution, as specified in Ghan et al. (2011). The number fraction activated is defined as the fraction of particles with wet sizes larger than their critical values (Nenes et al., 2001) when maximum supersaturation is achieved. Figs. D1–D6 demonstrate that the simulated maximum supersaturation and number fraction activated from the DCPM are in good agreement with the numerical solutions in Ghan et al. (2011) for a wide range of updraft velocities, aerosol number concentrations, geometric mean radii, geometric standard deviations, hygroscopicity, and condensation coefficients. As discussed in Sect. 4.4.2.1, collision-coalescence of cloud droplets is ineffective at early stages of the observed cloud due to small drop sizes developed and the condensation process dominates droplet growth in the 12 June case-study. Therefore, we can conclude

that this comparison supports the validity of the present model and justify the findings from its application to the IPHEx case-study.

**2 Details of the WRF model configuration**

A 5-day simulation (see the WRF domain configuration in Fig. 4-10a) over the SAM was performed using the advanced WRF model in version 3.5.1 (Skamarock et al., 2008) from 00:00 UTC 08 June for the first domain (06:00 UTC for second, third, and fourth domains) to 00:00 UTC 13 June 2014 for all four domains. The simulation was set up in a manner similar to Wilson and Barros (2015) and Sun and Barros (2012). One-way nested domains are configured with horizontal grid spacing of 15-, 5-, 1.25-, 0.25-km. This corresponds to grid sizes of 147×121, 267×288, 552×552, and 555×555 for the first (D01), second (D02), third (D03), and fourth (D04) domains, respectively. A terrain-following vertical grid with 90 layers is constructed with 30 levels in the lowest 1 km AGL and the model top is at 50 hPa. Initialization and lateral boundary conditions are updated every 6-hour using the National Centers for Environmental Prediction (NCEP) Final Operational Global Analysis (FNL) with 1°×1° horizontal resolution (Kalnay et al., 1996). The Kain-Fritsch cumulus parameterization scheme (Kain, 2004) is used in the D01 (15 km) and D02 (5 km) domains, and convection is resolved explicitly in the D03 (1.25 km) and D04 (0.25 km) domains. Other physics options include the Thompson cloud microphysics scheme (Thompson et al., 2008), a new version of the Rapid Radiative Transfer Model radiation scheme for longwave and shortwave (Iacono et al., 2008), and

the unified Noah land-surface model (Tewari et al., 2004) used for all four domains. The Mellor-Yamada-Janjic planetary boundary layer scheme (Janjic, 1994) is selected together with the Monin-Obukhov (Janjic Eta) surface layer scheme. The soil temperature and moisture fields are also initialized from the NCEP FNL data.

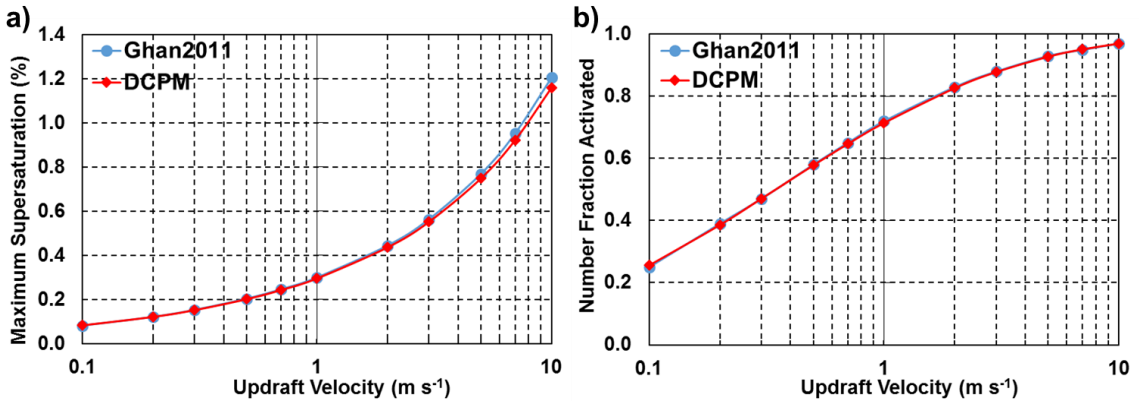


**Figure D1: Maximum supersaturation (a) and number fraction activated as a function of updraft velocity calculated by the DCPM (red lines) compared to the numerical solution in Ghan et al., (2011; blue lines) using the same initial conditions and aerosol properties. In the baseline case, the aerosols have number concentration of 1000 cm$^{-3}$, geometric mean radius of 0.05 μm, a geometric standard deviation of 2, and a hygroscopicity of 0.7; the condensation coefficient is 1.0 and the uniform updraft is 0.5 m s$^{-1}$.**

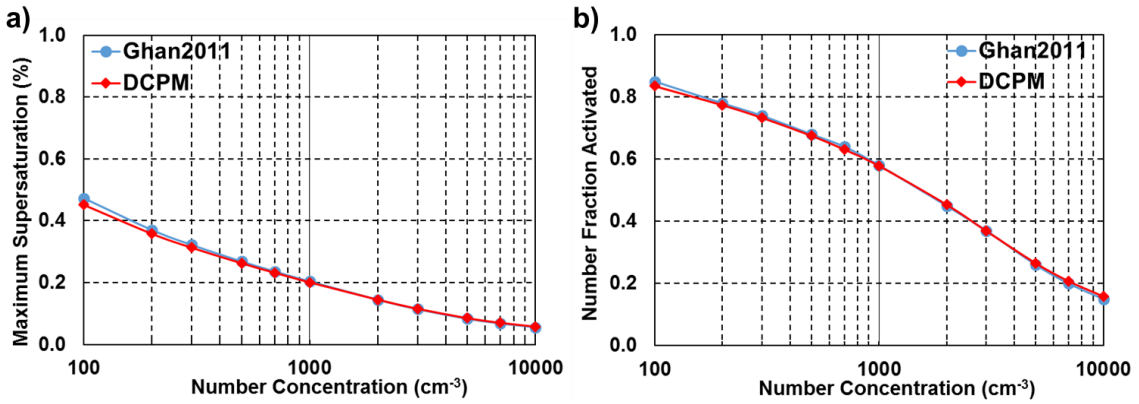


**Figure D2: As in Fig. D1 but as a function of aerosol number concentration.**

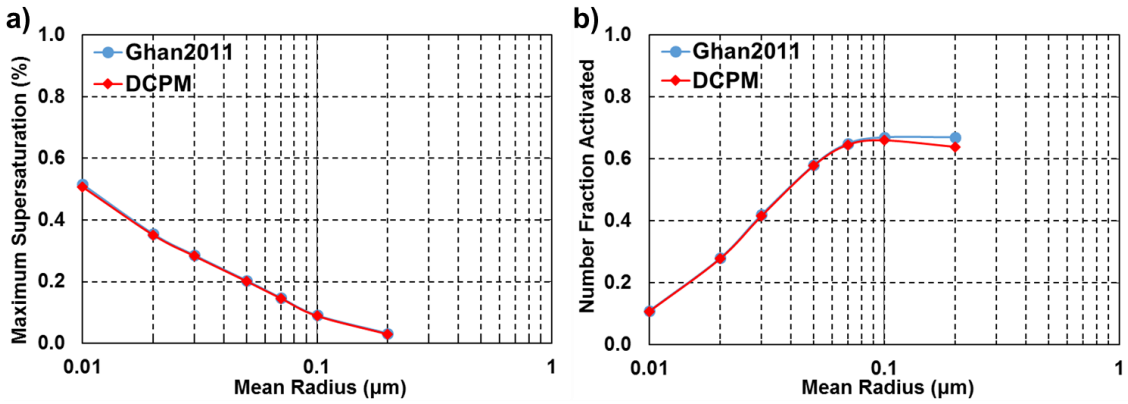


**Figure D3: As in Fig. D1 but as a function of geometric mean radius of the single lognormal aerosol distribution.**

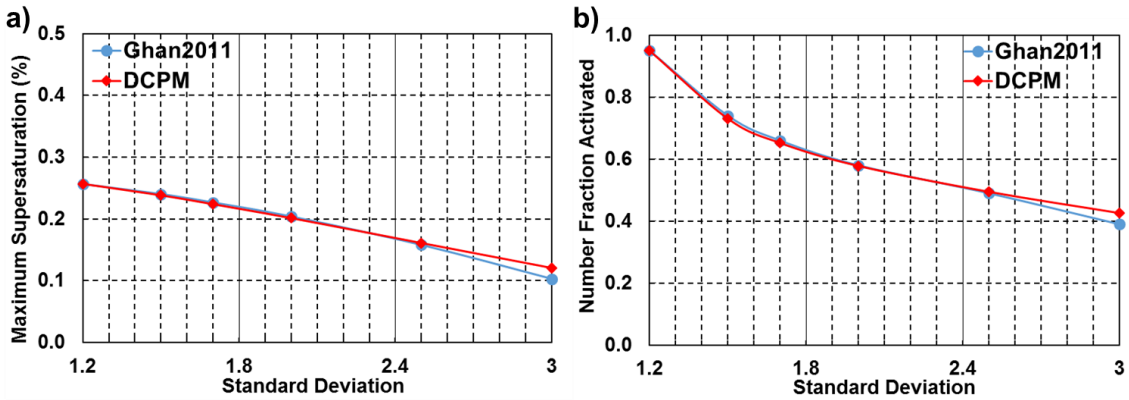


**Figure D4: As in Fig. D1 but as a function of geometric standard deviation of the single lognormal aerosol distribution.**

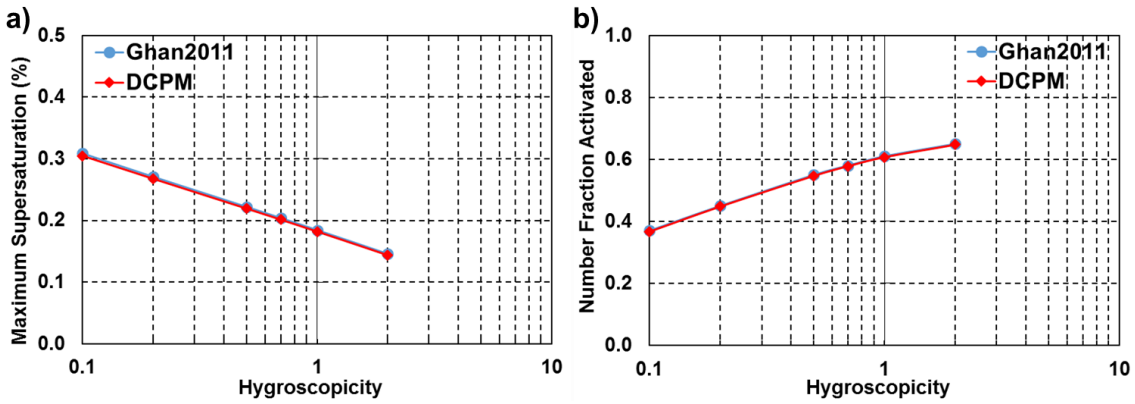


**Figure D5: As in Fig. D1 but as a function of hygroscopicity.**

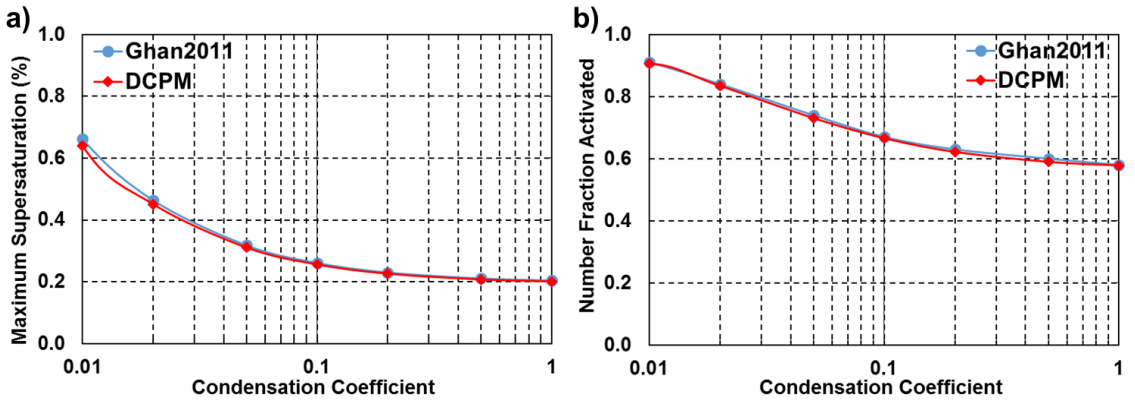


**Figure D6: As in Fig. D1 but as a function of condensation coefficient.**

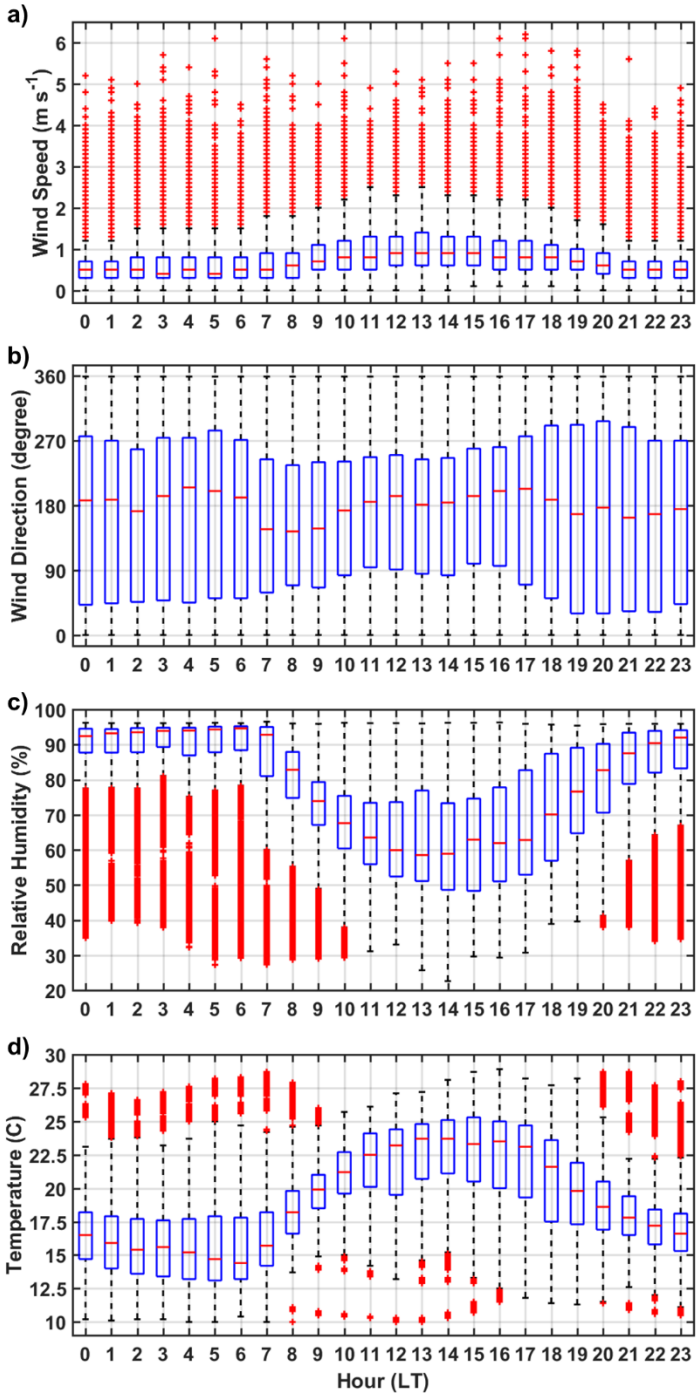


**Figure D7: Diurnal cycles in local meteorological variables: wind speed (a), wind direction (b), relative humidity (c), and ambient temperature (d), measured at MV during the IPHEx IOP. The blue box represents the interquartile range (IQR) from the lower quartile (25$^{th}$) to the upper quartile (75$^{th}$), and the red short horizontal line inside**

**the box indicates the median. The two horizontal black lines ("whiskers") extending from the central box denote the ±1.5 IQR interval, and red plus signs mark outliers that fall out of ± 1.5 IQR.**

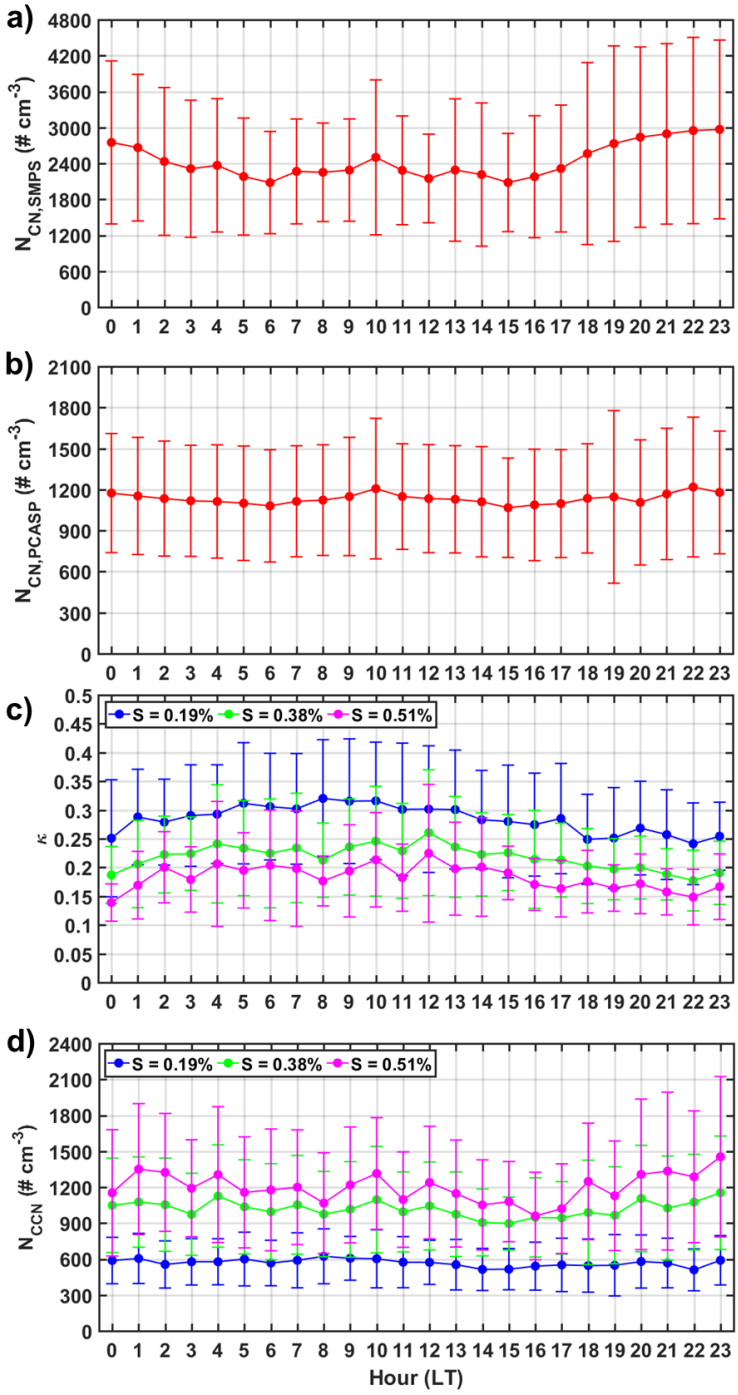

**Figure D8: Diurnal cycles in total aerosol number concentrations from the SMPS ($N_{CN,SMPS}$, a) and PCASP ($N_{CN,PCASP}$, b), and in hygroscopicity parameter (κ, c) and CCN concentration ($N_{CCN}$, d) at three supersaturation (S) levels measured at MV during the IPHEx IOP. Mean values are denoted as solid circles and sample variability is indicated by short vertical bars, representing plus and minus one standard deviation.**

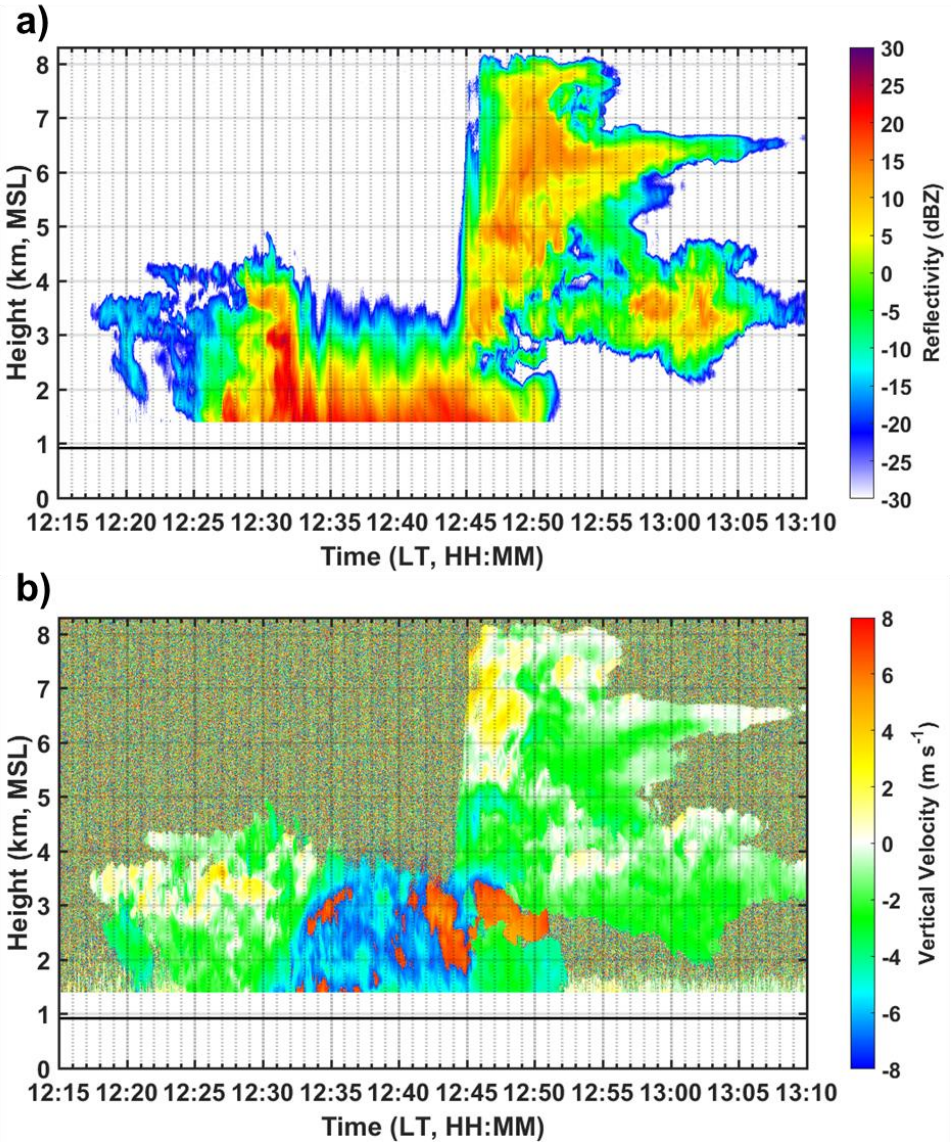


**Figure D9: Vertical profiles of W-band reflectivity (a) and vertical velocity (b) of cumulus congestus clouds observed at MV on 12 June 2014. The horizontal line depicts the elevation level of the MV supersite (~ 925 m MSL).**

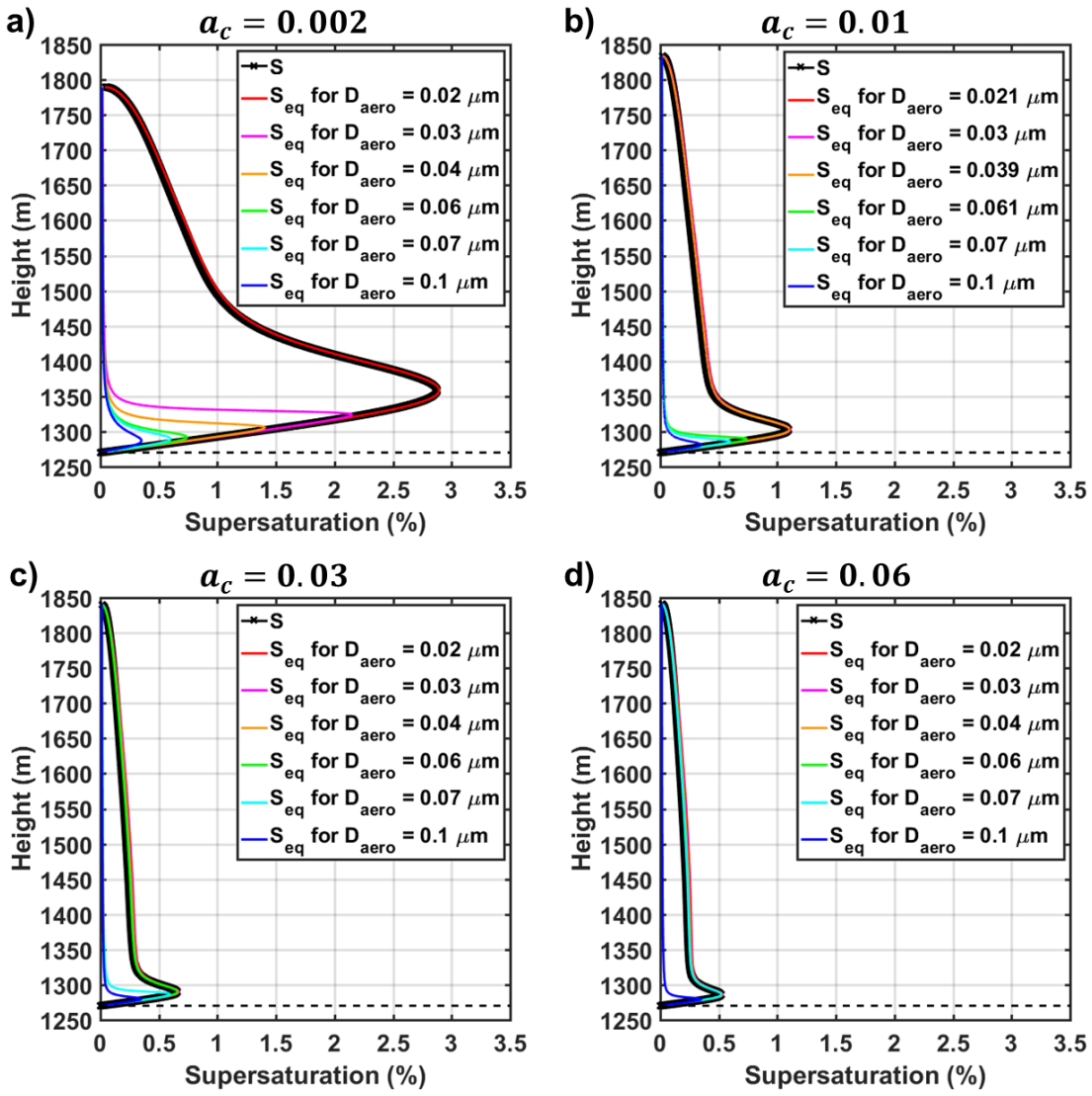


**Figure D10: Variations with height of the parcel supersaturation (S, black lines) and droplet equilibrium supersaturation ($S_{eq}$, coloured lines) for six representative diameters of dry aerosol particles ($D_{aero}$) for four simulations: a) $a_c$ = 0.002, b) $a_c$ = 0.01, c) $a_c$ = 0.03, and d) $a_c$ = 0.06. The horizontal dashed line depicts CBH.**

# Appendix E

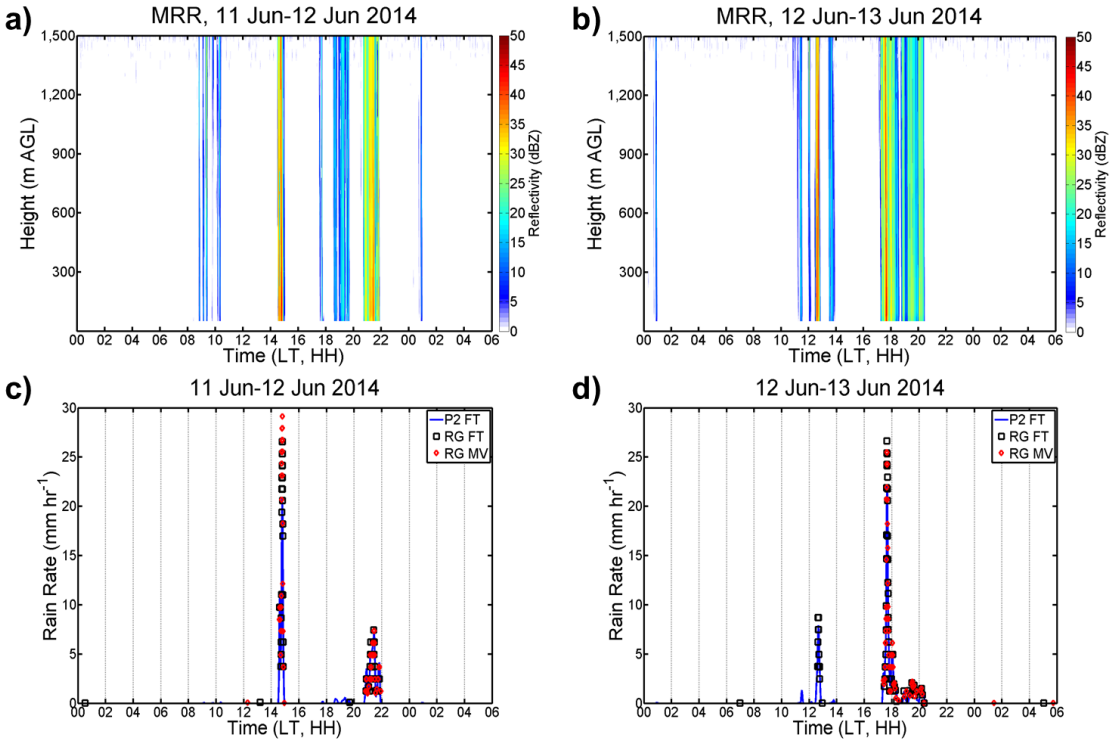


**Figure E1: Vertical profiles of MRR (K-band) reflectivity (a, b) and rain rate (c, d) observed by the RG and disdrometers at MV during 11–13 June 2014.**

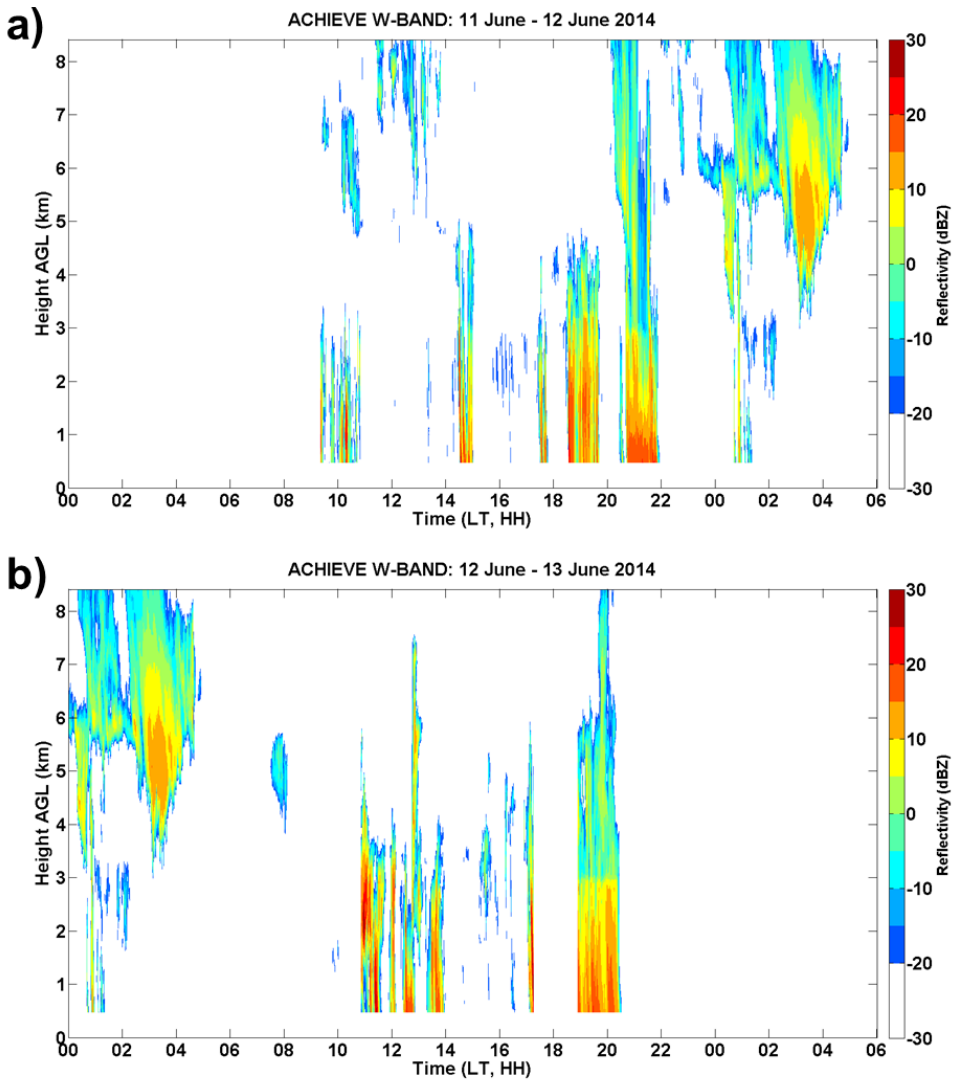


**Figure E2: Vertical profiles of W-band reflectivity observed at MV during 11–13 June 2014.**

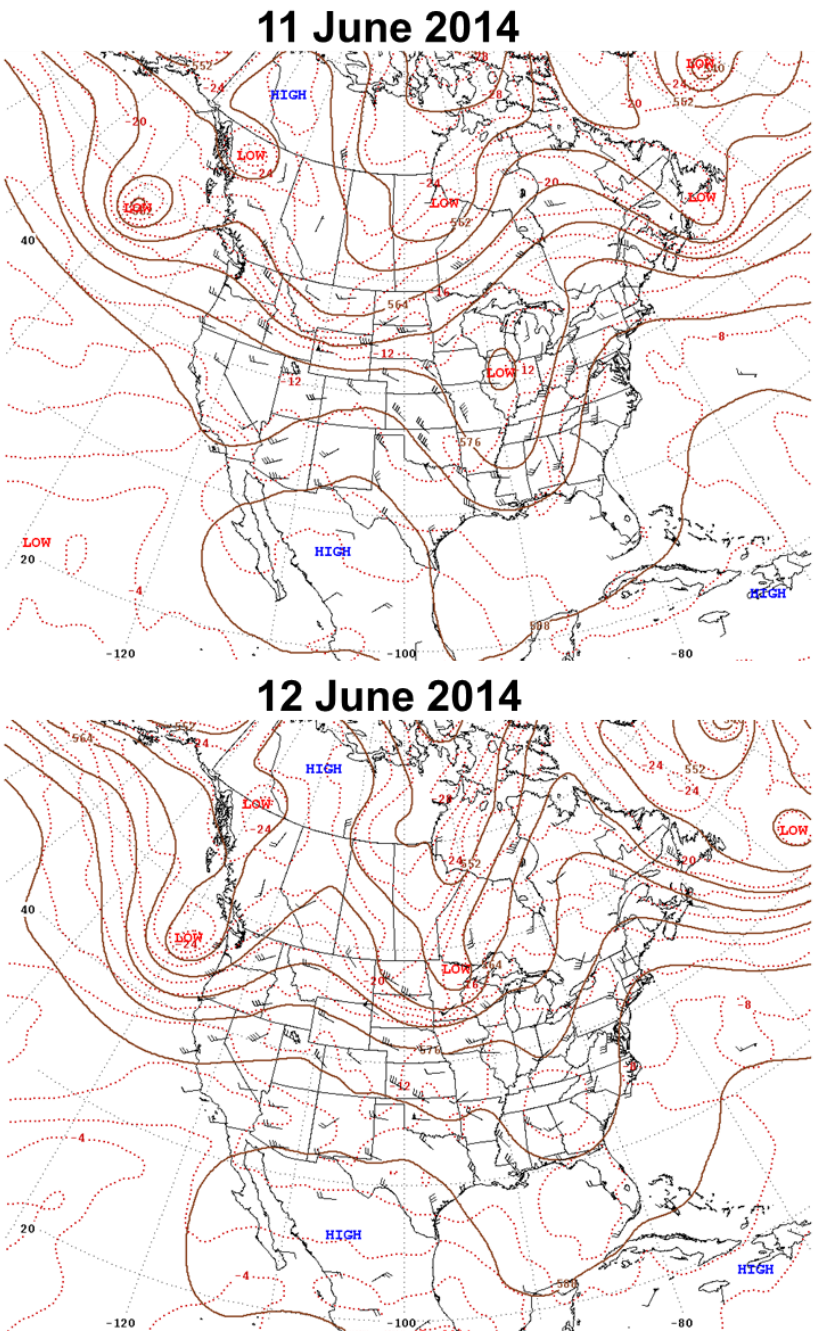


**Figure E3: Daily weather maps for 11 June and 12 June 2014. The map shows the height contours (solid lines), temperature (dashed lines), and wind (arrows) at the 500-millibar pressure level at 7:00 a.m., EST.**

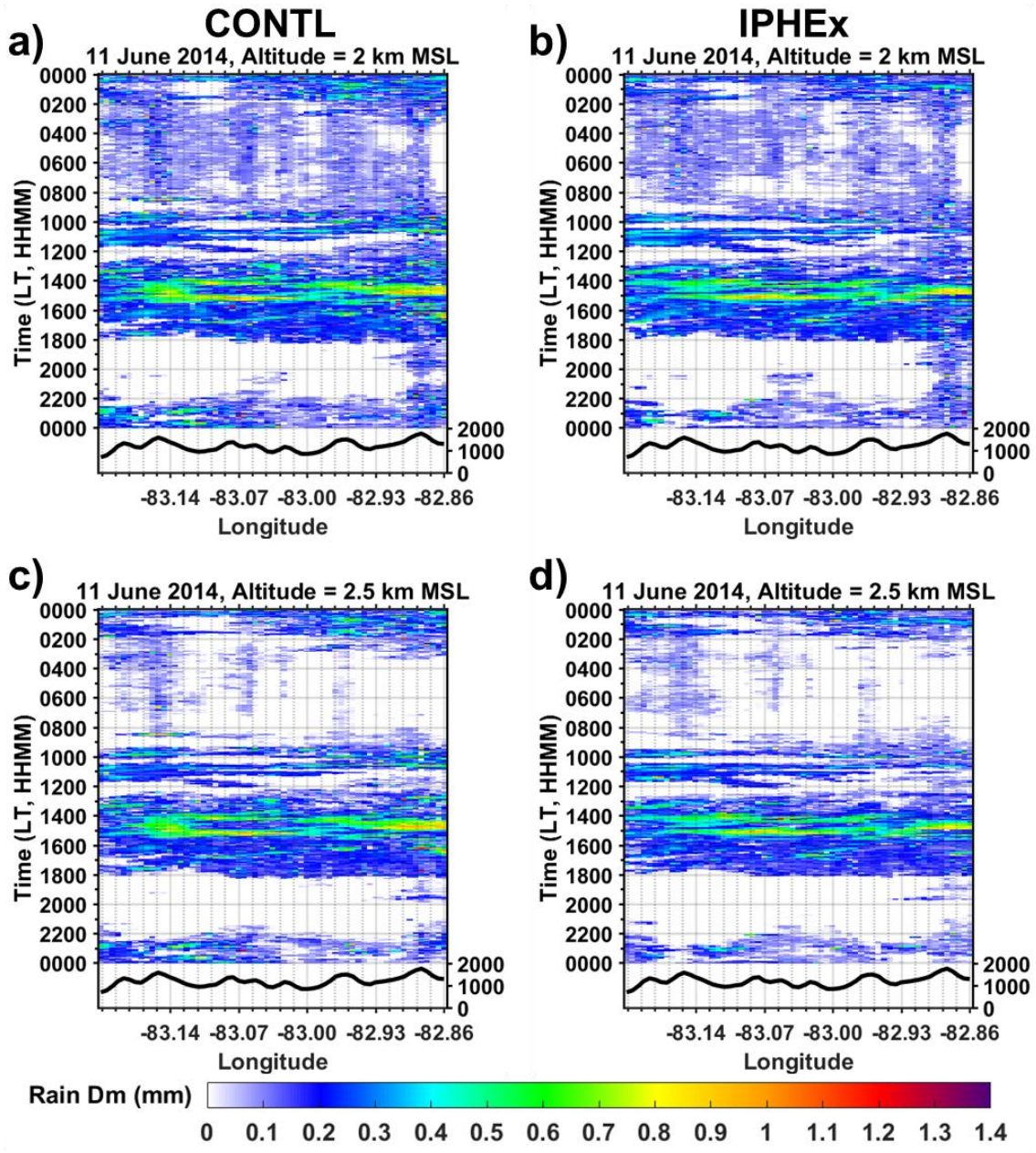


**Figure E4: Hovmöller diagrams of modeled rain $D_m$ at different altitudes (2 km and 2.5 km MSL) along the D-D′ cross section from the CONTL (a, c) and IPHEx (b, d) simulations for 11 June event.**

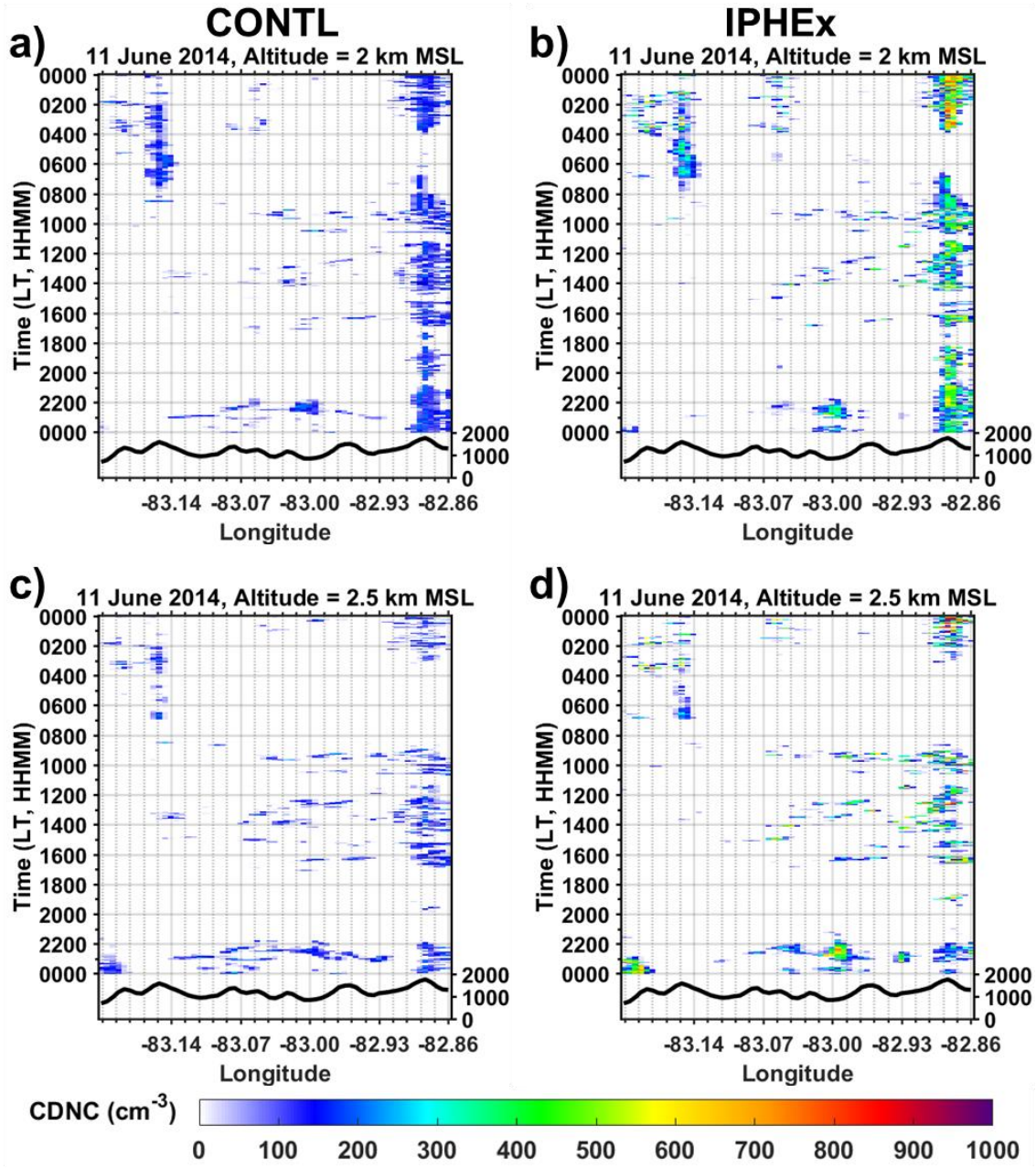


**Figure E5: Hovmöller diagrams of simulated cloud droplet number concentration (CDNC) at different altitudes (2 km, 2.5 km, and 2.9 km MSL) along the D-D′ cross section from the CONTL (left column) and IPHEx (right column) runs for 11 June event.**

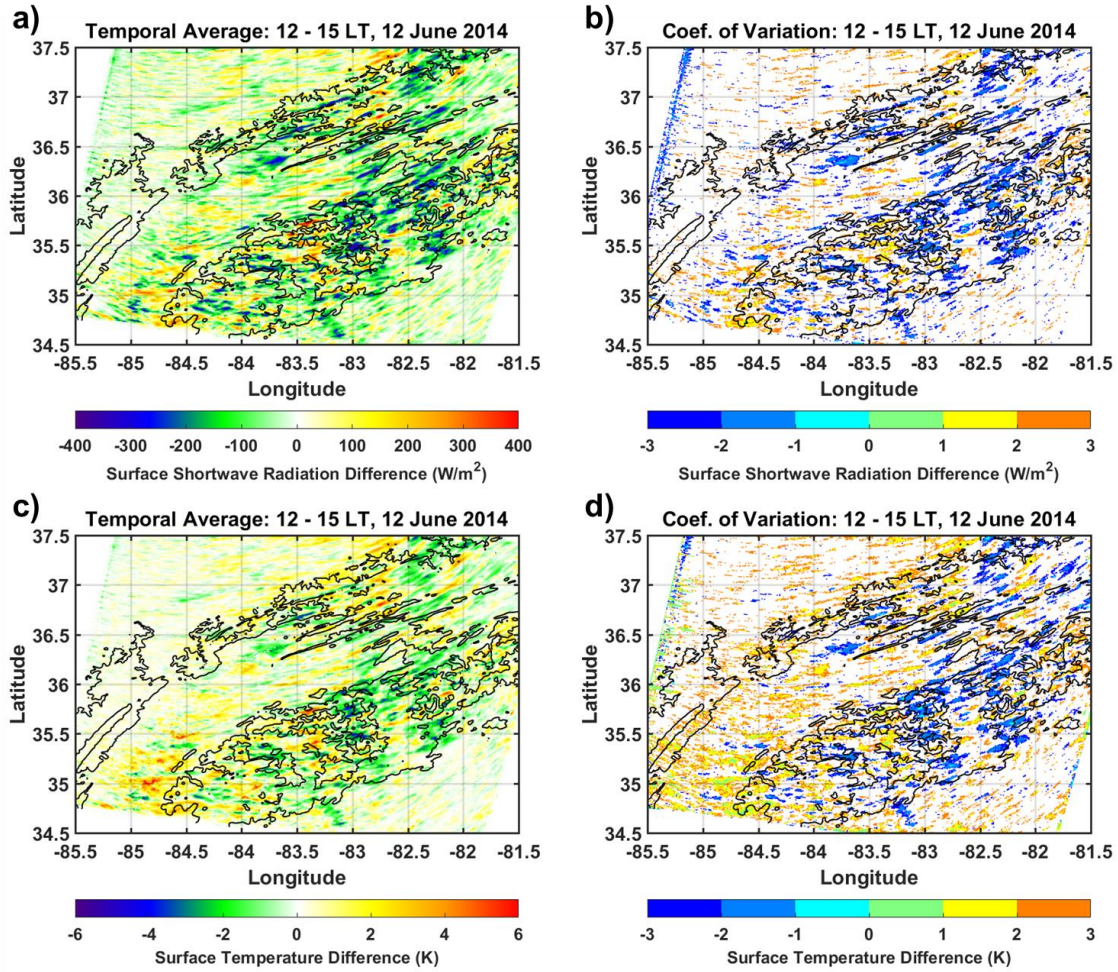


**Figure E6: Temperature average and coefficient of variance (CV) of differences in surface shortwave radiation (a, b) and surface temperature (c, d) during 12–15 LT on 12 June 2014, as highlighted by the yellow shade in Fig. 5-10a.**

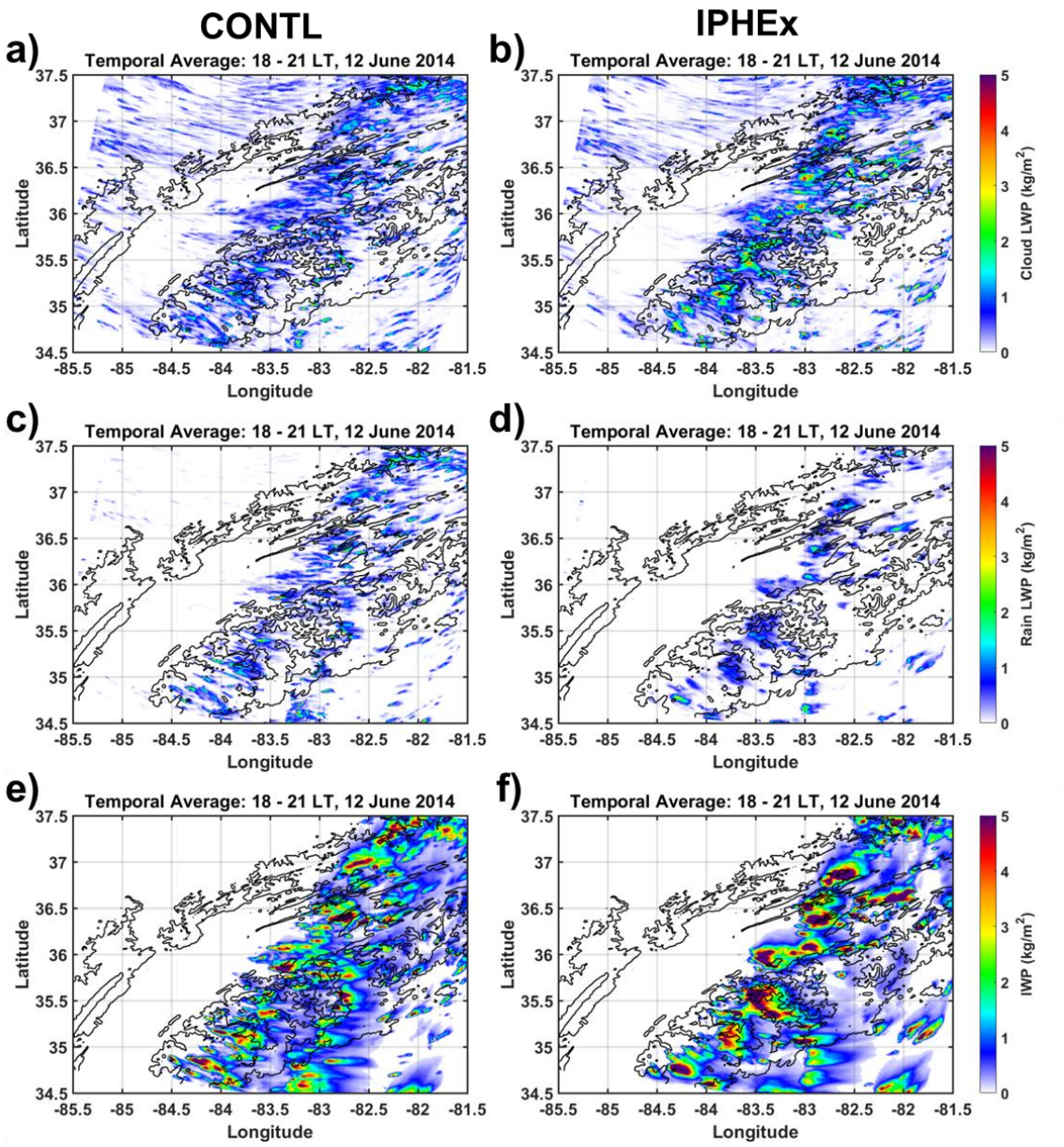


**Figure E7: Spatial variations of cloud LWP (a, b), rain LWP (c, d), and IWP (e, f) averaged over 1800 – 2100 LT on 12 June 2014 for the CONTL (left column) and IPHEx (right column) simulations.**

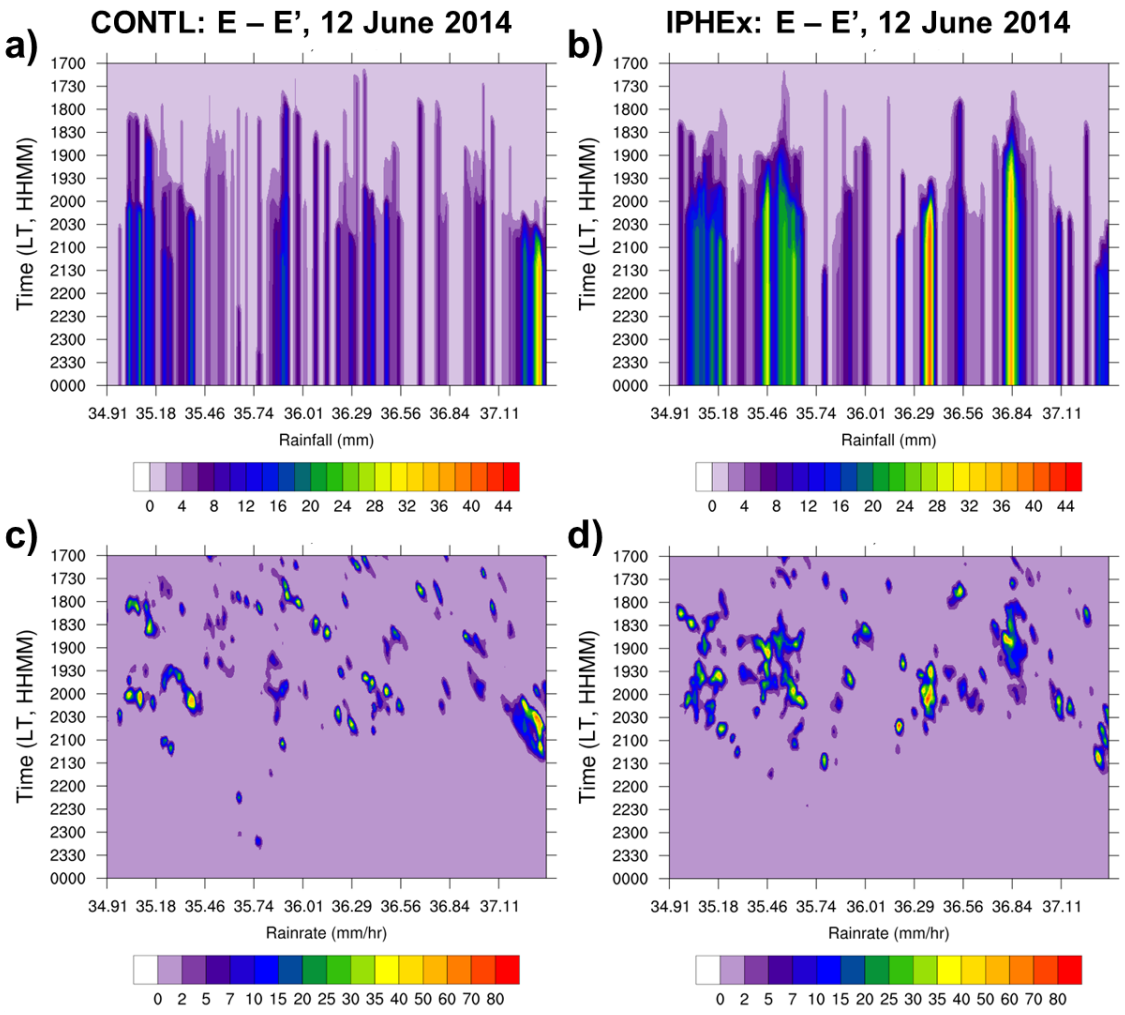


**Figure E8: Simulated rainfall accumulation (a, b) and rainrate (c, d) along the E-E' cross section from the CONTL (left column) and IPHEx (right column) runs for the evening event on 12 June 2014.**

# References


Abdul-Razzak, H., Ghan, S. J., and Rivera-Carpio, C.: A parameterization of aerosol activation: 1. Single aerosol type, Journal of Geophysical Research: Atmospheres, 103, 6123-6131, 10.1029/97jd03735, 1998.

Ackerman, S. A., Strabala, K. I., Menzel, W. P., Frey, R. A., Moeller, C. C., and Gumley, L. E.: Discriminating clear sky from clouds with MODIS, Journal of Geophysical Research, 103, 32141, 10.1029/1998jd200032, 1998.

Ackerman, S. A., Holz, R. E., Frey, R., Eloranta, E. W., Maddux, B. C., and McGill, M.: Cloud Detection with MODIS. Part II: Validation, Journal of Atmospheric and Oceanic Technology, 25, 1073-1086, 10.1175/2007jtecha1053.1, 2008.

Albrecht, B. A.: Aerosols, cloud microphysics, and fractional cloudiness, Science (New York, NY), 245, 1227, 1989.

Alexander, R. B., Boyer, E. W., Smith, R. A., Schwarz, G. E., and Moore, R. B.: The Role of Headwater Streams in Downstream Water Quality, J Am Water Resour Assoc, 43, 41-59, 10.1111/j.1752-1688.2007.00005.x, 2007.

Ames, R. B., Hand, J. L., Kreidenweis, S. M., Day, D. E., and Malm, W. C.: Optical Measurements of Aerosol Size Distributions in Great Smoky Mountains National Park: Dry Aerosol Characterization, Journal of the Air & Waste Management Association, 50, 665-676, 10.1080/10473289.2000.10464128, 2000.

Amitai, E., Llort, X., and Sempere-Torres, D.: Comparison of TRMM Radar Rainfall Estimates with NOAA Next-Generation QPE, Journal of the Meteorological Society of Japan, 87A, 109-118, 10.2151/jmsj.87A.109, 2009.

Amitai, E., Unkrich, C. L., Goodrich, D. C., Habib, E., and Thill, B.: Assessing Satellite-Based Rainfall Estimates in Semiarid Watersheds Using the USDA-ARS Walnut Gulch Gauge Network and TRMM PR, Journal of Hydrometeorology, 13, 1579-1588, 10.1175/jhm-d-12-016.1, 2012.

Andreae, M., and Rosenfeld, D.: Aerosol–cloud–precipitation interactions. Part 1. The nature and sources of cloud-active aerosols, Earth-Science Reviews, 89, 13-41, 2008.

Andreae, M. O., Rosenfeld, D., Artaxo, P., Costa, A. A., Frank, G. P., Longo, K. M., and Silva-Dias, M. A.: Smoking rain clouds over the Amazon, Science, 303, 1337-1342, 10.1126/science.1092779, 2004.

Angulo-Martínez, M., and Barros, A. P.: Measurement uncertainty in rainfall kinetic energy and intensity relationships for soil erosion studies: An evaluation using PARSIVEL disdrometers in the Southern Appalachian Mountains, Geomorphology, 228, 28-40, 10.1016/j.geomorph.2014.07.036, 2015.

ASOS Program Office Staff: Automated Surface Observing System Users Guide, ASOS Program Office, National Weather Service, Silver Spring, Md, 1998

Baker, M. B., Corbin, R. G., and Latham, J.: The influence of entrainment on the evolution of cloud droplet spectra: I. A model of inhomogeneous mixing, Quarterly Journal of the Royal Meteorological Society, 106, 581-598, 1980.

Barros, A. P., and Lettenmaier, D. P.: Dynamic modeling of the spatial distribution of precipitation in remote mountainous areas, Monthly weather review, 121, 1195-1214, 1993.

Barros, A. P., and Lettenmaier, D. P.: Incorporation of an evaporative cooling scheme into a dynamic model of orographic precipitation, Monthly weather review, 122, 2777-2783, 1994.

Barros, A. P., and Kuligowski, R. J.: Orographic effects during a severe wintertime rainstorm in the Appalachian Mountains, Monthly Weather Review, 126, 2648-2672, 1998.

Barros, A. P., Joshi, M., Putkonen, J., and Burbank, D. W.: A study of the 1999 monsoon rainfall in a mountainous region in central Nepal using TRMM products and rain gauge observations, Geophysical Research Letters, 27, 3683-3686, 10.1029/2000gl011827, 2000.

Barros, A. P., Prat, O. P., Shrestha, P., Testik, F. Y., and Bliven, L. F.: Revisiting Low and List (1982): Evaluation of Raindrop Collision Parameterizations Using Laboratory Observations and Modeling, Journal of the Atmospheric Sciences, 65, 2983-2993, 10.1175/2008jas2630.1, 2008.

Barros, A. P., and Tao, K.: A Space-Filling Algorithm to Extrapolate Narrow-Swath Instantaneous TRMM Microwave Rain-Rate Estimates Using Thermal IR Imagery, Journal of Atmospheric and Oceanic Technology, 25, 1901-1920, 10.1175/2008jtecha1019.1, 2008.

Barros, A. P.: Orographic Precipitation, Freshwater Resources, and Climate Vulnerabilities in Mountainous Regions, Climate Vulnerability: Understanding and Addressing Threats to Essential Resources, 57-78, 2013a.

Barros, A. P.: Orographic Precipitation, Freshwater Resources, and Climate Vulnerabilities in Mountainous Regions, 57-78, 10.1016/b978-0-12-384703-4.00504-9, 2013b.

Barros, A. P., Petersen, W., Schwaller, M., Cifelli, R., Mahoney, K., Peters-Liddard, C., Shepherd, M., Nesbitt, S., Wolff, D., Heymsfield, G., and Starr, D.: NASA GPM-Ground Validation: Integrated Precipitation and Hydrology Experiment 2014 Science Plan, Duke University, Durham, NC, 10.G8CC0XMR, 2014.

Baum, B. A., Menzel, W. P., Frey, R. A., Tobin, D. C., Holz, R. E., Ackerman, S. A., Heidinger, A. K., and Yang, P.: MODIS Cloud-Top Property Refinements for Collection 6, Journal of Applied Meteorology and Climatology, 51, 1145-1163, 10.1175/jamc-d-11-0203.1, 2012.

Baumgardner, D., Kok, G., Dawson, W., O'Connor, D., and Newton, R.: A new groundbased precipitation spectrometer: The Meteorological Particle Sensor (MPS), 11th Conf. on Cloud Physics, Amer. Meteor. Soc., Ogden, UT, 2002.

Beard, K. V.: Terminal velocity and shape of cloud and precipitation drops aloft, Journal of the Atmospheric Sciences, 33, 851-864, 1976.

Beard, K. V., and Ochs, H. T.: Collection and coalescence efficiencies for accretion, Journal of Geophysical Research: Atmospheres, 89, 7165-7169, 1984.

Beard, K. V., and Ochs III, H. T.: Collisions between small precipitation drops. Part II: Formulas for coalescence, temporary coalescence, and satellites, Journal of the atmospheric sciences, 52, 3977-3996, 1995.

Bell, T. L., Rosenfeld, D., Kim, K.-M., Yoo, J.-M., Lee, M.-I., and Hahnenberger, M.: Midweek increase in U.S. summer rain and storm heights suggests air pollution invigorates rainstorms, Journal of Geophysical Research, 113, 10.1029/2007jd008623, 2008.

Bergeron, T.: Problems and Methods of Rainfall Investigation Address of the Honorary Chairman of the Conference, Physics of Precipitation: Proceedings of the Cloud Physics Conference, Woods Hole, Massachusetts, 1960,

Bergeron, T.: On the low-level redistribution of atmospheric water caused by orography, the International Conference on Cloud Physics, Tokyo, 1965,

Berry, E. X., and Reinhardt, R. L.: An analysis of cloud drop growth by collection: Part I. Double distributions, Journal of the Atmospheric Sciences, 31, 1814-1824, 1974.

Berry, Z. C., and Smith, W. K.: Cloud pattern and water relations in Picea rubens and Abies fraseri, southern Appalachian Mountains, USA, Agricultural and Forest Meteorology, 162-163, 27-34, 10.1016/j.agrformet.2012.04.005, 2012.

Berry, Z. C., and Smith, W. K.: Ecophysiological importance of cloud immersion in a relic spruce-fir forest at elevational limits, southern Appalachian Mountains, USA, Oecologia, 173, 637-648, 10.1007/s00442-013-2653-4, 2013.

Berry, Z. C., Hughes, N. M., and Smith, W. K.: Cloud immersion: an important water source for spruce and fir saplings in the southern Appalachian Mountains, Oecologia, 174, 319-326, 10.1007/s00442-013-2770-0, 2014.

Best, A. C.: Empirical formulae for the terminal velocity of water drops falling through the atmosphere, Quarterly Journal of the Royal Meteorological Society, 76, 302-311, 1950.

Bindlish, R., and Barros, A. P.: Multifrequency Soil Moisture Inversion from SAR Measurements with the Use of IEM, Remote Sens. Environ., 71, 67–88, 10.1016/S0034-4257(99)00065-6, 2000.

Blando, J. D., Porcja, R. J., Li, T. H., Bowman, D., Lioy, P. J., and Turpin, B. J.: Secondary formation and the Smoky Mountain organic aerosol: An examination of aerosol polarity and functional group composition during SEAVS, Environmental science & technology, 32, 604-613, 1998.

Bott, A.: A flux method for the numerical solution of the stochastic collection equation, Journal of the atmospheric sciences, 55, 2284-2293, 1998.

Bott, A.: A flux method for the numerical solution of the stochastic collection equation: Extension to two-dimensional particle distributions, Journal of the atmospheric sciences, 57, 284-294, 2000.

Box, G. E., Hunter, W. G., and Hunter, J. S.: Statistics for experimenters: an introduction to design, data analysis, and model building, John Wiley & Sons, 1978.

Bradley, R. S., Vuille, M., Diaz, H. F., and Vergara, W.: Climate change. Threats to water supplies in the tropical Andes, Science, 312, 1755-1756, 10.1126/science.1128087, 2006.

Bruijnzeel, L. A.: Hydrological functions of tropical forests: not seeing the soil for the trees?, Agriculture, Ecosystems & Environment, 104, 185-228, 10.1016/j.agee.2004.01.015, 2004.

Budisulistiorini, S. H., Li, X., Bairai, S. T., Renfro, J., Liu, Y., Liu, Y. J., McKinney, K. A., Martin, S. T., McNeill, V. F., Pye, H. O. T., Nenes, A., Neff, M. E., Stone, E. A., Mueller, S., Knote, C., Shaw, S. L., Zhang, Z., Gold, A., and Surratt, J. D.: Examining the effects of anthropogenic emissions on isoprene-derived secondary organic aerosol formation during the 2013 Southern Oxidant and Aerosol Study (SOAS) at the Look Rock, Tennessee ground site, Atmospheric Chemistry and Physics, 15, 8871-8888, 10.5194/acp-15-8871-2015, 2015.

Budisulistiorini, S. H., Baumann, K., Edgerton, E. S., Bairai, S. T., Mueller, S., Shaw, S. L., Knipping, E. M., Gold, A., and Surratt, J. D.: Seasonal characterization of submicron aerosol chemical composition and organic aerosol sources in the southeastern United States: Atlanta, Georgia,and Look Rock, Tennessee, Atmospheric Chemistry and Physics, 16, 5171-5189, 10.5194/acp-16-5171-2016, 2016.

Cash, J. R., and Karp, A. H.: A variable order Runge-Kutta method for initial value problems with rapidly varying right-hand sides, ACM Transactions on Mathematical Software (TOMS), 16, 201-222, 1990.

Chen, R., Chang, F.-L., Li, Z., Ferraro, R., and Weng, F.: Impact of the Vertical Variation of Cloud Droplet Size on the Estimation of Cloud Liquid Water Path and Rain Detection, Journal of the Atmospheric Sciences, 64, 3843-3853, 10.1175/2007jas2126.1, 2007.

Chodes, N., Warner, J., and Gagin, A.: A determination of the condensation coefficient of water from the growth rate of small cloud droplets, Journal of the Atmospheric Sciences, 31, 1351-1357, 1974.

Christensen, S. I., and Petters, M. D.: The role of temperature in cloud droplet activation, J Phys Chem A, 116, 9706-9717, 10.1021/jp3064454, 2012.

Chuang, P. Y.: Measurement of the timescale of hygroscopic growth for atmospheric aerosols, Journal of Geophysical Research: Atmospheres, 108, 10.1029/2002jd002757, 2003.

Cohard, J. M., Pinty, J. P., and Bedos, C.: Extending Twomey's analytical estimate of nucleated cloud droplet concentrations from CCN spectra, Journal of the atmospheric sciences, 55(22), 3348-3357, 1998.

Cohard, J. M., and Pinty, J. P.: A comprehensive two-moment warm microphysical bulk scheme. I: Description and tests, Quarterly Journal of the Royal Meteorological Society, 126, 1815-1842, 2000.

Conant, W. C., VanReken, T. M., Rissman, T. A., Varutbangkul, V., Jonsson, H. H., Nenes, A., Jimenez, J. L., Delia, A. E., Bahreini, R., Roberts, G. C., Flagan, R. C., and Seinfeld, J. H.: Aerosol-cloud drop concentration closure in warm cumulus, Journal of Geophysical Research: Atmospheres, 109, 10.1029/2003jd004324, 2004.

Cooper, W. A.: Effects of variable droplet growth histories on droplet size distributions. Part I: Theory, Journal of the Atmospheric Sciences, 46, 1301-1311, 1989.

Cooper, W. A., Bruintjes, R. T., and Mather, G. K.: Calculations pertaining to hygroscopic seeding with flares, Journal of Applied Meteorology, 36, 1449-1469, 1997.

Del Genio, A. D., and Wolf, A. B.: The temperature dependence of the liquid water path of low clouds in the southern great plains, Journal of climate, 13, 3465-3486, 2000.

Delene, D. J.: Suitability of North Dakota for Conducting Effective Hygroscopic Seeding, The Journal of Weather Modification, 48, 43-67, 2016.

Diaz, H. F., Giambelluca, T. W., and Eischeid, J. K.: Changes in the vertical profiles of mean temperature and humidity in the Hawaiian Islands, Global and Planetary Change, 77, 21-25, 10.1016/j.gloplacha.2011.02.007, 2011.

Diehl, K., Simmel, M., and Wurzler, S.: Effects of drop freezing on microphysics of an ascending cloud parcel under biomass burning conditions, Atmospheric Environment, 41, 303-314, 10.1016/j.atmosenv.2006.08.011, 2007.

Doran, J. C., and Zhong, S.: Variations in mixed-layer depths arising from inhomogeneous surface conditions, Journal of climate, 8, 1965-1973, 1995.

Duan, Y., Wilson, A. M., and Barros, A. P.: Scoping a field experiment: error diagnostics of TRMM precipitation radar estimates in complex terrain as a basis for IPHEx2014, Hydrology and Earth System Sciences, 19, 1501-1520, 10.5194/hess-19-1501-2015, 2015.

Duan, Y., Petters, M. D., and Barros, A. P.: Understanding aerosol-cloud interactions in the development of orographic cumulus congestus during IPHEx, Atmospheric Chemistry and Physics Discussions, 1-55, 10.5194/acp-2017-396, 2017.

Durden, S. L., Haddad, Z. S., Kitiyakara, A., and Li, F. K.: Effects of nonuniform beam filling on rainfall retrieval for the TRMM precipitation radar, Journal of Atmospheric and Oceanic Technology, 15, 635-646, 1998.

Fan, J., Yuan, T., Comstock, J. M., Ghan, S., Khain, A., Leung, L. R., Li, Z., Martins, V. J., and Ovchinnikov, M.: Dominant role by vertical wind shear in regulating aerosol effects on deep convective clouds, Journal of Geophysical Research, 114, 10.1029/2009jd012352, 2009.

Feingold, G., and Chuang, P. Y.: Analysis of the influence of film-forming compounds on droplet growth: Implications for cloud microphysical processes and climate, Journal of the atmospheric sciences, 59, 2006-2018, 2002.

Fink, P. M.: Smoky Mountains history as told in place names. *East Tennessee Historical Society. Publ*, *6*, 3-11, 1934.

Fisher, B. L.: Climatological Validation of TRMM TMI and PR Monthly Rain Products over Oklahoma, J. Appl. Meteorol., 43, 519–535, 2004.

Flossmann, A. I., Hall, W. D., and Pruppacher, H. R.: A theoretical study of the wet removal of atmospheric pollutants. Part I: The redistribution of aerosol particles captured through nucleation and impaction scavenging by growing cloud drops, Journal of the atmospheric sciences, 42, 583-606, 1985.

Foster, P.: The potential negative impacts of global climate change on tropical montane cloud forests, Earth-Science Reviews, 55, 73-106, 2001.

Fountoukis, C., and Nenes, A.: Continued development of a cloud droplet formation parameterization for global climate models, Journal of Geophysical Research, 110, 10.1029/2004jd005591, 2005.

Fountoukis, C., Nenes, A., Meskhidze, N., Bahreini, R., Conant, W. C., Jonsson, H., Murphy, S., Sorooshian, A., Varutbangkul, V., Brechtel, F., Flagan, R. C., and Seinfeld, J. H.: Aerosol–cloud drop concentration closure for clouds sampled during the International Consortium for Atmospheric Research on Transport and Transformation 2004 campaign, Journal of Geophysical Research, 112, 10.1029/2006jd007272, 2007.

Frey, R. A., Ackerman, S. A., Liu, Y., Strabala, K. I., Zhang, H., Key, J. R., and Wang, X.: Cloud Detection with MODIS. Part I: Improvements in the MODIS Cloud Mask for Collection 5, Journal of Atmospheric and Oceanic Technology, 25, 1057-1072, 10.1175/2008jtecha1052.1, 2008.

Fukuta, N., and Walter, L.: Kinetics of hydrometeor growth from a vaper-spherical model, Journal of the Atmospheric Sciences, 27, 1160-1172, 1970.

Garnier, J. P., Ehrhard, P., and Mirabel, P.: Water droplet growth study in a continuous flow diffusion cloud chamber, Atmospheric research, 21, 41-51, 1987.

Gebremichael, M., and Barros, A.: Evaluation of MODIS Gross Primary Productivity (GPP) in tropical monsoon regions, Remote Sensing of Environment, 100, 150-166, 10.1016/j.rse.2005.10.009, 2006.

Ghan, S. J., Abdul-Razzak, H., Nenes, A., Ming, Y., Liu, X., Ovchinnikov, M., Shipway, B., Meskhidze, N., Xu, J., and Shi, X.: Droplet nucleation: Physically-based parameterizations and comparative evaluation, Journal of Advances in Modeling Earth Systems, 3, 10.1029/2011ms000074, 2011.

Gill, P. S., Graedel, T. E., and Weschler, C. J.: Organic films on atmospheric aerosol particles, fog droplets, cloud droplets, raindrops, and snowflakes, Reviews of Geophysics, 21, 903-920, 1983.

Givati, A., and Rosenfeld, D.: Quantifying precipitation suppression due to air pollution, Journal of Applied meteorology, 43, 1038-1056, 2004.

Givati, A., and Rosenfeld, D.: Separation between Cloud-Seeding and Air-Pollution Effects, Journal of Applied Meteorology, 43, 1038-1056, 2005.

Goldsmith, G. R., Matzke, N. J., and Dawson, T. E.: The incidence and implications of clouds for cloud forest plant water relations, Ecol Lett, 16, 307-314, 10.1111/ele.12039, 2013.

Goldstein, A. H., Koven, C. D., Heald, C. L., and Fung, I. Y.: Biogenic carbon and anthropogenic pollutants combine to form a cooling haze over the southeastern United States, Proceedings of the National Academy of Sciences, 106, 8835-8840, 2009.

Gotsch, S. G., Crausbay, S. D., Giambelluca, T. W., Weintraub, A. E., Longman, R. J., Asbjornsen, H., Hotchkiss, S. C., and Dawson, T. E.: Water relations and microclimate around the upper limit of a cloud forest in Maui, Hawai'i, Tree Physiol, 34, 766-777, 10.1093/treephys/tpu050, 2014.

Guenther, A., Karl, T., Harley, P., Wiedinmyer, C., Palmer, P. I., and Geron, C.: Estimates of global terrestrial isoprene emissions using MEGAN (Model of Emissions of Gases and Aerosols from Nature), Atmospheric Chemistry and Physics, 6(1), 107-173, 2006.

Gultepe, I., Tardif, R., Michaelides, S. C., Cermak, J., Bott, A., Bendix, J., Müller, M. D., Pagowski, M., Hansen, B., Ellrod, G., Jacobs, W., Toth, G., and Cober, S. G.: Fog Research: A Review of Past Achievements and Future Perspectives, Pure and Applied Geophysics, 164, 1121-1159, 10.1007/s00024-007-0211-x, 2007.

Gunthe, S. S., King, S. M., Rose, D., Chen, Q., Roldin, P., Farmer, D. K., Jimenez, J. L., Artaxo, P., Andreae, M. O., Martin, S. T., and Pöschl, U.: Cloud condensation nuclei in pristine tropical rainforest air of Amazonia: size-resolved measurements and modeling of atmospheric aerosol composition and CCN activity, Atmospheric Chemistry and Physics, 9, 7551-7575, 2009.

Habib, E., and Krajewski, W. F.: Uncertainty analysis of the TRMM ground-validation radar-rainfall products: Application to the TEFLUN-B field campaign, Journal of Applied Meteorology, 41, 558-572, 2002.

Hagen, D. E., Schmitt, J., Trueblood, M., Carstens, J., White, D. R., and Alofs, D. J.: Condensation coefficient measurement for water in the UMR cloud simulation chamber, Journal of the atmospheric sciences, 46, 803-816, 1989.

Hagihara, Y., Okamoto, H., and Yoshida, R.: Development of a combined CloudSat-CALIPSO cloud mask to show global cloud distribution, Journal of Geophysical Research, 115, 10.1029/2009jd012344, 2010.

Hagihara, Y., Okamoto, H., and Luo, Z. J.: Joint analysis of cloud top heights from CloudSat and CALIPSO: New insights into cloud top microphysics, Journal of Geophysical Research: Atmospheres, 119, 4087-4106, 10.1002/2013jd020919, 2014.

Hallquist, M., Wenger, J., Baltensperger, U., Rudich, Y., Simpson, D., Claeys, M., Dommen, J., Donahue, N., George, C., and Goldstein, A.: The formation, properties and impact of secondary organic aerosol: current and emerging issues, Atmospheric Chemistry and Physics, 9, 5155-5236, 2009.

Hamada, A., and Takayabu, Y. N.: Improvements in Detection of Light Precipitation with the Global Precipitation Measurement Dual-Frequency Precipitation Radar (GPM DPR), Journal of Atmospheric and Oceanic Technology, 33, 653-667, 10.1175/jtech-d-15-0097.1, 2016.

Hand, J. L., Ames, R. B., Kreidenweis, S. M., Day, D. E., and Malm, W. C.: Estimates of Particle Hygroscopicity during the Southeastern Aerosol and Visibility Study, Journal of the Air & Waste Management Association, 50, 677-685, 10.1080/10473289.2000.10464109, 2000.

Hartmann, D. L., Ockert-Bell, M. E., and Michelsen, M. L.: The effect of cloud type on Earth's energy balance: Global analysis, Journal of Climate, 5, 1281-1304, 1992.

Haynes, J. M., and Stephens, G. L.: Tropical oceanic cloudiness and the incidence of precipitation: Early results from CloudSat, Geophysical Research Letters, 34, 10.1029/2007gl029335, 2007.

Haywood, J., and Boucher, O.: Estimates of the direct and indirect radiative forcing due to tropospheric aerosols: A review, Reviews of Geophysics, 38, 513, 10.1029/1999rg000078, 2000.

Heymsfield, G. M., Geerts, B., and Tian, L.: TRMM Precipitation Radar Reflectivity Profiles as Compared with High-Resolution Airborne and Ground-Based Radar Measurements, J. Appl. Meteorol., 39, 2080–2102, 10.1175/1520-0450(2001)040<2080:TPRRPA>2.0.CO;2, 2000.

Hill, B. H., Kolka, R. K., McCormick, F. H., and Starry, M. A.: A synoptic survey of ecosystem services from headwater catchments in the United States, Ecosystem Services, 7, 106-115, 10.1016/j.ecoser.2013.12.004, 2014.

Hindmarsh, A. C.: ODEPACK, a systematized collection of ODE solvers, Scientific Computing, edited by: Stepleman, R., North-Holland, New York, 1983.

Holz, R. E., Ackerman, S. A., Nagle, F. W., Frey, R., Dutcher, S., Kuehn, R. E., Vaughan, M. A., and Baum, B.: Global Moderate Resolution Imaging Spectroradiometer (MODIS) cloud detection and height evaluation using CALIOP, Journal of Geophysical Research, 113, 10.1029/2008jd009837, 2008.

Holzinger, R., Sanhueza, E., von Kuhlmann, R., Kleiss, B., Donoso, L., and Crutzen, P. J.: Diurnal cycles and seasonal variation of isoprene and its oxidation products in the tropical savanna atmosphere, Global Biogeochemical Cycles, 16, 22-21-22-13, 10.1029/2001gb001421, 2002.

Hoose, C., Kristjánsson, J. E., Chen, J.-P., and Hazra, A.: A Classical-Theory-Based Parameterization of Heterogeneous Ice Nucleation by Mineral Dust, Soot, and Biological Particles in a Global Climate Model, Journal of the Atmospheric Sciences, 67, 2483-2503, 10.1175/2010jas3425.1, 2010.

HovmÖller, E.: The Trough-and-Ridge diagram, Tellus, 1, 62-66, 10.3402/tellusa.v1i2.8498, 1949.

Hu, J., and Riveros-Iregui, D. A.: Life in the clouds: are tropical montane cloud forests responding to changes in climate?, Oecologia, 180, 1061-1073, 10.1007/s00442-015-3533-x, 2016.

Hu, Z., and Srivastava, R. C.: Evolution of raindrop size distribution by coalescence, breakup, and evaporation: Theory and observations, Journal of the atmospheric sciences, 52, 1761-1783, 1995.

Iacono, M. J., Delamere, J. S., Mlawer, E. J., Shephard, M. W., Clough, S. A., and Collins, W. D.: Radiative forcing by long-lived greenhouse gases: Calculations with the AER radiative transfer models, Journal of Geophysical Research, 113, 10.1029/2008jd009944, 2008.

Iguchi, T., Kozu, T., Meneghini, R., Awaka, J., and Okamoto, K.: Rain-Profiling Algorithm for the TRMM Precipitation Radar, J. Appl. Meteorol., 39, 2038–2052, 10.1175/1520-0450(2001)040<2038:RPAFTT>2.0.CO;2, 2000.

Iguchi, T., Kozu, T., Kwiatkowski, J., Meneghini, R., Awaka, J., and Okamoto, K. i.: Uncertainties in the Rain Profiling Algorithm for the TRMM Precipitation Radar, Journal of the Meteorological Society of Japan, 87A, 1-30, 10.2151/jmsj.87A.1, 2009.

Jacobson, M. Z., and Turco, R. P.: SMVGEAR: A sparse-matrix, vectorized Gear code for atmospheric models, Atmospheric Environment, 28, 273-284, 1994.

Jacobson, M. Z., Turco, R. P., Jensen, E. J., and Toon, O. B.: Modeling coagulation among particles of different composition and size, Atmospheric Environment, 28, 1327-1338, 1994.

Jacobson, M. Z., and Turco, R. P.: Simulating Condensational Growth, Evaporation, and Coagulation of Aerosols Using a Combined Moving and Stationary Size Grid, Aerosol Science and Technology, 22, 73-92, 10.1080/02786829408959729, 1995.

Jacobson, M. Z.: Fundamentals of atmospheric modeling, 2nd ed., Cambridge university press, 2005.

Jaenicke, R.: Tropospheric aerosols, in: Aerosol-cloud-climate interactions, edited by: Hobbs, P. V., Academic Press, 1-31, 1993.

Janjic, Z. I.: The step-mountain eta coordinate model: Further developments of the convection, viscous sublayer, and turbulence closure schemes, Monthly Weather Review, 122, 927-945, 1994.

Jiang, J. H., Su, H., Schoeberl, M. R., Massie, S. T., Colarco, P., Platnick, S., and Livesey, N. J.: Clean and polluted clouds: Relationships among pollution, ice clouds, and precipitation in South America, Geophysical Research Letters, 35, 10.1029/2008gl034631, 2008.

Johnson, D. M., and Smith, W. K.: Low clouds and cloud immersion enhance photosynthesis in understory species of a southern Appalachian spruce–fir forest (USA), American Journal of Botany, 93, 1625-1632, 2006.

Juvik, J. O., and Nullet, D.: Comments on "A proposed standard fog collector for use in high-elevation regions", Journal of Applied Meteorology, 34, 2108-2110, 1995.

Kain, J. S.: The Kain–Fritsch convective parameterization: an update, J. Appl. Meteorol., 43, 170–181, 2004.

Kalnay, E., Kanamitsu, M., Kistler, R., Collins, W., Deaven, D., Gandin, L., Iredell, M., Saha, S., White, G., Woollen, J., Zhu, Y., Leetmaa, A., Reynolds, R., Chelliah, M., Ebisuzaki, W., Higgins, W., Janowiak, J., Mo, K. C., Ropelewski, C., Wang, J., Jenne, R., and Joseph, D.: The NCEP/NCAR 40-year reanalysis project, Bull. Am. Meteorol. Soc., 77, 437–471, 1996.

Kanakidou, M., Seinfeld, J., Pandis, S., Barnes, I., Dentener, F., Facchini, M., Van Dingenen, R., Ervens, B., Nenes, A., and Nielsen, C.: Organic aerosol and global climate modelling: a review, Atmospheric Chemistry and Physics, 5, 1053-1123, 2005.

Kaufman, Y. J., Tanré, D., and Boucher, O.: A satellite view of aerosols in the climate system, Nature, 419, 215-223, 2002.

Kelly, G. M.: Aerosol-precipitation interactions in the southern Appalachian Mountains, Master Thesis, Department of Geography and Planning, Appalachian State University, 2011.

Kerkweg, A., Wurzler, S., Reisin, T., and Bott, A.: On the cloud processing of aerosol particles: An entraining air-parcel model with two-dimensional spectral cloud microphysics and a new formulation of the collection kernel, Quarterly Journal of the Royal Meteorological Society, 129, 1-18, 10.1256/qj.02.52, 2003.

Khain, A., Ovtchinnikov, M., Pinsky, M., Pokrovsky, A., and Krugliak, H.: Notes on the state-of-the-art numerical modeling of cloud microphysics, Atmospheric Research, 55, 159-224, 2000.

Khain, A., Rosenfeld, D., and Pokrovsky, A.: Aerosol impact on the dynamics and microphysics of deep convective clouds, Quarterly Journal of the Royal Meteorological Society, 131, 2639-2663, 2005.

Khain, A. P., and Pinsky, M. B.: Turbulence effects on the collision kernel. II: Increase of the swept volume of colliding drops, Quarterly Journal of the Royal Meteorological Society, 123, 1543-1560, 1997.

Khairoutdinov, M., Randall, D., and DeMott, C.: Simulations of the atmospheric general circulation using a cloud-resolving model as a superparameterization of physical processes, Journal of the Atmospheric Sciences, 62, 2136-2154, 2005.

Kim, S.-W., Chung, E.-S., Yoon, S.-C., Sohn, B.-J., and Sugimoto, N.: Intercomparisons of cloud-top and cloud-base heights from ground-based Lidar, CloudSat and CALIPSO measurements, International Journal of Remote Sensing, 32, 1179-1197, 10.1080/01431160903527439, 2011.

King, M. D., Kaufman, Y. J., Menzel, W. P., and Tanre, D.: Remote sensing of cloud, aerosol, and water vapor properties from the Moderate Resolution Imaging Spectrometer (MODIS), Geoscience and Remote Sensing, IEEE Transactions on, 30, 2-27, 1992.

Kirstetter, P.-E., Hong, Y., Gourley, J. J., Schwaller, M., Petersen, W., and Zhang, J.: Comparison of TRMM 2A25 Products, Version 6 and Version 7, with NOAA/NSSL Ground Radar–Based National Mosaic QPE, Journal of Hydrometeorology, 14, 661-669, 10.1175/jhm-d-12-030.1, 2013.

Knollenberg, R. G.: The optical array: An alternative to scattering or extinction for airborne particle size determination, Journal of Applied Meteorology, 9, 86-103, 1970.

Kokhanovsky, A., and de Leeuw, G.: Satellite Aerosol Remote Sensing Over Land, Environmental Sciences, Springer-Verlag Berlin Heidelberg, 2009.

Koren, I., Kaufman, Y. J., Remer, L. A., and Martins, J. V.: Measurement of the effect of Amazon smoke on inhibition of cloud formation, Science, 303, 1342-1345, 10.1126/science.1089424, 2004.

Koren, I., Martins, J. V., Remer, L. A., and Afargan, H.: Smoke invigoration versus inhibition of clouds over the Amazon, Science, 321, 946-949, 10.1126/science.1159185, 2008.

Koren, I., Altaratz, O., Remer, L. A., Feingold, G., Martins, J. V., and Heiblum, R. H.: Aerosol-induced intensification of rain from the tropics to the mid-latitudes, Nature Geoscience, 2012.

Kovetz, A., and Olund, B.: The effect of coalescence and condensation on rain formation in a cloud of finite vertical extent, Journal of the Atmospheric Sciences, 26, 1060-1065, 1969.

Kozu, T., Kawanishi, T., Kuroiwa, H., Kojima, M., Oikawa, K., Kumagai, H., Okamoto, K., Okumura, M., Nakatsuka, H., and Nishikawa, K.: Development of precipitation radar onboard the Tropical Rainfall Measuring Mission (TRMM) satellite, IEEE Trans. Geosci. Remote Sens., 39, 102–116, 10.1109/36.898669, 2001.

Kreidenweis, S. M., Walcek, C. J., Feingold, G., Gong, W., Jacobson, M. Z., Kim, C. H., Liu, X., Penner, J. E., Nenes, A., and Seinfeld, J. H.: Modification of aerosol mass and size distribution due to aqueous-phase SO2 oxidation in clouds: Comparisons of several models, Journal of Geophysical Research, 108, 10.1029/2002jd002697, 2003.

Krueger, S. K., Su, C. W., and McMurtry, P. A.: Modeling entrainment and finescale mixing in cumulus clouds, Journal of the atmospheric sciences, 54, 2697-2712, 1997.

Kumar, S., and Ramkrishna, D.: On the solution of population balance equations by discretization—I. A fixed pivot technique, Chemical Engineering Science, 51, 1311-1332, 1996.

Lance, S., Brock, C. A., Rogers, D., and Gordon, J. A.: Water droplet calibration of the Cloud Droplet Probe (CDP) and in-flight performance in liquid, ice and mixed-phase clouds during ARCPAC, Atmospheric Measurement Techniques, 3, 1683-1706, 10.5194/amt-3-1683-2010, 2010.

Lance, S.: Coincidence Errors in a Cloud Droplet Probe (CDP) and a Cloud and Aerosol Spectrometer (CAS), and the Improved Performance of a Modified CDP, Journal of Atmospheric and Oceanic Technology, 29, 1532-1541, 10.1175/jtech-d-11-00208.1, 2012.

Lang, T. J., and Barros, A. P.: An investigation of the onsets of the 1999 and 2000 monsoons in central Nepal, Monthly Weather Review, 130, 1299-1316, 2002.

Leaitch, W. R., Strapp, J. W., Isaac, G. A., and Hudson, J. G.: Cloud droplet nucleation and cloud scavenging of aerosol sulphate in polluted atmospheres, Tellus B, 38, 328-344, 1986.

Lee, S., Donner, L., and Penner, J.: Thunderstorm and stratocumulus: How does their contrasting morphology affect their interactions with aerosols, Atmos. Chem. Phys, 10, 6819-6837, 2010.

Leroy, D., Wobrock, W., and Flossmann, A. I.: The role of boundary layer aerosol particles for the development of deep convective clouds: A high-resolution 3D model with detailed (bin) microphysics applied to CRYSTAL-FACE, Atmospheric Research, 91, 62-78, 10.1016/j.atmosres.2008.06.001, 2009.

Li, Z., Niu, F., Fan, J., Liu, Y., Rosenfeld, D., and Ding, Y.: Long-term impacts of aerosols on the vertical development of clouds and precipitation, Nature Geoscience, 4, 888-894, 2011.

Liao, L., and Meneghini, R.: Validation of TRMM Precipitation Radar through Comparison of Its Multiyear Measurements with Ground-Based Radar, Journal of Applied Meteorology and Climatology, 48, 804-817, 10.1175/2008jamc1974.1, 2009.

Link, M., Zhou, Y., Taubman, B., Sherman, J., Morrow, H., Krintz, I., Robertson, L., Cook, R., Stocks, J., West, M., and Sive, B. C.: A characterization of volatile organic compounds and secondary organic aerosol at a mountain site in the Southeastern United States, Journal of Atmospheric Chemistry, 72, 81-104, 10.1007/s10874-015-9305-5, 2015.

Lohmann, U., and Feichter, J.: Global indirect aerosol effects: a review, Atmospheric Chemistry and Physics, 5, 715-737, 2005.

Lohmann, U., and Hoose, C.: Sensitivity studies of different aerosol indirect effects in mixed-phase clouds, Atmospheric Chemistry and Physics, 9, 8917-8934, 2009.

Low, T. B., and List, R.: Collision, coalescence and breakup of raindrops. Part I: Experimentally established coalescence efficiencies and fragment size distributions in breakup, Journal of the Atmospheric Sciences, 39, 1591-1606, 1982.

Lowenthal, D., Zielinska, B., Mason, B., Samy, S., Samburova, V., Collins, D., Spencer, C., Taylor, N., Allen, J., and Kumar, N.: Aerosol characterization studies at Great

Smoky Mountains National Park, summer 2006, Journal of Geophysical Research, 114, 10.1029/2008jd011274, 2009.

MacDonald, L. H., and Coe, D.: Influence of headwater streams on downstream reaches in forested areas, Forest Science, 53, 148-168, 2007.

Mace, G. G., Zhang, Q., Vaughan, M., Marchand, R., Stephens, G., Trepte, C., and Winker, D.: A description of hydrometeor layer occurrence statistics derived from the first year of merged Cloudsat and CALIPSO data, Journal of Geophysical Research, 114, 10.1029/2007jd009755, 2009.

Mace, G. G., and Zhang, Q.: The CloudSat radar-lidar geometrical profile product (RL-GeoProf): Updates, improvements, and selected results, Journal of Geophysical Research: Atmospheres, 119, 9441-9462, 10.1002/2013jd021374, 2014.

Maddux, B. C., Ackerman, S. A., and Platnick, S.: Viewing Geometry Dependencies in MODIS Cloud Products, Journal of Atmospheric and Oceanic Technology, 27, 1519-1528, 10.1175/2010jtecha1432.1, 2010.

Marchand, R., Mace, G. G., Ackerman, T., and Stephens, G.: Hydrometeor Detection Using Cloudsat—An Earth-Orbiting 94-GHz Cloud Radar, Journal of Atmospheric and Oceanic Technology, 25, 519-533, 10.1175/2007jtecha1006.1, 2008.

Marchant, B., Platnick, S., Meyer, K., Arnold, G. T., and Riedi, J.: MODIS Collection 6 shortwave-derived cloud phase classification algorithm and comparisons with CALIOP, Atmospheric Measurement Techniques Discussions, 8, 11893-11924, 10.5194/amtd-8-11893-2015, 2015.

Marek, R., and Straub, J.: Analysis of the evaporation coefficient and the condensation coefficient of water, International Journal of Heat and Mass Transfer, 44, 39-53, 2001.

Mason, B. J., and Jonas, P. R.: The evolution of droplet spectra and large droplets by condensation in cumulus clouds, Quarterly Journal of the Royal Meteorological Society, 100, 23-38, 1974.

Matsui, T., Santanello, J., Shi, J. J., Tao, W. K., Wu, D., Peters-Lidard, C., Kemp, E., Chin, M., Starr, D., Sekiguchi, M., and Aires, F.: Introducing multisensor satellite radiance-based evaluation for regional Earth System modeling, Journal of Geophysical Research: Atmospheres, 119, 8450-8475, 10.1002/2013jd021424, 2014.

McCarthy, J.: Field verification of the relationship between entrainment rate and cumulus cloud diameter., Journal of the Atmospheric Sciences, 31, 1028-1039, 1974.

McFiggans, G., Artaxo, P., Baltensperger, U., Coe, H., Facchini, M. C., Feingold, G., &, and Mentel, T. F.: The effect of physical and chemical aerosol properties on warm cloud droplet activation, Atmospheric Chemistry and Physics, 6, 2593-2649, 2006.

McGill, M. J., Vaughan, M. A., Trepte, C. R., Hart, W. D., Hlavka, D. L., Winker, D. M., and Kuehn, R.: Airborne validation of spatial properties measured by the CALIPSO lidar, Journal of Geophysical Research, 112, 10.1029/2007jd008768, 2007.

Meneghini, R., Iguchi, T., Kozu, T., Liao, L., Okamoto, K., Jones, J. A., and Kwiatkowski, J.: Use of the Surface Reference Technique for Path Attenuation Estimates from the TRMM Precipitation Radar, J. Appl. Meteorol., 39, 2053–2070, 10.1175/1520-0450(2001)040<2053:UOTSRT>2.0.CO;2, 2000.

Menon, S.: Current uncertainties in assessing aerosol effects on climate, Annu. Rev. Environ. Resour., 29, 1-30, 2004.

Meskhidze, N., Nenes, A., Conant, W. C., and Seinfeld, J. H.: Evaluation of a new cloud droplet activation parameterization with in situ data from CRYSTAL-FACE and CSTRIPE, Journal of Geophysical Research: Atmospheres, 110, 10.1029/2004jd005703, 2005.

Milbrandt, J. A., and Yau, M. K.: A multimoment bulk microphysics parameterization. Part II: A proposed three-moment closure and scheme description, Journal of the atmospheric sciences, 62, 3065-3081, 2005a.

Milbrandt, J. A., and Yau, M. K.: A multimoment bulk microphysics parameterization. Part I: Analysis of the role of the spectral shape parameter, Journal of the atmospheric sciences, 62, 3051-3064, 2005b.

Morton, B. R.: Buoyant plumes in a moist atmosphere, Journal of Fluid Mechanics, 2, 127-144, 1957.

Mozurkewich, M.: Aerosol growth and the condensation coefficient for water: A review, Aerosol science and technology, 5, 223-236, 1986.

Muhlbauer, A., and Lohmann, U.: Sensitivity studies of the role of aerosols in warm-phase orographic precipitation in different dynamical flow regimes, Journal of the Atmospheric Sciences, 65, 2522-2542, 2008.

Nakajima, T., and King, M. D.: Determination of the optical thickness and effective particle radius of clouds from reflected solar radiation measurements. Part I: Theory, Journal of the Atmospheric Sciences, 47, 1878-1893, 1990.

Nakamura, K.: Biases of rain retrieval algorithms for spaceborne radar caused by nonuniformity of rain, Journal of Atmospheric and Oceanic Technology, 8, 363-373, 1991.

Nakanishi, M., and Niino, H.: An improved Mellor–Yamada level-3 model with condensation physics: Its design and verification, Boundary-layer meteorology, 112, 1-31, 2004.

National Climatic Data Center: *Climate atlas of the United States*. Ashville, N.C., U.S. Dept. of Commerce, National Oceanic and Atmospheric Administration, National Climatic Data Center, 2000.

National Park Service (NPS), 2015. Visitor Use Statistics. https://irma.nps.gov/Stats/Reports/Park/GRSM

Nenes, A., Ghan, S., Abdul-Razzak, H., Chuang, P. Y., and Seinfeld, J. H.: Kinetic limitations on cloud droplet formation and impact on cloud albedo, Tellus B, 53, 133-149, 2001.

Nenes, A., Charlson, R. J., Facchini, M. C., Kulmala, M., Laaksonen, A., and Seinfeld, J. H.: Can chemical effects on cloud droplet number rival the first indirect effect?, Geophysical Research Letters, 29, 1848, 10.1029/2002gl015295, 2002.

Nesbitt, S. W., Zipser, E. J. and Cecil, D. J.: A Census of Precipitation Features in the Tropics Using TRMM: Radar, Ice Scattering, and Lightning Observations, J. Clim., 13, 4087–4106, 10.1175/1520-0442(2000)013<4087:ACOPFI>2.0.CO;2, 2000.

Nguyen, T. K. V., Petters, M. D., Suda, S. R., Guo, H., Weber, R. J., and Carlton, A. G.: Trends in particle-phase liquid water during the Southern Oxidant and Aerosol Study, Atmospheric Chemistry and Physics, 14, 10911-10930, 10.5194/acp-14-10911-2014, 2014.

Okamoto, K., Meneghini, R., Iguchi, T., Awaka, J. and Shimizu, S.: TRMM PR algorithms version 6 status and plans for version 7, Asia-Pacific Remote Sensing, edited by

G. L. Stephens and T. Y. Nakajima, pp. 715208–715208–10, 10.1117/12.804932, 2008.

Oliveira, R. S., Eller, C. B., Bittencourt, P. R., and Mulligan, M.: The hydroclimatic and ecophysiological basis of cloud forest distributions under current and projected climates, Ann Bot, 113, 909-920, 10.1093/aob/mcu060, 2014.

Pacifico, F., Harrison, S. P., Jones, C. D., and Sitch, S.: Isoprene emissions and climate, Atmospheric Environment, 43, 6121-6135, 10.1016/j.atmosenv.2009.09.002, 2009.

Painemal, D., and Zuidema, P.: Assessment of MODIS cloud effective radius and optical thickness retrievals over the Southeast Pacific with VOCALS-REx in situ measurements, Journal of Geophysical Research: Atmospheres, 116, n/a-n/a, 10.1029/2011jd016155, 2011.

Paluch, I. R.: The entrainment mechanism in Colorado cumuli, Journal of the atmospheric sciences, 36, 2467-2478, 1979.

Pauliquevis, T., Lara, L. L., Antunes, M. L., and Artaxo, P.: Aerosol and precipitation chemistry measurements in a remote site in Central Amazonia: the role of biogenic contribution, Atmospheric Chemistry and Physics, 12, 4987-5015, 10.5194/acp-12-4987-2012, 2012.

Petters, M. D., and Kreidenweis, S. M.: A single parameter representation of hygroscopic growth and cloud condensation nucleus activity, Atmospheric Chemistry and Physics, 7(8), 1961-1971, 2007.

Petters, M. D., Carrico, C. M., Kreidenweis, S. M., Prenni, A. J., DeMott, P. J., Collett, J. L., and Moosmüller, H.: Cloud condensation nucleation activity of biomass burning aerosol, Journal of Geophysical Research, 114, 10.1029/2009jd012353, 2009.

Petters, S. S., and Petters, M. D.: Surfactant effect on cloud condensation nuclei for two-component internally mixed aerosols, J. Geophys. Res. Atmos., 121, 1878–1895, 10.1002/2015JD024090, 2016.

Petzold, A., Gysel, M., Vancassel, X., Hitzenberger, R., Puxbaum, H., Vrochticky, S., Weingartner, E., Baltensperger, U., and Mirabel, P.: On the effects of organic matter and sulphur-containing compounds on the CCN activation of combustion particles, Atmospheric Chemistry and Physics, 5(12), 3187-3203, 2005.

Pinsky, M., Khain, A., and Shapiro, M.: Collisions of small drops in a turbulent flow. Part I: Collision efficiency. Problem formulation and preliminary results, Journal of the atmospheric sciences, 56, 2585-2600, 1999.

Pinsky, M., Khain, A., and Shapiro, M.: Stochastic effects of cloud droplet hydrodynamic interaction in a turbulent flow, Atmospheric research, 53, 131-169, 2000.

Pinsky, M., Khain, A., and Shapiro, M.: Collision efficiency of drops in a wide range of Reynolds numbers: Effects of pressure on spectrum evolution, Journal of the atmospheric sciences, 58, 742-764, 2001.

Pinsky, M., Khain, A., and Krugliak, H.: Collisions of Cloud Droplets in a Turbulent Flow. Part V: Application of Detailed Tables of Turbulent Collision Rate Enhancement to Simulation of Droplet Spectra Evolution, Journal of the Atmospheric Sciences, 65, 357-374, 10.1175/2007jas2358.1, 2008.

Pinsky, M. B., and Khain, A. P.: Effects of in-cloud nucleation and turbulence on droplet spectrum formation in cumulus clouds, Quarterly Journal of the Royal Meteorological Society, 128, 501-534, 2002.

Platnick, S., Meyer, K. G., King, M. D., Wind, G., Amarasinghe, N., Marchant, B., Arnold, G. T., Zhang, Z., Hubanks, P. A., Holz, R. E., Yang, P., Ridgway, W. L., and Riedi, J.: The MODIS Cloud Optical and Microphysical Products: Collection 6 Updates and Examples From Terra and Aqua, IEEE Transactions on Geoscience and Remote Sensing, 55, 502-525, 10.1109/tgrs.2016.2610522, 2017.

Poellot, Michael: GPM Ground Validation UND Citation Cloud Microphysics IPHEx. Dataset available online [https://ghrc.nsstc.nasa.gov/home/field-campaigns/iphex] from the NASA Global Hydrology Resource Center Distributed Active Archive Center, Huntsville, Alabama, U.S.A., 2015.

Porcù, F., Milani, L., and Petracca, M.: On the uncertainties in validating satellite instantaneous rainfall estimates with raingauge operational network, Atmospheric Research, 144, 73-81, 10.1016/j.atmosres.2013.12.007, 2014.

Pöschl, U., Martin, S., Sinha, B., Chen, Q., Gunthe, S., Huffman, J., Borrmann, S., Farmer, D., Garland, R., and Helas, G.: Rainforest aerosols as biogenic nuclei of clouds and precipitation in the Amazon, Science, 329, 1513-1516, 2010.

Pounds, J. A., Fogden, M. P., and Campbell, J. H.: Biological response to climate change on a tropical mountain, Nature, 398, 611-615, 1999.

Prasetia, R., As-syakur, A. R., and Osawa, T.: Validation of TRMM Precipitation Radar satellite data over Indonesian region, Theoretical and Applied Climatology, 112, 575-587, 10.1007/s00704-012-0756-1, 2012.

Prat, O. P., and Barros, A. P.: Exploring the use of a column model for the characterization of microphysical processes in warm rain: Results from a homogeneous rainshaft model, Advances in Geosciences, 10, 145-152, 2007a.

Prat, O. P., and Barros, A. P.: A Robust Numerical Solution of the Stochastic Collection–Breakup Equation for Warm Rain, Journal of Applied Meteorology and Climatology, 46, 1480-1497, 10.1175/jam2544.1, 2007b.

Prat, O. P., Barros, A. P., and Williams, C. R.: An Intercomparison of Model Simulations and VPR Estimates of the Vertical Structure of Warm Stratiform Rainfall during TWP-ICE, Journal of Applied Meteorology and Climatology, 47, 2797-2815, 10.1175/2008jamc1801.1, 2008.

Prat, O. P., and Barros, A. P.: Exploring the Transient Behavior ofZ–RRelationships: Implications for Radar Rainfall Estimation, Journal of Applied Meteorology and Climatology, 48, 2127-2143, 10.1175/2009jamc2165.1, 2009.

Prat, O. P., and Barros, A. P.: Ground observations to characterize the spatial gradients and vertical structure of orographic precipitation – Experiments in the inner region of the Great Smoky Mountains, Journal of Hydrology, 391, 141-156, 10.1016/j.jhydrol.2010.07.013, 2010a.

Prat, O. P., and Barros, A. P.: Assessing satellite-based precipitation estimates in the Southern Appalachian mountains using rain gauges and TRMM PR, Advances in Geosciences, 25, 143-153, 10.5194/adgeo-25-143-2010, 2010b.

Prat, O. P., Barros, A. P., and Testik, F. Y.: On the Influence of Raindrop Collision Outcomes on Equilibrium Drop Size Distributions, Journal of the Atmospheric Sciences, 69, 1534-1546, 10.1175/jas-d-11-0192.1, 2012.

Press, W. H., Teukolsky, S. A., Vetterling, W. T., and Flannery, B. P.: Numerical Recipes: The art of scientific computing, 3rd ed., Cambridge university press, 2007.

Pringle, K. J., Tost, H., Pozzer, A., Pöschl, U., and Lelieveld, J.: Global distribution of the effective aerosol hygroscopicity parameter for CCN activation, Atmospheric Chemistry and Physics, 10, 5241-5255, 10.5194/acp-10-5241-2010, 2010.

Pruppacher, H. R., and Klett, J. D.: Microphysics of Clouds and Precipitation, Springer Netherlands, 1978.

Pruppacher, H. R., and Klett, J. D.: Microphysics of Clouds and Precipitation, Atmos. Oceanogr. Sci. Libr., Kulwer Academic Publishers, 1997.

Ramanathan, V., Crutzen, P., Kiehl, J., and Rosenfeld, D.: Aerosols, climate, and the hydrological cycle, Science, 294, 2119-2124, 2001.

Ramanathan, V. L. R. D., Cess, R. D., Harrison, E. F., Minnis, P., Barkstrom, B. R., Ahmad, E., and Hartmann, D.: Cloud-radiative forcing and climate: Results from the Earth Radiation Budget Experiment. , Science, 243, 57-63, 1989.

Randall, D., Khairoutdinov, M., Arakawa, A., and Grabowski, W.: Breaking the Cloud Parameterization Deadlock, Bulletin of the American Meteorological Society, 84, 1547-1564, 10.1175/bams-84-11-1547, 2003.

Rasmussen, K. L., Choi, S. L., Zuluaga, M. D., and Houze, R. A.: TRMM precipitation bias in extreme storms in South America, Geophysical Research Letters, 40, 3457-3461, 10.1002/grl.50651, 2013.

Reinhardt, K., and Smith, W. K.: Leaf gas exchange of understory spruce–fir saplings in relict cloud forests, southern Appalachian Mountains, USA, Tree physiology, 28, 113-122, 2008.

Richardson, A. D., Denny, E. G., Siccama, T. G., and Lee, X.: Evidence for a Rising Cloud Ceiling in Eastern North America, Journal of Climate, 16, 2093-2098, 2003.

Roesner, S., Flossmann, A. I., and Pruppacher, H. R.: The effect on the evolution of the drop spectrum in clouds of the preconditioning of air by successive convective elements, Quarterly Journal of the Royal Meteorological Society, 116, 1389-1403, 1990.

Rosenfeld, D., and Woodley, W. L.: Deep convective clouds with sustained supercooled liquid water down to -37.5 °C, Nature, 405, 440-442, 2000.

Rosenfeld, D., and Feingold, G.: Explanation of the discrepancies among satellite observations of the aerosol indirect effects, Geophysical research letters, 30, 1776, 2003.

Rosenfeld, D., and Givati, A.: Evidence of orographic precipitation suppression by air pollution-induced aerosols in the western United States, Journal of applied meteorology and climatology, 45, 893-911, 2006.

Rosenfeld, D., Dai, J., Yu, X., Yao, Z., Xu, X., Yang, X., and Du, C.: Inverse relations between amounts of air pollution and orographic precipitation, Science, 315, 1396-1398, 10.1126/science.1137949, 2007.

Rosenfeld, D., Lohmann, U., Raga, G. B., O'Dowd, C. D., Kulmala, M., Fuzzi, S., Reissell, A., and Andreae, M. O.: Flood or drought: how do aerosols affect precipitation?, Science, 321, 1309-1313, 10.1126/science.1160606, 2008.

Rudich, Y., Khersonsky, O., and Rosenfeld, D.: Treating clouds with a grain of salt, Geophysical Research Letters, 29, 10.1029/2002gl016055, 2002.

Scorer, R. S., and Ludlam, F.: Bubble theory of penetrative convection, Quarterly Journal of the Royal Meteorological Society, 79, 94-103, 1953.

Seifert, A., Khain, A., Blahak, U., and Beheng, K. D.: Possible effects of collisional breakup on mixed-phase deep convection simulated by a spectral (bin) cloud model, Journal of the atmospheric sciences, 62, 1917-1931, 2005.

Seinfeld, J. H., and Pandis, S. N.: Atmospheric chemistry and physics, John Wiley, New York, 1998.

Seinfeld, J. H., and Pandis, S. N.: Atmospheric Chemistry and Physics: From Air Pollution to Climate Change, 2nd ed., Wiley, 2006.

Seto, S., Iguchi, T., and Meneghini, R.: Comparison of TRMM PR V6 and V7 focusing heavy rainfall, Geoscience and Remote Sensing Symposium (IGARSS), 2011 IEEE International, 2582-2585, 2011.

Shaw, R. A., and Lamb, D.: Experimental determination of the thermal accommodation and condensation coefficients of water, The Journal of Chemical Physics, 111, 10659-10663, 10.1063/1.480419, 1999.

Shrestha, P.: Characterization of Pre-Monsoon Aerosol and Aerosol-Cloud-Rainfall Interactions in Central Nepal, PhD thesis, 2011.

Simmel, M., Diehl, K., and Wurzler, S.: Numerical simulation of the microphysics of an orographic cloud: Comparison with measurements and sensitivity studies, Atmospheric Environment, 39, 4365-4373, 10.1016/j.atmosenv.2005.02.017, 2005.

Skamarock, W. C., Klemp, J. B., Dudhia, J., Gill, D. O., Barker, D. M., Wang, W., and Powers, J. G.: A description of the advanced research WRF version 3. Report TN-475+STR, National Center For Atmospheric Research, Boulder CO, 2008.

Snider, J. R., Guibert, S., Brenguier, J. L., and Putaud, J. P.: Aerosol activation in marine stratocumulus clouds: 2. Köhler and parcel theory closure studies, Journal of Geophysical Research: Atmospheres, 108, 10.1029/2002jd002692, 2003.

Spira, T. P.: Wildflowers and Plant Communities of the Southern Appalachian Mountains and Piedmont: A Naturalist's Guide to the Carolinas, Virginia, Tennessee, and Georgia. Univ of North Carolina Press, 2011.

Squires, P., and Turner, J. S.: An entraining jet model for cumulo-nimbus updraughts, Tellus A, 14, 1962.

Stephens, G. L., Vane, D. G., Boain, R. J., Mace, G. G., Sassen, K., Wang, Z., Illingworth, A. J., O'Connor, E. J., Rossow, W. B., Durden, S. L., Miller, S. D., Austin, R. T., Benedetti, A., and Mitrescu, C.: The Cloudsat Mission and the A-Train: A New Dimension of Space-Based Observations of Clouds and Precipitation, Bulletin of the American Meteorological Society, 83, 1771-1790, 10.1175/bams-83-12-1771, 2002.

Stephens, G. L., Vane, D. G., Tanelli, S., Im, E., Durden, S., Rokey, M., Reinke, D., Partain, P., Mace, G. G., Austin, R., L'Ecuyer, T., Haynes, J., Lebsock, M., Suzuki, K., Waliser, D., Wu, D., Kay, J., Gettelman, A., Wang, Z., and Marchand, R.: CloudSat mission: Performance and early science after the first year of operation, Journal of Geophysical Research, 113, 10.1029/2008jd009982, 2008.

Stevens, B., and Feingold, G.: Untangling aerosol effects on clouds and precipitation in a buffered system, Nature, 461, 607-613, 2009.

Still, C. J., Foster, P. N., and Schneider, S. H.: Simulating the effects of climate change on tropical montane cloud forests, Nature, 398, 608-610, 1999.

Storer, R. L., Van Den Heever, S. C., and Stephens, G. L.: Modeling aerosol impacts on convective storms in different environments, Journal of the Atmospheric Sciences, 67, 3904-3915, 2010.

Sun, B., Karl, T. R., and Seidel, D. J.: Changes in Cloud-Ceiling Heights and Frequencies over the United States since the Early 1950s, Journal of Climate, 20, 3956-3970, 10.1175/jcli4213.1, 2007.

Sun, X., and Barros, A. P.: The Impact of Forcing Datasets on the High-Resolution Simulation of Tropical Storm Ivan (2004) in the Southern Appalachians, Monthly Weather Review, 140, 3300-3326, 10.1175/mwr-d-11-00345.1, 2012.

Tanner, R. L., Bairai, S. T., and Mueller, S. F.: Trends in concentrations of atmospheric gaseous and particulate species in rural eastern Tennessee as related to primary emission reductions, Atmospheric Chemistry and Physics, 15, 9781-9797, 10.5194/acp-15-9781-2015, 2015.

Tao, K., and Barros, A. P.: Using Fractal Downscaling of Satellite Precipitation Products for Hydrometeorological Applications, Journal of Atmospheric and Oceanic Technology, 27, 409-427, 10.1175/2009jtecha1219.1, 2010.

Tao, W.-K., Li, X., Khain, A., Matsui, T., Lang, S., and Simpson, J.: Role of atmospheric aerosol concentration on deep convective precipitation: Cloud-resolving model simulations, Journal of Geophysical Research, 112, 10.1029/2007jd008728, 2007.

Tao, W.-K., Chen, J.-P., Li, Z., Wang, C., and Zhang, C.: Impact of aerosols on convective clouds and precipitation, Reviews of Geophysics, 50, 10.1029/2011rg000369, 2012.

Telford, J. W., and Chai, S. K.: A new aspect of condensation theory, pure and applied geophysics, 118, 720-742, 1980.

Telford, J. W., Keck, T. S., and Chai, S. K.: Entrainment at cloud tops and the droplet spectra, Journal of the Atmospheric Sciences, 41, 3170-3179, 1984.

Testik, F. Y., and Barros, A. P.: Toward elucidating the microstructure of warm rainfall: A survey, Reviews of Geophysics, 45, 10.1029/2005rg000182, 2007.

Testik, F. Y.: Outcome regimes of binary raindrop collisions, Atmospheric Research, 94, 389-399, 10.1016/j.atmosres.2009.06.017, 2009.

Testik, F. Y., Barros, A. P., and Bliven, L. F.: Toward a Physical Characterization of Raindrop Collision Outcome Regimes, Journal of the Atmospheric Sciences, 68, 1097-1113, 10.1175/2010jas3706.1, 2011.

Tewari, M., Chen, F., Wang, W., Dudhia, J., LeMone, M. A., Mitchell, K., Ek, M., Gayno, G., Wegiel, J., and Cuenca, R. H.: Implementation and verification of the unified NOAH land surface model in the WRF model, In 20th conference on weather analysis and forecasting/16th conference on numerical weather prediction, pp. 11-15, 2004.

Thompson, G., Field, P. R., Rasmussen, R. M., and Hall, W. D.: Explicit Forecasts of Winter Precipitation Using an Improved Bulk Microphysics Scheme. Part II: Implementation of a New Snow Parameterization, Monthly Weather Review, 136, 5095-5115, 10.1175/2008mwr2387.1, 2008.

Tsigaridis, K., and Kanakidou, M.: Secondary organic aerosol importance in the future atmosphere, Atmospheric Environment, 41, 4682-4692, 2007.

Tunved, P., Hansson, H. C., Kerminen, V. M., Strom, J., Maso, M. D., Lihavainen, H., Viisanen, Y., Aalto, P. P., Komppula, M., and Kulmala, M.: High natural aerosol loading over boreal forests, Science, 312, 261-263, 10.1126/science.1123052, 2006.

Turner, J. S.: The motion of buoyant elements in turbulent surroundings, J. Fluid Mech, 16, 1963.

Twomey, S.: The nuclei of natural cloud formation part II: The supersaturation in natural clouds and the variation of cloud droplet concentration, Pure and Applied Geophysics, 43, 243-249, 1959.

Twomey, S.: The influence of pollution on the shortwave albedo of clouds, Journal of the atmospheric sciences, 34, 1149-1152, 1977.

Unger, N., Harper, K., Zheng, Y., Kiang, N. Y., Aleinov, I., Arneth, A., Schurgers, G., Amelynck, C., Goldstein, A., Guenther, A., Heinesch, B., Hewitt, C. N., Karl, T., Laffineur, Q., Langford, B., A. McKinney, K., Misztal, P., Potosnak, M., Rinne, J., Pressley, S., Schoon, N., and Serça, D.: Photosynthesis-dependent isoprene emission from leaf to planet in a global carbon-chemistry-climate model, Atmospheric Chemistry and Physics, 13, 10243-10269, 10.5194/acp-13-10243-2013, 2013.

U.S. Air Force: Surface weather observations, Air Force Manual 15–111, Washington, D. C., 1998.

Vaughan, M. A., Powell, K. A., Winker, D. M., Hostetler, C. A., Kuehn, R. E., Hunt, W. H., Getzewich, B. J., Young, S. A., Liu, Z., and McGill, M. J.: Fully Automated Detection of Cloud and Aerosol Layers in the CALIPSO Lidar Measurements, Journal of Atmospheric and Oceanic Technology, 26, 2034-2050, 10.1175/2009jtecha1228.1, 2009.

Viviroli, D., Archer, D. R., Buytaert, W., Fowler, H. J., Greenwood, G. B., Hamlet, A. F., Huang, Y., Koboltschnig, G., Litaor, M. I., López-Moreno, J. I., Lorentz, S., Schädler, B., Schreier, H., Schwaiger, K., Vuille, M. and Woods, R.: Climate

change and mountain water resources: overview and recommendations for research, management and policy, Hydrol. Earth Syst. Sci., 15, 471–504, 10.5194/hess-15-471-2011, 2011.

Wang, J., and Wolff, D. B.: Evaluation of TRMM Ground-Validation Radar-Rain Errors Using Rain Gauge Measurements, Journal of Applied Meteorology and Climatology, 49, 310-324, 10.1175/2009jamc2264.1, 2010.

Warner, J.: The microstructure of cumulus cloud. Part I. General features of the droplet spectrum, Journal of the Atmospheric Sciences, 26, 1049-1059, 1969a.

Warner, J.: The Microstructure of Cumulus Cloud. Part II. The Effect on Droplet Size Distribution of the Cloud Nucleus Spectrum and Updraft Velocity Journal of the Atmospheric Sciences, 26, 1272-1282, 1969b.

Weathers, K. C.: The importance of cloud and fog in the maintenance of ecosystems, Trends in Ecology & Evolution, 14, 214-215, 1999.

Weisz, E., Li, J., Menzel, W. P., Heidinger, A. K., Kahn, B. H., and Liu, C.-Y.: Comparison of AIRS, MODIS, CloudSat and CALIPSO cloud top height retrievals, Geophysical Research Letters, 34, 10.1029/2007gl030676, 2007.

Williams, A. P., Schwartz, R. E., Iacobellis, S., Seager, R., Cook, B. I., Still, C. J., Husak, G., and Michaelsen, J.: Urbanization causes increased cloud base height and decreased fog in coastal Southern California, Geophysical Research Letters, 42, 1527-1536, 10.1002/, 2015.

Wilson, A. M., and Barros, A. P.: An Investigation of Warm Rainfall Microphysics in the Southern Appalachians: Orographic Enhancement via Low-Level Seeder–Feeder Interactions, Journal of the Atmospheric Sciences, 71, 1783-1805, 10.1175/jas-d-13-0228.1, 2014.

Wilson, A. M., and Barros, A. P.: Landform controls on low level moisture convergence and the diurnal cycle of warm season orographic rainfall in the Southern Appalachians, Journal of Hydrology, 531, 475-493, 10.1016/j.jhydrol.2015.10.068, 2015.

Wilson, A. M.: Elucidating the Space-Time Structure of Low Level Warm Season Precipitation Processes in the Southern Appalachian Mountains Using Models and Observations (Doctoral dissertation), 2016.

Wilson, A. M., and Barros, A. P.: Orographic Land-Atmosphere Interactions and the Diurnal Cycle of Low Level Clouds and Fog, Journal of Hydrometeorology, 10.1175/jhm-d-16-0186.1, 2017.

Winker, D. M., Pelon, J. R., and McCormick, M. P.: The CALIPSO mission: Spaceborne lidar for observation of aerosols and clouds, International Society for Optics and Photonics, 2003, 1-11,

Winker, D. M., Hunt, W. H., and McGill, M. J.: Initial performance assessment of CALIOP, Geophysical Research Letters, 34, 10.1029/2007gl030135, 2007.

Winker, D. M., Vaughan, M. A., Omar, A., Hu, Y., Powell, K. A., Liu, Z., Hunt, W. H., and Young, S. A.: Overview of the CALIPSO Mission and CALIOP Data Processing Algorithms, Journal of Atmospheric and Oceanic Technology, 26, 2310-2323, 10.1175/2009jtecha1281.1, 2009.

Wolff, D. B., and Fisher, B. L.: Comparisons of Instantaneous TRMM Ground Validation and Satellite Rain-Rate Estimates at Different Spatial Scales, Journal of Applied Meteorology and Climatology, 47, 2215-2237, 10.1175/2008jamc1875.1, 2008.

Yang, S., and Nesbitt, S. W.: Statistical properties of precipitation as observed by the TRMM precipitation radar, Geophysical Research Letters, 41, 5636-5643, 10.1002/2014gl060683, 2014.

Yildiz, O., and Barros, A. P.: Elucidating vegetation controls on the hydroclimatology of a mid-latitude basin, Journal of Hydrology, 333, 431-448, 10.1016/j.jhydrol.2006.09.010, 2007.

Young, S. A., and Vaughan, M. A.: The Retrieval of Profiles of Particulate Extinction from Cloud-Aerosol Lidar Infrared Pathfinder Satellite Observations (CALIPSO) Data: Algorithm Description, Journal of Atmospheric and Oceanic Technology, 26, 1105-1119, 10.1175/2008jtecha1221.1, 2009.

Yu, L., Shulman, M., Kopperud, R., and Hildemann, L.: Fine organic aerosols collected in a humid, rural location (Great Smoky Mountains, Tennessee, USA): Chemical and temporal characteristics, Atmospheric Environment, 39, 6037-6050, 10.1016/j.atmosenv.2005.06.043, 2005.

Zhang, C., Wang, Y., Lauer, A., Hamilton, K., and Xie, F.: Cloud base and top heights in the Hawaiian region determined with satellite and ground-based measurements, Geophysical Research Letters, 39, 10.1029/2012gl052355, 2012.

Zou, Y. S., and Fukuta, N.: The effect of diffusion kinetics on the supersaturation in clouds, Atmospheric research, 52, 115-141, 1999.

# Biography

Yajuan was born in 1987 in Xinxiang, Henan, China. She received her B.S. in Civil and Environmental Engineering at University of Macau at Macau in 2011, her M.S in Civil and Environmental Engineering at University of California-Los Angeles at Los Angeles in 2012. She earned the Ph.D. degree in Civil and Environmental Engineering at Duke University in 2017.

Yajuan has authored and co-authored two peer reviewed publications and two more publication in review in the areas of flood nonstationarity, remote sensing, aerosol-cloud interactions in the Journal of Hydrologic Engineering, Hydrology and Earth System Sciences, Atmospheric Chemistry and Physics, and Remote Sensing. One additional publication from her Ph.D. research is in preparation for publication in Atmospheric Research.